Estimating Centre of Mass Trajectory and Subject-Specific Body Segment Parameters Using Optimisation Approaches

by

Mark Andrew Jaffrey

2008

A thesis submitted in complete satisfaction of the requirements of the degree of

Doctor of Philosophy

School of Human Movement, Recreation and Performance

Faculty of Arts, Education and Human Development

Victoria University

Melbourne, Australia

Principal Supervisor: Dr. Russell J. Best

Co-supervisor: Mr. Tim V. Wrigley

Abstract

Whole body dynamics analyses are compromised by various error sources including body segment parameter (BSP) and ground reaction force (GRF) measurement errors. This research employed nonlinear optimisation techniques, attempting to account for such errors and, thus, improve dynamical representation of whole body movement activities. The first experiments demonstrated new optimisation-based integration approaches (IA optimisation methods) for determining whole body centre of mass (CM) trajectory based on double numerical integration of acceleration data derived exclusively from GRF measurements. The zero-point-to-zero-point (ZPZP) method of representing CM horizontal trajectory (King and Zatsiorsky, 1997; Zatsiorsky and Duarte, 2000) was modified by including a GRF measurement offset error term and other design variables in an optimisation process for determining CM trajectory relative to centre of pressure data. Much smoother, more realistic CM trajectory was produced by the new ZPZP IA optimisation method. New IA optimisation techniques for estimating CM trajectory during jumping activities were also demonstrated. The vertical dimension methods were all appropriate for determining transient jump performance parameters commonly calculated in jumping assessments (Hatze, 1998), including CM jump height, work and power. The final experiment presented methods of optimising inverse dynamics analyses by selecting optimal GRF measurement offset error terms and BSPs. Feasible and realistic GRF offset error terms were invariably produced. However, approximately 50% of all estimated BSPs were unrealistic under most tested conditions. Improved modelling and more contemporary motion capture technology may improve results, and may ultimately lead to the development of a versatile, relatively non-invasive and subject-specific BSP estimation method.

Student Declaration

I, Mark Jaffrey, declare that the PhD thesis entitled 'Estimating Centre of Mass Trajectory and Subject-Specific Body Segment Parameters Using Optimisation Approaches' is no more than 100,000 words in length including quotes and exclusive of tables, figures, appendices, bibliography, references and footnotes. This thesis contains no material that has been submitted previously, in whole or in part, for the award of any other academic degree or diploma. Except where otherwise indicated, this thesis is my own work.

Signature Date: 30 June 2008

Dedications

Witheld – personal in confidence.

Acknowledgements

Dr. Russell Best, my principal supervisor, for your challenging questions, patience and understanding throughout this process and for providing me with all the space I needed to produce this work.

Mr. Tim Wrigley, my co-supervisor, for the technical support you provided, particularly with respect to the force platform data acquisition software, but also for generally being a great sounding board for many of my ideas.

Dr. Anton van den Bogert, for permission to use your generalised cross-validation spline software (van den Bogert, 2000), based on the code of Woltring (1986), and your 2-D inverse dynamics software (van den Bogert, 1996b) and noiseless gait simulation data (van den Bogert, 1996a). Your assistance with interpreting the output of the 2-D inverse dynamics software in terms of precision and significant digits was greatly appreciated.

I also wish to thank my examiners, Professors V. Zatsiorsky, R. Marshall and R. Bartlett for their positive and informative feedback.

Table of Contents

Abstract i

Student Declaration ii

Dedications iii

Acknowledgements iv

Table of Contents v

List of Figures x

List of Tables xix

List of Equations xxii

Acronyms and Abbreviations xxiv

Notation xxvi

Unit Symbols xxxvi

1. INTRODUCTION 1

2. REVIEW OF LITERATURE 7

2.1 CM Kinematics Derived from Force Platform Data: Platform-Based Methods 8

2.1.1 Platform-Based Methods for Posturographic Analysis 8

2.1.2 Platform-Based Methods for Gait Analysis 25

2.1.3 Platform-Based Methods for Other Movement Analyses 30

2.1.4 Evaluation of Platform-Based Methods Using Segmental Kinematic (SK) Analysis 36

2.2 Body Segment Parameter Estimation 37

2.2.1 Body Segment Parameter Estimation and Measurement Techniques 38

2.2.1.1 Cadaver-Specific Techniques 39

2.2.1.2 Volumetric and Geometric Modelling Techniques 43

2.2.1.3 Medical Imaging Techniques 53

2.2.1.4 Predictive Techniques (Regression Equations) 62
2.2.1.5 Dynamics and Optimisation Techniques 65
2.2.1.5.1 Segment-specific Dynamics Techniques 66
2.2.1.5.2 Whole Body Dynamics and Optimisation Techniques 69
2.2.2 Evaluation of Living-Subject BSP Estimation Methods 86
2.2.3 The Influence of BSP Estimate Errors on Dynamics Analyses 95
2.3 Summary 99

3. RESEARCH AIMS 101

3.1 Rationale for the Research 101

3.2 Aims 101

4. GENERAL METHODOLOGY 104

4.1 Ethical Approval and Subject Recruitment 104

4.2 Subject Preparation 104
4.2.1 Marker Placement 105
4.2.2 Marker Designs 108

4.3 Data Capture 110
4.3.1 Subject Data 110
4.3.2 Marker Motion Capture 110
4.3.3 Kinetic Data Capture 113
4.3.4 Movement Activities Performed 114

4.4 Data Processing 115
4.4.1 Whole Body Model 115
4.4.1.1 Virtual Marker Definitions 115
4.4.1.2 Complete Definition of the Model 123
4.4.1.3 Body Segment Parameter Definitions 125
4.4.2 Marker and Kinematic Data Processing 128
4.4.3 Force Platform Data Processing 134

5. ZPZP TECHNIQUES FOR ESTIMATING CM KINEMATICS DURING STANCE 137

5.1 Research Design **137**
5.1.1 The Modified ZPZP Methods 137
5.1.2 ZPZP Method Comparisons 149
5.1.3 Hypotheses and Statistical Approaches 150
5.2 Results **153**
5.3 Discussion **170**
5.3.1 Unconventional ZPZP Methods 170
5.3.2 Conventional ZPZP Methods 172
5.3.3 Sampling Rate: 40 Hz *versus* 1000Hz 175
5.3.4 Estimating Fy_O: De-trending *Fy versus* Optimisation Approaches 175
5.3.5 Low-Pass Filtering of GRF Data: Effect of Cut-off Frequency 178
5.3.6 Conventional *versus* Unconventional Optimised ZPZP Approaches 179
5.3.7 The Best Method, Future Improvements and Assessments 182
5.3.8 Summary 188

6. INTEGRATION APPROACH (IA) OPTIMISATION TECHNIQUES FOR ESTIMATING CM KINEMATICS DURING JUMPING ACTIVITIES 190

6.1 Research Design **190**
6.1.1 The IA Optimisation Methods 190
6.1.1.1 Definition of the Core IA Optimisation Approaches 191
6.1.1.2 Variations of the Definition of Quasi-static Phase Duration 197
6.1.1.3 Summary of the Seven Methods 199
6.1.2 Assessment of the IA Optimisation Methods 201
6.1.2.1 IA-SK RMS Parameters and Associated Hypotheses 201
6.1.2.2 Qualitative Assessment 205
6.1.2.3 Practical Assessment Using Jump Performance Parameters. 206
6.1.2.4 Generic Parameter 207
6.1.3 Assessment of the Influence of $CM'[z]_{IA}(0)$, Fz_O and m_{WB} 208
6.1.4 Identification and Zeroing of Airborne Phase GRF Values 210
6.2 Results **212**

6.2.1 Vertical Dimension Methods 212
6.2.2 Antero-Posterior Dimension Methods 220
6.2.3 The Influence of $CM'[z]_{IA}(0)$, Fz_O and m_{WB} 225
6.2.4 Additional Analysis of Drift 232

6.3 Discussion 240

6.3.1 Relative Performance of the Methods 242
6.3.1.1 Vertical Dimension Methods 242
6.3.1.2 Antero-Posterior Dimension Methods 246
6.3.2 Quasi-static Phase Duration: *Max versus 2000* 249
6.3.3 The Influence of $CM'[z]_{IA}(0)$, Fz_O and m_{WB} 250
6.3.4 Potential Sources of Drift Error 253
6.3.5 Summary 255

7. COMBINED DYNAMICS AND OPTIMISATION TECHNIQUES FOR ESTIMATION OF BSPS 259

7.1 Research Design 260

7.1.1 The Combined Dynamics and Optimisation Methods 260
7.1.1.1 Movement Activities and Trial Formulation 260
7.1.1.2 Design Variables and Constraints 261
7.1.1.3 The First Three Dynamics-Based Objective Functions 266
7.1.1.4 Code Development, Validation and Observations 277
7.1.1.5 The Fourth Dynamics-Based Objective Function 278
7.1.2 Kinematic Data Filtering: Assessed Conditions 279
7.1.3 Assessment of the Objective Functions, Force Offset Error Terms, BSP Estimates and Degree of Filtering 282

7.2 Results 284

7.2.1 Objective Function Values 284
7.2.2 BSP and Force Offset Error Term Estimates 286
7.2.3 Filtering Approaches 289

7.3 Discussion 291

7.3.1 Objective Function Values 291
7.3.2 Filtering Approaches 293
7.3.3 Force Offset Error Term Design Variables 295
7.3.4 BSP Estimates 296

7.3.5 Comparison of the Current Research with Vaughan (1980) and Vaughan et al. (1982a) 298
7.3.6 Rationale for Future Research 305
7.3.7 Recommendations for Future Research 306
7.3.8 Summary 307

8. CONCLUSION 309

REFERENCES 313

Primary References 313

Secondary References 330

Appendix A : The Sensitivity of the *ZPZP4U* and *ZPZP5C* Objective Functions and other Parameters to Perturbations of the Design Variables 333

Appendix B : Testing and Ensuring Convergence 344

List of Figures

Figure 1. The quiet stance plots from figure 2 of Lafond et al. (2004), reprinted with permission of Elsevier, showing the good agreement between the CM trajectory plots derived from the SK approach (labelled COM*) and the ZPZP method of Zatsiorsky and Duarte (2000) (labelled* GLP*), and less agreement with the CM trajectory plot derived from the low-pass filter method of Caron et al. (1997) (labelled* LPF*). More significantly, the relationship between COP trajectory (labelled* COP*) and* LPF *is clearly unrealistic (e.g. for the first three seconds,* LPF *CM trajectory changes direction several times while* COP *remains on one side of* LPF*).* 10

Figure 2. The very different CM(*t*) *plots resulting from the 'trend eradication' (*GL-2*) and 'threshold' (*GL-3*) methods of King and Zatsiorsky (1997). Reprinted and adapted from figure 3, King and Zatsiorsky (1997) with permission of Elsevier.* 19

Figure 3. Plot of CM(*t*) *(*GL-3*) resulting from the application of the 'threshold' method (King and Zatsiorsky, 1997), for quiet standing, eyes closed. The function does not appear to be smooth at the first IEP at* Time ≈ 0.8 *s, and possibly at several other IEPs. Reprinted and adapted from figure 4, King and Zatsiorsky (1997) with permission of Elsevier.* 22

Figure 4. Flow diagram outlining the overall objective and aims of the research, and broad descriptions of the approaches adopted to address these aims. 103

Figure 5. The locations of the LED markers on the subject. Note, the foot and hand markers are illustrated more clearly and labelled in Figs. 6 and 7, respectively. 105

Figure 6. The locations of the LED markers positioned on the lateral malleolus and dorsum of the foot. 107

Figure 7. The locations of the LED markers positioned on the dorsum of the hand over the wrist and tip of the middle digit. 107

Figure 8. The various LED marker types used in this research. All markers were placed on the subject so that the LED light beams were projected laterally with respect to the subject: (a) the marker designed for the Ankle; (b) the double-LED marker, designed for the Vertex and all trunk markers, pictured here with LED beams projecting towards the top and bottom of the page; (c) the most common marker, designed for lateral placement on the body over a joint centre, pictured here with the LED beam projecting out of the page; and (d) the Ball marker designed for placement on the dorsum of the foot, pictured here with the LED beam projecting towards the bottom of the page. 108

Figure 9. The 2-D, 15-segment model developed for this research. All segments and joints are labelled, with the exception of the left limbs

and the Lower Arm segment. The Lower Arm segment is defined in section 4.4.1.2. 116

Figure 10. Example of how the position of an actual unilateral Hip marker was expressed relative to the C7-T1 and Suprasternale marker positions during Step 1 of virtual marker calculation Method B. The position of the Hip marker was expressed in a local coordinate system with origin at C7-T1 and one of the reference axes passing through the Suprasternale marker. Local coordinates were expressed in terms of proportions of Γ, the length from C7-T1 to Suprasternale. This example is for illustrative purposes only and does not show true Hip coordinates. 119

Figure 11. Stick figure representation of the model defined for this research: The model, with associated actual and virtual markers, is shown superimposed on a photograph of the subject. Refer also to Tables 1 and 2 for definitions of the segments and joints incorporated into the model, and to section 4.4.1.1 for relevant virtual marker definitions. 122

Figure 12. The segment-based reference system, with axes L and P, used to locate each segment's cm_{seg} BSP. l_{seg} is segment length. The example cm_{seg} BSP of $(cm[L]_{seg}, cm[P]_{seg}) = (0.6, -0.1)$ depicted by the black dot is for illustrative purposes only and is not necessarily realistic. 126

Figure 13. The position and orientation in the sagittal plane of the segment-based reference systems used to locate each respective segment's centre of mass position. 127

Figure 14. The global coordinate system used in this research with an origin at the centre of the top surface of the force platform, positive Z *in the upwards direction, positive* Y *in the posterior-to-anterior direction, and* OYZ *representing the (sagittal) plane of motion. The positive* X *axis was defined by the right-hand rule, relative to the other two axes and was from the left to the right side of the subject for all movement trials.* 129

Figure 15. Demonstration of the potential effect on the timing and number of zero-force-crossings in a quiet stance trial elicited by adding an offset error term (Fy_O) to the antero-posterior GRF (Fy) measurements. Such a change may alter the ZPZP results. For example, there are 10 IEPs shown above in the original Fy measurements. However, with the inclusion of an error term, $Fy_O = -0.45$ N, the timing of those IEPs within the trial shifts and there are now an additional 4 IEPs. 139

Figure 16. Range plot showing the median, range and raw data points of the IEP Displacement Parameter values across the six trials assessed in this research, for each of the unconventional ZPZP methods (ANOVA χ^2 [df = 3, N = 6] = 13.4, p = 0.00385). 154

Figure 17. Range plot showing the median, range and raw data points of the IEP Velocity Parameter values across the six trials assessed in this

research, for each of the conventional ZPZP methods (ANOVA χ^2 [df = 4, N = 6] = 20.8, p = 0.00035). 154

Figure 18. Plot of CM[y]$_{IA}$(t) (blue dashed line) and COP[y](t) (red solid line) with IEPs (squares), resulting from the ZPZP1U method (trial '4463'), indicating unrealistic CM[y]$_{IA}$(t) estimates. 155

Figure 19. Plot of CM[y]$_{IA}$(t) and COP[y](t) with IEPs, resulting from the application of method ZPZP2U, again indicating unrealistic CM[y]$_{IA}$(t) estimates. For this trial ('4463'), the inclusion of de-trended Fy in the ZPZP2U method has produced a greater number of IEPs, but negligible improvement towards what, in theory, should be the co-location of CM[y]$_{IA}$(t) and COP[y](t) at the IEPs. 156

Figure 20. Plot of CM[y]$_{IA}$(t) and COP[y](t) with IEPs, resulting from method ZPZP3U (trial '4463'). The use of data sampled at 1000 Hz in ZPZP3U, as opposed to 40 Hz in ZPZP2U, made no discernable improvement (compared to Fig. 19). Hence, the scale of this plot was matched to that of the ZPZP4U plot in Fig. 22, thus permitting a more meaningful comparison of these two figures. 156

Figure 21. Plot of CM[y]$_{IA}$(t) and COP[y](t) with IEPs, resulting from the ZPZP1U method (trial '4461'), indicating better but still unrealistic CM[y]$_{IA}$(t) estimates and an unrealistically short interval (t = 5.85 to 8.65 s) spanning the first and last IEPs. 157

Figure 22. Plot of CM[y]$_{IA}$(t) and COP[y](t) with IEPs, resulting from method ZPZP4U (trial '4463'), showing more realistic, yet still somewhat unrealistic CM[y]$_{IA}$(t) estimates, particularly during the 1 to 6 second period. 158

Figure 23. A more realistic plot of CM[y]$_{IA}$(t) relative to COP[y](t), resulting from the application of method ZPZP4U (trial '4462'). Note, relative to Fig. 22, the more inclusive nature of CM[y]$_{IA}$(t) within the surrounding COP[y](t) trajectory, and the closer approximation of CM[y]$_{IA}$(t) to the IEPs. 159

Figure 24. Plot of CM'[y]$_{IA}$(t) for trial '4463' (method ZPZP4U). As for all unconventional ZPZP methods, the velocity function is smooth and continuous. The values seem realistic for quiet stance, all being within a range of ±0.011 m/s. 159

Figure 25. Plot of CM[y]$_{IA}$(t) and COP[y](t) with IEPs resulting from the application of method ZPZP1C (trial '4463'), indicating unrealistic CM[y]$_{IA}$(t) 'humps'. 161

Figure 26. Plot of CM'[y]$_{IA}$(t) for trial '4463' (method ZPZP1C). The velocity function is not continuous at the IEPs. 161

Figure 27. Plot of CM[y]$_{IA}$(t) and COP[y](t) with IEPs resulting from the ZPZP2C method. For this trial ('4463'), the inclusion of de-trended Fy in the ZPZP2C method has produced more IEPs and noticeable improvement in CM[y]$_{IA}$(t) trajectory, although sharp turning points are apparent at some IEPs. 162

Figure 28. Plot of CM'[y]$_{IA}$(t) for trial '4463' (method ZPZP2C). The velocity function was not continuous at the IEPs and it often had negative slope for several consecutive ZPZP intervals. The ZPZP3C method produced an essentially equivalent plot. 162

Figure 29. Plot of CM[y]$_{IA}$(t) and COP[y](t) with IEPs resulting from the ZPZP5C method (trial '4463'). ZPZP5C produced noticeable improvement in the smoothness of the CM[y]$_{IA}$(t) trajectory, relative to ZPZP2C. 163

Figure 30. Plot of CM'[y]$_{IA}$(t) for trial '4463' (method ZPZP5C). The velocity function is not continuous at the IEPs, but the discrepancies are less than those for methods ZPZP1C to ZPZP3C. Note also that the slope of CM'[y]$_{IA}$(t) alternates between positive and negative from ZPZP interval to ZPZP interval. 164

Figure 31. Plot of CM[y]$_{IA}$(t) and COP[y](t) with IEPs resulting from the ZPZP6C method (trial '4463'), which produced a noticeable improvement in the smoothness of the CM[y]$_{IA}$(t) trajectory, relative to the ZPZP5C method. 165

Figure 32. Plot of CM'[y]$_{IA}$(t), with IEPs marked, for trial '4463' (method ZPZP6C). The inset magnification shows what would otherwise appear to be a continuous function at the given IEP. However, a small discrepancy still exists (0.00008 m/s). Although the velocity function is not continuous at the IEPs, the discrepancies are less than those for all other conventional ZPZP methods. 165

Figure 33. Range plot showing the median, range and raw data points of the IEP Displacement Parameter values across the six trials assessed in this research, for unconventional method ZPZP4U and conventional method ZPZP6C. 166

Figure 34. Range plot showing the median, range and raw data points of the IEP Velocity Parameter values for the ZPZP5C method, across the six trials assessed in this research, that resulted when the supplied data were smoothed at various cut-off frequencies (ANOVA χ^2 [df = 9, N = 6] = 40.7, p = 0.00001). 168

Figure 35. Plot of CM[y]$_{IA}$(t) and COP[y](t) with IEPs resulting from the ZPZP5C method (trial '4466') for force data low-pass filtered at 30 Hz. 169

Figure 36. Plot of CM[y]$_{IA}$(t) and COP[y](t) with IEPs resulting from the ZPZP5C method (trial '4466') for force data low-pass filtered at 6 Hz. 169

Figure 37. Plots of COP[y](t) (labelled COP*) and CM[y]$_{IA}$(t) (labelled* GLP*), reprinted and adapted from figure 5 of King and Zatsiorsky (2002), with permission of Elsevier. The inset magnification shows instances between approximately 18 to 19 s when the CM[y]$_{IA}$(t) plot is not smooth, inferring CM'[y]$_{IA}$(t) is not continuous at these points in time.* 174

Figure 38. Record of Fz versus time from just prior to the commencement of the airborne phase until just after the completion of the airborne

phase of a typical trial captured in this study. Note that Fz does not return to zero during the airborne phase. 211

Figure 39. Range plots of Quasi-static and Airborne RMS $CM[z]_{IA\text{-}SK}$ Parameter values (Eq. (39) and Eq. (40), respectively) across six trials assessed in this research, for each of the four vertical dimension IA optimisation methods, illustrating the relationship between relative $CM[z]_{IA}$ and $CM[z]_{SK}$ values is significantly closer during the quasi-static phase compared to the airborne phase. 213

Figure 40. Plots of relative $CM[z]_{IA}(t)$ and relative $CM[z]_{SK}(t)$ for a typical countermovement jump (trial '5208'). Only IA optimisation Methods AMax and BMax are shown up to and including the airborne phase. The end of the defined quasi-static phase is indicated (t_{QSfin}). 214

Figure 41. Plots of relative $CM[z]_{IA}(t)$ and relative $CM[z]_{SK}(t)$ for the airborne phase of the same trial as Fig. 40 (trial '5208'). All four vertical dimension IA optimisation methods are shown, with A2000 and B2000 $CM[z]_{IA}(t)$ plots offset relative to the AMax and BMax plots (the offset procedure is explained on page 218 and the rationale for its application is depicted clearly in Fig. 42. Peak Height differences between IA methods of up to 9.2 mm are depicted, with 14.9 mm between the SK method and Method AMax. 215

Figure 42. Plots of relative $CM[z]_{IA}(t)$ and relative $CM[z]_{SK}(t)$ for the quasi-static phase and the start of the countermovement phase of trial '5208'. The A2000 and B2000 relative $CM[z]_{IA}(t)$ plots are adjusted with respect to the AMax and BMax plots, as described in the above text, to enable a valid graphical comparison. The start of the quasi-static phases, as defined by the Max and 2000 methods, and the end of the quasi-static phase, which has a common definition in both methods, are shown here as $t_{QSini\ (Max)}$, $t_{QSini\ (2000)}$ and $t_{QSfin\ (both)}$, respectively. 218

Figure 43. Plots of relative $CM[z]_{IA}(t)$ and relative $CM[z]_{SK}(t)$ for the airborne and landing phases of the same trial as Figs. 40, 41 and 42 (trial '5208'). The A2000 and B2000 relative $CM[z]_{IA}(t)$ plots are adjusted with respect to the AMax and BMax plots, as described on page 218. The start and finish of the airborne phase are indicated by t_{ABini} and t_{ABfin}, respectively. 219

Figure 44. Range plot showing the median, range and raw data points of the Quasi-static RMS $CM[y]_{IA\text{-}SK}$ Parameter values (Eq. (37)) across the six trials assessed in this research, for the three antero-posterior dimension IA optimisation methods (ANOVA χ^2 [df = 2, N = 6] = 10.3, p = 0.00570). 222

Figure 45. Plots of relative $CM[y]_{IA}(t)$, relative $CM[y]_{SK}(t)$ and relative $COP[y](t)$ for the quasi-static phase for trial '5210'. All three antero-posterior [y] dimension IA optimisation methods are shown, with the relative $COP[y](t)$ plot and the ZPZP5U and B2000 relative $CM[y]_{IA}(t)$ plots adjusted with respect to the BMax plot, as described on page 222, to enable a valid graphical comparison. The start of the

quasi-static phases, as defined by the BMax, B2000 and ZPZP5U methods, are shown here as $t_{QSini\ (BMax)}$, $t_{QSini\ (B2000)}$ and $t_{QSini\ (ZPZP5U)}$, respectively. 223

Figure 46. Plots of relative $CM[y]_{IA}(t)$ and relative $CM[y]_{SK}(t)$ for the quasi-static, countermovement and airborne phases for the same trial as depicted in Fig. 45 (trial '5210'). The ZPZP5U and B2000 relative $CM[y]_{IA}(t)$ plots are adjusted with respect to the BMax plot, as described on page 222, to enable a valid graphical comparison. $t_{QSini\ (BMax)}$, $t_{QSini\ (B2000)}$ and $t_{QSini\ (ZPZP5U)}$ denote the start of the quasi-static phases, as defined by the three antero-posterior [y] methods. The end of the quasi-static stance phase (t_{QSfin}) is also shown, as are the start and finish of the airborne phase (t_{ABini} and t_{ABfin}). 224

Figure 47. Plots of relative $CM[z]_{SK}(t)$, relative $CM[z]_{IA}(t)$ and $CM'[z]_{SK\text{-}IA}(t)$ for Method B2000[z] (trial '5209'). This full-scale graph shows the relatively erratic behaviour of the $CM'[z]_{SK\text{-}IA}(t)$ plot during the dynamic phases of the trial (shaded) and its relative consistency during the pre- and post-jump quasi-static phases. 233

Figure 48. Zoomed plot of $CM'[z]_{SK\text{-}IA}(t)$ for Method B2000[z] (trial '5209'), concentrating on the unshaded, pre- and post-jump quasi-static stance phases. A linear regression line fitted to the post-jump quasi-static phase data (not shown) had a gradient of -0.0052, suggesting the presence of a quadratic drift, with respect to t, in post-landing $CM[z]_{IA}(t)$ calculations. Trials '5211', '5212' and '5217' produced similar results. 235

Figure 49. Zoomed plot of $CM'[y]_{SK\text{-}IA}(t)$ for Method ZPZP5U[y] (trial '5212'), concentrating on the unshaded, pre- and post-jump quasi-static stance phases. A linear regression line fitted to the post-jump quasi-static phase data (not shown) had a gradient of -0.0011, suggesting the presence of a subtle quadratic drift, with respect to t, in post-landing $CM[y]_{IA}(t)$ calculations. Trials '5209' and '5217' produced similar results but with progressively more pronounced quadratic drifts (see also Fig. 51 for trial '5217'). 236

Figure 50. Zoomed plot of $CM'[y]_{SK\text{-}IA}(t)$ for Method ZPZP5U[y] (trial '5211'), concentrating on the unshaded, pre- and post-jump quasi-static stance phases. A linear regression line fitted to the post-jump quasi-static phase data had an essentially negligible gradient of -0.0001 and a mean value, essentially, of zero, suggesting the presence of no drift or, possibly, a subtle linear or quadratic drift, with respect to t, in post-landing $CM[y]_{IA}(t)$ calculations. 237

Figure 51. Plot (not zoomed in) of $CM'[y]_{SK\text{-}IA}(t)$ for Method ZPZP5U[y] (trial '5217'), concentrating on the unshaded, pre- and post-jump quasi-static stance phases. A linear regression line fitted to the post-jump quasi-static phase data had a gradient of 0.0288, suggesting the presence of a quadratic drift, with respect to t, in post-landing $CM[y]_{IA}(t)$ calculations. This plot was not zoomed to the same scale as the previous two figures due to the comparatively large gradient of

$CM'[y]_{SK\text{-}IA}(t)$. A larger scale was also required for the left axis because this trial was the broad jump. 238

Figure 52. Two of the possible five orders of progression of entire body IDA calculations for the model used in this research. Arrows indicate the directions in which the IDA calculations proceed. The left figure illustrates how an IDA commencing with Distal-to-Proximal (DP) calculations for the limbs leads to Proximal-to-Distal (PD) net force and moment calculations for the trunk-neck joint, the head-neck joint and the vertex of the head. The right figure shows how commencing with DP calculations for the non-supported 'extremities' leads to PD net force and moment calculations for the hip, knee and ankle joints and the distal end of the support leg. Once IDA calculations have been conducted through the entire body using all five possible orders of progression (i.e. one terminating at each of the five 'extremities'), a pair of PD and DP net forces and moments has been calculated for all joints and distal segment end-points. 270

Figure 53. A free body diagram of a segment and the 2-D components of the net joint forces (Fy and Fz) and the moments (Mx) acting on the segment at both its commencing and terminating end-points of the IDA (viz. Comm and Term). The 2-D position coordinates of Comm and Term and of the segmental centre of mass are bracketed and shown in red. 271

Figure 54. A two-segment system (left box), linked at the joint inside the grey circle. The main part of the figure, showing the free body diagrams of both segments, illustrates the bi-directional (DP and PD) IDA calculations possible at the joint linking both segments. $Fy_{TermA}(DP)$, $Fz_{TermA}(DP)$ and $Mx_{TermA}(DP)$ are the net external force and moment acting at point TermA, as determined by a DP IDA of segA. $Fy_{TermB}(PD)$, $Fz_{TermB}(PD)$ and $Mx_{TermB}(PD)$ are the net external force and moment acting at point TermB, as determined by a PD IDA of segB. For a theoretically perfect system, these kinetic quantities are equal and opposite. That is, $Fy_{TermA}(DP) + Fy_{TermB}(PD)$, $Fz_{TermA}(DP) + Fz_{TermB}(PD)$ and $Mx_{TermA}(DP) + Mx_{TermB}(PD)$ should all equal zero. 273

Figure 55. The minimised objective function values of objective functions IDA_{Foot}, IDA_{Foot} and IDA_{All} (Foot, Hip and All, respectively), under each of the four kinematic data filtering conditions (70%GCV, 80%GCV, 90%GCV and GCV). 284

Figure 56. DP-PD net moment residuals (mean values across entire trial) at each of the joints and at each extremity distal segment end-point, prior to and after the application of IDA_{All} (Starting Point – SP, and Optimised - Opt, respectively), for a typical low acceleration trial (Low Acc Trial A; 70%GCV) and a typical high acceleration trial (High Acc Trial D; 70%GCV). 285

Figure 57. The number of active BSP bound constraints for objective functions IDA_{Foot}, IDA_{Foot}, IDA_{All} and IDA_{All_2} (Foot, Hip, All and

All_2, respectively), under each of the four kinematic data filtering conditions (70%GCV, 80%GCV, 90%GCV and GCV). 286

Figure 58. The percentage of all 64 cases (i.e. 4 trials × 4 objective functions × 4 filtering conditions) for which each BSP's lower and upper bound constraints became active. 288

Figure 59. The minimised objective function values of objective functions IDA_{Foot}, IDA_{Hip}, IDA_{All} and IDA_{All_2} (Foot, Hip, All and All_2, respectively) for trials A and B, under each of the four kinematic data filtering conditions (70%GCV, 80%GCV, 90%GCV and GCV). 289

Figure 60. The minimised objective function values of objective functions IDA_{Foot}, IDA_{Hip}, IDA_{All} *and* IDA_{All_2} *(Foot, Hip, All and All_2, respectively) for trials C and D, under each of the four kinematic data filtering conditions (70%GCV, 80%GCV, 90%GCV and GCV).* 290

Figure 61. The number of active BSP bound constraints for the four kinematic data filtering conditions (70%GCV, 80%GCV, 90%GCV and GCV), for each of the objective functions (IDA_{Foot}, IDA_{Foot}, IDA_{All} and IDA_{All_2}). 290

Figure 62. Oblique view of the surface map of feasible ZPZP4U solutions, with respect to Eqs. (25), in the Fz_C-Mx_O subspace (trial '4461'), showing the relative insensitivity of the objective function to the broadly feasible range of Fz_C and Mx_O perturbations (0.121 mm difference; cf. Figs. 63 and 64). 334

Figure 63. Oblique view of the surface map of feasible ZPZP4U solutions, with respect to Eqs. (25), in the Fz_C-Fy_O subspace (trial '4461'). The relative insensitivity and sensitivity, respectively, of the objective function to feasible perturbations of Fz_C and Fy_O is indicated by the plotted surface: a valley with steep sides in the Fy_O dimension but relatively negligible slope in the Fz_C dimension. 334

Figure 64. Oblique view of the surface map of feasible ZPZP4U solutions, with respect to Eqs. (25), in the Fy_C-Fy_O subspace (trial '4461'). The sensitivity of the objective function to feasible perturbations of both Fy_C and Fy_O is indicated by the plotted surface: a valley with steep sides in both the Fy_C and Fy_O dimensions and a long axis, with essentially zero slope, projected diagonally onto the Fy_C-Fy_O plane. 335

Figure 65. Same surface map as in Fig. 64, but now as viewed from 'side-on' at (Fy_C, Fy_O, Objective-Function) = (1, 2.23, 0), indicating the relatively negligible change along the valley's long axis (< 0.023 mm difference for trial '4461'). 335

Figure 66. The relationship between Fy_O and the subsequent number of IEPs and the ZPZP4U objective function value for a typical quiet stance trial ('4461'). 345

Figure 67. Non-feasible CM[y](t) and COP[y](t) resulting from the application of ZPZP4U (trial '4461') with Fy_O assigned a value of -0.5 N, well below its feasible range, with respect to Eqs. (25), of 1.489 to 1.515 N. 346

Figure 68. Non-feasible CM[y](t) and COP[y](t) resulting from the application of ZPZP4U (trial '4461') with Fy_O assigned a value of 1.44 N, still somewhat below its feasible range, with respect to Eqs. (25), of 1.489 to 1.515 N. *346*

Figure 69. Non-feasible CM[y](t) and COP[y](t) resulting from the application of ZPZP4U (trial '4461') with Fy_O assigned a value of 1.52 N, just above its feasible range, with respect to Eqs. (25), of 1.489 to 1.515 N. Note that min(CM[y](t)) is just less than min(COP[y](t)). *347*

Figure 70. Non-feasible CM[y](t) and COP[y](t) resulting from the application of ZPZP4U (trial '4461') with Fy_O assigned a value of 3.8 N, well above its feasible range, with respect to Eqs. (25), of 1.489 to 1.515 N. *347*

Figure 71. 'Corrected' Fy (trial '4461') with Fy_O assigned a value well above its feasible range (3.8 N). The ZPs are marked with squares. See related Fig. 70. *348*

Figure 72. 'Corrected' Fy (trial '4461') with Fy_O assigned a value just above its feasible range (1.52 N). The ZPs are marked with squares. See related Fig. 69. *349*

List of Tables

Table 1. Segment definitions in terms of the various markers (actual and virtual) used to represent the distal and proximal segment end-points. Virtual markers are subscripted with an A, B, or C, reflecting one of the three different methods applied to derive such markers (see section 4.4.1.1). Inferior and superior trunk end-points were considered proximal and distal, respectively. L/R refers to left or right. 123

Table 2. Joint definitions in terms of the various actual and virtual markers used and derived, respectively, to represent the joint centres. Virtual markers are subscripted with an A, B, or C, reflecting one of the three different methods applied to derive such markers (see section 4.4.1.1). For any joint centre that was, by definition, co-located with one or more of the defined segment end-point locations, such end-points are listed in parentheses. Inferior and superior trunk end-points were considered proximal and distal, respectively. L/R refers to left or right. 124

Table 3. The bound constraints initially applied to the proposed design variables, but later rejected, based on the sensitivity analyses (see Appendix A). Also shown are the initial estimates of the proposed design variables that were used for all ZPZP4U and ZPZP5C optimisations. 145

Table 4. Summary of all the ZPZP methods assessed in this experiment. Methods with the suffix C denote 'conventional' methods, in which the ZPZP algorithm (see page 17) was applied in the conventional manner across each and every ZPZP interval, as per Zatsiorsky and Duarte (2000). Methods with the suffix U denote 'unconventional' methods, in which the ZPZP algorithm was applied in an unconventional manner once only across the entire interval spanned by the initial and final identified ZPs. 148

Table 5. Results of the Friedman rank-order ANOVA tests (N = 6) used to assess Hypotheses 1 and 2. 153

Table 6. Results of the Wilcoxon matched pairs tests (N = 6) used to assess Hypotheses 3 and 4. 166

Table 7. Results of the Friedman rank-order ANOVA tests (N = 6) used to assess Hypotheses 5 and 6. 168

Table 8. The three core approaches to IA optimisation developed and assessed in this experiment (column 1). Column 2 indicates each specific method formulated under each basic category, based on different definitions of the duration of the quasi-static stance phase. The dimension and the design variables relevant to each method's objective function are indicated in columns 3 and 4, respectively. Design variables TOL_0 and TOL_{fin} are defined in section 6.1.1.1 on page 194. 200

Table 9. Median and range values for the duration of the quasi-static phase for all variable-duration methods (N= 6). By definition, the other methods (A2000[z], B2000[z] and B2000[y]) all had quasi-static phases with a set duration of 2000 ms. 212

Table 10. Results of the Friedman rank-order ANOVA tests (N = 6) used to assess the vertical IA optimisation methods (Hypotheses 7 and 8). 213

Table 11. Jump performance parameters $Height_J$ and $Height_P$ that resulted from the application of each of the vertical dimension IA methods for all six trials, and the maximum between-method differences expressed in absolute terms (mm) and as a percentage (%) of the maximum parameter value produced for that trial (the bolded result in the relevant row). It is evident that no particular method consistently produced the largest or smallest values across all trials. 216

Table 12. Jump performance parameters $Work_P$, $Max\ Power_P$ and $Ave\ Power_P$ that resulted from the application of each of the vertical dimension IA methods for all six trials, and the maximum between-method differences expressed in absolute terms (J/kg or W/kg) and as a percentage (%) of the maximum parameter value produced for that trial (the bolded result in the relevant row). It is evident that no particular method consistently produced the largest or smallest values across all, or even most trials for these parameters. 217

Table 13. Results of the Friedman rank-order ANOVA tests (N = 6) used to assess the antero-posterior IA optimisation methods (Hypotheses 9 and 10). 221

Table 14. For Methods A2000[z] and B2000[z], the maximum, mean and SD of the changes (Δ) in the jump performance parameters $Height_J$, $Height_P$, $Work_P$, $Max\ Power_P$ and $Ave\ Power_P$ (all defined in section 6.1.2.3) across all trials, produced by setting $CM'[z]_{IA}(0)$ to zero (Condition 2). These changes are expressed in absolute terms (mm, J/kg or W/kg) and, except for SD, as percentages (%) of the parameter values derived from the originally optimised solutions (Condition 1). Negative values denote reductions. 226

Table 15. For Methods A2000[z] and B2000[z], the maximum, mean and SD of the changes (Δ) in the jump performance parameters $Height_J$, $Height_P$, $Work_P$, $Max\ Power_P$ and $Ave\ Power_P$ (all defined in section 6.1.2.3) across all trials, produced by perturbing the originally optimised Fz_O value by +1 N (Condition 3). These changes are expressed in absolute terms (mm, J/kg or W/kg) and, except for SD, as percentages (%) of the parameter values derived from the originally optimised solutions (Condition 1). Negative values denote reductions. 228

Table 16. For Methods A2000[z] and B2000[z], the maximum, mean and SD of the changes (Δ) in the jump performance parameters $Height_J$, $Height_P$, $Work_P$, $Max\ Power_P$ and $Ave\ Power_P$ (all defined in section 6.1.2.3) across all trials, produced by including m_{WB} as a design variable and setting Fz_O to zero (Condition 4). These changes are expressed in absolute terms (mm, J/kg or W/kg) and, except for

SD, as percentages (%) of the parameter values derived from the originally optimised solutions (Condition 1). Negative values denote reductions 230

Table 17. For Methods A2000[z] and B2000[z], the maximum, mean and SD of the changes (Δ) in the generic parameter Peak Height (defined in section 6.1.2.4) across all trials, produced by setting $CM'[z]_{IA}(0)$ to zero (Condition 2), perturbing the originally optimised Fz_O value by +1 N (Condition 3), and including m_{WB} as a design variable and setting Fz_O to zero (Condition 4). These changes are expressed in absolute terms (mm) and, except for SD, as percentages (%) of the parameter values derived from the originally optimised solutions (Condition 1). Negative values denote reductions. 231

Table 18. Gradients of the linear regression lines fitted to the $CM'_{SK\text{-}IA}(t)$ data separately for the pre- and post-jump quasi-static (QS) phases across the four relevant trials for Methods B2000[z] and ZPZP5U[y]. 234

Table 19. The initial values and lower and upper bound constraints applied to each of the m_{seg} and I_{seg} BSP design variables included in the optimisations. Each segment's mass (m_{seg}) is expressed as a proportion of whole body mass (m_{WB}) and the principal segmental moments of inertia about the subject's transverse axis through each segment's centre of mass (I_{seg}) are expressed in kgm^2. 263

Table 20. The initial values and lower and upper bound constraints applied to each of the segmental centre of mass BSP design variables. Each segment's longitudinal and perpendicular segmental centres of mass ($cm[L]_{seg}$ and $cm[P]_{seg}$) are expressed as proportions of segment length. 264

Table 21. The design variable coordinates for which absolute and relative $COP[y](t_i)$ and $CM[y]_{IA}(t_i)$ parameters were calculated. Cases with shaded cells in the same column were used to assess the sensitivity of these parameters to perturbations in each corresponding design variable. (wrt = 'with respect to'). 340

Table 22. Results of sensitivity analyses showing the largest differences observed across all trials for each of the relative and absolute parameters ΔABS1, ΔABS2, ΔREL1, ΔREL2, *and* RMS REL3. *All measures are in metres. Negative values in the* ΔREL1 *and* ΔREL2 *columns indicate that these relative parameters increased as the relevant design variable increased. See Table 21 for definitions of case numbers.* 341

List of Equations

Equation (1) *12*
Equation (2) *12*
Equation (3) *13*
Equation (4) *13*
Equation (5) *13*
Equations (6) *15*
Equation (7) *33*
Equation (8) *33*
Equation (9) *40*
Equation (10) *72*
Equation (11) *72*
Equation (12) *80*
Equation (13) *80*
Equations (14) *80*
Equations (15) *131*
Equations (16) *131*
Equation (17) *132*
Equations (18) *133*
Equations (19) *133*
Equation (20) *134*
Equations (21) *135*
Equations (22) *136*
Equation (23) *141*
Equation (24) *143*
Equations (25) *143*
Equations (26) *146*
Equation (27) *146*
Equation (28) *192*
Equation (29) *192*
Equation (30) *192*
Equation (31) *193*
Equation (32) *193*

Equation (33) *193*
Equation (34) *193*
Equation (35) *197*
Equation (36) *199*
Equation (37) *203*
Equation (38) *203*
Equation (39) *203*
Equation (40) *203*
Equation (41) *207*
Equation (42) *207*
Equation (43) *207*
Equations (44) *209*
Equations (45) *262*
Equation (46) *266*
Equation (47) *267*
Equation (48) *267*
Equation (49) *267*
Equation (50) *268*
Equation (51) *269*
Equation (52) *269*
Equation (53) *269*
Equation (54) *272*
Equation (55) *272*
Equation (56) *272*
Equation (57) *274*
Equation (58) *274*
Equation (59) *274*
Equation (60) *276*
Equation (61) *276*
Equation (62) *276*

Acronyms and Abbreviations

2-D	Two-dimensional
3-D	Three-dimensional
AOJ	Atlanto-Occipital Joint
AVI	Audio Video Interleave
BSP	Body Segment Parameter
CCTV	Closed Circuit Television
CM	Whole Body Centre of Mass
COP	Centre of Pressure
CT	Computed Tomography (also known as Computed Axial Tomography, or Computer Aided Tomography)
DEXA	Dual Energy X-ray Absorptiometry (also referred to as DXA)
DP	Distal-to-Proximal (IDA calculations) (see page 270)
ESU	Event Synchronisation Unit
FDA	Forward Dynamics Approach (see page 3)
GCV	Generalised Cross-Validation (see page 129)
GRF	Ground Reaction Force
HAT	Head-arms-trunk (segment)
H_{CM}	Whole body angular momentum about the CM
H'_{CM}	Rate of change of H_{CM}, with respect to time
HNJ	Head-Neck Joint
IA	Integration Approach (see page 4)
IDA	Inverse Dynamics Approach (see page 2)
IEP	Instant equilibrium point (see page 17)

LED	Light Emitting Diode
MRI	Magnetic Resonance Imaging
OTNJ	Optimised Trunk-Neck Joint (see page 120)
PD	Proximal-to-Distal (IDA calculations) (see page 270)
RMS	Root-mean-square
SD	Standard Deviation
SE	Standard Error
SK	Segmental Kinematic (see page 3)
TNJ	Trunk-Neck Joint
TTL	Transistor-transistor Logic
ZP	Zero-point (see page 17)
ZPZP	Zero-point-to-zero-point Integration Approach (see page 17)

Notation

Note: Only the notation used in this research is included in this table. Notation presented by other authors is sometimes reproduced in the text for illustrative purposes, but it is not summarised in this table. Commonly used subscripts, such as *i*, that were simply used to define iterative processes that applied to a particular equation or sequence of equations locally within the text are also not listed in this table. Such subscripts may have been used independently in different sequences of equations, so they are only defined locally within the text.

$Ave\ Power_P$	Average vertical translational power per kilogram of body mass for the upward propulsive phase of a countermovement jump (see section 6.1.3)
cm_{seg}	Centre of mass position of segment '*seg*' (e.g. cm_{foot})
$cm[L]_{seg}$	Centre of mass coordinate of segment '*seg*' along the longitudinal axis (L) in the segment-based reference system (see Fig. 12)
$cm[P]_{seg}$	Centre of mass coordinate of segment '*seg*' along the perpendicular axis (P) in the segment-based reference system (see Fig. 12)
$CM(t)$	Whole body centre of mass displacement as a function of time
$CM'(t)$	Whole body centre of mass velocity as a function of time
$CM''(t)$	Whole body centre of mass acceleration as a function of time

$CM_{IA}(t)$	$CM(t)$ determined using force platform data and an IA
$CM'_{IA}(t)$	$CM'(t)$ determined using force platform data and an IA
$CM_{SK}(t)$	$CM(t)$ determined using full body SK data and a weighted average of segmental centre of mass estimates
$CM'_{SK}(t)$	$CM'(t)$ determined using full body SK data and a weighted average of segmental centre of mass velocity estimates
$CM'_{SK\text{-}IA}(t)$	$CM'_{SK}(t)$ - $CM'_{IA}(t)$
$CM[y]_{IA}(t)$	Antero-posterior component of $CM_{IA}(t)$ (in Chapters 5 and 6)
$CM'[y]_{IA}(t)$	Antero-posterior component of $CM'_{IA}(t)$ (in Chapters 5 and 6)
CMy	Horizontal coordinate of the CM position vector in the global coordinate system (in Chapter 7)
$cm[y]_{seg}$	Horizontal component [y] of the displacement of the centre of mass of segment '*seg*' in the global coordinate system
$cm[y']_{seg}$	Horizontal component [y] of the velocity of the centre of mass of segment '*seg*' in the global coordinate system
$cm[y'']_{seg}$	Horizontal component [y] of the acceleration of the centre of mass of segment '*seg*' in the global coordinate system
$CM[z]_{IA}(t)$	Vertical component of $CM_{IA}(t)$ (in Chapters 5 and 6)
$CM'[z]_{IA}(t)$	Vertical component of $CM'_{IA}(t)$ (in Chapters 5 and 6)
$cm[z]_{seg}$	Vertical component [z] of the displacement of the centre

	of mass of segment '*seg*' in the global coordinate system
$cm[z']_{seg}$	Vertical component [z] of the velocity of the centre of mass of segment '*seg*' in the global coordinate system
$cm[z'']_{seg}$	Vertical component [z] of the acceleration of the centre of mass of segment '*seg*' in the global coordinate system
Comm	Commencing end of the segment undergoing an IDA (see page 271)
Comm[y]	Horizontal position of the commencing end of the segment undergoing an IDA (see page 271), with respect to the global coordinate system origin
Comm[z]	Vertical position of the commencing end of the segment undergoing an IDA (see page 271), with respect to the global coordinate system origin
COP[y]	Antero-posterior component of the centre of pressure location (in Chapters 5 and 6)
COPy	Horizontal coordinate of the COP position vector in the global coordinate system (in Chapter 7)
$Dist[y]_{seg}$	The horizontal component [y] of the position of the distal end-point of segment '*seg*' in the global coordinate system
$Dist[z]_{seg}$	The vertical component [z] of the position of the distal end-point of segment '*seg*' in the global coordinate system
F	Net ground reaction force

f	Frequency of data sampling ($1/\Delta t$)
F_C	Force platform calibration factor error in F (see page 31)
F_O	Force platform offset error in F (see page 33)
Fy	Antero-posterior component of the net ground reaction force measured by the force platform
Fy_C	Force platform calibration factor error term for Fy
Fy_{Comm}	Horizontal component of the net force acting on the commencing end (*Comm*) of the segment in question in an IDA (see page 271)
Fy_O	Force platform offset error term for Fy
Fy_{Term}	Horizontal component of the net force acting on the terminating end (*Term*) of the segment in question in an IDA (see page 271)
Fz	Vertical component of the net ground reaction force measured by the force platform
$\overline{Fz}$	Quasi-static mean Fz (see page 197)
Fz_C	Force platform calibration factor error term for Fz
Fz_{Comm}	Vertical component of the net force acting on the commencing end (*Comm*) of the segment in question in an IDA (see page 271)
Fz_O	Force platform offset error term for Fz
Fz_{Term}	Vertical component of the net force acting on the terminating end (*Term*) of the segment in question in an IDA (see page 271)

g	Acceleration due to gravitational force, which was -9.80 ms^{-2} at sea level in Melbourne, Australia (International Society of Geodesy, 1971), where the research was conducted
$Height_J$	Jumping height, representing the increase in vertical CM displacement from take-off to the peak of CM flight (see section 6.1.3)
$Height_P$	Increase in vertical CM displacement from the minimum point in the countermovement to the take-off point during a countermovement jump (see section 6.1.3)
IEP_i	*i*th IEP in a sequence of IEPs
IEP_n	Final IEP in a sequence of IEPs
IEP_0	Initial IEP in a sequence of IEPs
I_{seg}	Moment of inertia (assumed to be the principal moment of inertia) of segment '*seg*', about the transverse axis through the segment's centre of mass
L	The longitudinal axis of the segment-based reference system (see page 125 and Fig. 12).
l_{seg}	Length of the segment '*seg*'
m_{WB}	Whole body mass
Mx	Measured moment about the *x*-axis of the force platform
Mx_C	Force platform calibration factor error term for Mx
Mx_{Term}	Net moment acting about the *x*-axis at the terminating end (*Term*) of the segment in question in an IDA (see

	page 271)
Mx_O	Force platform offset error term for *Mx*
Mx_{Comm}	Net moment acting about the *x*-axis at the commencing end (*Comm*) of the segment in question in an IDA (see page 271)
m_{seg}	Mass of segment '*seg*'
$Max\ Power_P$	Maximum vertical translational power per kilogram of body mass during the upward propulsive phase of a countermovement jump (see section 6.1.3)
P	Perpendicular axis of the segment-based reference system (see page 125 and Fig. 12)
Peak Height	Height of the CM at the peak of CM flight trajectory, relative to the height of the CM at the start of the pre-jump quasi-static phase ($RelCM[z]_{IA}(t_{PH})$)
$Prox[y]_{seg}$	The horizontal component [*y*] of the position of the proximal end-point of segment '*seg*' in the global coordinate system
$Prox[z]_{seg}$	The vertical component [*z*] of the position of the proximal end-point of segment '*seg*' in the global coordinate system
$\vec{r}_{seg}$	Position vector of the segmental centre of mass relative to the global coordinate system origin
$\ddot{\vec{r}}_{seg}$	Second derivative of $\vec{r}_{seg}$
$RelCM_{IA}(t)$	*Relative* $CM_{IA}(t)$; that is, $CM_{IA}(t)$ *relative to* $CM_{IA}(t_{QSini})$

$RelCM_{SK}(t)$	*Relative* $CM_{SK}(t)$; that is, $CM_{SK}(t)$ *relative to* $CM_{SK}(t_{QSini})$
S_0	IA parameter representing the initial displacement of the CM
$\hat{S}_0$	Estimated S_0
S_ε	Error in estimated S_0
$S[y]_0$	IA parameter representing the initial absolute antero-posterior displacement of the CM [the y coordinate of $CM(0)_{IA}$]
$S[z]_0$	IA parameter representing the initial absolute vertical displacement of the CM [the z coordinate of $CM(0)_{IA}$]
$Tx(t)$	Net torque about the x-axis produced by the whole body weight force acting at the CM, and the GRF acting at the COP, with respect to the global coordinate system origin
$Term[y]$	Horizontal position of the terminating end of the segment undergoing an IDA (see page 271), with respect to the global coordinate system origin
$Term[z]$	Vertical position of the terminating end of the segment undergoing an IDA (see page 271), with respect to the global coordinate system origin
t	Time
t_{ABini}	Time of commencement of the airborne (*AB*) phase of a countermovement jump (see page 203)
t_{ABfin}	Time of completion of the airborne (*AB*) phase of a countermovement jump (see page 203)

t_i	ith instant in a time series
t_{maxCMy}	Time at which max($CM[y]_{IA}(t)$) occurs (see page 143)
t_{minCMy}	Time at which min($CM[y]_{IA}(t)$) occurs (see page 143)
t_{Pfin}	Time of completion of the upward propulsive phase of a countermovement jump (see page 206)
t_{Pini}	Time of commencement of the upward propulsive phase of a countermovement jump (see page 206)
t_{PH}	Time coinciding with the peak of CM flight trajectory
t_{QSfin}	Time of completion of the pre-jump quasi-static (*QS*) stance phase of a countermovement jump (see page 192)
t_{QSini}	Time of commencement of the pre-jump quasi-static (*QS*) stance phase of a countermovement jump (see page 192)
Tx	Net external torque acting on the body with respect to the global coordinate system origin
TOL_{fin}	*Tolerance* in final IEP (design variable in *ZPZP5U*; see page 194)
TOL_i	*Tolerance* in IEP*i* (design variables in *ZPZP6C*; see page 146)
TOL_0	*Tolerance* in initial IEP (design variable in *ZPZP5U*; see page 194)
V_0	IA parameter representing the initial velocity of the CM
$\hat{V}_0$	Estimated V_0
V_ε	Error in estimated V_0
$V[y]_0$	IA parameter representing the initial antero-posterior

	velocity of the CM [the *y* coordinate of $CM'(0)_{IA}$]
$V[z]_0$	IA parameter representing the initial vertical velocity of the CM [the *z* coordinate of $CM'(0)_{IA}$]
$Work_P$	Vertical translational work done per kilogram of body mass in accelerating the CM upwards during the upward propulsive phase of a countermovement jump (see section 6.1.3)
$\ddot{y}_{seg}$	Horizontal linear acceleration of the segmental centre of mass (see page 267)
$\ddot{z}_{seg}$	Vertical linear acceleration of the segmental centre of mass (see page 267)
α_{seg}	Angular segmental acceleration of segment '*seg*'
$\Delta\ Ave\ Power_{P\ (Condition\ i)}$	*Ave Power*$_P$ under *Condition i*, relative to that under *Condition 1* (see page 209)
$\Delta\ Height_{J\ (Condition\ i)}$	*Height*$_J$ under *Condition i*, relative to that under *Condition 1* (see page 209)
$\Delta\ Height_{P\ (Condition\ i)}$	*Height*$_P$ under *Condition i*, relative to that under *Condition 1* (see page 209)
$\Delta\ Max\ Power_{P\ (Condition\ i)}$	*Max Power*$_P$ under *Condition i*, relative to that under *Condition 1* (see page 209)
$\Delta\ Peak\ Height_{(Condition\ i)}$	*Peak Height* under *Condition i*, relative to that under *Condition 1* (see page 209)
$\Delta\ t$	The change in time between adjacent data samples ($1/f$)

$\Delta\ Work_{P\ (Condition\ i)}$	$Work_P$ under *Condition i*, relative to that under *Condition 1* (see page 209)
Γ	The distance in the sagittal plane between two given trunk markers (see Fig. 10)
θ_{seg}	Angular segmental displacement of segment '*seg*'
ω_{seg}	Angular segmental velocity of segment '*seg*'

Unit Symbols

cm	centimetre
Hz	hertz
J	joule
kg	kilogram
m	metre
mA	milliampere
mcd	millicandela
mm	millimetre
mrad	millirad
ms	millisecond
mSv	millisievert
N	newton
s	second
V	volt
W	watt

1. INTRODUCTION

Human biomechanics research provides a wealth of practical benefits to society, spanning medical, clinical, occupational, sporting and artistic domains. It encompasses the measurement, description, explanation and prediction of human mechanics from the cellular level to whole body mechanics. A myriad of research approaches of broadly varying complexity are applied across this field of endeavour. Quantitative techniques range from relatively simple temporal measurements to high-precision acquisition of total system kinematics and kinetics. Mathematical modelling and simulation approaches of vastly different levels of sophistication are employed.

By finding the correct balance between simplicity and complexity, researchers can apply the most efficient yet effective measurement and modelling tools for achieving their specific research objectives. Whole body motion, for example, is complex by nature of the inherently intricate structural and functional design of the human musculoskeletal system. In order to analyse this motion, researchers often model the human as a simplified system of rigid segments linked by frictionless joints that are spanned by several muscles. For many applications, it is possible to simplify the model further. This may involve reducing the analysis of each joint to a net force and moment when knowledge about the individual contribution of each muscle is not required. Sometimes 2-D analysis is deemed sufficient for essentially planar human performance and occupational activities such as countermovement jumps (e.g. Kibele, 1998) and some manual lifting tasks (e.g. Wrigley et al., 2005).

A kinematic representation of a human's segmental motion is possible when the complete position-time history of the model's joint centres and segment end-points is known as a result of stereophotogrammetric recording of the human's movement. Under certain conditions, subsequent kinetic analysis can be conducted to estimate the external forces acting on the human body and the internal net joint forces and moments that govern the measured kinematics. The process of calculating such kinetic quantities by first measuring the resultant kinematics is commonly called the inverse dynamics approach (IDA).

For non-support and single-support open-loop situations (Vaughan et al., 1982b), only the kinematic data described above and the inertial properties of the segments need to be supplied to the system of motion equations in order to calculate body kinetics using the IDA. For open-loop situations involving n extremities in contact with the external environment, force transducing devices are also required to measure the external forces acting on at least n-1 of the extremities if the IDA is to be applied (Vaughan et al., 1982b). Therefore, if the number of force transducing devices used equals the number of extremities in contact with the external environment, the system of motion equations is over-determined. In such circumstances, the external force acting at the distal end of any stipulated extremity can be calculated by an inverse dynamics analysis and compared with the value measured empirically or known to be zero in the case of a segment not in contact with the external environment (Vaughan et al., 1982a).

The opposite approach to solving dynamics equations is called the direct or forward dynamics approach (FDA). The FDA is commonly applied in human movement simulation studies. It involves determining the system kinematics by providing the equations of motion with the forces and moments that drive the model. IDA and FDA solutions also rely on the provision of the model's segmental inertial properties.

Segmental inertial properties or body segment parameters (BSPs) include each segment's mass, centre of mass position and inertia tensor. For 2-D dynamics analysis of motion that is assumed to occur exclusively in the anatomical sagittal plane, only each segment's mass (m_{seg}), centre of mass location in the sagittal plane (cm_{seg}) and principal moment of inertia about the transverse axis through the segment's centre of mass (I_{seg}) are required[1].

When system kinematics have been captured by stereophotogrammetric means and BSP estimates are available, it is also possible to estimate whole body centre of mass (CM) trajectory by determining the weighted average of all the segments' centre of mass positions for each sampled point in time (Winter, 1990). This can be referred to as segmental kinematic (SK) determination of CM kinematics. The

1 Strictly speaking, the segmental moments of inertia about the anatomical axes are only principal moments of inertia if the principal axes of inertia and the anatomical axes are aligned. All 2-D human dynamics studies reviewed by the author have assumed alignment of these axes, either explicitly or implicitly.

whole body angular momentum about the CM (H_{CM}) can also be calculated (Hay et al., 1977).

All of the approaches described thus far require BSP data. Except for FDA simulations, they also require the complex and time-consuming process of measuring segmental kinematics. However, relatively inexpensive and less time-consuming strategies for determining CM kinematics have been developed that require minimal or no segmental kinematics data acquisition or BSP estimation. Such strategies have been applied to posturographic (e.g. Benda et al., 1994; Caron et al., 1997), gait (e.g. Crowe et al., 1993; Eames et al., 1999; Whittle, 1997) and other movement (e.g. Hatze, 1998; Zok et al., 2004) analyses. Essentially, they involve the reduction of the data obtained with one or more force platforms for single-stance or double-stance open-loop situations, with little or no reliance on kinematic measurements. For example, the integration approach (IA) can be used if the only external forces acting on the body are gravitational force and ground reaction forces acting on the feet as measured by one or two force platforms. This approach involves calculating the acceleration-time history of the CM from the ground reaction force (GRF) data, and twice integrating this data numerically, with respect to time, in order to determine the velocity-time and position-time histories of the CM (e.g. Kibele, 1998; Rabuffetti and Baroni, 1999; Zatsiorsky and King, 1998). The two integration constants formed by this process, namely the initial position and initial velocity of the CM, need to be known or estimated to complete this method.

The accuracy of CM kinematic data calculated using the Integration Approach (IA) is dependent upon the accuracy of:

- kinetic data acquisition, reduction and smoothing tools and techniques
- assumed or estimated values of the integration constants.

Many variations of the IA have been proposed over recent years. An assessment of the relative merits of these techniques and the possible refinement and amalgamation of the most promising aspects of these methods is warranted.

Similarly, the accuracy of a variety of human biomechanics data provided by whole body segmental modelling approaches depends upon the accuracy and validity of:

- data acquisition, reduction and smoothing techniques
- the model developed to describe the mechanical structure and function of the human (including the estimated BSPs, joint centres and segment end-points).

The use of subject-specific BSP estimates in human movement analysis has been advocated (Pearsall and Reid, 1994; Reid and Jensen, 1990) in order to reduce this error source. However, only a few currently available methods approach subject-specificity, and direct measurement techniques are not easily and readily applied (Zatsiorsky, 2002).

Clearly, reducing the magnitude of some or all of the abovementioned error sources will improve biomechanical representation, explanation and simulation of human movement. Notwithstanding the desirability of minimising all error sources, this research concentrates on attempts to:

- improve estimation of sagittal plane CM kinematics by applying variations of the IA, and
- improve segmental modelling for whole body sagittal plane dynamics analyses by applying new subject-specific BSP estimation techniques.

A précis of this research follows:

The Problem: Dynamics analyses of human movement are limited by inaccurate input parameters, such as erroneous force platform calibration parameters, IA integration constants and BSP estimates.

The Aims: This research aims to improve the accuracy of these input parameters and subsequently, to improve the IA CM kinematics calculations and BSP-dependent dynamics solutions.

The Approach: Nonlinear optimisation is the key methodological approach underpinning attempts to achieve these aims. The experimental design ensures that enough sources of measurable data are captured to produce a complete or an over-determined system of dynamics equations. This situation is then exploited by applying optimisation searches to find the activity-specific and subject-specific input parameter values that produce the dynamics solutions that most closely correspond to the empirically-measured data (e.g. force platform measurements), mathematically-calculated data (e.g. SK determination of CM trajectory) or theoretically-expected solutions.

2. REVIEW OF LITERATURE

This research aims to improve inverse dynamics analyses and whole body centre of mass representations of sagittal-plane human movement by developing techniques to improve the accuracy of force platform calibration parameters, IA integration constants and BSP estimates. Relevant methods already developed and assessed by other researchers are now reviewed and areas for further development are identified. Methods of determining CM kinematics mainly or exclusively from force platform data are considered first. They are categorised in relation to the different activities to which they have or could be applied, namely stance, walking and other dynamic activities. Evaluations of these methods relative to SK determination of CM kinematics are also covered. The other main area reviewed in this chapter is the broad range of methods developed for measurement and estimation of BSPs. These methods are sub-divided into five methodological categories: cadaver-specific; volumetric and geometric modelling; medical imaging; predictive (regression equations); and dynamics and optimisation techniques. A more detailed review is conducted of many of the dynamics and optimisation techniques because of their direct relevance to this research. Finally, evaluations of living-subject BSP estimation methods and the influence that BSP estimate errors can have on various BSP-dependent dynamics calculations are reviewed in order to identify dynamics quantities and movement patterns that might be effective for estimating various BSPs in this research.

2.1 CM Kinematics Derived from Force Platform Data: Platform-Based Methods

SK determination of CM kinematics is generally considered more complicated than methods using force platforms (Levin and Mizrahi, 1996; Zok et al., 2004), particularly for clinical settings (Iida and Yamamuro, 1987; Morasso et al., 1999). Approaches using mainly or exclusively force platform data are relatively inexpensive and less time-consuming (Barbier et al., 2003). They also expose the subject to less physical and psychological interference, making them more appealing in research and clinical settings (Conforto et al., 2001). Several methods of CM kinematics estimation that rely on little or no kinematic data acquisition have been proposed. They are categorised and discussed below in terms of the movement patterns to which they have, or could be applied. Some are limited to specific applications due to their reliance on movement-specific models and assumptions, whereas others are more versatile and applicable to more generic movement patterns.

2.1.1 Platform-Based Methods for Posturographic Analysis

Various methods for estimating CM kinematics, based principally on force platform measurements, have been applied to posturographic analyses. Some of these rely on inverted pendulum models (e.g. Barbier et al., 2003; Karlsson and Lanshammar, 1997; King and Zatsiorsky, 1997; Morasso et al., 1999) that are only applicable to analyses of postural sway about the ankles and often require the provision of anthropometric information. Others have attempted to estimate the CM kinematics by low-pass filtering the centre of pressure (COP) data, claiming

this approach is also applicable to gait analysis (e.g. Benda et al., 1994; Caron et al., 1997).

Lenzi et al. (2003) compared the method of Caron et al. (1997) with the IA methods of Shimba (1984) and Zatsiorsky and King (1998), which are described in more detail on pages 14 to 24. The latter two IA methods were rated more favourably than the low-pass filter method, in terms of CM trajectory estimation performance, when these methods were compared with a computer-simulated segmental kinematic (SK) model and in terms of sensitivity to BSP errors. Lafond et al. (2004) compared both the low-pass filter method of Caron et al. (1997) and an IA method developed by Zatsiorsky and Duarte (2000) with an SK determination of CM kinematics. The Zatsiorsky and Duarte (2000) method is described in more detail on pages 17-24. Lafond et al. (2004) found that the low-pass filter method produced significantly different antero-posterior CM trajectories to the SK and Zatsiorsky and Duarte (2000) methods for several posturographic activities (viz. quiet standing, one-legged stance, voluntary oscillation about the ankles, and voluntary oscillation about the hips and ankles), whereas, there was no significant difference between the latter two methods. They also provided graphical evidence that the low-pass filter method produced unrealistic results for quiet stance and one-legged stance, insofar as the CM trajectory was not always confined within the dynamic range of the COP trajectory, as expected during quiet standing (Winter et al., 1996a). For example, Fig. 1 is a reproduction of figure 2 from Lafond et al. (2004), showing plots of CM trajectory for the SK, ZPZP and low-pass filter methods, relative to COP

trajectory for quiet stance. The graph indicates that the method of Caron et al. (1997) produced results that were clearly unrealistic.

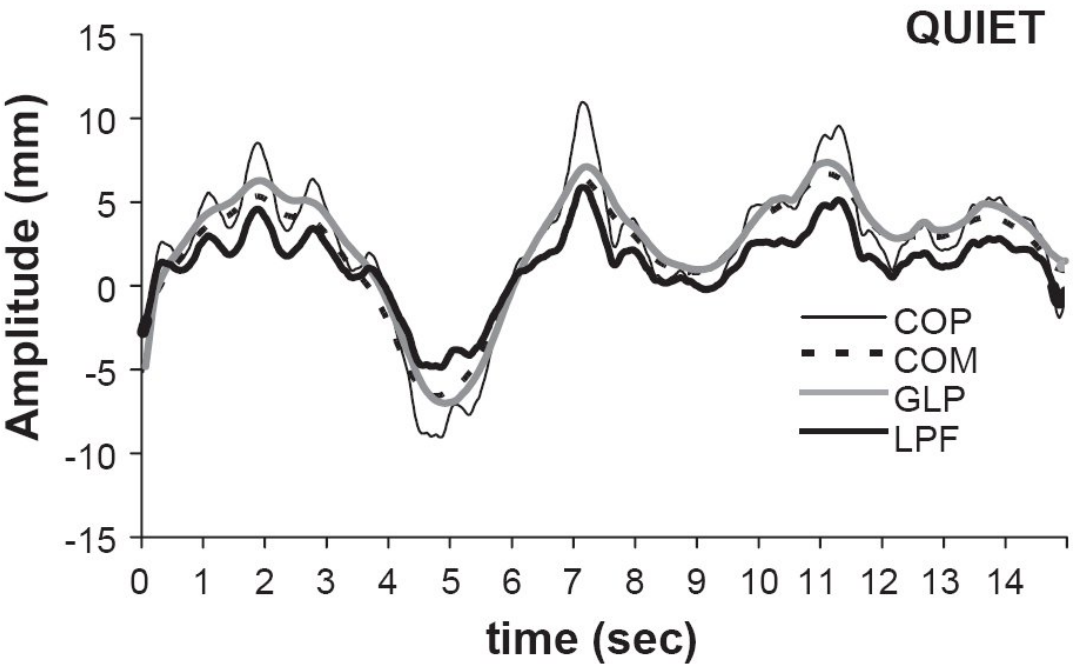

Figure 1. The quiet stance plots from figure 2 of Lafond et al. (2004), reprinted with permission of Elsevier, showing the good agreement between the CM trajectory plots derived from the SK approach (labelled COM*) and the ZPZP method of Zatsiorsky and Duarte (2000) (labelled* GLP*), and less agreement with the CM trajectory plot derived from the low-pass filter method of Caron et al. (1997) (labelled* LPF*). More significantly, the relationship between COP trajectory (labelled* COP*) and* LPF *is clearly unrealistic (e.g. for the first three seconds,* LPF *CM trajectory changes direction several times while* COP *remains on one side of* LPF*).*

Caron et al. (1997) reported that they did not apply their method to quiet stance, "because of the 'noise' of the instrumentation" affecting their determination of the antero-posterior acceleration of the CM. Paradoxically though, Caron et al. (1997) claimed their method was suitable for quiet stance on theoretical grounds (Prince et al., 2005), even though they chose not to demonstrate this. It appears

likely from the results of Lafond et al. (2004) that such a demonstration may have been difficult for Caron et al. (1997) to achieve, even if they had tried. Caron (2005) questioned how Lafond et al. (2004) had implemented the low-pass filter method, and claimed the method of Caron et al. (1997) was "more precise" than the ZPZP method. In reply, Prince et al. (2005) confirmed they had followed the procedure of Caron et al. (1997) and also highlighted the shortcomings of the claims by Caron et al. (1997) and Caron (2005) regarding the suitability and accuracy, respectively, of their low-pass filter method for quiet stance.

The validity of low-pass filtering approaches was also questioned by Zatsiorsky and King (1998) on the fundamental grounds that such approaches do not account for phase differences between transverse plane CM and COP trajectories and that results are dependent on the choice of low-pass filter cut-off frequency. Benda et al. (1994), who themselves used a low-pass filter method, mentioned the out-of-phase nature of CM and COP trajectories but only urged for cautious interpretation of the results when low-pass filtering methods are applied to activities that are more dynamic than quiet stance. Considering the phase differences between CM and COP trajectories and the results published by Lafond et al. (2004), low-pass filtering of COP data appears to be an invalid approach for estimating CM trajectory for quiet stance activities.

Several researchers have applied the integration approach (IA) to estimate CM kinematics for posturographic analysis (Eng and Winter, 1993; King and Zatsiorsky, 1997; Levin and Mizrahi, 1996; Shimba, 1984; Zatsiorsky and King, 1998; Zatsiorsky and Duarte, 2000). Note that the basic procedure underpinning

the IA for posturographic analyses applies equally to gait and more generic movement pattern analyses because it is based on Newton's 2nd Law. If the only external forces acting on the body are gravitational force and the ground reaction forces acting on the feet measured by one or two force platforms (implying aerodynamic forces are considered negligible), then the acceleration of the CM can be determined by dividing the net force acting on the body by whole body mass:

$$CM''(t) = \frac{F(t)}{m_{WB}} + g \tag{1}$$

where $CM''(t)$ is the acceleration of the CM at time t, $F(t)$ is the net ground reaction force (GRF) of the reaction forces applied to both feet at time t, m_{WB} is the whole body mass and g is gravitational acceleration. Subsequently, integration of $CM''(t)$ with respect to time allows determination of CM velocity:

$$CM'(t) = \frac{1}{m_{WB}} \int F(t)dt + g\,t + V_0 \tag{2}$$

where $CM'(t)$ is the velocity of the CM at time t and V_0 is the first integration constant representing the initial velocity of the CM at $t = t_0$. Similarly, integration of $CM'(t)$ allows determination of the CM displacement:

$$CM(t) = \frac{1}{m_{WB}} \iint F(t)dt + \frac{1}{2} g\, t^2 + V_0\, t + S_0 \tag{3}$$

where $CM(t)$ is the displacement-time history of the CM and S_0 is the second integration constant representing the initial displacement of the CM at $t = t_0$. Although analytical integration notation is used above, in practice, digitised ground reaction force data can only be integrated numerically. V_0 and S_0 are usually not known precisely. If they can be estimated, then:

$$V_0 = \hat{V}_0 + V_\varepsilon, \text{ and} \tag{4}$$

$$S_0 = \hat{S}_0 + S_\varepsilon \tag{5}$$

where $\hat{V}_0$ and $\hat{S}_0$ are the estimates and S_ε and V_ε are the associated error terms. If V_0 cannot be estimated, only relative $CM'(t)$ can be determined. If V_0 can be estimated, absolute $CM'(t)$ and relative $CM(t)$ can be estimated. Further, if S_0 can be estimated, absolute $CM(t)$ can also be estimated. However, accurate estimation of V_0 and S_0 is usually problematic. The error (S_ε) in estimating the second integration constant will introduce an offset error in calculated $CM(t)$. Even more critically, the error (V_ε) in estimating the first integration constant will introduce a cumulative error in calculated $CM(t)$. The cumulative error increases linearly as time elapses. Thus, errors in estimating initial CM velocity and displacement values must be minimised if the IA is to be used successfully to determine CM displacement. Most importantly, initial CM velocity must be known accurately in order to avoid cumulative integration errors.

Eng and Winter (1993) evaluated the IA for calculating antero-posterior $CM(t)$ for posturographic applications. They suggested that cumulative errors made the method only suitable for transient activities. An attempt to define what might be the maximum length of time applicable to the term 'transient' was not made. However, it is clear that the more accurately V_0 is estimated, the longer the analysis can continue before $CM(t)$ errors become unacceptably large. Approaches for determining V_0 and S_0 for posturographic activities have ranged from the oversimplified assumption that $V_0 = 0$ (Eng and Winter, 1993), to more complex approaches (e.g. King and Zatsiorsky, 1997; Levin and Mizrahi, 1996; Shimba, 1984; Zatsiorsky and King, 1998).

Using a least squares approach, Shimba (1984) estimated V_0, S_0 and an offset error term in the GRF measurements, by fitting the IA $CM(t)$ function with an alternative function that was also claimed to approximate $CM(t)$. The alternative function was related to the Newtonian principle that the rate of change of angular momentum of a body about the body's CM (H'_{CM}) is equal to the net external torque acting on the body about its CM. Shimba chose to regard the unknown value of H'_{CM} as negligible, thus reducing the alternative $CM(t)$ function, $E(t)$, to one comprised almost entirely of force platform measured quantities:

$$E(t) = x_p + \frac{z_G F_{0x}}{F_{0z}} \text{ in the } x \text{ direction, and}$$

$$E(t) = y_p + \frac{z_G F_{0y}}{F_{0z}} \text{ in the } y \text{ direction} \quad (6)$$

where x_p and y_p were the coordinates of the transverse plane COP, and F_{0x}, F_{0y} and F_{0z} were the components of the GRF. The other parameter, z_G, was the height of the CM above the ground, so Shimba's method required some knowledge or estimation of the anthropometry of the subject to determine z_G.

Levin and Mizrahi (1996) agreed with Shimba's assumption that the unknown value of H'_{CM} as negligible for posturographic applications. They extended the work of Shimba by using bilateral force platforms and introducing an iterative process to evaluate H'_{CM} and subsequently refine the estimate of CM trajectory. However, this process required the provision of even more anthropometric data and a five-segment body model. Lenzi et al. (2003) evaluated Shimba's method by comparison to benchmark simulation data. Contrary to Levin and Mizrahi (1996), Lenzi et al. (2003) suggested that H'_{CM} was not always negligible for quiet stance. Whether or not this is so, it is reasonable to suggest that the influence of H'_{CM} becomes significant when these methods of determination of the initial conditions are applied to more dynamic activities. Levin and Mizrahi (1996) suggested their method would overcome this issue but conceded that it would require more iterations to converge (i.e. to arrive at the solution). However, this was not assessed in their work and the author is unaware of any subsequent

attempts by other researchers to apply Levin and Mizrahi's method to more dynamic tasks. The application of the approach proposed by Levin and Mizrahi (1996) has similar limitations to that of Shimba (1984). Both require some anthropometric data and both assume the height of the CM to be constant. The latter point clearly prevents their use for activities such as lifting tasks and stair climbing. Levin and Mizrahi's approach also requires the foot (or feet) to be flat on the force platform throughout the analysis.

King and Zatsiorsky (1997) proposed two IA methods with different algorithms for estimating the initial conditions when determining antero-posterior $CM(t)$ for stance activities. They called the first algorithm the 'trend-eradication' technique. Only relative $CM(t)$ was determined with this method as S_0 was not known. It involved assuming initially that V_0 was zero when double-integrating the CM antero-posterior acceleration. The resultant CM displacement-time history was then fitted with a linear regression line. The slope of this line was then accepted as the improved estimate of V_0. King and Zatsiorsky (1997) ensured the analysis commenced and finished when the COP trajectory was "at peak values of COP." However, a source of error exists because the two peak COP displacements may not always correspond to two peak CM displacements; and even if they did, the two peak CM displacements will not necessarily be equivalent. Consider the case when the real initial and final CM displacements are not equivalent at the times corresponding to the chosen initial and final COP peaks and where true V_0 is actually zero. Using this algorithm, V_0 would be judged to be non-zero. However, the "large time interval" (at least 30 seconds) employed by King and Zatsiorsky (1997) would reduce the error expected as part of this process.

Knowledge of the true initial and final CM positions would overcome this problem and permit analysis over shorter time spans.

The other IA method proposed by King and Zatsiorsky (1997) was the 'zero-point-to-zero-point' integration (ZPZP) method. This method aimed to determine the first instant (and all subsequent instants) in time when the CM and COP antero-posterior displacements coincided. The first such instant in time was then assigned as the starting point for the analysis, rather than attempting to determine the initial conditions at the very beginning of the trial. Their approach was based on the assertion that, during stance, antero-posterior CM displacement and COP coincide whenever the antero-posterior GRF is momentarily zero (King and Zatsiorsky, 1997; Zatsiorsky and King, 1998). Zatsiorsky and Duarte (1999, 2000) called these absolute antero-posterior COP positions the 'zero-force points' or 'instant equilibrium points' (IEPs). Fundamentally, the step-by-step algorithm applied by all of these researchers in the antero-posterior dimension was as follows:

Step 1: Find the first two IEPs (the experimentally recorded COP values at the first two instants when the antero-posterior GRF is zero). Assign these values to IEP_0 and IEP_1, respectively.

Step 2: Assign the value of IEP_0 to the initial displacement integration constant (S_0). Assign an interim value of zero to the initial velocity integration constant (V_0).

Step 3: Calculate the double integral of the acceleration of the CM across the time period bounded by the times t_0 and t_1 (i.e. the times corresponding to IEP_0 and IEP_1).

Step 4: Subtract the final ($t = t_1$) CM displacement calculated in *Step 2* from IEP_1 and divide this result by (t_1 - t_0). The final result is the 'actual' initial velocity integration constant, V_0.

Step 5: Repeat *Step 3* with the 'actual' value of V_0, then go to *Step 6*.

Step 6: Find the next IEP (IEP_2) at time t_2. Let $IEP_0 = IEP_1$. Let $t_0 = t_1$. Let $IEP_1 = IEP_2$. Let $t_1 = t_2$. Repeat *Steps 2 to 6* until all IEPs in the trial have been subjected to this process.

For *Step 1*, King and Zatsiorsky (1997) defined a threshold range around zero to determine the IEPs, recognising that digitally sampled force values are rarely exactly zero. They stated that the threshold required to reliably and accurately find the IEPs is dependent on sampling frequency and the frequency content of the assessed postural task. They sampled force platform signals at 200 Hz and defined threshold ranges of ±0.05 N and ±0.4 N for quiet standing and swaying tasks, respectively.

Inspection of the 'fast hip sway' $CM(t)$ plots for the 'trend eradication' and the 'threshold' ZPZP techniques (GL-2 and GL-3, respectively, in figure 3, King and Zatsiorsky, 1997) suggests that both methods cannot be valid (see Fig. 2). Differences of up to approximately 60 mm are observable. However, from the data provided, it is difficult to determine which one, if either, is valid.

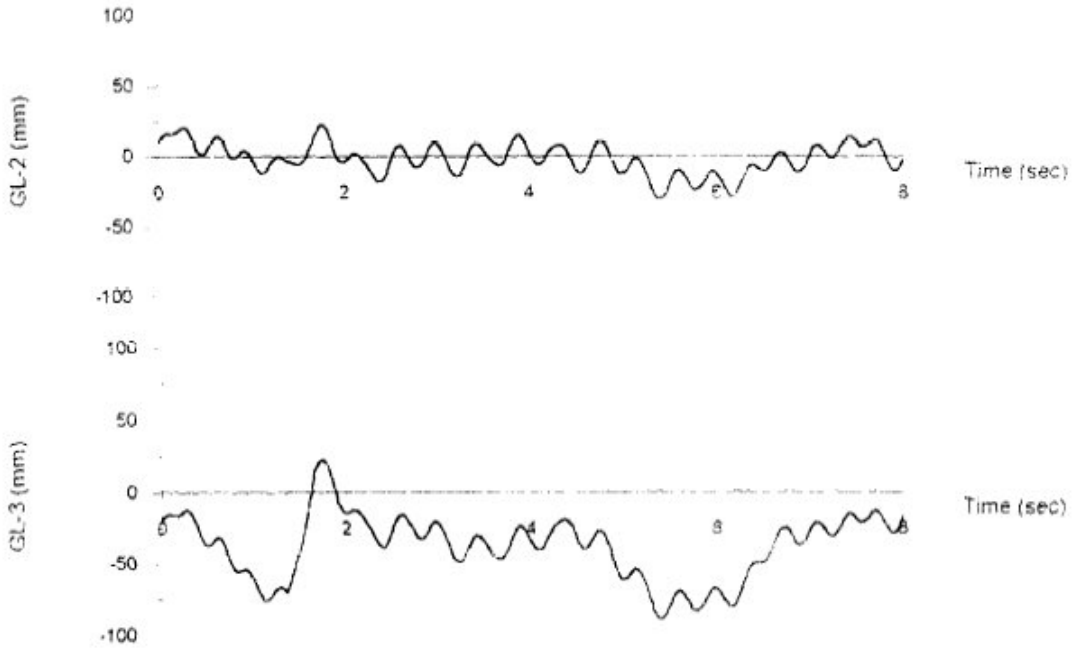

*Figure 2. The very different CM(t) plots resulting from the 'trend eradication' (*GL-2*) and 'threshold' (*GL-3*) methods of King and Zatsiorsky (1997). Reprinted and adapted from figure 3, King and Zatsiorsky (1997) with permission of Elsevier.*

Zatsiorsky and King (1998) also employed the threshold technique for *Step 1* of the ZPZP algorithm for subjects standing on one leg, but there is no indication of the threshold range they used. They sampled the force platform signals at 30 Hz. Their results consisted of cross-correlations between the ZPZP method of $CM(t)$ determination and a SK determination of $CM(t)$ and a comparison of the root-mean-square (RMS) $CM(t)$ values of both methods. Although not reported, it is assumed the RMS values were simply the square-root of the mean of the deviation scores of each $CM(t)$ value from zero. With a sample size of only five subjects, there were no significant differences between the ZPZP and SK methods' RMS values (paired t-test, $p > 0.05$; mean ± SD = 9.3 ± 3.0 for ZPZP and 9.0 ± 4.2 mm for SK). The authors described the cross-correlation values (0.79 - 0.96) as high, and only offered errors in the SK method as one of the

reasons for the less-than-perfect correlations. They concluded that the ZPZP method is a valid technique for determination of antero-posterior $CM(t)$ during standing tasks. Considering they had no 'gold standard' method with which to compare the ZPZP method, their claim of validity for the ZPZP method seems premature. The more conservative comment in the abstract, "…that the zero-point-to-zero-point-integration is an acceptable technique…," seems more appropriate.

Considering the limitations of the segmental kinematic comparison approach, the validity of the ZPZP method might be assessed better by other means. Note that successive executions of the ZPZP algorithm (see page 17) produce two potentially different values for $CM'(t)$ for each moment in time t_i that corresponds with an Instant Equilibrium Point (IEP_i). The first $CM'(t_i)$ value is calculated by numerical integration during *Step 5* of the ZPZP algorithm executed for the ZPZP interval *ending* at IEP_i. The second value is the 'actual' initial CM velocity at t_i ($V_0(t_i)$), calculated during *Step 4* of the *next* execution of the ZPZP algorithm for the ZPZP interval *commencing* at IEP_i. Although the method was designed primarily to determine $CM(t)$, it seems reasonable to hypothesise that the method needs to be valid for $CM'(t)$ determination if it is also to be valid for $CM(t)$ determination. That is, for each instant at which an IEP occurs in the movement sequence, except for the initial and final IEPs[2], $CM'(t_i)$ calculated by numerical

[2] Only $V_0(t_i)$ can be calculated at the instant corresponding with the initial IEP in the movement sequence because there is no preceding ZPZP interval, and only $CM'(t_i)$ can be calculated at the instant corresponding with the final IEP in the movement sequence because there is no proceeding ZPZP interval.

integration in *Step 5* of the ZPZP algorithm should equal $V_0(t_i)$ as calculated for the same instant in *Step 4* of the following execution of the ZPZP algorithm.

This hypothesis is difficult to review from the data published to date by the researchers who have used this method. Some insight can be gained from inspecting the 'quiet standing, eyes closed' $CM(t)$ plot presented by King and Zatsiorsky (1997, figure 4, plot GL-3). Although the graphical resolution is limited, there appears to be several instances where the function is not smooth, particularly the IEP at $t \approx 0.8$ s (see Fig. 3). $CM'(t)$ appears to be discontinuous at $t \approx 0.8$ s. That is, the final CM velocity for the double integration period ending at $t \approx 0.8$ s would not be the same as the initial CM velocity determined for the numerical integration period commencing at $t \approx 0.8$ s).

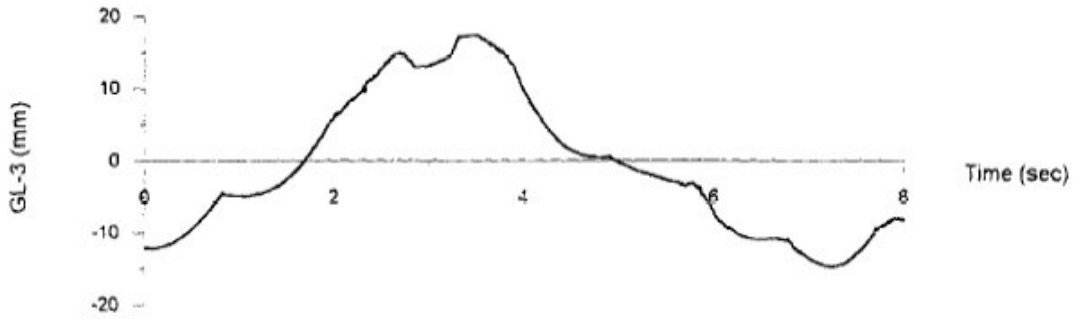

*Figure 3. Plot of CM(t) (*GL-3*) resulting from the application of the 'threshold' method (King and Zatsiorsky, 1997), for quiet standing, eyes closed. The function does not appear to be smooth at the first IEP at* Time *≈ 0.8 s, and possibly at several other IEPs. Reprinted and adapted from figure 4, King and Zatsiorsky (1997) with permission of Elsevier.*

The ZPZP method developed by King and Zatsiorsky (1997) shows some promise. However, the above observations and interpretations suggest that the assertion upon which the ZPZP method is based (viz. during stance, antero-posterior CM displacement and COP coincide exactly whenever the antero-posterior GRF is momentarily zero) may be flawed, although possibly only in combination with one or both of the following explanations:

1. other error sources existed in the measured force data;
2. the numerical integration method was not precise enough or the sampling frequency was too low for accurate numerical integration.

With respect to 1, other researchers have suggested ways of accounting for force measurement errors such as offset errors, if they exist (e.g. Kibele, 1998; Rabuffetti and Baroni, 1999) and these are discussed in section 2.1.3. With respect to 2, the method of numerical integration applied by King and Zatsiorsky (1997) was not reported. One or both of these explanations may be correct. Regardless, the ZPZP method presented by King and Zatsiorsky (1997) and

Zatsiorsky and King (1998) may still be useful for $CM(t)$ determination compared with other available methods, particularly if it can be improved. Further, improving the representation of $CM'(t)$ during stance may facilitate better position-velocity interaction assessments of dynamic balance (e.g. Pai, 1997) and help to improve measures of the degree of dynamic stability during stance (e.g. Hof et al., 2005).

Zatsiorsky and Duarte (2000) modified this technique for quiet standing. Firstly, they low-pass filtered the force data (captured at 40 Hz) with a 4^{th} order zero-lag phase Butterworth filter with a cut-off frequency of 8 Hz. The low-pass filtering they employed prevented multiple local zero-crossings associated with high frequency random noise in the force signals. They did not use the 'threshold' technique (King and Zatsiorsky, 1997) for IEP determination. Instead, whenever adjacent antero-posterior force samples changed polarity, a local linear interpolation was used to approximate the IEP instants, followed by a similar linear interpolation of the COP data to find the IEP instants (Duarte, 2005). Arguably, this improves the precision of these estimates, however, the chosen cut-off frequency might alter the times at which IEPs occur and possibly even the number of recorded IEPs. Zatsiorsky and Duarte (2000) actually used the trapezoid rule method of numerical integration (Duarte, 2005), although the equation they reported only involved summing the areas of piecewise rectangles. The methods of numerical integration used by King and Zatsiorsky (1997) and Zatsiorsky and King (1998) were not reported. King and Zatsiorsky (1997) did not report any low-pass filtering procedure. Indeed, the noisy appearance of the

force plots they presented suggests that the force data was not filtered. Zatsiorsky and Duarte (2000) did not report that any data filtering was carried out either.

Lafond et al. (2004) compared the IA method of Zatsiorsky and Duarte (2000) with the SK determination of CM kinematics and the low-pass filter method of Caron et al. (1997). For the Zatsiorsky and Duarte (2000) ZPZP method, Lafond et al. (2004) low-pass filtered the force data (captured at 20 Hz) with a 6^{th} order zero-lag phase Butterworth filter with a cut-off frequency of 10 Hz. The RMS difference between each possible pair of the three methods' antero-posterior CM trajectories was determined for several trials representing quiet standing, one-legged stance, voluntary oscillation about the ankles, and voluntary oscillation about the hips and ankles. The RMS differences between the SK and Caron et al. (1997) methods and the Zatsiorsky and Duarte (2000) and Caron et al. (1997) methods were not significantly different, but both were significantly larger than the RMS difference between the SK and Zatsiorsky and Duarte (2000) methods for antero-posterior CM calculations for quiet stance (p-value not published), one-legged stance ($p < 0.001$) and voluntary oscillation tasks ($p < 0.02$). Lafond et al. (2004) concluded that the Zatsiorsky and Duarte (2000) method "gives similar" CM trajectories compared to the SK method and that the Caron et al. (1997) method produced significantly different results to the former methods.

The choice of low-pass filter cut-off frequency, the sampling frequency and the accuracy of the force measurements may all affect the validity of the ZPZP method as implemented by the aforementioned researchers. Apart from

evaluating the continuity of $CM'(t)$ at the IEPs (see page 20), another approach would be to apply the ZPZP method in an 'unconventional' way across only the first and last IEPs in a movement sequence and not to all intermediate pairs of adjacent IEPs. It could be argued that if the ZPZP method is valid, the IA-determined $CM(t)$ values at instants coinciding with the intermediate IEPs should equal the COP values at the same instants, regardless of whether a 'conventional' or an 'unconventional' ZPZP approach is applied. This warrants investigation.

2.1.2 Platform-Based Methods for Gait Analysis

Clinicians and researchers more frequently wish to assess gait than the initiation of gait, so patients or subjects are usually already walking when they cross one or more force platforms. Hence, the ZPZP method cannot be applied in this situation. However, other IA methods have been applied by many researchers to estimate CM kinematics during gait.

Crowe et al. (1993) expanded the GRF signals as a Fourier series with fundamental frequency equal to the inverse of the stride time. By assuming the net vertical and lateral displacements during the single stride analysed to be zero, and by assuming the forward displacement to be equal to stride time multiplied by the average measured forward velocity, the Fourier series representing the GRF signals was reduced to only sinusoidal components. The function was then analytically integrated twice to determine $CM(t)$. Cavagna (1975) attempted to approximate the external work done over a complete stride. Part of this process involved the single and double numerical integration of, respectively, the

horizontal and vertical acceleration data derived from the force signals. This allowed the determination of the kinetic energy and the change in potential energy of the CM. Many researchers have used methodologies very similar to Cavagna since then. For example, Donelan et al. (2002) and Tesio et al. (1998a) used this method for normal subjects; Tesio et al. (1998b) assessed unilateral lower limb amputees; Iida and Yamamuro (1987) assessed normal subjects, patients with unilaterally osteoarthritic hip joints before and after total hip replacement, and hemiplegia patients; Tesio et al. (1985) patients with hemiplegia and unilateral hip osteoarthritis; and Lee and Farley (1998) applied this method to walking and running activities.

Cavagna (1975), Crowe et al. (1993), Donelan et al. (2002) and Tesio et al. (1985) assumed the average lateral and vertical CM velocities across one or more gait cycles to be zero. They subsequently assumed the initial lateral and vertical CM velocities to be zero. They estimated the initial antero-posterior CM velocity as the value of the average forward velocity measured with two photo cells or infrared lamps (timing devices) positioned a known distance apart. These measured values are dependent on which part of the body triggers the timing devices and at which points in the gait cycle these devices are triggered. The assumption is that the part of the body that triggers the devices will be in the same position relative to the CM at both triggering instants, and that these instants will coincide at the same points in successive gait cycles. Even if this was the case, the initial velocities may not equal their average values over the entire gait cycle. Hence, a squared error would be introduced to kinetic energy calculations and a cumulative drift error would be introduced to potential energy calculations. Lee

and Farley (1998) determined the integration constant (initial velocity) for the vertical direction by requiring the average vertical CM velocity over a stride to be zero. Iida and Yamamuro (1987) used a similar approach in all three dimensions. The approach of these researchers represented an improvement to the method, but it still assumes strictly repeating gait cycles, which is not a valid assumption (Hausdorff et al., 1996). Some researchers have aimed to avoid significant violations of this assumption by setting criteria governing inclusion or rejection of individual trials from their analyses. Sometimes these criteria have been only qualitative observational assessments. For example, Iida and Yamamuro (1987) stated that the "basis for selection was the naturalness of gait and the similarity of the wave patterns." Conversely, Crowe et al. (1993) mandated unambiguously that the durations of the two consecutive gait cycles they recorded per trial had to be within 1.5% of each other to be accepted.

Only the change in displacement rather than absolute displacement can be determined with the above gait IA methods. Other than applying a more complicated SK method, there is no way of making an accurate estimate of the initial CM displacement (S_0) at the instant the subject makes contact with the force platform because he or she is already in motion. Further, these methods are hampered by problems associated with assigning an assumed value, or a value averaged over one or more gait cycles, to an initial CM velocity component constant (Thirunarayan et al., 1996). Adjacent gait cycles are not strictly repeatable; stride-to-stride variability is inherent in human gait (Hausdorff et al., 1996). Any discrepancy between the assigned and the true value results in a drift error in CM displacement calculations. Whether or not the imprecision of these

estimates is of practical significance, when relative CM displacement calculations are subsequently made with the above IA methods, has not been reported.

Other researchers have evaluated the performance of IA versus kinematic methods for gait analysis applications. Thirunarayan et al. (1996) compared the IA and two kinematic methods in terms of relative vertical CM displacement. The first of the kinematic methods simply involved a single marker affixed to the pelvis that was assumed to have represented the CM and hence involved no SK analysis. The other involved a limited SK analysis in which the upper body was modelled as a single head-arms-trunk segment. They calculated the mean relative vertical CM displacement for each trial for each method. Although they did not conduct parametric nor non-parametric ANOVA tests first, they found no significant differences between any pair of means using Johnson's t-tests, Wilcoxon signed rank tests and signed tests (all reported $p \geq 0.10$). Although insignificant difference findings certainly do not imply the methods are equivalent, the conclusion by Thirunarayan et al. (1996) that the single marker and SK methods are "likely more accurate" than the IA method is highly questionable. Their IA method involved a technique to determine V_0 similar to the 'trend-eradication' technique of King and Zatsiorsky (1997), however a complete gait cycle of force platform data was not available, so the starting and final positions in the analysis could not have been at the same point in adjacent gait cycles. This would have had a detrimental effect on the IA method that is specific to gait IA methods. Saini et al. (1998) conducted a similar study to Thirunarayan et al. (1996) and reached similar conclusions. Whittle (1997) compared a similar simplified kinematic method (three pelvic markers representing the 'centre of the pelvis' in

three dimensions) and an IA method for 3-D $CM(t)$ determination similar to Lee and Farley (1998) in terms of estimation of the initial conditions. Whittle (1997) reported that the centre of the pelvis underwent greater excursions than the IA-determined CM. He also reported that the phasing between the centre of the pelvis and the CM was the same in the lateral and vertical dimensions, but the antero-posterior motion of the CM was 5° out of phase with the centre of the pelvis motion. This led Whittle (1997) to recommend further work aimed at assessing the contribution of the arm, leg and trunk movement on $CM(t)$.

Eames et al. (1999) extended the work of Whittle (1997) by comparing the same centre of the pelvis and IA methods with a full body, 12-segment SK method for able-bodied adults and children, and children with lumbosacral myelomeningocoele. Eames et al. (1999) found similar results to Whittle (1997) with respect to the differences between the IA and pelvis marker methods. The centre of pelvis method always produced greater excursions than the IA or SK method. Eames et al. (1999) also found no significant difference between the IA and the full body SK methods. Wilcoxon ranked tests were reportedly used, but they only reported non-significant p values as "p not below 0.185". They argued that arm, trunk and head movements contributed significantly to defining $CM(t)$ for the full body SK method. In contrast, the kinematic models of Thirunarayan et al. (1996) and Saini et al. (1998) were not sensitive to arm, trunk and head movements because of the head-arms-trunk segment they used. Gard et al. (2004) also compared pelvis marker, IA and SK methods in terms of vertical $CM(t)$. Performance of the three methods was compared for gait at four different speeds (0.8, 1.2, 1.6 and 2.0 ms^{-1}). They found no significant differences between the

methods for the slowest speed. Once again, this does not mean that the methods were equivalent at this speed. It may be that there was a smaller effect size (smaller excursion in the pelvis marker) at this speed that prevented potential differences from being identified. Regardless, at all other speeds, the pelvis marker method predicted significantly ($p < 0.001$) more vertical $CM(t)$ amplitude than the IA and SK methods. Despite the claims of Thirunarayan et al. (1996) and Saini et al. (1998), the findings of Gard et al. (2004) and Eames et al. (1999) suggest that IA methods will out-perform pelvis marker methods in terms of producing results closer to those produced by SK methods that employ full body models. However, the IA method for gait analysis would be improved by refinements to the estimation of the initial conditions for this activity.

2.1.3 Platform-Based Methods for Other Movement Analyses

Other researchers have estimated CM kinematics for activities other than stance or gait using IA methods. Papa and Cappozzo (1999) used the IA for sit-to-stand movements. However, they determined S_0 by SK analysis, thus defeating the purpose somewhat of using an IA method in order to avoid an SK analysis. Kerwin (1986) calculated CM kinematics as part of his method to determine H'_{CM} at take-off for gymnasts performing flic-flacs (reverse handsprings) by calculating the torque about the CM. S_0 was estimated by a full SK analysis because absolute $CM(t)$ was required to calculate H'_{CM}. As SK analysis was required, albeit only for the start of the analysis, Kerwin's claim that the method is a platform-only method was incorrect. Further, V_0 was simply assumed to be zero. Although the flic-flacs started with a quasi-static phase (when V_0 is essentially zero), the actual value would have been a small non-zero value, which would have introduced a

cumulative drift error to H'_{CM} calculations that may have been practically significant by the time take-off was reached.

Hatze (1998) and Kibele (1998) used IA methods to determine relative vertical $CM(t)$ for jumping activities. These approaches were completely independent of SK analyses. Hatze (1998) assumed $V_0 = 0$ for the countermovement jumps he analysed. He also analysed series of rebound jumps, for which V_0 was assumed to be zero at the commencement of such jump series. The initial velocity (at the time of impact) for each subsequent rebound jump in a series was determined from the time elapsed whilst airborne prior to impact and the calculated final velocity (at take-off) of the previous jump in that series. This approach is dependent on the accuracy of the assumption that $V_0 = 0$ prior to the first jump and the accuracy of estimates of the airborne phase durations. Although not stated explicitly, it appears that Kibele (1998) also assumed that $V_0 = 0$. Once again, the discrepancy between $V_0 = 0$ and the actual value of V_0 may introduce a practically significant drift error to $CM(t)$ calculations, particularly for the longer duration series of rebound jumps.

Kibele's approach was different to Hatze's in that he determined a specific body weight for each trial. He described the vertical GRF as "constant" during both the aerial phase and the quasi-static phase prior to countermovement jump commencement (minimum duration 0.3 s). The body weight was defined as the difference between these two readings for each trial. The advantage of this approach is that it negates the need to consider the possibility of a force calibration factor error (F_C) in the GRF signal (i.e. the error in the calibration

factor which is used to convert force platform voltage signals into units of force, usually from mV into N). Because F_C would also be present in the GRF readings used for determining m_{WB}, this error factor would be present in both the numerator and the denominator of the first term in Eq. (3), and would therefore cancel out and play no role in $CM(t)$ determination. However, the fundamental disadvantage of this approach is that subject mass does not change from trial-to-trial in reality. Further, vertical GRF is not constant during quiet stance and 0.3 s is arguably an insufficient time period over which to average this signal in order to estimate body mass accurately. Kibele stated that the "body weight value does not vary significantly (less than 1%) between trials." The effect on $CM(t)$ calculations of the different body mass values observed in his study were not reported by Kibele (1998). Whether or not body mass variations of 1% introduce $CM(t)$ errors of practical significance for activities as transient as countermovement jumps, the effect on longer duration activities is more likely to be practically significant.

Vanrenterghem et al. (2001) also determined trial-specific body mass values when they applied the IA to ten simulated countermovement jump trials. They reported using an "optimising loop" to find the body mass value that resulted in no net vertical displacement of the CM during the two-second stance phase prior to jump initiation. They also assumed vertical V_0 to be zero. Vanrenterghem et al. advocated trial-specific selection of body weight and claimed that this "results in the best possible correct jump height parameters."

Rabuffetti and Baroni (1999) also determined $CM(t)$ using an IA optimisation method that involved trial-specific determination of body mass, though their

method also required a full body SK analysis to be conducted. They assessed jumping, bending and kneeling activities. Importantly, they attempted to account for another potential source of error by introducing a GRF offset error term (F_O) into the equation for calculating $CM(t)$:

$$CM(t) = \frac{1}{m_{WB}} \iint F dt + \frac{1}{2}\left(\frac{F_O}{m_{WB}} + g\right)t^2 + V_0\, t + S_0 \tag{7}$$

In addition to trial-specific body mass values, Rabuffetti and Baroni (1999) also searched for the values of S_0, V_0 and F_O that minimised, in a least squares sense, the function:

$$CM(t)_{SK} - \left[\frac{1}{m_{WB}} \iint F dt + \frac{1}{2}\left(\frac{F_O}{m_{WB}} + g\right)t^2 + V_0\, t + S_0\right] \tag{8}$$

where $CM(t)_{SK}$ is the whole body CM determined by a full body SK analysis. Necessary BSP estimates were derived from Zatsiorsky and Seluyanov (1983). The results they presented for one trial indicated a value of 0.079 ms^{-1} for medio-lateral V_0, which is arguably non-feasible for this parameter for a normal subject during quiet stance[3], particularly considering that stance is more stable in the medio-lateral dimension than the antero-posterior dimension (Winter et al., 1996a). Indeed, even for an eyes-closed condition, Masani et al. (2003) reported maximum antero-posterior CM velocity values less than 0.03 ms^{-1}. The

[3] The jump was commenced with a quasi-static stance phase.

apparently unrealistic V_0 value might have been caused by shortcomings in the optimisation algorithm's searching performance near the minimum. It is also possible that errors inherent in the joint coordinate data and BSP estimates contributed to the derivation of a non-feasible value of V_0.

Jaffrey et al. (2003) questioned the validity of the trial-specific body mass determinations proposed by Kibele (1998), Vanrenterghem et al. (2001) and Rabuffetti and Baroni (1999), based on the fact that body mass does not change from trial-to-trial. Jaffrey et al. (2003) also used an IA optimisation method to determine relative $CM(t)$ for a countermovement jump. Their objective was similar, though not identical, to that of Vanrenterghem et al. (2001). They minimised an objective function representing the sum of squared relative $CM(t)$ values during the two-second quasi-static stance phase prior to jump initiation. The advantage of this approach (and that of Vanrenterghem et al., 2001) over the approach of Rabuffetti and Baroni (1999) was that a full body SK analysis was not necessary.

To support the theoretical argument against varying body mass, Jaffrey et al. (2003) demonstrated the different effects of varying body mass versus holding body mass constant when minimising their objective function. Three parameters in Eq. (7) were addressed in their assessment: m_{WB}, V_0 and F_O (S_0 was omitted from their objective function based on the argument that only relative displacement was sought). Various combinations of these parameters were either held constant or allowed to vary and the resultant optimised $CM(t)$ was assessed by comparing the corresponding jump amplitudes. Firstly, m_{WB} was assigned the

constant value obtained from accurate mass measurement on precision scales (64.21 kg), and only F_O and V_0 were allowed to vary. The resultant value of V_0 was 0.00352 ms^{-1}. Although no values for vertical CM velocity during quiet stance were retrieved from the literature, this value for V_0 does not appear to be excessive for the vertical dimension during quiet stance. When m_{WB} was also allowed to vary, the resultant value of m_{WB} was unrealistically 1.1 kg greater than the accurately measured value; the value of V_0 only changed by 0.00006 ms^{-1}; and F_O increased by 10.75 N, apparently compensating quite well for the mass error (1.15 kg × 9.8 ms^{-2} = 10.78 N). However, the calculated jump amplitude in the variable body mass condition was more than 0.01 m less than the jump amplitude for the constant (accurate) body mass condition.

The major limitation of the work presented by Jaffrey et al. (2003) was that only a single trial was assessed. However, they demonstrated that accurate mass determination and the use of a force offset error variable produced different $CM(t)$ results to those produced by allowing body mass alone to vary. Coupled with the knowledge that m_{WB} does not vary from trial-to-trial in reality, they concluded that body mass should be determined accurately on precision scales and included in the objective function as a constant. Further, they supported the proposal of Rabuffetti and Baroni (1999) to include a GRF offset error parameter.

For movement analyses commencing with quasi-static phases, V_0 will not usually be precisely zero. This supports the inclusion of this parameter in any IA optimisation method. The realistic values obtained for V_0 by Jaffrey et al. (2003) support its inclusion in IA optimisation methods, particularly for longer duration

activities where even a small error in V_0 will have a cumulative, practically significant influence on $CM(t)$ as time progresses. However, the arguably non-feasible V_0 value presented by Rabuffetti and Baroni (1999) highlights the need to consider the effects of the implemented optimisation search algorithm and the formulation of the objective function.

Objective functions like those of Vanrenterghem et al. (2001) and Jaffrey et al. (2003), and the ZPZP method of Zatsiorsky and Duarte (2000), present possible means for accurate determination of the initial conditions parameters (V_0 and S_0) and optimisation of $CM(t)$ for any activities that can be commenced with a quasi-static phase. The inclusion of GRF force calibration factor (Kibele, 1998) and offset (Rabuffetti and Baroni, 1999) error parameters may minimise the influence of force platform errors and, therefore, improve IA optimisation methods. The author is unaware of any IA optimisation research to date that has incorporated all of these parameters concurrently. Ultimately, such an IA optimisation method may provide a relatively simple and accurate alternative to SK determination of CM kinematics for a wide range of movement activities.

2.1.4 Evaluation of Platform-Based Methods Using Segmental Kinematic (SK) Analysis

Many of the aforementioned researchers, who determined CM kinematics principally from force platform data, evaluated their methods by comparing them with a SK method. However, Lenzi et al. (2003) and Kibele (1998) have argued that SK determination of CM kinematics is not the 'gold standard'. Lenzi et al.

(2003) found that 10% errors in BSP parameters produced RMS errors of up to 20% of the CM displacement ranges for simulated sitting and standing tasks. Kibele (1998) showed that trunk flexion during countermovement jumps introduced significant errors in segmental kinematic $CM(t)$ calculations because his model's trunk segment was assumed to be rigid. The author's review of the literature found that no IA or SK approach has been demonstrated to be the most definitive for determining CM kinematics. The possibility exists to reduce error sources inherent in both approaches. New IA optimisation methods have already been identified in section 2.1.3. Optimisation techniques may also improve the accuracy of subject-specific BSP estimation techniques when applied to SK analyses. This argument is developed in ensuing sections.

2.2 Body Segment Parameter Estimation

Since Harless (1860) demonstrated several methods for measuring and estimating the body segment parameters (BSPs) of cadavers, several improved cadaveric techniques and many creative approaches for living humans have been developed. However, different methods available for application to living subjects can produce very different BSP estimates for the same subject (Cappozzo and Berme, 1990; Kingma et al., 1996b). The major contributions that have been made to the development of BSP measurement and estimation techniques are summarised in section 2.2.1. Studies that have compared the performance of various BSP estimation techniques and those that have addressed accuracy or validity considerations are reviewed in section 2.2.2. Studies that have evaluated the

effects of anticipated BSP estimate errors on various dynamics calculations are addressed in section 2.2.3.

2.2.1 Body Segment Parameter Estimation and Measurement Techniques

Several review articles have been published on BSP estimation and measurement techniques, and different approaches have been employed to categorise the various methods. For example, some authors have divided the methods into those performed on living subjects and those performed on cadavers (Reid and Jensen, 1990), whereas others have separated the methods into different chronological periods (Pearsall and Reid, 1994) or different methodological approaches (Contini, 1972; Drillis et al., 1964). The present review partitions the various BSP measurement and estimation approaches into five broad methodological categories:

- Cadaver-Specific Techniques
- Volumetric and Geometric Modelling Techniques
- Medical Imaging Techniques
- Predictive Techniques (Regression Equations)
- Dynamics and Optimisation Techniques.

Major contributions to BSP measurement and estimation made under each of the first four categories are summarised in sections 2.2.1.1 to 2.2.1.4. The reader is also referred to the aforementioned review articles and a more recent review by Zatsiorsky (2002a) for additional summaries of these and related studies. In

section 2.2.1.5, dynamics and optimisation techniques are reviewed. In particular, a more detailed review is conducted in section 2.2.1.5.2 of BSP estimation methods that rely on whole body dynamics analyses, due to their direct relevance to the author's research.

2.2.1.1 Cadaver-Specific Techniques

Cadaver-specific techniques for the determination of the BSPs of isolated segments, by definition, are only applicable to sectioned cadavers. Although some techniques discussed in proceeding sections can be applied similarly on both cadavers and living subjects, the techniques discussed in this section involve direct, more definitive BSP measurement techniques that are only possible on sectioned cadavers.

Harless (1860) presented data from two cadavers, each dissected into 15 segments, though Drillis et al. (1964) reported that he had dissected five male and three female cadavers. Harless weighed each segment to determine its mass and measured the centre of mass with the aid of a balance board. Once a segment was positioned on the board such that the board-segment system was in equilibrium, the centre of mass of the segment was known to lie directly above the line of the board's fulcrum. The cadavers studied by Harless (1860) were decapitated prisoners and were not frozen, so an unknown amount of body fluid would have been lost before the measurements were made (Reid and Jensen, 1990). Though the data were consequently not reliable, these and other techniques presented by Harless (see also section 2.2.1.2) marked the commencement of BSP measurement.

In the late 1800's, others dissected a small number of cadavers. Meeh (1895) measured the segment masses but not the other BSPs of four infant cadavers ranging in age from premature to 22 months (Dempster, 1955). Braune and Fischer (1889; 1892) measured the segment mass and centre of mass BSPs of three muscular male cadavers aged between 18 and 50 years. As reported by Reid and Jensen (1990), segments were frozen and the centre of mass BSPs were determined by a suspension method. Three thin metal rods were driven through each segment in an orthogonal configuration, each one perpendicular to one of the cardinal planes. After suspending a segment from each rod, the point within the segment coincident to all three planes of equilibrium was deemed the centre of mass. The moments of inertia about two of these axes (according to Reynolds, 1978, the longitudinal and transverse anatomical axes) were also measured empirically by a compound pendulum approach, in which the period of small oscillations (T) of the segment about the axis of rotation (in this case, the metal rod) is measured and the segment's moment of inertia about this axis (I) is then calculated with the equation:

$$I = \frac{MgdT^2}{4\pi^2} \tag{9}$$

where M is the mass, g is gravitational acceleration, and d is the distance between the axis of rotation and the centre of mass.

Dempster (1955) dissected eight middle-aged and elderly Caucasian cadavers and determined the mass, centre of mass, and moments of inertia about the transverse anatomical axis through the centre of mass, of the segments using weighing, balance board and compound pendulum techniques, respectively. According to Reid and Jensen (1990), at the time of their publication, the BSP results reported by Dempster (1955) had been adopted extensively for human dynamics research, even though they were derived from the cadavers of somewhat emaciated males ranging in age from 52 to 83 years. Using techniques similar to Dempster (1955), Clauser et al. (1969) measured the mass and centre of mass BSPs of preserved male cadavers. Using preserved cadavers allowed them to be more selective than Dempster (1955) with respect to their choice of appropriate cadavers for their study. As a result, their sample of 13 cadavers had a mean and standard deviation of 49.31 ± 13.69 years for age, 66.52 ± 8.70 kg for weight, and 172.72 ± 5.94 cm for height. The main development introduced by Clauser et al. (1969) was the 73 anthropometric measurements they made on each cadaver for the purposes of developing regression equations for estimating the BSPs of living subjects (see section 2.2.1.4). They did not measure the segmental moments of inertia.

The most recent substantial cadaveric study was conducted by Chandler et al. (1975). It remains the most comprehensive cadaveric study of segmental inertia tensor measurements. Recognising that previous researchers had only measured the moments of inertia with respect to axes other than the principal axes of inertia, Chandler et al. (1975) applied a compound pendulum technique about six different rotational axes in order to obtain the full inertia tensor for each segment,

incorporating the three principal moments of inertia and the six products of inertia.

Lephart (1984) has since refined the methodology for measuring cadaver segment moments of inertia, highlighting a validity issue that should be considered when evaluating any pendulum method used prior to or since his work. Lephart validated his method using objects of known geometric shape and homogenous composition. Calculating the criterion values of the objects' moments of inertia was a trivial process involving integral calculus, considering that the geometry and density of each object were known precisely. Lephart (1984) reported a systematic error in moment of inertia measurements made with his pendulum device; the heavier an object, the more overestimated was the moment of inertia. Lephart attributed this observation to the presence of a frictional force slowing down the timed series of oscillations applied to Eq. (9). Subsequently, he applied a regression analysis to produce time-correction equations based on object mass, resulting in mean absolute percentage errors for his pendulum method of less than 1.4%, and a maximum absolute error for all tests of less than 5%. The measured directional angles for the principal axes of inertia were never greater than 2% different to the geometrically pre-defined values for the criterion objects.

Some of the abovementioned techniques are arguably the most accurate and valid methods available for measuring BSPs. For instance, weighing is an empirical measurement technique that is accepted without question for mass determination applications of this type. However, the accuracy of pendulum methods is questionable (Durkin et al., 2002). Even the relatively rigorous methodology

employed by Lephart (1984) produced absolute errors approaching 5%. Regardless, in terms of determining the BSPs of individual segments, these methods are only applicable for sectioned cadaver segments. Consequently, weighing, reaction board, suspension and compound pendulum methods, as described above, can only be applied to living subjects for determining whole body inertial measurements (e.g. de Leva, 1993; McKinon et al., 2004; Schultz et al., 1997). The main application of the various cadaver data sets has been the development of regression equations for estimating the BSPs of living subjects, but these predictive equations have limitations that must be considered before they are adopted (see section 2.2.1.4). Hence, many alternative approaches for estimating the BSPs of living subjects have been proposed. Some of these methods have also been applied on intact or segmented cadavers, where applicable.

2.2.1.2 Volumetric and Geometric Modelling Techniques

Living subject BSPs have been derived from measurements of other segmental physical properties, such as segment volume and anthropometric measurements. Various water immersion and body surface scanning techniques have been proposed by many researchers. Segment volumes have also been estimated by first modelling the segments as geometric solids and then scaling the dimensions of the geometric solids for each individual based on certain anthropometric measurements. However, all such methods rely on assumptions regarding the density or mass distribution of tissues within the segments, as shall be discussed at the end of this section.

Segment volume measurement allows segment mass estimation if segment density is known. One group of techniques used to measure segment volume involve the immersion of segments in water. Harless (1860) was the first to use an immersion method. He assumed that the measured volume of displaced water was equal to the volume of the submerged segment. Although Harless used this method on cadavers, others have since used similar approaches on living subjects by progressively immersing limb segments, one segment at a time (e.g. Bernstein et al., 1936; Clauser et al., 1969; Dempster, 1955; Drillis et al., 1964). According to Drillis et al. (1964), Bernstein et al. (1936) measured the limb segment BSPs of 76 males and 76 females aged 12 to 75 years. Details of the methodology they employed were not published in English. Dempster (1955) weighed the displaced water rather than measure the volume directly. Dempster's displaced water weight measurements were corrected for temperature by Clauser et al. (1969). Drillis et al. (1964) advocated that immersion vessels should be of similar volume to that of the segments for which they are designed and recommended that segments should be inserted into the empty vessels prior to a known volume of water being added. Drillis et al. (1964) also demonstrated a method for estimating the centre of volume position of living subject's segments by incremental immersion of 2 cm 'slices' of each subject. By assuming the segmental centre of volume to coincide with the segmental centre of mass, an estimate of the latter parameter was generated by this procedure. However, Clauser et al. (1969) showed that the volume of water displaced when a cadaver segment was submerged, proximal end first, up to its directly measured centre of mass position, was as much as 57.5% of the totally submerged segment's displaced water volume, rather than the 50% assumed by Drillis et al. (1964). This also casts

doubt on the segmental moment of inertia calculations also made by Drillis et al. (1964), which also required the additional assumption that the 2 cm incrementally submerged segment sections were cylindrical in shape.

Various techniques of body surface mapping based on stereophotogrammetry have also been applied for estimating whole body and segment volumes (Ertaud et al., 1999; McConville et al., 1980; Young et al., 1983). Young et al. (1983) found that the stereophotogrammetric method they employed overestimated total body volume in 12 measured subjects by an average of more than 10%, compared with the criterion measurements they made using a water immersion technique. Since then, stereophotogrammetry technology has improved, with higher resolution imaging now available. Ertaud et al. (1999) reported a 3.13% overestimate of the volume of a mannequin for the five-camera system they employed. Pain and Challis (2001) used a 3-D sonic digitiser for body surface mapping. To assess the accuracy of the method, they used a wooden test object of known dimensions, the mass and volume of which were measured directly. Subsequently, four operators digitised the test object to estimate its volume and then calculated its mass using the density value derived from the previously-described direct measurements of mass and volume. The mass values derived from the scans were then compared with the directly measured mass. The mean absolute difference was 0.9%, with individual values ranging from 0.1 to 2.3%. Because the test object density was known, these values also reflect the error in volume measurement by the 3-D sonic digitisation method. Norton et al. (2002) demonstrated the use of a 3-D near infrared whole body surface scanner for mapping the surface and measuring the volume of leg segments. They reported volume measurement errors of less than

1% for all ten legs measured, when compared to the corresponding water immersion criterion volume measurements. However, they did not explain why they only measured or reported the results for either the left or right leg for eight of their nine subjects and why they measured and reported the results for both legs of the ninth subject. Further assessment of 3-D scanners of this type requires validation with criterion objects and reporting of data on all other body segments. Although the cost of such scanners is reducing, they remain expensive at present, which limits the uptake of this method.

All of the above volumetric approaches require cumbersome or expensive measurement apparatus and involve time-consuming methodologies. Also, in order to determine BSP estimates, these methods require either the assumption of uniform segmental density or more complicated modelling concerning the densities and distributions of the various tissues within the segments. Geometric modelling techniques also require the uniform density assumption or density profiling. However, the appeal of geometric methods is that they are relatively inexpensive to apply and they require more basic measurement equipment and techniques than volumetric approaches.

The irregular shape of human body segments makes their volume difficult to measure, as was highlighted during the preceding discussion. However, if the shape of a segment can be well approximated by one or a series of geometric solids, segment volume can be estimated easily by calculating mathematically the volume of the geometric solid(s). Subject-specific dimensions of the geometric solids are derived from specified measurements of segmental anthropometry.

Usually, by assuming the segment to be of homogenous composition (i.e. assuming uniform density) and with the provision of a density value from the literature, estimates of all modelled segments' BSPs can be calculated.

In addition to the cadaveric and volumetric methods proposed by Harless (1860), he also introduced the method of geometric modelling for the trunk segment. Others have since modelled all the segments to varying degrees of complexity. Hanavan (1964) created a 15-segment model comprised of a circular ellipsoid for the head, elliptical cylinders for two trunk segments, spheres for the hands and frustra of circular cones for the other limb segments. Individualised geometric solid dimensions were based on 25 anthropometric measurements. Chandler et al. (1975) tested Hanavan's model, as adapted by Tieber and Lindemuth (1965), with the empirically measured BSPs from their six cadavers. They found large discrepancies between measured and predicted segment masses and moments of inertia for many segments and concluded that the geometric shapes chosen by Hanavan were not valid, particularly those chosen to represent the head, trunk and hands. Hanavan's model has seldom been used since then.

Jensen (1976, 1978) developed a geometric model based on the original method of Weinbach (1938). Often termed the elliptical zone model, Jensen modelled each of 16 segments as a stack of two-centimetre high elliptical cylinder slices. A photogrammetric approach was used to produce frontal and sagittal images of the subject, allowing subsequent measurement of the length of the two semi-axes of each elliptical slice of each segment. By adopting segmental density values from the literature, the BSPs could then be calculated. Over the years, Jensen and

colleagues have improved the method by using more representative segment-specific density data (Jensen, 1986) and introducing digitisation of images to speed up processing time (Jensen and Fletcher, 1993). The elliptical zone model takes individual differences in segment morphology into consideration. For example, it is one of very few methods that can be applied with any confidence to estimating the trunk BSPs during pregnancy (Jensen et al., 1996). However, the use of elliptical cross-sections to model various parts of the trunk has been challenged by Yeadon (1990b) and Erdmann (1997), who have illustrated that cross-sections of the trunk at various heights are shaped more like stadia than ellipses.

Hatze (1980) developed, arguably, the most comprehensive and detailed geometric model for BSP estimation, comprising 17 segments and requiring 242 anthropometric measurements for complete definition. He used multiple and often more complex geometric solids to model each segment's morphology and, where applicable, its asymmetry. For instance, some cross-sectional components of the trunk segments were modelled as pairs of unequal semi-ellipses. The large number of subject-specific anthropometric measurements used to define the segments included various skin-fold measurements and segmental height, width, breadth and circumference measurements. Not assuming uniform density, Hatze assigned different tissue density values to many of the component geometric solids. Hatze (1980) claimed that such a comprehensive approach allowed more accurate predictions of subject-specific BSPs, including more accurate determination of the principal axes of inertia. He also asserted that his model was applicable to subjects of diverse morphologies, ranging from pregnant women to

obese men and young children. The use of Hatze's method by Schneider and Zernicke (1992) for infant limb segments and the modification made by Dillon et al. (1999) to model a partial-amputee's foot segment support this assertion. However, Hatze's method is probably most conspicuous because of the rarity of its utilisation by other researchers[4], suggesting that it may often be considered too complicated or too time-consuming (Kwon, 1996) to implement for many practical applications. Indeed, even Schneider and Zernicke (1992) only applied Hatze's limb segment models, which represent some of the less complex segments in Hatze's overall model. Hatze (1980) reported that almost 80 minutes are required to collect all the anthropometric measurements necessary for his technique and this was confirmed by Sprigings et al. (1987).

Yeadon (1990b) introduced a geometric model for determining BSPs as part of a four-paper series describing the measurement, modelling and simulation of 3-D aerial human movement (Yeadon, 1990a; 1990b; 1990c; Yeadon et al., 1990). Yeadon's most significant and novel contribution was the introduction of stadium solids to represent the trunk segments. He demonstrated that a stadium more closely approximates the cross-sectional shape of the human torso than does an ellipse. He also used stadium solids to model the hands and feet, as has Challis (1999). Yeadon's (1990b) model requires 95 anthropometric measurements, which he reported required 20-30 minutes to collect per subject.

---

[4] The author was only able to find two other applications of this method, Sprigings et al. (1987) and Hedoux et al. (2000), the former of which appears to be the only study that has applied Hatze's method to all body segments.

All volumetric and geometric modelling techniques for BSP estimation involve measuring or estimating segment morphology and/or volume. They do not involve direct measurement of tissue composition and distribution, so they all require assumptions regarding the density of segmental tissues before inertial characteristics can be derived. The most commonly applied assumption is that each segment is of uniform density with segment-specific density values assigned to each segment (e.g. Jensen, 1978), usually based on the cadaver data of Dempster (1955) or Clauser et al. (1969). However, even these researchers demonstrated the invalidity of the uniform density assumption.

Dempster (1955) sectioned one frozen embalmed cadaver into one-inch-thick transverse sections and then dissected each section into its constituent tissues: skin, muscle, adipose, bone and other organ tissues. As a result, he was able to illustrate that the relative proportions and distribution of each tissue type varied quite considerably along the length of the body. Others have illustrated similar findings based on medical imaging techniques (see section 2.2.1.3). Clauser et al. (1969) determined the percentage of segmental volume proximal to the directly-measured segmental centre of mass for several cadaver limb segments. They estimated that the centre of volume lay up to 3 cm proximal to the centre of mass of the limb segments. Ackland et al. (1988b) also showed that the density profile of the shank segment varied markedly along the long axis when measured by computed tomography. Computed tomography is a medical imaging technique; it is described in section 2.2.1.3).

Wei and Jensen (1995) made a limited assessment of the effects of the uniform density assumption on BSP calculations. They used the elliptical zone method (Jensen, 1978) to determine the BSPs of 50 subjects. BSP values were calculated twice for each subject: once using the uniform segmental density values of Dempster (1955) (for the trunk segments) and Clauser et al. (1969) (for the other segments); and once applying the averaged segmental axial density profiles of 50 Chinese females aged 18-23 years that they reported were measured by Zheng et al. (1990) using computed tomography. For the ten subjects most similar to those reportedly measured by Zheng et al. (viz. 22 to 34 year old females, according to Wei and Jensen, 1995)[5], they found mean differences for each BSP of up to 12%. Obviously, differences for specific BSPs of individual subjects were even greater in some cases. Although some of this variation may be explained by differences between the subjects used in this study and those from which the density data were drawn (e.g. ethnicity, age and gender differences), and although they could not determine which approach was more accurate from their limited assessment,

---

[5] Wei and Jensen (1995) cited Zheng et al. (1990) as the source of this data. Retrieval of the corresponding publication listed in their bibliography revealed that only an abstract was published, which did not report the averaged segmental axial density profiles of those measured. Indeed, the abstract only reported the scanning of 15 males and four cadavers, making no mention of 50 female subjects. Further, only the first author was listed as an author, so it is cited hereafter in this thesis as Zheng (1990). The results of the averaged segmental axial density data for the trunks of 50 females presented in figure 1 of Wei and Jensen (1995) may have been presented at the conference pertaining to Zheng (1990) or published elsewhere. However, they were not published in Zheng (1990).

Wei and Jensen (1995) recommended the use of density profiles to allow for axial variation in density.

Norton et al. (2002) didn't assume uniform density when they used a near infrared whole body surface scanner for measuring the volume of leg segments. They made attempts to estimate the distribution of bone mass within the mapped segment volume and used both bone and soft tissue uniform density values for leg segments. A water displacement technique was used to produce comparison data to assess their scanner method. Differences in volume and centre of mass location, measured across 10 legs, were less than 1% and 4%, respectively.

Challis and Kerwin (1992) compared the use of uniform density data (Chandler et al., 1975; Clauser et al., 1969; Dempster, 1955) and variable density data (Rodrigue and Gagnon, 1983) for calculating the moments of inertia of the forearm with a geometric model comprised of two truncated cones. They reported that the variable density data did not improve the accuracy of the forearm moment of inertia estimates in their study, compared with uniform density values. However, they postulated that a larger database of variable density information may improve geometric model BSP estimation accuracy. Ackland et al. (1988b) reported only "minor errors" in shank BSPs derived from uniform density data compared with variable density profile data, however, only two shanks were assessed in their study. Although it remains unclear whether the uniform density assumption is generally acceptable for the shank and other limb segments, it may not be reasonable for certain individuals, and it is likely that such an assumption will be inadequate for the trunk, which has more extreme variation of tissue

density throughout its length (Ackland et al., 1988b; Erdmann, 1997; Huang and Suarez, 1983; Pearsall et al., 1996; Wei and Jensen, 1995). Thus, methods applicable to living subjects that are able to measure mass distribution within segments present a distinct advantage over methods that rely on the uniform density assumption.

2.2.1.3 Medical Imaging Techniques

Several medical imaging technologies have been applied to the task of determining BSPs, including gamma scanning, dual energy x-ray absorptiometry (DEXA), computed tomography (CT), and magnetic resonance imaging (MRI). These technologies allow measurement of tissue mass and mass distribution within the segment and can be applied to living subjects.

Gamma-ray, DEXA and CT scanners all work based on the same underlying principles. In simplified terms, when gamma and X-rays are passed through a body, energy is lost as some of the photons interact with the electrons within the body. By measuring the intensity of the radiation beam before and after it has passed through the body and accepting certain other assumptions, it is possible to estimate the mass of the matter through which the beam has passed. The amount of photons absorbed depends on the atomic composition of the body and the energy of the radiation beam before it passes through the matter (Webber, 1995). A more detailed explanation of the theory behind this method is available from the aforementioned publication.

Casper et al. (1971) demonstrated the potential of gamma scanning for BSP estimation when they scanned wooden, aluminium and plexiglass objects. According to Reid and Jensen (1990), they calculated the mass, centre of mass and moment of inertia parameters for these inanimate objects and determined the accuracy of their calculations to be within ±1%. Brooks (1973) and Brooks and Jacobs (1975) adapted this technique for biological matter. Using legs of lamb, they obtained mass, centre of mass and moment of inertia values within 1%, 2.1% and 4.8% error, respectively, when compared with weighing, reaction board and pendulum measurement methods, respectively. They had to account for the presence of hydrogen in the tissues. Hydrogen has a 1:1 ratio of nucleons (protons and neutrons) to electrons, whereas all other commonly found elements in mutton and human tissue have a ratio of approximately 2:1. They used a scaling factor to account for the over-prediction of mass resultant from their apparatus being calibrated with an aluminium object.

Zatsiorsky and colleagues were also working with gamma scanners during the mid-1970's (Zatsiorsky, 2002b), though their work was not published in English until the following decade. They were able to apply this technology to scan the whole body of living subjects. Zatsiorsky and Seluyanov (1983) reported the scanning of 100 young adult male Caucasians. Zatsiorsky et al. (1990b) added data for 15 young adult female Caucasians. Mass, mass centroids and moments of inertia about three orthogonal axes were reported for 16 segments, though it is not clear from the authors' English-language publications related to this topic (Zatsiorsky and Seluyanov, 1983; 1985; Zatsiorsky et al., 1990a; 1990b; Zatsiorsky, 2002b) how the moments of inertia about three different axes were

derived, considering that each individual scan only provided 2-D mass distribution information, and there was no indication that multiple scans were conducted about multiple axes. Durkin and Dowling (2003) have made a similar observation.

Zatsiorsky (2003) reported that the radiation dose from a whole body gamma scan did not exceed 10 mrad (0.1 mSv), which is less than 5% of the average yearly whole body radiation dose due to natural background radiation in the United Kingdom (Directorate-General for the Environment of the European Commission, 2000) and 2% of the recommended annual dose constraint for participants in Australian-based medical research (Australian Radiation Protection and Nuclear Safety Agency, 2002). Although the radiation dose delivered by a gamma scan is arguably low, Pearsall and Reid (1994) suggested that the sparsity of its application to BSP measurement is primarily due to the potential health risks associated with exposure to gamma radiation. The author is only aware of one other case of gamma scanning being applied to living subjects (Duval-Beaupere and Robain, 1987). Other possible contributing factors to the lack of application of this method include the cost of equipment and the complexity of the methodology.

Another similar BSP measurement method for living subjects is dual energy x-ray absorptiometry (DEXA). DEXA is used more often for measuring bone mineral content and the proportions of bone, lean tissue and fat tissue in the body (Webber, 1995). More recently, Durkin and Dowling (2003) and Ganley and Powers (2004b) have used DEXA scanners for measuring BSPs.

A detailed description of the underlying physics applicable to DEXA is available in Webber (1995). In basic terms, DEXA involves scanning the body with X-rays at two distinct energy levels. X-rays at different energy levels are attenuated to differing degrees for a given element. They are also attenuated differently by the different elemental components of the tissue through which they are passed. Hence, when dual energy X-rays of known energy levels are used to scan the body and assumptions are made regarding the elemental composition of bone and soft tissues, estimates of bone mineral content and body composition can be made. However, the similar photon attenuation properties of muscle and fat tissues presents methodological problems that need to be overcome if DEXA is to be used for precise body composition measurement (Webber, 1995). Dowling (2003) has pointed out that this is not an issue if only the overall mass distribution of the material in the path of the area scanned by the beam is required, because such an objective only requires x-rays at one energy level (140 keV) for BSP measurement with DEXA because the attenuation properties for the elements found in non-negligible proportions in human tissues are very similar at this energy level.

After scanning human subjects, Durkin et al. (2002) used only the 140 keV x-ray attenuation results from the scan data, and a mass calibration constant derived from a scanned textbook of known mass and of elemental composition assumed to be representative overall of human tissue. By scanning objects with empirically measured and geometrically calculated inertial characteristics for validation purposes (viz. a homogenous plastic cylinder and a cadaver leg), they reported

that DEXA was capable of measuring inertial characteristics with an accuracy of 3.2%. Durkin and Dowling (2003) used frontal plane DEXA scans to determine the segment masses and frontal plane centres of mass and moments of inertia of the limb segments of 100 subjects.

Ganley and Powers (2004a; 2004b), on the other hand, used data from both the 140 keV and 70 keV x-ray beams and applied assumed constant density values for each tissue type. They scanned segments with less resolution than Durkin and Dowling (2003), only scanning in slices of 3.9 cm. Ganley and Powers (2004a) reported that pilot studies had shown the BSP values calculated from 3.9 cm sections "did not statistically differ" from those calculated from 1.3 cm sections. The reported coefficients of variation ranging from 0 to 0.03% but did not report relevant *p*-values. However, it is beneficial to avoid any unnecessary reduction in scanning resolution. Ganley and Powers (2004a; 2004b) did not attempt to validate their application of DEXA to BSP measurement; instead simply comparing the DEXA results with BSPs derived from the predictive equations of Dempster (1955).

Based on currently published work, the approach of Durkin and Dowling (2003) appears to be the more reliable DEXA-based methodology for BSP measurement. However, use of DEXA for this purpose has certain limitations. DEXA involves exposing the subject to a radiation dose of 0.02 mSv for a whole body scan. However, this is only one fifth of the dose reported by Zatsiorsky (2003) for gamma scanning and therefore is only 0.4% of the recommended annual dose constraint for participants in Australian-based medical research (Australian

Radiation Protection and Nuclear Safety Agency, 2002). Like gamma scanning, DEXA can only provide 2-D mass distribution information. Scanning is limited to the frontal plane (Durkin, 1998), at least for some segments. Sagittal scans of the more distal segments of the extremities should be possible. However, attempts to determine sagittal plane BSPs for the upper arm, thigh and trunk segments would be confounded by the overlapping of the proximal limb and trunk segments in the sagittal plane (Durkin et al., 2002). 3-D medical imaging technologies (viz. CT and MRI) overcome this problem. They allow volumetric analysis and 3-D determination of mass distribution.

Computed Tomography (CT), also known as Computed Axial Tomography or Computer Aided Tomography, is also based on ionising radiation technology. Rather than a discrete scan of the whole body in one plane, a CT scanner rotates around the body, making multiple scans from many different angles. In addition, these multiple scans are completed for each of a series of narrow, horizontal cross-sectional slices of the body. Computational algorithms subsequently create a 3-D model of the mass distribution of the body.

Huang and Suarez (1983) were the first researchers to demonstrate the use of CT scanning for BSP measurement when they determined the BSPs of the head and neck of a porcine specimen and a 3-year-old female cadaver. Rodrigue and Gagnon (1983) used CT to measure the density of 20 cadaveric forearms, and Ackland et al. (1988b) used CT to measure the BSPs of the shank of a living subject and a cadaver. Much of the work completed on BSP estimation with CT has concentrated on the trunk (Erdmann, 1997; Pearsall et al., 1996; Reid, 1984)

due to the relative lack of validity of applying the uniform density assumption to volumetric and geometric BSP estimation techniques for this segment (Ackland et al., 1988b). Others have used whole body CT scanning to determine the BSPs of all body segments. Hui et al. (1999) reported measuring the BSPs of 50 young male and 50 young female Chinese subjects aged 18 to 22 years and Zheng (1990) used CT to measure the BSPs of 15 Chinese males and four cadavers.

The more extensive nature of CT scanning, relative to the other radiation techniques already discussed, is the source of both its advantages and its drawbacks. Multiple scans associated with CT provide 3-D mass distribution profiles but do so at a cost of longer scanning time and a much higher radiation dose to the living subject. For example, a diagnostic CT scan of the abdomen or pelvis delivers an effective dose of 10 mSv, which is approximately 4.5 times the average yearly whole body radiation dose due to natural background radiation in the United Kingdom (Directorate-General for the Environment of the European Commission, 2000) and twice the recommended annual dose constraint for participants in Australian-based medical research (Australian Radiation Protection and Nuclear Safety Agency, 2002). Indeed, the majority of the CT studies described above were conducted on cadaveric specimens or on patients for whom the CT scans were performed for other medical reasons. The only study clearly identified to have been conducted on healthy volunteers was that of Hui et al. (1999), presumably because most research ethics committees would not accept whole body CT scanning of healthy subjects for the sake of BSP measurement research.

The other form of 3-D medical imaging that has been used for BSP measurement, Magnetic Resonance Imaging (MRI), does not use ionising radiation. Hence, MRI does not pose the subject to the potential health risks associated with the aforementioned radiation techniques. The majority of applications of MRI take advantage of the relatively large magnetic moment, or dipole, of the hydrogen nucleus. An MRI scan requires a subject to be placed in a strong, stable magnetic field produced by the MRI machine. The hydrogen nuclei in the body are aligned relative to the line of action of the magnetic field. Systematic alterations to the magnetic field are made locally to small sub-divisions of the scanned volume, one sub-division at a time, accompanied by the application of radio wave pulses, which momentarily change the alignment of the hydrogen nuclei in the specific region of interest. After the radio frequency pulse ceases, the hydrogen nuclei return to their stable state in the main magnetic field, emitting radio waves in the process. The rate of emission is measured and this allows subsequent determination of the concentration of hydrogen atoms in the region of interest (Dixon and Dugdale, 1988).

Thus, MRI technology does not measure mass distribution directly. Rather, it determines hydrogen atom concentration and distribution throughout the body. The hydrogen found in human tissue is mainly associated with the water content of the tissues and the different water content of the various tissues allows discrimination between them and excellent contrasting imaging of their 3-D distribution within the body (Yochum and Rowe, 1987). Subsequent calculation of mass distribution data and BSPs requires density values for each of the various tissue types to be supplied.

Martin et al. (1989) demonstrated that the mean percent differences between baboon cadaver BSPs determined with MRI and those measured by direct measurement techniques were less than 7%, but up to 10.2% for individual cases. MRI consistently overestimated segment mass and moment of inertia. Mungiole and Martin (1990) were the first researchers to use MRI to measure the BSPs of living humans' legs. They showed acceptable agreement with commonly-used geometric modelling and predictive BSP estimation techniques (predictive techniques are described in section 2.2.1.4). Matsuo et al. (1991) found the BSPs of five females using whole body MRI scans and found the results to be similar to those estimated for the same individuals as measured by water immersion and reaction change[6] methods. Pearsall et al. (1994) used MRI to measure the trunk BSPs of 26 adult males. Their method involved up to 14 scans of 10 mm thick slices along the length of the trunk, 50 mm apart. Based on the repeated measurement of one subject only, they determined that all trunk BSPs could be measured reliably within 2.5%. With more than 14 scan slices per subject, this figure may have been smaller. Cheng et al. (2000) used MRI to measure all the BSPs of eight living Chinese males and claimed some apparent differences from available data for Caucasians. However, they did not use cadaveric specimens to assess the accuracy of their methodology against direct, criterion measurements.

The accuracy and reliability of measuring BSPs by MRI is deemed to be comparable to other methods such as CT (Pearsall et al., 1994), if not better than

---

[6] Reaction change methodology is described in section 2.2.1.5.

other methods (Nigg, 1999). The author is not aware of any attempts in the last 10 years to reassess the capability of MRI in these respects, yet MRI technology has continued to improve through this period. Further, very few MRI-based BSP estimation studies have been conducted during the last decade. The sparsity of its use for BSP estimation may be a function of its cost and availability (Pearsall and Reid, 1994). The other main disadvantage of MRI as a method for routine BSP measurement is the length of time required for a full body scan, which may be more than an hour for high resolution imaging. However, the 3-D nature of MRI and its relative safety for subjects makes it the most promising medical imaging method for BSP estimation. Advancing technology and decreasing costs may eventually lead to more widespread use of MRI for this purpose.

2.2.1.4 Predictive Techniques (Regression Equations)

Regression analyses have been conducted on the BSP data sets produced by many of the aforementioned cadaver and living-subject studies in order to develop various BSP predictive equations. Biomechanics researchers sometimes use these equations to estimate subjects' individual BSPs because the procedures involved are often cheaper, simpler and less time-consuming than the subject-specific measurement techniques already discussed. However, coupled with convenient methodology is the probability of reduced BSP estimate accuracy.

Regression equations have been developed from the cadaver studies of Braune and Fischer (1889; 1892), Fischer (1906), Dempster (1955), Clauser et al. (1969), Liu and Wickstrom (1973), Chandler et al. (1975) and Clarys and Marfell-Jones (1986). Barter (1957) also developed regression equations for segment mass

prediction from the amalgamated cadaver data of Braune and Fischer (1889; 1892) and Dempster (1955), though the validity of combining data from studies with different methodologies is questionable (Reid and Jensen, 1990). Several other researchers (e.g. Ackland et al., 1988a; Drillis et al., 1964; Durkin and Dowling, 2003; Hinrichs, 1985; McConville et al., 1980; Young et al., 1983; Zatsiorsky and Seluyanov, 1985) have also conducted regression analyses on BSP data sets derived from the living-subject studies described in the preceding sections.

Before applying any regression technique, consideration should be given to the proportion of variance accounted for by the technique. For example, until the study of Clauser et al. (1969), cadaver-derived regression equations were restricted to only one predictor variable, namely whole body mass, height or segment length, depending on the BSP being estimated. Clauser et al. (1969) collected 73 anthropometric measurements from each cadaver and developed multiple step-wise linear regression equations for predicting mass and centre of mass BSPs using the three best anthropometric predictor variables for each BSP, thus improving predictive power. Zatsiorsky and Seluyanov (1985) also used multiple step-wise regression analysis, using subject height and weight as the predictive variables. Ackland et al. (1988a) used up to five anthropometric measurements to develop predictive BSP equations for trunk and leg segments. Others who have used additional anthropometric measurements and demonstrated improved predictive power include Pearsall et al. (1994) and Zatsiorsky et al. (1990a).

Consideration must also be given to the size of the sample from which the regression equations are derived. With the possible exception of Zatsiorsky et al. (1990a) and the related works by these authors, who scanned 100 male subjects, most other regression analyses have been derived from relatively small sample sizes of less than 20 subjects. The accuracy of the methods from which the regression equations are derived must also be considered. For instance, when considering cadaver-based derivations, frozen and unfrozen segment measurements produce different challenges for the measurer. Freezing cadaver segments prevents fluid loss, but the fluid turns to ice and reduces the density of segments prior to measurement (Pearsall et al., 1994). The use of regression equations, derived from cadaver studies of small sample size, is not recommended for most applications and individuals (Reid and Jensen, 1990). The different segment boundaries associated with the different methods also need to be considered. Hinrichs (1990) and de Leva (1996a; 1996b) have suggested adjustments to the data provided by Clauser et al. (1969), Zatsiorsky et al. (1990b) and Chandler et al. (1975), respectively, to improve their accuracy.

Another important factor to consider before applying a set of regression equations to a specific individual is the physical similarity of that individual to the sample population from which the regression equations were derived. Confidence is reduced when the characteristics of a subject are known to vary from those of the sample used to derive the regression equations. This consideration has led several researchers to develop regression equations for more specific sub-populations. Hui et al. (1999) have developed equations for the BSPs of male and female Chinese adults. Jensen (1986; 1989), Jensen and Nassa (1988), and Ackland et

al. (1988a) have also addressed the BSPs of children and adolescents. Jensen et al. (1997), Sun (1992) and Schneider and Zernicke (1992) derived regression equations to estimate infants' BSPs. The BSPs of elderly males and females received the attention of Jensen and Fletcher (1993; 1994) and Pavol et al. (2002), and the BSPs of pregnant women have been addressed by Jensen et al. (1996).

Clearly, several issues must be considered when deciding whether to use regression equations for BSP estimation and to determine which set to use. The convenience of regression equations is necessarily reduced whenever such care is exercised. When the researcher requires accurate, subject-specific BSPs, regression equations are unlikely to produce the desired degree of specificity. None of the BSP estimation methods described thus far can provide accurate results for any specific, living individual, whilst also being considered safe, affordable and achievable in a typical biomechanics laboratory.

2.2.1.5 Dynamics and Optimisation Techniques

An individual's BSP estimates are often coupled with measurements of segmental kinematics and external forces acting on the body, in order to solve the system of dynamics equations using the inverse dynamics approach. However, if sufficient segmental kinematics and kinetics information are measured or known, the system of dynamics equations is over-determined (Vaughan et al., 1982b). In such circumstances, rather than provide BSP estimates *to* the equations of motion, it is sometimes possible to calculate subject-specific BSP values *from* the equations of motion. Living subject methods that derive BSP estimates from the equations of

motion and the observed dynamics of the subject are categorised henceforth as *dynamics* techniques. In some circumstances, mathematical *optimisation* techniques can be used to optimise dynamics solutions by searching for the set of subject-specific BSP values that produces the closest agreement between BSP-dependent calculations of dynamics quantities and those quantities experimentally measured or known to exist (Vaughan, 1980). *Dynamics* and *optimisation* BSP estimation techniques require knowledge and/or measurement of system dynamics for the whole body or, in the case of segment-specific techniques, only for the segment of interest. Several researchers have developed dynamics techniques only applicable to limb segments. Most of these methods only allow estimation of the segment's moment of inertia in the sagittal plane about the proximal joint. For these reasons, and because the author's research considers techniques applicable to all body segments simultaneously, only brief descriptions of research employing single segment methods are outlined below in section 2.2.1.5.1. A more detailed review is conducted in section 2.2.1.5.2 of BSP estimation methods that rely on whole body dynamics analyses, due to their direct relevance to the author's research.

2.2.1.5.1 Segment-specific Dynamics Techniques

Fenn et al. (1931) described an early version of a technique called the quick release method, which they applied to the combined shank and foot segment. Since then, Drillis et al. (1964) has described the quick release technique for the combined forearm and hand segment. They stated that the proximal joint must be positioned so that it does not move. The segment is then subjected to a known

constant force at a known distance from the axis of rotation (viz. the moment arm) near its distal end by means of a cord or cable angled perpendicularly to the segment's long axis. This force is countered by voluntary isometric contraction by the subject to keep the segment static. The cord or cable is released quickly and the 'instantaneous' acceleration of the limb is measured by means of two accelerometers affixed to the segment. The 'instantaneous' force exerted by the subject on the segment at release is considered to be equal to the known constant force. Using Newton's second Law for angular kinetics, the moment of inertia is calculated to be the measured constant force times the measured moment arm divided by the measured angular acceleration. Bouisset and Pertuzon (1968) applied a similar quick release technique for the combined forearm and hand segment and Cavanagh and Gregor (1974) for the combined shank and foot segment. Stijnen et al. (1983) applied a similar technique to both upper and lower limb segments.

Hatze (1975) applied a damped oscillation technique to determine the moment of inertia of the leg segment by measuring the period of oscillation, and the decreasing amplitude on several successive oscillations, of the relaxed, splinted leg attached to a spring system. Allum and Young (1976) used a method they called the relaxed oscillation technique, in which forced oscillations were imposed on the relaxed upper limb. Peyton (1986) developed a method for the upper limb incorporating aspects of the methods of Hatze (1975) and Allum and Young (1976). These 'relaxed' methods assume a negligible net joint moment is being applied by the muscles and other tissues about the joint of interest during measurement. The major limitation of all of the above single segment methods is

the inability to apply them to all body segments and about all three axes of rotation (Reid and Jensen, 1990).

Arguably, the compound pendulum method (see section 2.2.1.1) is a dynamics BSP estimation technique because it is also based on observations and an understanding of system oscillatory dynamics. However, this method has been categorised as a cadaver-specific technique in this review because it has mainly been applied to cadavers and it has generally been considered to be inappropriate for use *in vivo* (Allum and Young, 1976; Bouisset and Pertuzon, 1968), due to the inability to ensure complete muscular relaxation about the axis of rotation[7]. Similarly, balance board, suspension and even weighing methods have been categorised as cadaver-specific techniques, even though they also rely on the measurement of system statics, a subset of dynamics, because they are only strictly applicable to sectioned cadaver segments. However, balance boards have been used with living subjects for the reaction change method.

The reaction change method uses a force platform (e.g. Kingma et al., 1995; Pataky et al., 2003) or a balance board (e.g. Bernstein et al., 1936; Contini, 1972) to estimate living subjects' mass or centre of mass BSPs. It involves conducting a kinematic analysis of the limb segments under investigation and measuring the centre of pressure of a subject of known mass in various postures (usually

[7] It should be noted, however, that contrary to the recommendations of earlier researchers, the compound pendulum method was used relatively recently on living subjects by Lebiedowska and Polisiakiewicz (1997), who considered electromyographic activity below 50 μV to be representative of negligible muscular activity.

recumbent postures with changes to the positions of the limb segments). By capturing data for two different static postures for each limb segment, two equations are established that can be solved simultaneously to find the segment mass if the value for the segmental centre of mass is supplied, or *vice versa*. Although Pataky et al. (2003) presented a sound argument for assuming knowledge about segment centres of mass rather than segment masses in order to minimise error, both approaches to the reaction change method introduce unavoidable errors in the calculated BSPs, based on the inherent errors in the *a priori* estimated BSPs. The reaction change method is fundamentally compromised by the fact that determination of some BSPs requires the assumption of *a priori* knowledge of the accurate values of other BSPs. Further, being a statics methodology, the reaction change technique cannot be used to determine moments of inertia.

2.2.1.5.2 Whole Body Dynamics and Optimisation Techniques

Some dynamics techniques for BSP estimation have been augmented by the introduction of mathematical optimisation techniques. The general term *optimisation* refers to a process of maximising or minimising an outcome by varying the magnitudes of the factors that influence the outcome. In mathematical terms, the outcome is the dependent variable, which is expressed as a function of the independent variables or design variables that influence the outcome. The function expressing the dependent variable in terms of the design variables is called the objective function. Conditions are often imposed on the design variables, restricting the set of possible values that they can be assigned to values

known *a priori* to be realistic or *feasible*. These restrictions, in a mathematical sense, are expressed as equality and inequality constraint equations of the relevant design variables. Under such restrictions, the optimisation problem is said to be constrained.

For combined dynamics and optimisation BSP estimation techniques, the BSPs are the design variables and the objective function expresses the difference between the quantities calculated with the over-determined, BSP-dependent equations of motion and the experimentally-measured dynamics quantities. A commonly applied equality constraint requires the sum of all segmental masses to equal the total body mass. Inequality constraints often include range or *bound* constraints that restrict the possible values of the relevant design variable to be within a feasible range of values, such as the centre of mass of a forearm segment being restricted to values within the range of 30% to 70% of the segment's length. Depending on the representation of the BSP design variables in the equations of motion, linear least squares or more complex nonlinear optimisation techniques are used to find the set of BSP values that is considered optimal insofar as it minimises the differences between the measured dynamics data and the calculated, BSP-dependent dynamics solutions.

The first attempt to estimate BSPs using whole body dynamics information and optimisation techniques, though not reported as such, may have been conducted by Hay et al. (1977) as a minor component of a broader study. Their main objective was to present a method for computing the total body angular momentum about the transverse axis through a subject's CM. This required the

2-D segmental kinematic history of a subject during the performance of an airborne activity and estimates of the subject's BSPs. According to Newton's Laws of motion, the angular momentum should be constant during flight if drag is assumed negligible. However, they observed variability in the computed airborne angular momentum values for a subject performing a front somersault, which they attributed to inaccurate estimates of the subject's BSPs. They reported, "Several attempts were made to identify which specific items of segmental data might be responsible for the errors." It was not reported whether these attempts involved employing a systematic mathematical optimisation method or a less exhaustive, trial-and-error approach. Nevertheless, they found that a reduction in upper arm mass and a caudal movement in the position of the trunk centre of mass "markedly improved" the computed angular momentum by decreasing its variability throughout flight. Though it appears unlikely that Hay et al. (1977) used mathematical optimisation to adjust the BSPs, they demonstrated the potential to find subject-specific BSPs that can improve whole body dynamics computations.

Dainis (1980) also used assumed knowledge about airborne motion to demonstrate a method for estimating segment mass and centre of mass BSPs, based on only an SK analysis of an airborne individual and an optimisation technique. Assuming negligible air drag and based on Newtonian principles of constant acceleration motion, he expressed the horizontal (x) and vertical (y) components of the consequent parabolic CM path as the usual linear and quadratic functions of time (t), respectively:

$$CMx(t) = CMx_0 + CMx'_0 \,.\, t \text{, and} \tag{10}$$

$$CMy(t) = CMy_0 + CMy'_0 \,.\, t + \frac{1}{2} \,.\, g \,.\, t^2 \tag{11}$$

where CMx_0, CMy_0, CMx'_0 and CMy'_0 are four initial condition parameters representing the horizontal and vertical CM displacements at take-off and the horizontal and vertical CM take-off velocities, respectively, and *g* represents gravitational acceleration. However, in this study, time (*t*) was measured, so Eqs. (10) and (11) are actually linear with respect to *g* and the four unknown take-off parameters. Dainis (1980) chose to consider *g* to be the fifth unknown parameter, thus enabling him to use the calculated value of *g* to test the validity of his method. He also expressed airborne CM displacement as an algebraic manipulation of the usual SK representation of CM displacement, in which CM trajectory is determined from the weighted average of all the segments' centre of mass positions for each sampled point in time. With all SK data provided, his reformulation of CM displacement as a function of time was linear with respect to the independent variables, which he termed "structure parameters." The *n* structure parameters described nonlinear relationships between the mass and centre of mass BSPs of the *n* segments. Hence, Dainis (1980) possessed two representations of airborne CM displacement as a function of time that were both linear with respect to the independent variables. He asserted that, given provision of correct values for the *n* structure parameters, four take-off parameters and *g*, the two functions should produce equivalent trajectories. On this basis, and with more than $n + 5$ time samples of kinematic data available, Dainis solved these equations by a linear least squares method. Hence, he claimed that the trajectory

of the CM could be determined accurately for an airborne, linked segment system, without knowledge of the individual's mass or centre of mass BSPs.

Dainis (1980) tested the validity of his method with the kinematic data obtained from the airborne motion of a linked, three-segment, inanimate object. The segments were comprised of thin rods of known mass and centre of mass. Rather than substituting the known value of *g* into the equations and reducing the required number of equations by one, Dainis solved the equations for *g* as well, as an extra validity test. The acceleration due to gravity is dependent on the altitude above sea level and the latitude position on the earth's surface, since the earth is not perfectly spherical (Halliday and Resnick, 1978). Dainis (1980) did not state the criterion value for *g* for the location of his study; it could have been -9.81 ± 0.04 ms^{-2}, depending on the latitude and altitude of the location used for filming. When known segment masses were supplied, he reported a calculated value of -9.84 ms^{-2} for *g* and calculated segment centre of mass values within 2% of actual values. These results were described as satisfactory by Vaughan et al. (1982a). However, when Dainis (1980) tested his method on kinematic data of an airborne gymnast with unknown BSPs, results were less convincing.

The first activity that Dainis (1980) analysed was the pre-landing flight phase of a vault in a layout position, for which the three segments defined for this movement (viz. lower extremities; combined trunk and head; and upper extremities) were essentially in alignment throughout. Dainis stated that the BSPs for these segments could not be determined accurately by his method, because they remained parallel to each other, essentially resulting in linear dependence between

the equations used to solve for the structure parameters. However, he claimed the CM flight path could still be determined accurately. He reported the calculated value of *g* was -9.87 ms^{-2} for this activity.

Another analysis was conducted of the gymnast performing a backward somersault in a tucked position, this time using a six-segment model. The model was comprised of feet, shanks, thighs, combined trunk and head, upper arms, and combined forearms and hands. The pre- and post-tuck phases were also analysed, ensuring the existence of circumstances in which the segments did not remain parallel throughout flight, thus avoiding the linear dependence problem experienced with the layout position. Under these circumstances, Dainis claimed that centre of mass BSPs for the larger, more proximal segments (viz. thighs: 64.6% of the distance from the knee to the hip; and trunk/head: 66.6% of the distance from the inferior to the superior end) could be determined "quite accurately". This statement is questionable because the segmental mass BSPs of Dempster (1955), as presented by Plagenhoef (1971), were used to determine the segmental centre of mass BSPs from the structure parameters. These values were unlikely to represent the actual BSPs of the gymnast. The gymnast's anthropometric information and sex were not reported, but it is unlikely that the anthropometric characteristics would have corresponded closely with those of the elderly male cadavers from which Dempster's BSP data were derived. Dainis suggested the poor predictions of centre of mass BSP values for the smaller, distal segments (viz. feet: -133%; shanks: 67.9%; upper arms: -9.8%; head: -71.2%) were due to their small influence on the system's CM location. Indeed, three of

these predictions are clearly non-feasible due to their negative sign. The calculated value for *g* was -9.85 ms^{-2}.

As is the case for the reaction change method, the approach of Dainis (1980) requires an assumption of accurate *a priori* knowledge of segmental centre of mass BSP values if the values of the segmental mass BSPs are to be estimated, or *vice versa*. However, Dainis (1980) presented a novel approach for determining airborne CM trajectory and relationships between the segmental mass and centre of mass BSPs, which he called structure parameters. He also demonstrated that segments should not remain parallel to each other throughout flight, to ensure linear independence between the equations that he used to define the structure parameters.

Jaffrey et al. (1998) also applied an optimisation technique in an attempt to estimate BSPs from the kinematic data of an airborne gymnast. Two objective functions were formulated, based on the assumptions of constant horizontal velocity and constant angular momentum during flight. Jaffrey et al. used a tabulation search method (Box et al., 1969) to estimate the centre of mass BSPs for the thighs, trunk and head segments; all other BSPs were assigned constant values from the literature (Clauser et al., 1969; Whitsett, 1963). The two objective functions produced different solutions and both produced some non-feasible BSP values, particularly for the head centre of mass, which was calculated to lie superior to the vertex of the head. Proposed explanations for these results included errors in kinematic data and the fact that the trunk and head segments essentially remained parallel throughout the flight phase. The latter

explanation is much the same as the linear dependence explanation provided by Dainis (1980) for the non-feasible BSP estimates he reported, however, Jaffrey et al. (1998) suggested that non-feasible results are also likely whenever two segments remain in the same relative orientation, whether or not that orientation is parallel. Another partial explanation for the results obtained by Jaffrey et al. (1998) is that head centre of mass estimates may have compensated artificially for errors in the assumed values of the other BSPs, which were held constant in this study. Errors in the assumed values of other BSPs and/or kinematic data errors might also explain the different results produced by each objective function. Jaffrey et al. (1998) concluded that the formulation of the objective function for dynamics and optimisation techniques is crucial to the efficacy of such BSP estimation methods.

Kingma et al. (1995) adapted the reaction change method and introduced a simple form of optimisation to determine the trunk centre of mass. They conducted a full body kinematic analysis and measured centre of pressure for quasi-static standing postures involving three different trunk angles of approximately 0, 45 and 90 degrees. In the presence of postural sway, it was assumed that the average value of the centre of pressure during each quasi-static position should coincide with the vertical projection of the whole body centre of mass value as calculated by a full body SK analysis. All BSPs bar the trunk centre of mass were assigned values that were assumed to be accurate. Because the resultant system of simultaneous equations was over-determined (i.e. three postures provided three equations with only one unknown BSP), they were able to use a linear least squares approach to determine the optimal trunk centre of mass BSP. The desired BSP value was

considered to be the one which minimised, across all three postures, the difference between the average centre of pressure and the vertical projection of the whole body centre of mass in the sagittal plane as determined by the SK analysis. Kingma et al. (1995) noted that their procedure could be applied to all body segments. However, as with Pataky et al. (2003), and as with the structure parameters of Dainis (1980), the equations are only linear in the unknown BSPs if either the mass or centre of mass of each segment is assumed to be known accurately. Though the methods of Dainis (1980), Kingma et al. (1995) and Pataky et al. (2003) cannot be used to estimate BSPs without this assumption and although they cannot be used to estimate segmental moments of inertia, they can provide information about the relationships between segmental mass and centre of mass BSPs. This information could be used in the form of nonlinear constraint equations to improve the effectiveness of combined dynamics and optimisation BSP estimation techniques that are capable of estimating all types of BSPs. For example, one constraint equation derived from one of the above methods would be $m_{foot}cm_{foot} = c$, where c is a constant.

Chen et al. (2003) also estimated BSPs by minimising the differences between the transverse plane coordinates of the CM (as determined by SK analysis) and the measured centre of pressure, using a set of ten different static postures for their procedure. Their approach was unique insofar as they combined a geometric modelling technique with an optimisation approach to select appropriate segmental density values. Details of the optimisation method and the geometric representations of the segments were not reported. Only the segmental density values were varied during the optimisation process. They assessed the BSPs

produced by their method against BSPs derived from Dempster's (1955) regression equations by applying them to a second set of ten static postures. Chen et al. (2003) used the same centre of pressure versus the transverse plane coordinates of the CM criterion for assessing the BSPs. For the second set of static postures, the optimised BSPs produced transverse plane CM coordinates that more closely matched the empirically measured COP values than the CM coordinates that were produced by the BSPs derived from Dempster's (1955) regression equations. However, the method of Chen et al. (2003) had certain limitations. The segmental centre of mass BSPs were predefined by the geometric model and were independent of the segmental density values, and the segmental moments of inertia did not feature in the objective function. Only the segmental masses influenced the objective function when the density values were varied.

The only study to estimate all the sagittal plane BSPs of a living subject by combined dynamics and optimisation techniques was conducted by Vaughan (1980) (doctoral dissertation) and published by Vaughan et al. (1982a). Open-loop dynamics solutions of airborne activities are over-determined, as are single-support dynamics solutions coupled with ground reaction force measurements (Vaughan et al., 1982b). Under these conditions, the net external force and its effective point of application on any stipulated distal segment of the subject are either known *a priori* not to exist (when that extremity is not in contact with the external environment) or they can be measured with appropriate force transducing devices. These values can also be calculated by an IDA, which requires BSP estimates. However, due to errors including (but not restricted to) BSP estimate errors, a difference, or residual, will exist between the empirically

measured or *a priori* known values and the IDA-derived values. Vaughan et al. (1982a) exploited this fact when they formulated an objective function based on these residuals, in which the BSPs were the design variables.

The non-support and single-support phases of three essentially planar, open-loop activities performed by one individual were filmed and subsequently the segmental kinematic data were digitised. Force platform data were also recorded for the single-support phases of the stipulated distal segment. The activities were running, long jumping and a football kicking action without a ball. A nonlinear optimisation technique was used to search for the set of BSP values that minimised the sum of squared residuals between the time-matched force platform measurements (or the *a priori* known values of zero) and the IDA-derived values of the ground reaction force and the torque acting on the body at the stipulated distal segment.

The problem was subjected to linear equality constraints, including bilateral limb BSP equality, and constraining the sum of all segmental mass BSPs to equal the subject's measured whole body mass. Nonlinear equality constraints were also imposed, based on the Newtonian principles that the net external force and torque acting on the whole body equal, respectively, the rates of change of the linear and angular momentum of the whole body. Hence, the GRF and COP measured by the force platform and the known whole body gravitational force were used to determine the net external force and torque acting on the body, and the kinematic data and BSPs were used to calculate the rates of change of the whole body linear and angular momentum. Thus, two equality constraints were developed for the

two orthogonal sagittal plane components of the linear relationship and one equality constraint was developed for the angular relationship:

$$\left(\sum_{seg=1}^{14} m_{seg} \ddot{x}_{seg} \right) - GRF_x = 0 \tag{12}$$

$$\left(\sum_{seg=1}^{14} m_{seg} \left(\ddot{y}_{seg} - g \right) \right) - GRF_y = 0 \tag{13}$$

$$\left(\sum_{seg=1}^{14} I_{seg} \ddot{\theta}_{seg} \right) + \left(\sum_{seg=1}^{14} \vec{r}_{seg} \times m_{seg} \dddot{\vec{r}}_{seg} \right) - T_z = 0 \tag{14}$$

where $\ddot{x}_{seg}$ and $\ddot{y}_{seg}$ are the second derivatives of the horizontal and vertical linear displacement of the segmental centre of mass, respectively; GRF_x and GRF_y are the horizontal and vertical components of the measured GRF, respectively; $\ddot{\theta}$ is the second derivative of the segmental angular displacement; $\vec{r}_{seg}$ is the position vector of the segmental centre of mass relative to the reference system origin and $\dddot{\vec{r}}_{seg}$ is its second derivative; and T_z is the net external torque acting on the body with respect to the reference system origin (comprised of the torques produced by the whole body weight force acting at the CM, and the GRF acting at the COP, with respect to the reference system origin).

In reality, noiseless data are not achievable, so the zero equalities in constraint Eqs. (12), (13) and (14) would not have been attained exactly. The degree to which they were relaxed was not reported by Vaughan et al. (1982a). It is worth noting that these constraint equations could have been combined to form an

alternative objective function, or combined with the IDA-based objective function to create an even more comprehensive objective function, rather than be used as equality constraints as was done by Vaughan et al. (1982a). Indeed, Eq. (14) could stand alone as an objective function in its own right because it involves all the BSPs. The relative performance of these alternative approaches with respect to the approach of Vaughan et al. (1982a) are not known at present.

Inequality bound constraints were also imposed on the BSPs, restricting their feasible values to between lower and upper bounds of, respectively, 0.6 and 1.4 times the initial BSP values supplied to the objective function. For example, based on an initial value of 35.142 kg for the trunk mass BSP (m_{trunk}), the bound constraint was $21.085 \text{ kg} \leq m_{trunk} \leq 49.199 \text{ kg}$. Initial optimisation attempts produced segmental centre of mass BSPs in the distal half of the forearm, thigh, shank and foot segments. Vaughan et al. (1982a) noted that these segments are "obviously more massive proximally" and subsequently set their upper bound constraints to 50% of segment length from the proximal end.

The data from the three activities were not combined. Rather, three separate optimisations were performed. Like Dainis (1980), Vaughan et al. (1982a) produced non-feasible values for some of the more distal segments' centre of mass BSPs. They reported that the bound constraints for the shank and foot centre of mass BSPs "became active" for the running activity. That is, the values shifted to the upper bound (viz. 50% of segment length). This also occurred for the forearm centre of mass BSP for the kicking activity. Though not reported by Vaughan et al. (1982a), the bound constraints for several other BSPs appear to

have become active, although it is possible that these values fell just within the bounds, but were rounded off when reported, giving the appearance that the bound constraints had become active. These BSPs included the hand moment of inertia values for the running and jumping activities, and the foot moment of inertia value for the kicking activity. Note that these are the BSPs of small, distal segments with low moments of inertia. In the absence of large angular accelerations of these segments during the associated activity, the objective function would be less sensitive to perturbations of these moment of inertia BSPs, compared with perturbations of the BSPs of more massive segments. In the presence of measurement errors and by employing a model that is less than a perfect biomechanical representation of the subject, it is possible that the BSP bound constraints of less massive segments would preferentially become active. Most of the non-feasible BSP estimates reported by Dainis (1980) and Vaughan et al. (1982a) were associated with the less massive, more distal segments. The head centre of mass values reported by Vaughan et al. for the running and jumping optimisations also appear to have been driven to the lower bound of the feasible region defined by the researchers. This result might be expected if the head and trunk segments remained in essentially the same relative angular orientation throughout these activities, similar to the findings already discussed for Dainis (1980) and Jaffrey et al. (1998). Nevertheless, it may be prudent to ensure all segments change relative orientation to all other segments if feasible BSP estimates are to be yielded from any combined dynamics and optimisation method.

The BSPs derived by Vaughan et al. (1982a) for the three different activities were generally in good agreement. For example, respective segmental mass BSPs were all within 12% of each other, with a mean absolute difference of less than 6%. Segmental centre of mass BSPs were generally within 4% of segment length of each other, except those segments for which the bound constraints became active. The largest discrepancy was 20.1% of segment length for the shank, between the jumping and kicking optimisations. The fact that each activity produced unique BSPs suggests that subject-specific BSP estimates produced by dynamics and optimisation methods may also be activity-specific, reflecting the non-rigid nature of human body segments and the ever-changing distribution of soft tissues across the joints during motion (Hatze, 2002b).

Kingma et al. (1995) questioned whether their enhanced reaction change approach yielded an accurate estimate of the trunk centre of mass, or whether it merely produced the best relationship between the average measured centre of pressure values and the corresponding calculated CM positions. Vaughan et al. (1982a) also posed the possibility that their optimisation process only served to minimise an objective function that had "no link with reality." However, their objective function represented at least a reasonable approximation to the dynamics of the system under investigation and therefore, at least a reasonable link with reality. Using as many sources as possible of measured and *a priori* known information about the system dynamics under investigation may also improve the objective function's 'link with reality'. For instance, combining the data from all three activities into one objective function, rather than treating them as separate

optimisation problems, may also have produced exclusively feasible BSP estimates.

Fregly and Reinbolt (2004) recently extended the work of Vaughan et al. (1982a) to a 3-D method and used gait as the motion for dynamical analysis. From experimentally measured kinematic and ground reaction force data for one subject, they produced "a noiseless synthetic gait data set for which all model parameters and inputs were known precisely." This involved assigning unspecified BSP values that were "estimated from the literature" and then smoothing and modifying the segmental kinematics until they were able to "satisfy the dynamics equations exactly." They subsequently applied a nonlinear optimisation technique similar to Vaughan et al. (1982a) to estimate all the BSPs. Their objective was to minimise the residual loads at the pelvis, whereas Vaughan et al. (1982a) aimed to minimise the residual loads at a distal extremity. Fregly and Reinbolt (2004) perturbed all the BSPs randomly by ±50% prior to applying the optimisation technique. Like Vaughan et al. (1982a), they assumed bilateral BSP symmetry, but they did not employ the nonlinear equality constraint Eqs. (14) (see page 80) of Vaughan et al. (1982a). Fregly and Reinbolt (2004) reported that their method was able to reproduce the original BSP values with "essentially zero pelvis residual loads" from the BSP-perturbed noiseless data. This demonstrated that the optimisation algorithm was formulated correctly and that gait data contains "enough information to accurately determine BSPs given perfect experimental measurements."

Because perfect experimental measurements are not possible, Fregly and Reinbolt (2004) also added noise to their data set and reapplied the combined dynamics and optimisation BSP estimation method. They reported that their method produced large errors in BSPs for some segments for the noisy data, though they did not report the estimated or the known BSP values. They did not identify which segmental BSPs were non-feasible. However, with a maximum error of 4.09 kgm^2, at least one segmental moment of inertia must have been non-feasible. Regardless, they suggested the inaccurate results indicated that errors in kinematic inputs may have been the main limiting factor. In particular, errors present in displacement data are amplified when these data are numerically differentiated (Hatze, 2002b), a process that is required to derive velocity and acceleration data. Acceleration data produced by double differentiation is particularly sensitive to errors in the displacement data (Kuo, 1998). Vaughan et al. (1982a) also derived acceleration values from displacement data and this may explain some of the non-feasible BSP estimates they reported.

Fregly and Reinbolt (2004) demonstrated that combined dynamics and optimisation techniques are, at least theoretically, capable of producing accurate BSP estimates. However, accurate measurement and modelling approaches and appropriate objective function formulations appear to be critical to making this technique suitable for real applications. Objective functions that include as much *a priori* known and measured dynamics information as possible may help to overcome the confounding effects of kinematic measurement errors. For example, the method applied by Vaughan et al. (1982a) to a single foot segment could also be applied concurrently to all the other distal segments (Jaffrey et al.,

2002) and all the joints (Kingma et al., 1996b), thus providing many more sources of information upon which to refine the BSP estimates.

The technique of combining dynamics analyses and mathematical optimisation has been applied sparingly to the task of BSP estimation. The BSPs estimated by this approach are, in theory, subject-specific and possibly even activity-specific. However, methodological improvements are required to overcome the non-feasible BSP values reported by previous researchers.

2.2.2 Evaluation of Living-Subject BSP Estimation Methods

Reid and Jensen (1990) stated that no BSP estimation method attracts universal acceptance as the best approach. The author's review of more contemporary literature suggests that this statement remains true. New methods continue to be developed (Durkin et al., 2002) and questioned (Zatsiorsky, 2003). Although accurate mass and centre of mass BSPs are obtainable for dissected cadaver segments by applying direct measurement techniques (see section 2.2.1.1), there is an "inherent difficulty" (Andrews and Mish, 1996) associated with assessing the accuracy of living-subject BSP estimates.

The exceptions to this statement are BSP estimation methods that can be applied to both living subjects and cadavers (or cadaver segments). Accuracy assessment is possible with such methods by applying them to intact or sectioned cadavers, followed by direct measurement of the sectioned cadavers' BSPs using validated cadaver-specific techniques. For example, the BSPs of cadaver segments can be measured with medical imaging techniques and then measured directly for

validation purposes. Brooks and Jacobs (1975) evaluated the gamma mass scanning technique by scanning and direct measurement of the inertial parameters of nine legs of lamb. They obtained mass, centre of mass and moment of inertia values with less than 1%, 2.1% and 4.8% variation from the criterion values, respectively. Ackland et al. (1988b) evaluated CT-measured BSPs for a single cadaver leg with criterion values derived with balance and pendulum techniques. Errors for mass, centre of mass and moment of inertia were within 2.8%, 1.2% and 4.8%, respectively. In the first application of MRI technology to the task of BSP estimation, Martin et al. (1989) scanned eight cadaveric baboon segments and reported errors of up to 10.2% for individual BSP estimates when compared with weighing, reaction board and pendulum measurement techniques. MRI technology has improved substantially since 1989. Durkin et al. (2002) conducted DEXA scans of a plastic cylinder and an embalmed human shank segment. Criterion mass and centre of mass BSPs were calculated by weighing and knife-edge methods. Percentage errors for these BSPs were less than 3.2% for both objects. As with the aforementioned studies, criterion moment of inertia values were measured using a pendulum technique. Percentage errors were 14.3% for the cylinder and 8.19% for the cadaveric shank. Durkin et al. (2002) attributed these larger discrepancies to "uncertainty in the pendulum technique". A second criterion moment of inertia was calculated for the homogenous cylinder using the standard geometric formula relating a cylinder's moment of inertia to its mass, length and radius. The resultant error for the scanned value was 2.63% when compared with the geometric calculation.

In order to evaluate living subject BSP estimation methods that cannot also be applied to cadavers or cadaver segments, researchers have had to resort to less definitive, yet pragmatic alternatives. At least two alternatives are available. The first evaluation approach involves comparing a given method's BSP estimates with those derived from another living-subject estimation method. Such an approach is merely an assessment of inter-method BSP estimate differences, rather than a direct assessment of either method's accuracy or validity. Several researchers have used this approach, though some have made dubious claims regarding the 'accuracy' of their own method in the process. For example, Hatze (1980) claimed his geometric model (see page 48) had an "overall accuracy … better than 3%", though he only compared the centre of mass BSP estimates of his subjects to "comparable cadaver data of Dempster (1955)". Considering that Hatze's subjects consisted of three males and a female aged 12, 23, 26 and 31 years, respectively, making claims regarding the accuracy of his method based on a comparison to the elderly male cadaver data of Dempster (1955) is questionable. Further, Hatze did not assess most of the moment of inertia BSPs obtained using his mathematical model against any criterion values, which make his claims of "overall" accuracy somewhat misleading.

Many researchers have assessed inter-method BSP estimate differences, demonstrating how different methods can sometimes produce quite divergent BSP estimates. Kingma et al. (1996b) compared a simple univariate regression method based on Plagenhoef et al. (1983) with a geometric model based on Yeadon (1990b) and produced significantly different ($p < 0.05$) BSPs for almost all segment parameters. Other researchers have reported significantly different

($p < 0.05$) BSP estimates when comparing different estimation techniques. They include Ganley and Powers (2004a; 2004b) for lower limb BSPs measured with DEXA and estimated by cadaver-based regression methods; Pearsall and Costigan (1999) for lower limb BSP estimates produced by various regression and geometric methods; and Larivière and Gagnon (1999a) for pelvis, abdomen and thorax segment BSP estimates produced by geometric and regression methods. Other researchers have also demonstrated that different BSP estimates can arise when regression and geometric techniques are applied to the same subjects, including Durkin and Dowling (2003), Mungiole and Martin (1990) and Vaughan et al. (1982a). Pearsall et al. (1994) compared MRI- and CT-based measurements of three 10 mm transverse slices of the trunks of two subjects. They found that most of the mean differences between the inertial property measurements derived from the respective scanning techniques were within 2%, with the exception being the moments of inertia, for which the mean difference values were not reported. Challis and Kerwin (1992) and Challis (1996) compared the directly measured cadaveric limb BSP data of Chandler et al. (1975) to BSP estimates derived from several of the aforementioned regression and geometric modelling techniques. The directly measured cadaveric anthropometric data reported by Chandler et al. (1975) were used as input data for the regression and geometric models. Comparisons to the directly measured cadaveric BSPs showed that different BSP estimates resulted for each estimation technique. Although simply reporting significantly different BSP estimates between methods does not identify which method is the most accurate, it clearly indicates that not all currently available methods are accurate.

The alternative approach for evaluating living subject BSP estimation methods that cannot also be applied to cadavers or cadaver segments involves the comparison of BSP-dependent dynamics calculations with the measured or *a priori* known values of the same dynamics quantities. This approach goes beyond the mere comparison of BSP estimates derived from different estimation techniques. It allows an evaluation of how well the different sets of BSP estimates reproduce measured or known dynamics quantities. It may be reasonable to suggest that, compared with an inaccurate set of BSP data, an accurate set will result in a higher correlation between calculated and measured (or known) dynamics quantities. Indeed, this is the underpinning principle upon which combined dynamics and optimisation BSP estimation techniques are based (see section 2.2.1.5). Although only the researchers whose techniques are described in section 2.2.1.5 have employed this data to estimate BSPs, many other researchers have used dynamics comparisons of this nature to evaluate BSPs derived by other means.

The simplest and easiest dynamics comparison is actually a statics comparison, which involves comparing directly measured whole body mass with the calculated sum of all segmental mass estimates. Many researchers have made limited validation assessments of various BSP estimation techniques using this information, including Durkin (1998), Hatze (1980), Jensen (1978), Jensen and Fletcher (1994), Kwon (1996), Miller and Morrison (1975), Pavol et al. (2002) and Yeadon (1990b). However, although all the segment mass estimates may sum to 100% of whole body mass, some individual BSP estimates may be underestimates or overestimates of their true values and these errors may cancel

each other out when they are all summed. Other static or quasi-static comparisons have also been demonstrated. For quasi-static postures, Kingma et al. (1996b) assumed centre of pressure measurements coincided with the vertical projection of the whole body centre of mass (CM). They compared centre of pressure measurements to the CM values derived from an SK analysis using different sets of mass and centre of mass BSP estimates. CM can also be measured empirically using a reaction board and then compared with SK determinations of CM derived from different sets of BSP estimates (de Leva, 1993; McKinon et al., 2004; Schultz et al., 1997).

Several dynamics comparisons have also been applied to evaluate different BSP estimation methods. Schultz et al. (1997) assessed the moment of inertia BSPs predicted by a geometric model by measuring the whole body moment of inertia using a torsional pendulum technique. This measured quantity was then compared with the same quantity derived from the set of predicted moment of inertia BSPs using the parallel axes theorem combined with a full SK analysis. They reported that the predicted whole body principal moments of inertia were consistently 5% to 30% lower than the measured values for their geometric modelling technique.

As mentioned previously, for open-loop activities, the potential exists to compare net external force calculated via a BSP-dependent IDA with the force measured empirically or known *a priori* (Kingma et al., 1996a; Vaughan et al., 1982a). Different sets of BSP estimates will produce different discrepancies, or residuals, between these two quantities. Similarly, net joint force and moment residuals can

be determined by producing two separate IDA solutions that terminate at two different extremities (Kingma et al., 1996a; MacKinnon and Winter, 1993). When both feet are on the ground, the two separate IDA solutions are often referred to as 'bottom-up' and 'top-down' IDA approaches. When one or two force platforms are used to measure ground reaction forces, the bottom-up approach is more commonly employed, which commences at the feet and terminates at the hands. Conversely, the top-down approach commences at the hands and head and terminates at the feet. Kingma et al. (1996b) used both of these approaches to evaluate regression and geometric BSP estimation methods. Larivière and Gagnon (1999a) also used the top-down versus bottom-up approach to calculate the net L5-S1 joint moment residual, based on pelvis, abdomen and thorax BSPs derived from both geometric and univariate regression techniques. In both studies, lifting activities were assessed and the researchers considered the set of BSPs that produced the smaller residuals to be more appropriate. Both groups of researchers presented findings that favoured the geometric methods overall, but Kingma et al. (1996b) found that different lifting activities were capable of producing residuals that favoured different BSP estimation methods. This finding supports the notion that some methods may be somewhat activity-specific.

Comparisons have also been made between different BSP estimation methods based on dynamics quantities calculated for airborne activities. Kwon (1996) calculated 3-D whole body angular momentum for gymnasts during flight for ten sets of BSPs derived from different regression and geometric methods. Assuming aerial angular momentum to be constant, Kwon demonstrated significant

differences between many of the methods by comparing mean flight angular momentum values derived from the various sets of BSP estimates. However, no set of BSPs produced significantly different variability in calculated airborne angular momentum about the mean airborne value. For each of ten subjects performing aerial acrobatics on a trampoline, Sprigings et al. (1987) used a SK analysis and a least squares technique to determine the gravitational acceleration (g) of the CM during flight for three different BSP estimation methods. They illustrated that different BSP-dependent values of g were derived between subjects and between BSP estimation methods, which included the regression equations of Dempster (1955) and Clauser et al. (1969) and the geometric technique of Hatze (1980). More importantly, because the absolute value of g was known *a priori* for this dynamics comparison, Sprigings et al. (1987) were able to assess which method produced the most accurate values of g. They asserted that the method of Hatze (1980) was superior to the others for the data utilised in this study. However, a *post-hoc* t-test comparison of the absolute differences between calculated g values and the known value of -9.81 ms^{-1} reveals that neither the method of Hatze (1980) nor Dempster (1955) provided a significantly more accurate determination of g ($p = 0.36$).

From the limited number of dynamics comparison studies conducted thus far, no BSP estimation technique has consistently outperformed all others for all individuals and movement activities. Significantly different sets of BSP estimates and significantly different BSP-dependent dynamics quantities reported in the literature demonstrate that not all the available methods can be valid for all applications. Kingma et al. (1996b) demonstrated that different dynamics

comparisons and different movement activities can produce different rankings of assessed BSP estimation methods.

Methods aimed at subject-specificity are recommended in preference to those that simply apply proportionate information based on regression equations developed from small sample sizes. Volumetric and medical imaging approaches require cumbersome or expensive measurement apparatus and involve time-consuming methodologies. Geometric modelling techniques are relatively inexpensive to apply and they require more basic measurement equipment and techniques than volumetric approaches. Combined dynamics and optimisation techniques usually require only standard biomechanics laboratory equipment (viz. force platform and motion capture system) and certainly aim to produce subject-specific BSPs.

Cappozzo and Berme (1990) summarised the findings of several BSP estimation methods commonly applied in biomechanics studies (viz. Chandler et al., 1975; Clauser et al., 1969; McConville et al., 1980; Zatsiorsky and Seluyanov, 1985). They reported errors in BSPs derived from different methods that typically spanned a range of 5 to 20%. The influence of typical BSP errors on dynamics calculations must also be considered when selecting an appropriate method for biomechanics research applications.

2.2.3 The Influence of BSP Estimate Errors on Dynamics Analyses

Although BSP estimation dates back over 140 years, only in recent times have assessments been made of the influence that BSP estimate errors can have on various BSP-dependent dynamics calculations such as whole body angular momentum and net joint forces and moments. To the author's knowledge, Cappozzo (1983) was the first researcher to attempt a sensitivity analysis to assess hypothesised BSP errors when he assessed the effects of these errors on the net joint force and moment at the fourth lumbar vertebra as a small component of that study. Likewise, Cappozzo and Berme (1990) subsequently advocated conducting *a priori* sensitivity analyses to evaluate the degree to which anticipated BSP estimate errors will alter the outcomes of planned dynamics analyses. Likewise, Ackland et al. (1988b) also highlighted the desirability of quantifying the effect of BSP estimate errors on dynamics quantities derived from kinematic data.

Several researchers have performed such sensitivity analyses in recent years, for various dynamics applications. Some have claimed that BSP errors had only a small effect on IDA-calculated net joint moments at the ankle during dynamic jumping activities (Arampatzis et al., 1997) and the net joint forces and moments at the hip, knee and ankle joints during walking (Challis, 1996; Davis, 1992; Pearsall and Costigan, 1999). Krabbe et al. (1997) even suggested that the contribution of segmental inertial components to IDA calculations of net ankle joint forces and moments during the stance phase of running at 5 ms^{-1} were so

insignificant that they could be ignored. Challis (1996) reported that segmental moment of inertia errors of up to 8% only had small effects on net joint moments on the specific activities of walking, vertical jumping and rapid elbow extensions[8]. For walking and vertical jumping, he reported %RMS differences between the resultant joint moments calculated with perturbed and non-perturbed BSPs of less than 2%. For the rapid elbow extensions, 5% perturbations to forearm moments of inertia produced 4.1% RMS differences. He did not assess the error propagation caused by errors in segmental mass and centre of mass BSPs; however, these types of BSP errors may have a greater effect on net joint forces and moments for activities involving greater segmental accelerations and, in some cases, lower external loads, such as the swing phase of gait or kicking motions (Ganley and Powers, 2004b). Challis (1996) pointed out that segmental moment of inertia errors might have a greater effect on other biomechanical analysis approaches than they did on his IDA calculations. This was the case for the ten BSP estimation techniques assessed by Kwon (1996). CM calculated by a SK analysis varied between the methods assessed by Kwon by up to 3.5% of body height and mean airborne angular momentum varied by up to 10.4% between methods. For simulated sitting and standing activities, Lenzi et al. (2003) found that combined errors of up to 10% in shank-foot, thigh and head-arms-trunk BSPs produced RMS errors in CM displacement of up to 20% of the total CM displacement range exhibited during such activities.

[8] Peak angular velocity for the forearm was reported to be 22.5 radians per second.

Arampatzis et al. (1997) claimed that using BSPs derived by either the method of Zatsiorsky or Hanavan[9] did not make "any great difference" to calculated net joint moments at the hip, knee and ankle joints during dynamic jumping activities. Considering net joint moment differences ranged between ±8%, ±5% and ±3%, respectively, their claim is questionable, particularly for the hip results. Likewise, the claim of Ganley and Powers (2004a) is questionable. They stated, "based on gait analysis of three children, it is likely that the differences between DXA-derived and cadaver-based estimates would have a negligible effect on the calculation of net joint moments during gait in 7-13 year-old children." However, conservative interpretation of their reported results indicates that the maximum difference in net hip joint moment calculations for the 7 year-old subject was at least 12%. Chiu and Salem (2005) calculated the BSPs of an elite male weight-lifter using a DEXA scanner and by using the regression equations of Dempster (1955). During a snatch pull exercise, they found the two sets of BSPs produced differences in calculated net knee and hip joint moments of up to 5% and 10%, respectively. The maximal differences were observed during the second pull phase, the phase during which the shank and thigh accelerations are at their greatest. Andrews and Mish (1996) demonstrated that, for a simulated rigid shank-foot segment oscillating through 45 degrees with a period of one second, a 5% perturbation of the segment's three BSPs elicited up to a 12% error in net knee joint moment calculations.

[9] The specific references for Zatsiorsky and Hanavan were not cited by Arampatzis et al. (1997), but were likely to have been Zatsiorsky and Seluyanov (1985) and Hanavan (1964).

Many of the aforementioned researchers have asserted or implied that small differences in calculated dynamics quantities caused by anticipated BSP errors are of no practical significance. Conversely, in their review paper, Pearsall and Reid (1994) argued that as biomechanical models become more complex, the need for accurate, individual-specific BSPs becomes more critical in order to prevent errors in calculated dynamics quantities "arising from BSP lacking the sensitivity equivalent to the model's goal." Nigg (1999) stated that BSP accuracy is less important for within-subjects study designs. However, following this argument, small differences in calculated dynamics quantities caused by anticipated BSP errors are clearly more important for between-subjects designs, which are more common than within-subject designs in biomechanics research.

Regardless of experimental design, the sensitivity of various dynamics quantities to BSP errors depends upon the movement activity under investigation (Challis and Kerwin, 1996; Challis, 1999; Kingma et al., 1996b). For example, BSP errors would have a relatively more significant effect on net joint force and moment calculations for certain open-loop movements. These movements would include activities during which limb segments undergo relatively large accelerations, such as running (Pearsall and Costigan, 1999) and activities with low external loads (Challis and Kerwin, 1996) such as throwing (Pearsall and Costigan, 1999), kicking (Ganley and Powers, 2004b) and the swing phase of gait (Chester and Jensen, 1998; Ganley and Powers, 2004b). Furthermore, the benefit of using accurate trunk BSP estimates has been demonstrated to reduce differences between bottom-up and top-down IDA calculations of net L5-S1 joint moments about the transverse axis for lifting tasks (Desjardins et al., 1998; Larivière and

Gagnon, 1999a; Larivière and Gagnon, 1999b; Plamondon et al., 1996). The top-down approach was demonstrated to be more sensitive to perturbations in trunk BSPs.

BSP-dependent dynamics calculations have been used frequently to compare different BSP estimation techniques and to assess the effects of BSP estimate errors on many practical applications. BSP-dependent dynamics quantities appear to provide the most objective, defendable and widely accepted means of evaluating living-subject BSP estimation methods. Hence, combined dynamics and optimisation BSP estimation techniques warrant further investigation, because such techniques are based on the same underpinning principles. The results of aforementioned sensitivity analyses also help to identify movement patterns, dynamics quantities and objective function formulations that might be effective for estimating various BSPs.

2.3 Summary

In section 2.1 of this review, some promising IA methods for determining CM trajectory for quiet stance and more dynamic activities that require only force platform data were identified. These methods need to be improved by eradicating sources of drift error. Accounting for force platform measurement errors and accurately estimating initial CM conditions are crucial to this process. In section 2.2, it was argued that various dynamics calculations require accurate BSP estimates, and that no existing subject-specific BSP estimation or measurement technique has been demonstrated to be accurate and reliable for all applications.

Combined dynamics and optimisation methods for subject-specific BSP estimation and improved dynamics solutions warrant further investigation, recognising that BSP-dependent dynamics quantities provide the most objective means of evaluating living-subject BSP estimation methods. Potential methodological improvements to IA methods of CM trajectory determination and to combined dynamics and optimisation methods of subject-specific BSP estimation are developed and assessed in the following chapters.

3. RESEARCH AIMS

This chapter outlines the rationale for the research described hereafter. The overall objective and broad aims of this work are declared, as are the general approaches employed to achieve them.

3.1 Rationale for the Research

Both the IA and SK approach can be used to determine CM kinematics. The IA is relatively inexpensive and time-efficient. However, it has been demonstrated that force platform measurement errors and inaccurate estimates of the initial CM conditions currently prevent the IA from being appropriate for many movement studies. SK approaches, and other dynamics calculations, require accurate kinematics data and BSP estimates. BSP estimates are often of dubious accuracy for the specific subject and movement activity under investigation. A safe, accurate and inexpensive method for subject-specific BSP estimation that can be applied routinely in biomechanics laboratories has not been demonstrated in the literature. Optimisation techniques may provide means of overcoming some of the limitations of both IA and SK approaches.

3.2 Aims

The overall objective of this research is to explore different ways to improve the representation of sagittal plane whole body human dynamics using nonlinear optimisation techniques. Fig. 4 outlines the two broad aims of the research and

provides basic descriptions of the approaches to be employed to address the aims. The broad aims are:

- to assess various IA optimisation approaches for determining CM kinematics from force platform data (primarily addressed by Approach 1 in Fig. 4)
- to assess various combined dynamics and optimisation techniques in an attempt to improve dynamics solutions by estimating subject-specific BSPs (primarily addressed by Approach 2 in Fig. 4).

Each optimisation approach investigated in this research is defined by a unique objective function relating various dynamics calculations, empirical measurements, and/or different *a priori* knowledge or assumptions about the system dynamics.

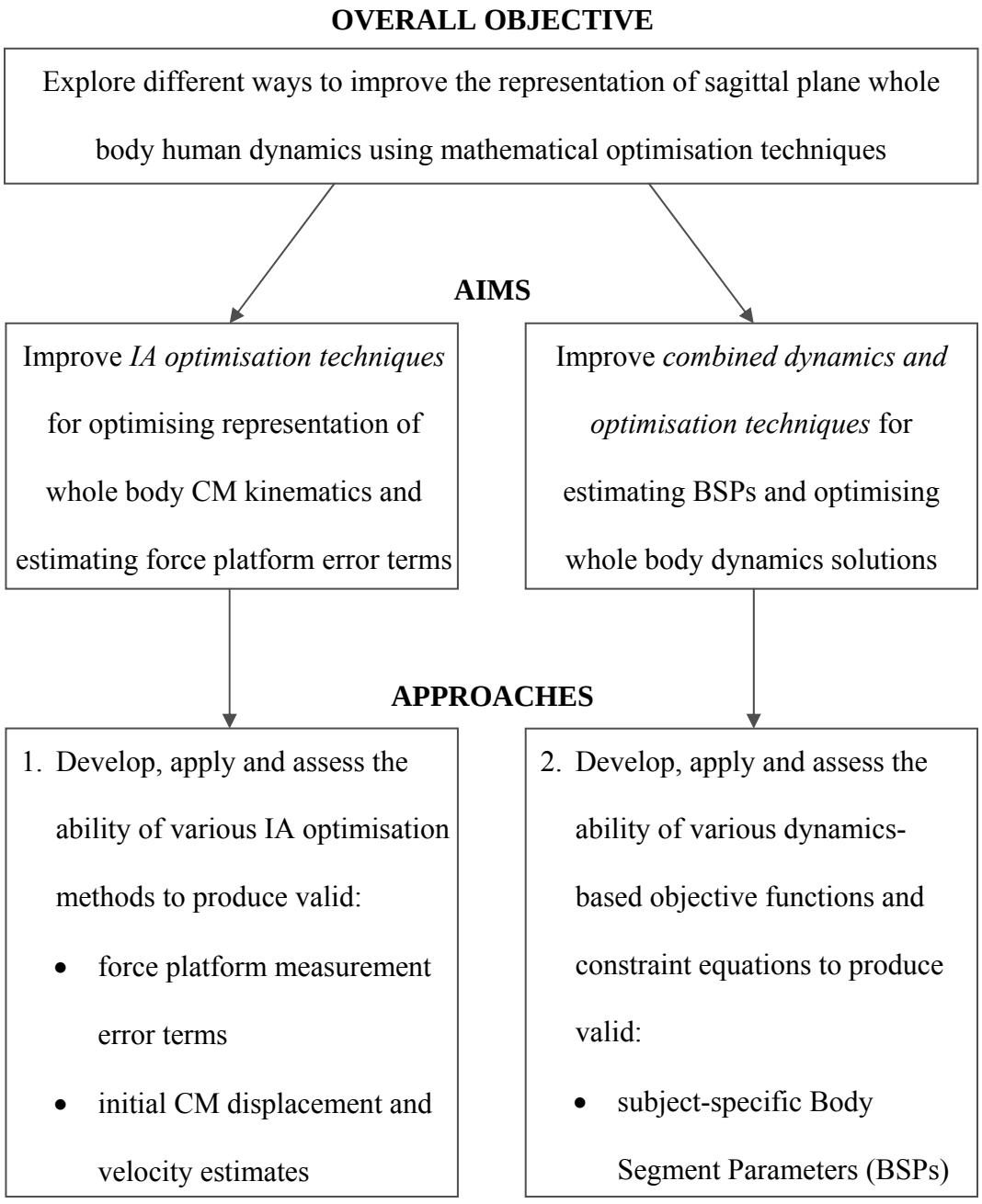

Figure 4. Flow diagram outlining the overall objective and aims of the research, and broad descriptions of the approaches adopted to address these aims.

4. GENERAL METHODOLOGY

This chapter outlines the generic methodology that was used to collect and derive the data that was common to more than one of the experiments conducted during this research. Subsequent chapters cover specific experiments, including the data acquisition and analysis methodologies that were exclusive to each experiment, the specific research hypotheses and the way they were tested.

4.1 Ethical Approval and Subject Recruitment

Approval for this study was sought and obtained from the Human Research Ethics Committee, Victoria University. The study was designed to explore the application of many methodological approaches on a number of different movement patterns. Considering the exploratory nature of this research, it was deemed that recruitment of a single subject was justified. The subject recruited for the study provided written informed consent.

4.2 Subject Preparation

The subject was unshod and dressed only in swimming briefs and a baseball cap for all the data capture activities. This enabled all the kinematic markers to be placed on the necessary body landmarks. Wearing a cap tightly on the head flattened the subject's hair and allowed the placement of the vertex marker close to the scalp and minimised marker movement.

4.2.1 Marker Placement

Light-emitting diode (LED) markers were placed on selected body landmarks as outlined below. Fourteen LEDs were visible on each side of the body (Fig. 5). With the exception of the 'Elbow' markers, all markers were affixed to the subject whilst the subject was standing in the anatomical position. Head markers were placed at the vertex ('Vertex' marker) and the tragus of the ear ('Tragus' marker). Trunk markers were placed on suprasternale ('Suprasternale' marker), the xiphoid process of the sternum ('Xiphoid' marker), between the spinous processes of the seventh cervical and first thoracic vertebrae ('C7-T1' marker), and at the superior edge of the sacrum ('Sacrum' marker).

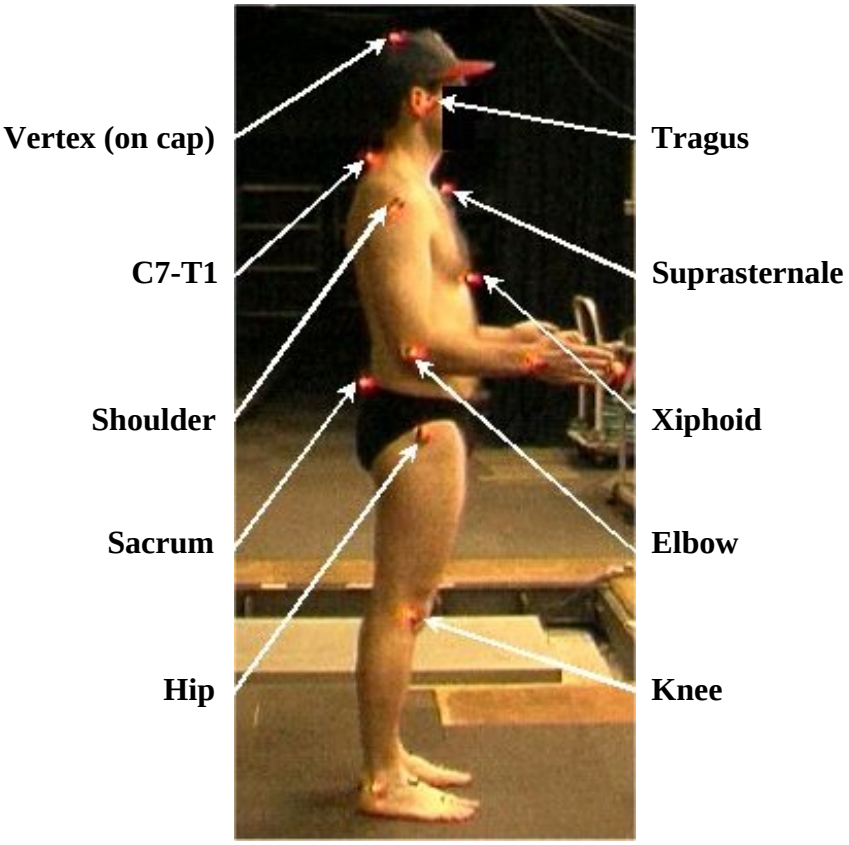

Figure 5. The locations of the LED markers on the subject. Note, the foot and hand markers are illustrated more clearly and labelled in Figs. 6 and 7, respectively.

Shoulder (glenohumeral), elbow, hip and knee joint centres were estimated using palpation and the X-ray drawings of Plagenhoef (1971). 'Shoulder' markers were placed on the lateral aspect of each shoulder at the estimated position of the glenohumeral joint centre. With the arms flexed 90 degrees, 'Elbow' markers were placed over the lateral epicondyle of each humerus at the estimated position of the elbow joint centre. 'Hip' markers were placed on the lateral aspect of each thigh at the estimated position of the hip joint centre. 'Knee' markers were placed on the lateral aspect of the lateral condyle of each femur at the estimated position of the knee joint centre.

Fig. 6 shows the placement of the 'Ankle' and 'Ball' markers on the feet in more detail. Ankle markers were placed on the most lateral point of each lateral malleolus. Ball markers, representing the 'balls' of the feet, were positioned on the dorsum of each foot in the fossa just lateral to the extensor hallucis longus tendon at the level of the first metatarso-phalangeal joint. During pilot testing, it was observed that placing this marker directly above the first metatarso-phalangeal joint, over the extensor hallucis longus tendon, caused unacceptable skin movement artefact. Ball markers were positioned 4 mm above the skin surface and 25 mm above the estimated positions of the first metatarso-phalangeal joint centres. Fig. 7 shows more detail of the placement of the 'Wrist' and 'Tip' markers on the hands. The 'Wrist' markers were placed on the dorsal aspect of each wrist just distally to the radius, over the extensor indicis tendon. Markers were also placed at the distal tip of the middle digits ('Tip' markers).

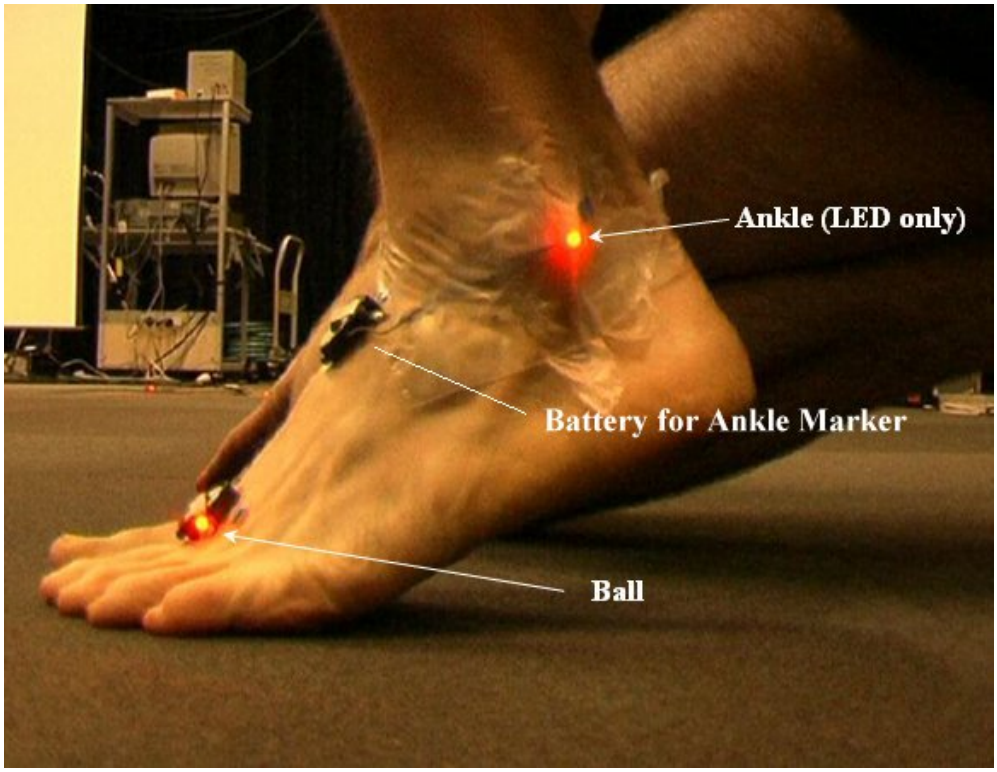

Figure 6. The locations of the LED markers positioned on the lateral malleolus and dorsum of the foot.

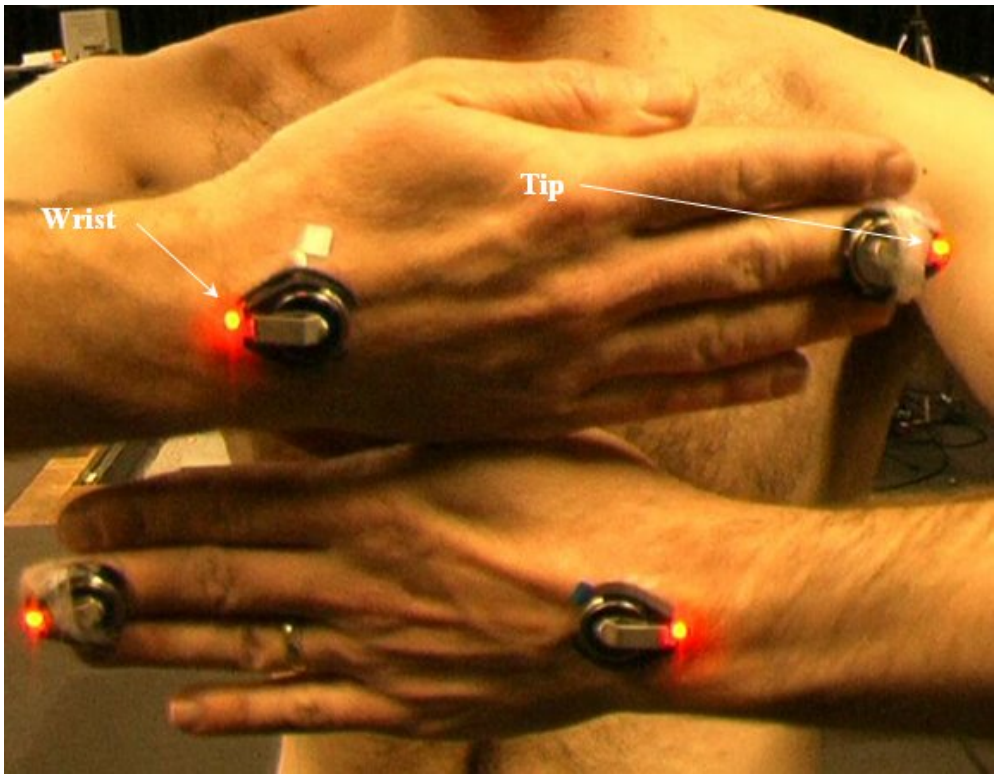

Figure 7. The locations of the LED markers positioned on the dorsum of the hand over the wrist and tip of the middle digit.

4.2.2 Marker Designs

Fig. 8 shows the four basic design variants of the visible LED markers that were developed for this study. The diffused lens LEDs were deep red with a specified brightness of 160 mcd at 20 mA (Agilent Technologies, Palo Alto, CA., U.S.A.). Diode dimensions were 2.2 mm by 2.2 mm, with a height of only 2.9 mm to minimise parallax error introduced by any slightly out-of-plane motion.

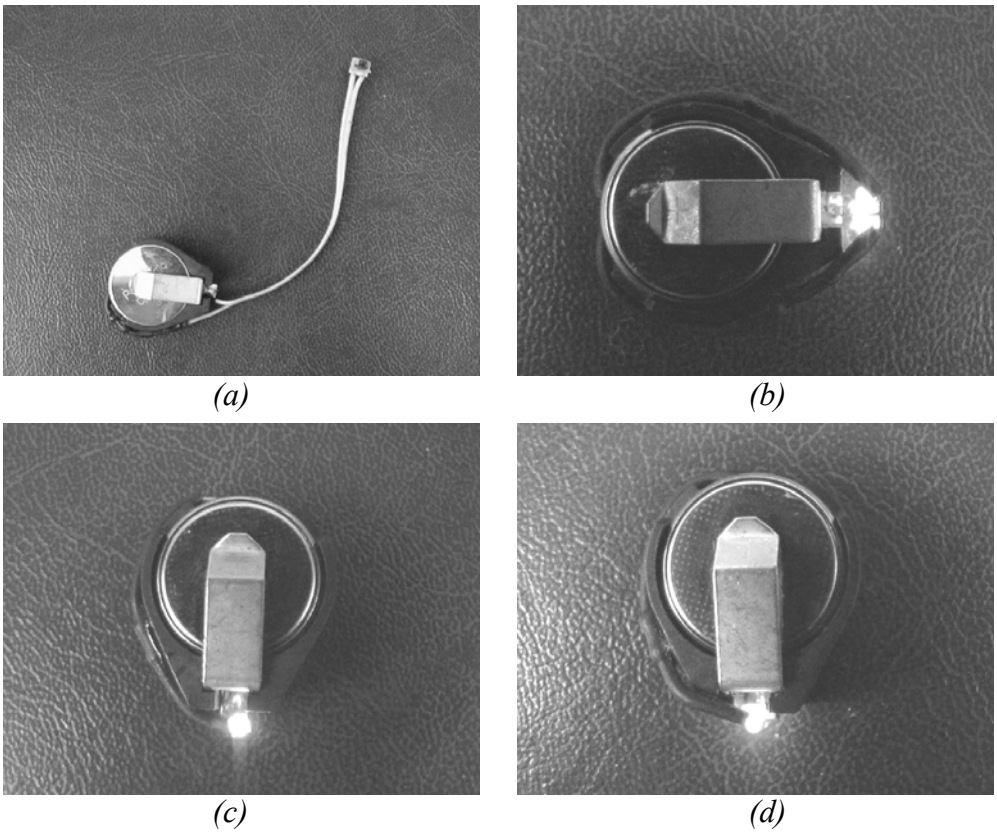

(a) *(b)*

(c) *(d)*

Figure 8. The various LED marker types used in this research. All markers were placed on the subject so that the LED light beams were projected laterally with respect to the subject: (a) the marker designed for the Ankle; (b) the double-LED marker, designed for the Vertex and all trunk markers, pictured here with LED beams projecting towards the top and bottom of the page; (c) the most common marker, designed for lateral placement on the body over a joint centre, pictured here with the LED beam projecting out of the page; and (d) the Ball marker designed for placement on the dorsum of the foot, pictured here with the LED beam projecting towards the bottom of the page.

For all but the Ankle markers, the LEDs were mounted on the side of battery holders, each containing a Panasonic CR2032 3 V battery (Panasonic Matsushita Electric Corporation of America, Secaucus, NJ, U.S.A.). For the Ankle markers, the LEDs were connected to the battery holder by a 40 mm lead (see Fig. 8a), allowing just the LED to be taped directly onto the peak of the lateral malleolus (see Fig. 6). During pilot testing, this design was observed to minimise skin movement artefact for the Ankle markers. The marker type used for the Vertex and all the trunk markers was designed to be positioned on the median sagittal plane of the body and be visible from both sides of the subject. These markers consisted of a pair of LEDs aligned back-to-back in order to project light beams in opposite directions (see Fig. 8b). The vertex marker was attached to a baseball cap, which was made tight on the subject's head, thus flattening the subject's hair and ensuring minimal marker movement during trials. The Vertex LED was positioned 7 mm above the scalp. For joint markers designed to be placed over a joint centre, aligned with the joint's estimated transverse axis and visible only from one side of the body (viz. Tragus, Shoulder, Elbow, Wrist, Tip, Hip and Knee markers), the marker type pictured in Fig. 8c was used. The Ball markers were designed as pictured in Fig. 8d.

Each Knee and Elbow marker was mounted on an anatomically customised closed-cell foam wedge. This was observed to minimise marker movement away from the estimated joint axis of rotation throughout the range of joint motion during pilot testing. Trunk markers were mounted on layers of closed-cell foam to ensure the LEDs were not obscured from the cameras by the pectoral or paraspinal musculature. The Suprasternale, Xiphoid, C7-T1 and Sacrum marker

LEDs were positioned 19, 21, 11 and 17 mm, respectively, above the skin surface. The closed-cell mountings also provided an objective means of assessing out-of-sagittal-plane trunk motion. That is, if a trunk marker was not visible at any time during a trial for reasons other than being obscured by the upper arm, it was deemed that trunk motion was sufficiently out of the sagittal plane at that moment to warrant rejection of that part of the trial. This was, of course, unless the trunk marker was being obscured temporarily by the transit of the upper arm. Each customised marker weighed less than ten grams and was adhered to the body using double-sided adhesive tabs.

4.3 Data Capture

4.3.1 Subject Data

The subject was a 36 year old male of standing height 1.66 m and mass (m_{WB}) of 62.715 kg, which included the swimming briefs, cap and markers. Height was measured with a stadiometer and mass was measured to the nearest 0.005 kg with the subject seated on calibrated precision scales. Relevant anthropometric measurements were also made to enable the application of the BSP regression equations of Clauser et al. (1969) and McConville et al. (1980).

4.3.2 Marker Motion Capture

Sagittal-planar motion was captured with two Panasonic W-V-CL350 50 Hz CCTV cameras (Panasonic Matsushita Electric Corporation of America, Seraucus, NJ, U.S.A.), positioned perpendicularly to the subject's sagittal plane. The two cameras faced each other, one on either side of the subject and both aligned along

the same optical axis. The cameras were set up as far away from the subject as possible, within the confines of the laboratory, and then zoomed in to maximise subject image resolution. Due to the position of the force platform in the laboratory, the respective cameras were 13.5 m and 19.5 m away from the force platform at an elevation of 1.06 m above floor level. Cameras were also rolled 90° in order to optimise the field of view, and maximise the resolution of the image, for the standing activities performed by the subject.

Although all trial activities were essentially confined to the subject's sagittal plane and the motion analysis was planned to be only two-dimensional, motion capture in 3-D would have been preferable. Two gen-lockable cameras is the absolute minimum number required for 3-D reconstruction of a single marker, however, more cameras are required to achieve 3-D reconstruction for all markers in a full body motion analysis (Chiari et al., 2005). The decision to conduct a 2-D data capture process was based on the capabilities and limitations of the available resources. Although automatic digitising software was used (Peak Motus Version 4.3.3; Peak Performance Technologies, Inc., Englewood, Colorado, U.S.A.), this early version of the software requires a great deal of operator intervention to accurately recognise and digitise markers from video recordings. Four to six cameras would have been necessary to do this satisfactorily for the current study. Even if enough cameras had been available, the possibility of using more than two cameras was ruled out by the labour-intensive intervention process required to ensure the success of the automatic digitising software for the large number of long-duration trials used in this study. The use of two cameras bilaterally was

deemed the best approach, given the available resources and considering that all trial activities were designed to be confined to the subject's sagittal plane.

Camera shutter speeds were set to 0.001 s. Lighting was kept dim and the iris of each camera adjusted to produce the brightest and yet sharpest (not overexposed) LED marker images possible, on a uniformly dark background. This was to enable successful automatic digitising to be conducted during marker data processing. The bilateral cameras were gen-locked. A thumb switch was connected to an Event Synchronisation Unit (Peak Performance Technologies, Inc., Englewood, CO., U.S.A.), which enabled the generation of a TTL signal by the Event Synchronisation Unit (ESU). The composite video output signal from each camera was also connected to the ESU, where a visual identifier was added to each video signal every time the TTL signal was generated, thus enabling bilateral video data to be synchronised later by visual inspection. The video signals were then passed through synchronised European Broadcasting Union time code generators. Finally, the video signals were fed into Panasonic digital video cameras (Panasonic Matsushita Electric Corporation of America, Seraucus, NJ, U.S.A.) where the signals were converted from composite video to digital video and recorded onto digital videotapes.

A calibration rod, with two LED markers of the type shown in Fig. 8c placed 2.032 m apart, was video-recorded to allow subsequent data scaling. It was positioned vertically in the middle of each camera's field of view, in the middle of the force platform Two double-sided LED markers (see Fig. 8b) were also fixed to the force platform, one on each side of the platform on its longitudinal midline.

Each of these LEDs was positioned at the same height as the surface of the force platform and 8 mm beyond the ends of the platform. These LEDs acted as the reference points for marker data processing (see section 4.4.2).

4.3.3 Kinetic Data Capture

3-D ground reaction force and moment data were measured by an AMTI LG6-4-1 force platform, of length 1.219 m, and amplified with an AMTI SGA6-4 amplifier (Advanced Mechanical Technology, Inc., Newton, MA., U.S.A.). The surface of the force platform was bare and surrounding sections of the laboratory false floor were removed to ensure the subject made no inadvertent contact beyond the force platform (see Fig. 5, background). While the force platform was unloaded prior to each trial, signals were zeroed. Signals were sampled at 1000 Hz with an AMLAB II 16-bit analogue-to-digital converter data acquisition system (AMLAB Technologies, Lewisham, N.S.W., Australia). Software and computer processor and storage limitations prevented the use of a higher sampling rate. The gain was set to 4000 and the excitation was 10 V for all activities (except the jumps, for which the gain was 2000), in order to maximise the data resolution without clipping any peak force values. The calibration matrix provided by the force platform manufacturer was used to convert the voltage signal into newtons. A real-time analogue anti-alias low-pass filter with a cut-off frequency of 500 Hz was applied to the six signals prior to digital conversion and subsequent saving of the data on a personal computer hard drive.

The thumb switch TTL signal from the ESU was connected to the AMLAB system and was used to control the recording of kinetic data. A 50 Hz vertical

synchronisation signal from the ESU identified the instant when the gen-locked cameras were sampling video data. Recorded with the force platform data, the video synchronisation signal allowed subsequent manual alignment of the kinematic data to within 0.001 s of the kinetic data.

4.3.4 Movement Activities Performed

Each type of movement activity performed by the subject was designed to provide appropriate data for analysing one or more of the optimisation objective functions investigated in this research. More detailed descriptions of the specific movement activities adopted for this research follow in ensuing chapters, accompanying the descriptions of the optimisation problems for which they were designed.

Common to all movement patterns was the way they were contrived to minimise segment movement out of the sagittal plane with respect to the segment's longitudinal axis and to minimise segmental rotation about that axis. With respect to the latter, the aim was to restrict each segment's orientation about its longitudinal axis to that depicted in Fig. 5, thereby fulfilling the assumptions of the model adopted for this research (see section 4.4.1). The trunk was kept as straight and rigid as possible in all movement activities to reflect the trunk rigidity assumption of the model. The subject was instructed to restrict forward flexion of the humerus to less than 60 degrees from the anatomical position to avoid excessive scapular and clavicular elevation and misalignment of the shoulder marker with respect to the glenohumeral joint. The forearms and hands were maintained in a straight, rigid formation at the wrist and phalangeal joints as shown in Fig. 5.

4.4 Data Processing

4.4.1 Whole Body Model

A two-dimensional, sagittal plane, linked segment model was adopted for this research. The defined segments were assumed to be rigid and linked by frictionless hinge joints. All hinge joint axes were assumed to remain parallel to the body's transverse axis. The orientation of each segment about its longitudinal axis was assumed to remain the same as shown in Fig. 5, namely, the orientation observed for each segment about its longitudinal axis when the body is in the anatomical position, with the exception of the forearms and hands. The forearms were assumed to be in a neutral orientation, pronated 90 degrees with respect to the anatomical position. As a result, the hands were assumed to lie in the sagittal plane with the palms facing medially. The 15-segment model developed for this research is depicted in Fig. 9, with the segment and joint names labelled.

4.4.1.1 Virtual Marker Definitions

Most of the model's joint centres and segment end-points were represented directly by 'actual' markers (i.e. LED markers) that were only visible unilaterally. However, a few of the joint centre and segment end-point definitions required the calculation of 'virtual' markers, based on stipulated spatial relationships with actual markers. Virtual markers were subscripted A, B or C, reflecting one of the three methods used to define them.

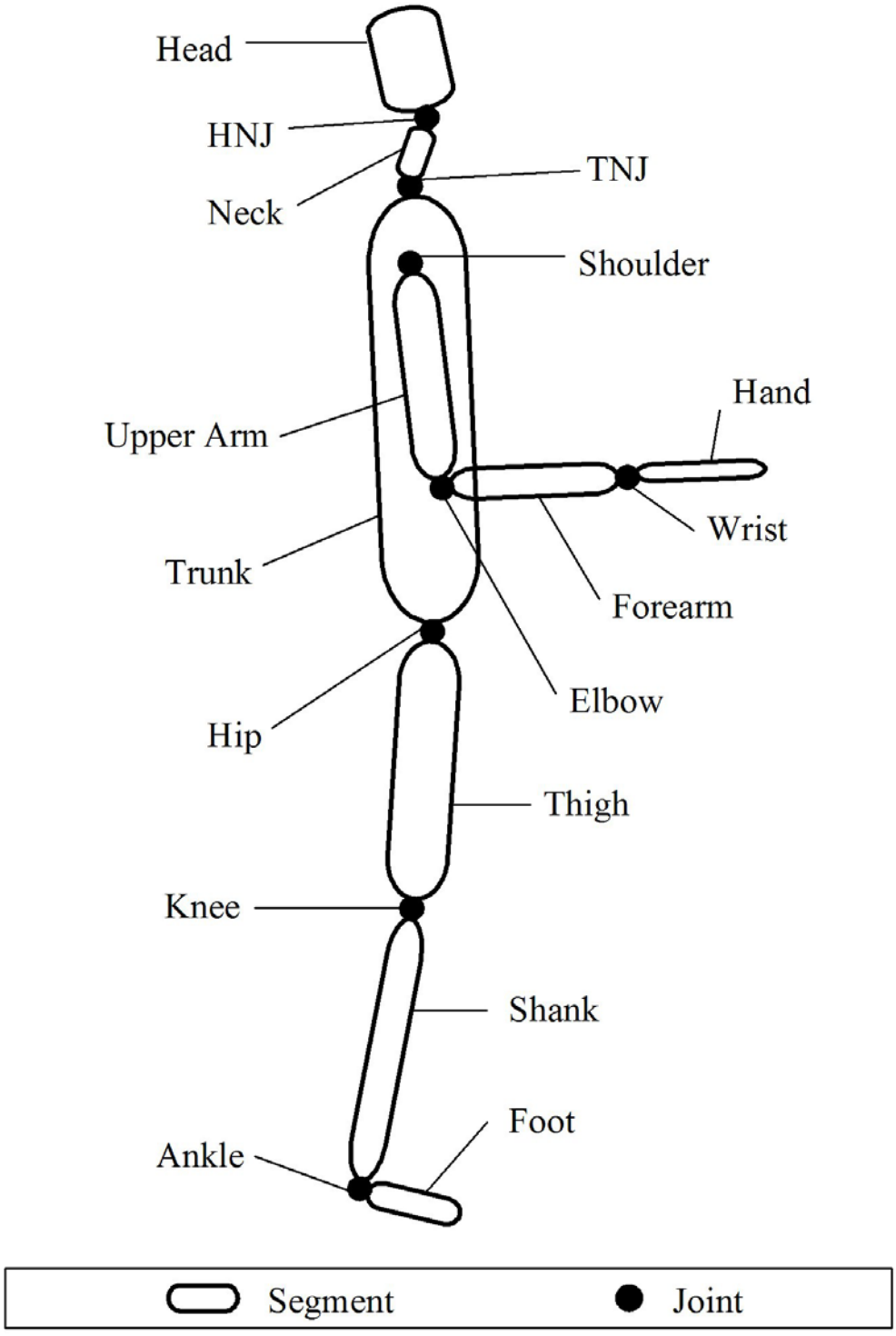

Figure 9. The 2-D, 15-segment model developed for this research. All segments and joints are labelled, with the exception of the left limbs and the Lower Arm segment. The Lower Arm segment is defined in section 4.4.1.2.

Method A involved calculating the mid-point between a contralateral pair of markers for a particular marker label. For example, the Mid-Vertex$_A$ marker was defined as the mid-point between the left and right Vertex markers. Similarly, mid-point between the left and right Tragus markers defined the Mid-Tragus$_A$ virtual marker. Mid-points were calculated for every sampled time throughout a movement trial, based on the filtered position-time histories of the relevant pair of contralateral markers.

Method B was used to determine the inferior trunk end-point (ITE$_B$) virtual marker, which represented the proximal (inferior) Trunk segment end-point. In many previous studies using 2-D whole body analyses (e.g. Vaughan et al., 1982a), Trunk segment inferior and superior end-points have conventionally been determined using the average of the left and right Hip markers and the average of the left and right Shoulder markers, respectively. Method B was hypothesised to be more appropriate for determining the inferior Trunk end-point because it involved direct determination from the relative locations of markers located on the trunk itself, and because these trunk markers, relative to the Hip markers, were less affected by skin movement artefacts associated with limb movement. For similar reasons, Method C (described on page 120) was developed for determining the superior Trunk end-point, which coincided with the Trunk-Neck Joint. The superiority of the methods used in this study (viz. the combined application of Methods B and C) over the conventional 2-D method (e.g. Vaughan et al., 1982a) was verified by comparing the within-trial Trunk segment length variability produced by the application of both these approaches to each of the 28 trials used for the experiment described in Chapter 7. The marker data in these

trials was smoothed as described on page 129. Within-trial Trunk segment length variability was defined as the SD of Trunk segment length within each trial and it was hypothesised to be less for the method used in this research than the conventional 2-D method. A t-test of dependent means provided extremely strong support for the combined application of Methods B and C in this research ($t = 8.077$, $p < 0.000001$, $N = 28$). Method B involved three steps.

Step 1 involved defining the unilateral position of the inferior Trunk segment end-point relative to the positions of each of the six possible combinations of actual ipsilateral trunk marker pairs. These spatial relationships were established separately for each side of the body using the unfiltered coordinates from the initial phases of 14 standing trials, during which the subject maintained the quasi-static stance posture depicted in Fig. 5 on p. 105. Coordinates were averaged over 44 s of quasi-static stance. The unilateral position of the inferior Trunk segment end-point was defined as the point coinciding with the average position of the ipsilateral Hip marker during the 44 s of quasi-static stance. The location of this averaged virtual point relative to the average positions of each of the six possible combinations of the actual ipsilateral trunk marker pairs was then determined. As an example, consider a local coordinate system with an origin at the left C7-T1 marker and one reference axis in the direction of the left Suprasternale marker (Fig. 10). The position of the left Hip marker, relative to this pair of trunk markers, was expressed in terms of two coordinates relative to the local origin. These coordinates were expressed as proportions of Γ, the length from C7-T1 to Suprasternale. Similar local coordinate systems were also established for the other five possible combinations of ipsilateral trunk marker

pairs (i.e. left Sacrum/Suprasternale, C7-T1/Sacrum, C7-T1/Xiphoid, Sacrum/Xiphoid and Suprasternale/Xiphoid).

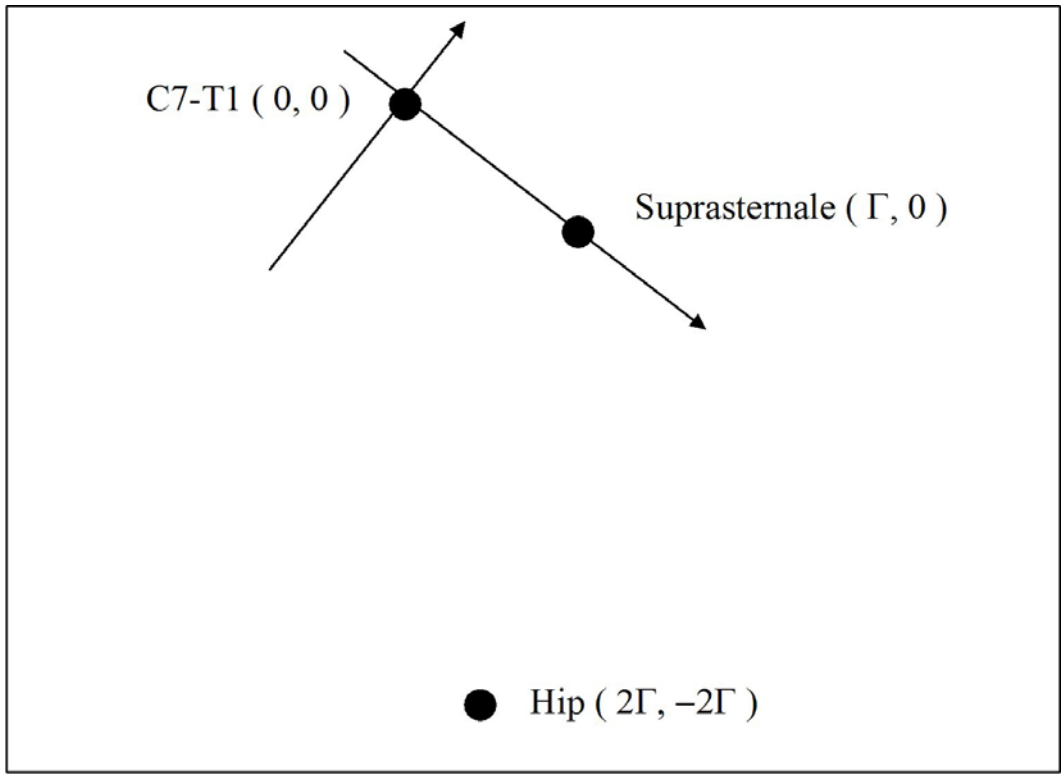

Figure 10. Example of how the position of an actual unilateral Hip marker was expressed relative to the C7-T1 and Suprasternale marker positions during Step 1 of virtual marker calculation Method B. The position of the Hip marker was expressed in a local coordinate system with origin at C7-T1 and one of the reference axes passing through the Suprasternale marker. Local coordinates were expressed in terms of proportions of Γ, the length from C7-T1 to Suprasternale. This example is for illustrative purposes only and does not show true Hip coordinates.

Step 2 of Method B involved using the left and right side spatial relationships established in Step 1 to calculate virtual left and right inferior Trunk end-point coordinates for every sampled time during a given movement trial. Filtered kinematic trial data was used for this purpose. The upper limbs sometimes

obscured trunk markers and, hence, only the spatial relationships involving pairs of trunk markers that remained visible throughout a movement trial were used to calculate virtual hip joint coordinates. For example, if the left Xiphoid marker became obscured during any stage of a trial, only the coordinates estimated by the spatial relationships established in Step 1 for the remaining visible left trunk marker pairs (i.e. left Sacrum/Suprasternale, C7-T1/Suprasternale and C7-T1/Sacrum) were used to determine the left virtual inferior trunk end-point coordinates. Hence, for each sampled time, the left and right virtual inferior trunk end-point coordinates were calculated separately, as the mean of the coordinates derived from the spatial relationships associated with each of the continuously-visible ipsilateral trunk marker pairs. If all four ipsilateral trunk markers were continuously visible throughout a trial, then all six possible pairs of ipsilateral trunk markers were used. If one marker was obscured at any stage in a trial, only the three remaining pairs of markers were used. If two markers were obscured, the one remaining trunk marker pair was used. If three or four ipsilateral trunk markers were missing, the trial was discarded.

Finally, Step 3 of Method B involved determining the ITE_B virtual marker position for each time sample in the movement trial by averaging the left and right virtual inferior trunk end-point values established in Step 2.

Method C was used for the determination of virtual marker $OTNJ_C$, the optimised Trunk-Neck joint. This method was similar to the approach used in Method B. However, instead of defining virtual markers based on the position of actual markers during quasi-static postures, Method C involved determination of the

virtual position of the TNJ by an optimisation procedure applied across seven combined trials (a total of 30 s of data) in which the subject was standing with the trunk essentially static but with a combined Head/Neck[10] segment undergoing angular displacement in the sagittal plane. The average positions of the left and right C7-T1 and Suprasternale trunk markers were calculated. The same local coordinate system as depicted in Fig. 10 was used. In both dimensions, TNJ was assigned an initial estimate of 0.5Γ, where Γ was the displacement from C7-T1 to Suprasternale. TNJ global coordinates were subsequently calculated for all time samples. The length of the Neck segment (the distance from TNJ to Mid-Tragus$_A$) was then calculated for all time samples.

The objective function for the optimisation process was defined as the standard deviation (SD) of all Neck segment length calculations. The chosen objective function was based on the fact that, for an ideal linked segment model, segment length will be constant throughout all segment angular displacements (and therefore, SD = 0) if the marker representing the joint about which the segment rotates is an accurate representation of that joint. The two scalars representing the local coordinates of TNJ were then varied until the objective function was minimised. OTNJ$_C$ was then assigned the final, optimised value of TNJ in the local coordinate system, which was subsequently used to determine TNJ throughout each trial used in this research, relative to the left/right-averaged C7-T1 and Suprasternale trunk markers. The quasi-Newton algorithm in the Solver add-in within Microsoft Excel 2000 (Microsoft Corporation, Redmond,

[10] The Head and Neck segments were held rigid, relative to each other, for this exercise.

WA., U.S.A.) was used to calculate $OTNJ_C$, using the smallest programmable convergence criterion and the greatest precision setting. Fig. 11 illustrates all the actual and virtual markers used to define the segments, joints and segment end-points.

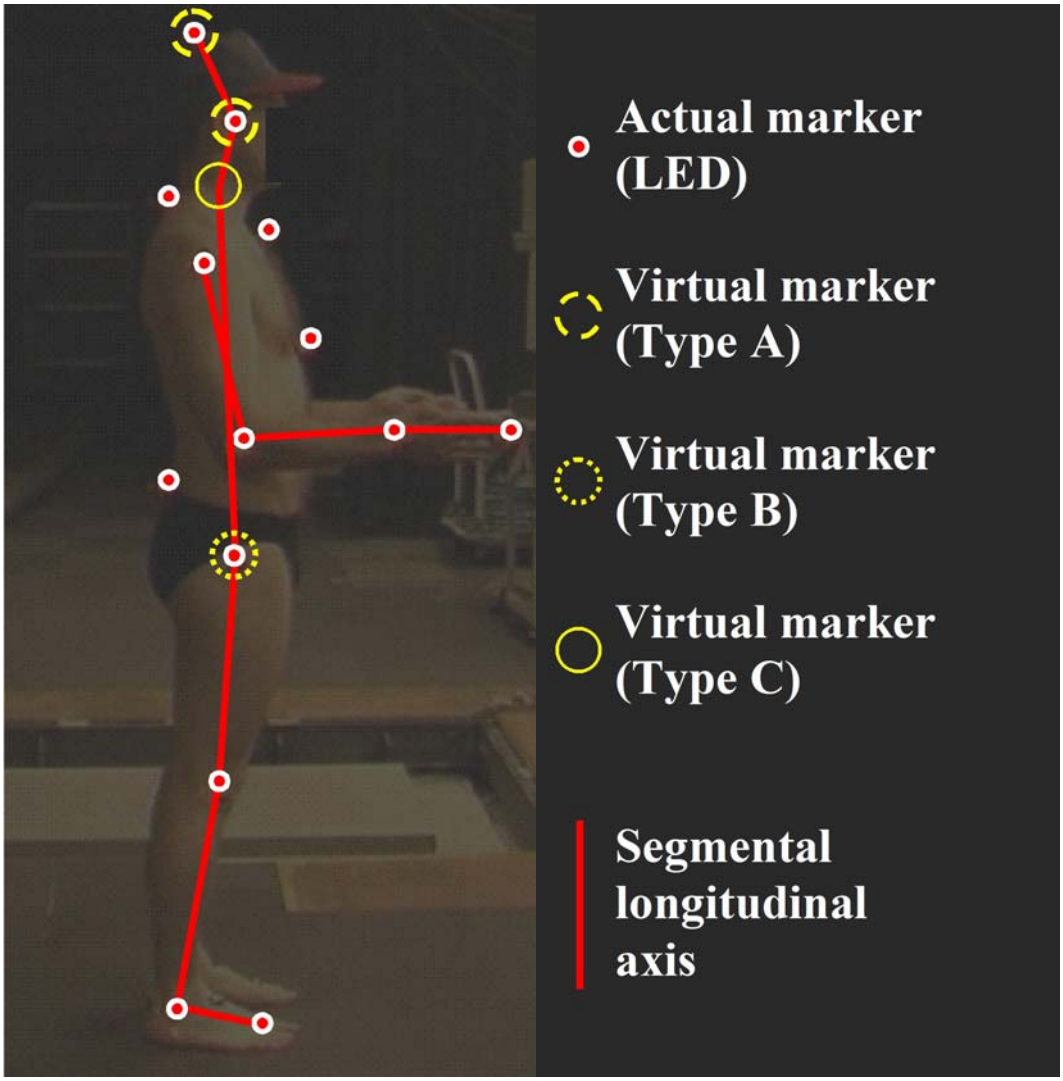

Figure 11. Stick figure representation of the model defined for this research: The model, with associated actual and virtual markers, is shown superimposed on a photograph of the subject. Refer also to Tables 1 and 2 for definitions of the segments and joints incorporated into the model, and to section 4.4.1.1 for relevant virtual marker definitions.

4.4.1.2 Complete Definition of the Model

The 15-segment model included left and right Feet, Shanks, Thighs, Hands, Forearms and Arms, plus Trunk, Neck and Head segments, as illustrated in Figs. 9 and 11. The relationships between each segment, its end-points, the adjacent joint centres and the relevant virtual and actual markers are now documented. Table 1 summarises the segment definitions, in terms of the markers used to represent the each segment's proximal and distal end-points.

Table 1. Segment definitions in terms of the various markers (actual and virtual) used to represent the distal and proximal segment end-points. Virtual markers are subscripted with an A, B, or C, reflecting one of the three different methods applied to derive such markers (see section 4.4.1.1). Inferior and superior trunk end-points were considered proximal and distal, respectively. L/R refers to left or right.

Segment	**Distal End-point Marker**	**Proximal End-point Marker**
L/R Foot	L/R Ball	L/R Ankle
L/R Shank	L/R Ankle	L/R Knee
L/R Thigh	L/R Knee	L/R Hip
L/R Hand	L/R Tip	L/R Wrist
L/R Forearm	L/R Wrist	L/R Elbow
L/R Lower Arm	L/R Wrist	L/R Elbow
L/R Upper Arm	L/R Elbow	L/R Shoulder
Trunk	$OTNJ_C$	ITE_B
Neck	$Mid\text{-}Tragus_A$	$OTNJ_C$
Head	$Mid\text{-}Vertex_A$	$Mid\text{-}Tragus_A$

$OTNJ_C$ = Optimised Trunk-Neck joint marker

Lower Arm consists of Forearm and Hand

Table 2 summarises all the model's joint centre definitions, in terms of the markers used to represent them. By definition, some segment end-points were co-located with one or more joint centres. Such cases are also documented in Table 2.

Table 2. Joint definitions in terms of the various actual and virtual markers used and derived, respectively, to represent the joint centres. Virtual markers are subscripted with an A, B, or C, reflecting one of the three different methods applied to derive such markers (see section 4.4.1.1). For any joint centre that was, by definition, co-located with one or more of the defined segment end-point locations, such end-points are listed in parentheses. Inferior and superior trunk end-points were considered proximal and distal, respectively. L/R refers to left or right.

Joint Centre	**Joint Marker (and Co-located Segment End-point/s)**
L/R Ankle Joint	L/R Ankle (Proximal Foot, Distal Shank)
L/R Knee Joint	L/R Knee (Proximal Shank, Distal Thigh)
L/R Hip Joint	L/R Hip (Proximal Thigh)
L/R Wrist Joint	L/R Wrist (L/R Proximal Hand, L/R Distal Forearm, L/R Distal Lower Arm)
L/R Elbow Joint	L/R Elbow (Proximal Forearm, Proximal Hand/Forearm, Distal Upper Arm)
L/R Shoulder Joint	L/R Shoulder (Proximal Upper Arm)
TNJ	$OTNJ_C$ (Distal Trunk, Proximal Neck)
HNJ	$Mid\text{-}Tragus_A$ (Proximal Head, Distal Neck)

TNJ = Trunk-Neck joint

HNJ = Head-Neck joint

$OTNJ_C$ = Optimised Trunk-Neck joint marker.

Ultimately, the ipsilateral Forearm and Hand segments were combined to form left and right Lower Arm segments, thus reducing the model to only 13 segments.

Only the 13-segment model was subsequently used in this research. Hence, for all trials, the subject was instructed to avoid Hand rotation about the Wrist joints, with respect to the Forearms.

4.4.1.3 Body Segment Parameter Definitions

The BSPs defined for this research were the segmental masses (m_{seg}), the segmental centre of mass locations in the sagittal plane (cm_{seg}) and the segmental moments of inertia about the subject's transverse axis through each segment's centre of mass (I_{seg}). For each segment, m_{seg} was expressed as a proportion of total body mass (m_{WB}), cm_{seg} was expressed as a proportion of segment length along and perpendicular to the segmental longitudinal axis, and I_{seg} was assumed to be the principal moment of inertia.

A 2-D local reference system, fixed within each segment and assumed to remain in the sagittal plane, was used to define each cm_{seg}. Each segment-based reference system had an origin at the proximal end-point of the segment[11], a longitudinal axis passing through the segment's proximal and distal end-points, and a second axis running perpendicularly to the first (see Fig. 12). The positive direction of the longitudinal axis (+*L*) was proximal-to-distal and the positive direction of the perpendicular axis (+*P*) was always 90° anticlockwise with respect to +*L*, as depicted in Fig. 12. The unit of scale in each segment-based reference system was the respective segment length (l_{seg}). Segment length (l_{seg}) was the distance

[11] In the case of the Trunk segment, the proximal end-point was assumed to be the inferior end-point.

between the segment's end-points, as projected in the sagittal plane. Hence, each segment's distal end-point location was always represented by the segment-based coordinate pair (0, 1).

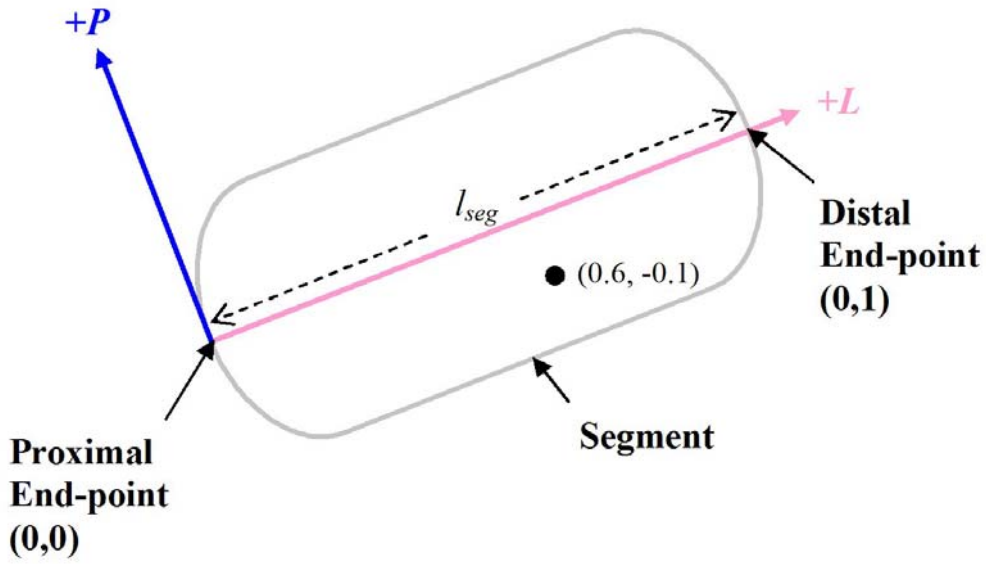

Figure 12. The segment-based reference system, with axes L and P, used to locate each segment's cm_{seg} BSP. l_{seg} is segment length. The example cm_{seg} BSP of $(cm[L]_{seg}, cm[P]_{seg}) = (0.6, -0.1)$ depicted by the black dot is for illustrative purposes only and is not necessarily realistic.

Each cm_{seg} BSP was defined by segment-based coordinates $(cm[L]_{seg}, cm[P]_{seg})$. Thus, as an example, $(cm[L]_{seg}, cm[P]_{seg}) = (0.6, -0.1)$ would represent a segment centre of mass position that is 60% of l_{seg} distal to the segment's proximal end-point along the longitudinal axis and 10% of l_{seg} perpendicular to and 'below' this axis (see Fig. 12). If, for example, the segment in Fig. 12 was a Foot segment, the segmental centre of mass position defined by (0.6, -0.1) would be on the plantar side of the longitudinal axis.

Fig. 13 shows the sagittal plane position and orientation of the segment-based reference systems in all the segments. Each +*P* axis is a 90° anticlockwise rotation of the associated +*L* axis. Hence, +*P* was *plantar-to-dorsal* for the Foot segments and *posterior-to-anterior* for the other limb segments. Conversely, for the Trunk, Head, and Neck segments, whose proximal-distal orientation are opposite to that of the limbs when in the anatomical position, +*P* was *anterior-to-posterior* with respect to the anatomical position.

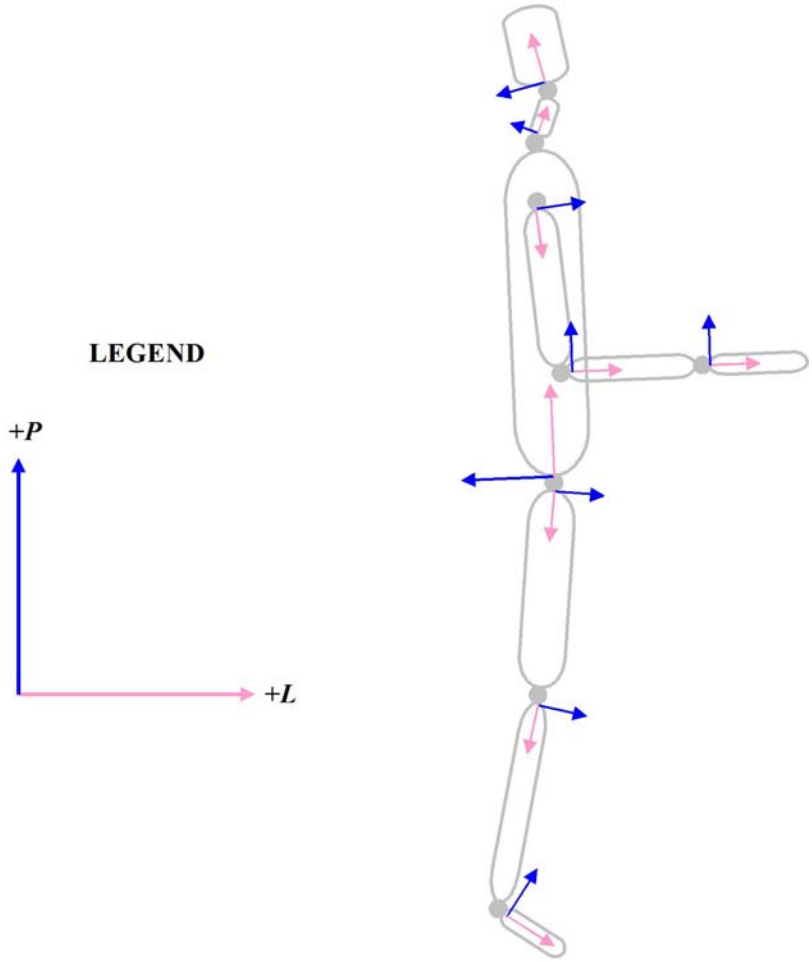

Figure 13. The position and orientation in the sagittal plane of the segment-based reference systems used to locate each respective segment's centre of mass position.

4.4.2 Marker and Kinematic Data Processing

The digital video was captured to a personal computer hard drive in DV AVI file format. Peak Motus Version 4.3.3 (Peak Performance Technologies, Inc., Englewood, Colorado, U.S.A.) was used to automatically digitise and determine the centroids of all markers that were visible in the left and right side digital video files. No attempt was made to predict missing marker positions when they became obscured from view of the cameras due to out-of-plane motion or rotation of a segment about its longitudinal axis. When this occurred, trials were sub-divided, creating smaller sub-trials in the process. The LEDs had a narrow projection angle of 35°, so out-of-plane motion and rotation about a segment's longitudinal axis was deemed minor and acceptable as long as the markers remained visible to the cameras, because this represented a deviation of less than 17.5°. Sub-trials were also created by the removal of data associated with ground impact events during jumping and hopping activities, due to the inability of quintic spline filtering algorithm used in this research to deal with such transients (Giakas et al., 2000).

The calibration rod (see section 4.3.2) enabled life-size scaling of both left- and right-side raw marker data sets. The coordinates of the two reference LED markers positioned at opposite ends of the force platform (see section 4.3.2) were used to perform appropriate linear and rotational transformations of the left- and right-side scaled data so that both data sets shared the same global coordinate system as the force platform data. This included a 180° rotation of the left-side data about the vertical axis. Subsequently, for each trial, the left- and right-side

marker data sets were merged and then filtered. Finally, all virtual marker coordinates were calculated, as per the description in section 4.4.1.1. This resulted in the creation of a single data set for each trial containing the filtered displacement-time histories of all actual and virtual markers within the same global coordinate system, with the origin situated at the centre of the top surface of the force platform and axes as defined in Fig. 14.

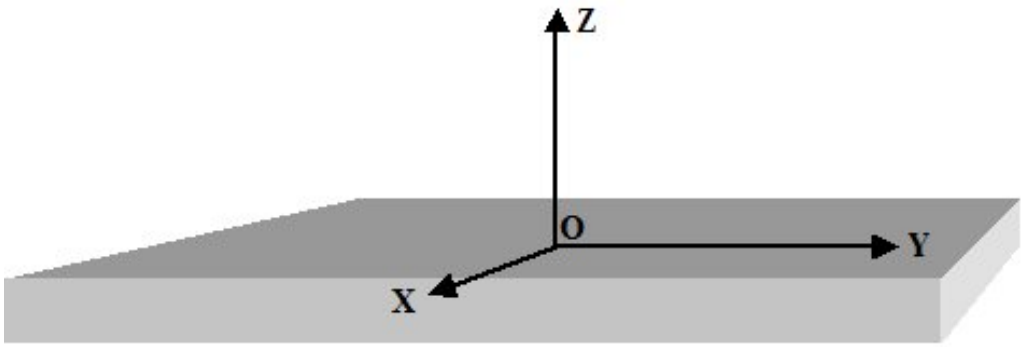

Figure 14. The global coordinate system used in this research with an origin at the centre of the top surface of the force platform, positive Z *in the upwards direction, positive* Y *in the posterior-to-anterior direction, and* OYZ *representing the (sagittal) plane of motion. The positive* X *axis was defined by the right-hand rule, relative to the other two axes and was from the left to the right side of the subject for all movement trials.*

The actual marker coordinates were low-pass filtered using quintic splines. Quintic splines have been demonstrated to produce less 'endpoint errors'[12] than other smoothing techniques commonly used in biomechanics, such as Butterworth

[12] Also referred to as 'boundary problems' by Woltring (1985), Vint and Hinrichs (1996) described endpoint errors as the "erratic behaviour at the beginning and end of the computed acceleration data which is commonly observed after smoothing and differentiating raw displacement data".

digital filtering and Fourier series methods (Vint and Hinrichs, 1996). Even when Vint and Hinrichs (1996) applied Butterworth, Fourier and cubic spline smoothing techniques to raw data augmented with extrapolated data, based on either linear or reflection techniques, they found that acceleration results were less favourable than those produced by quintic splines applied only to the unpadded raw data. Hence, the executable Fortran 77 program GCV, a quintic spline smoothing program, based on the code developed by Woltring (1986) and written by van den Bogert (2000)[13], was used to smooth the merged marker data sets. Details regarding how this software was used in each specific experiment conducted for this research are provided in the ensuing chapters.

For each relevant model, the smoothed kinematic data were used to calculate all segmental linear and angular displacements, velocities and accelerations. Segmental linear displacements were expressed in terms of each segment's centre of mass location as a function of time (t). For all t, each segment's centre of mass displacement, with respect to the global coordinate system, was represented by coordinates $cm[y]_{seg}(t)$ and $cm[z]_{seg}(t)$ and calculated as follows:

[13] This software is available from the International Society of Biomechanics website at http://isbweb.org/software/sigproc.html

$$cm[y]_{seg}(t) = Prox[y]_{seg}(t) + cm[L]_{seg}\left(Dist[y]_{seg}(t) - Prox[y]_{seg}(t)\right) - cm[P]_{seg}\left(Dist[z]_{seg}(t) - Prox[z]_{seg}(t)\right)$$

$$cm[z]_{seg}(t) = Prox[z]_{seg}(t) + cm[L]_{seg}\left(Dist[z]_{seg}(t) - Prox[z]_{seg}(t)\right) + cm[P]_{seg}\left(Dist[y]_{seg}(t) - Prox[y]_{seg}(t)\right) \quad (15)$$

where $Prox[y]$, $Prox[z]$, $Dist[y]$ and $Dist[z]$ represent the horizontal $[y]$ or vertical $[z]$ position of the proximal and distal segment end-points in the global coordinate system; and $cm[L]_{seg}$ and $cm[P]_{seg}$ represent the segmental centre of mass BSP coordinates in the local, segment-based coordinate system, expressed in terms of proportion of segment length (l_{seg}). The coordinates of the whole body centre of mass in the global coordinate system were calculated by SK analysis as follows:

$$CM[y]_{SK}(t) = \frac{1}{n}\sum_{seg=1}^{seg=n} cm[y]_{seg}(t) * m_{seg}$$

$$CM[z]_{SK}(t) = \frac{1}{n}\sum_{seg=1}^{seg=n} cm[z]_{seg}(t) * m_{seg} \quad (16)$$

where n is the number of segments in the relevant model.

A two-part process was adopted to determine angular segmental displacements (θ_{seg}). Firstly, θ_{seg} was determined as follows:

$$\theta_{seg}(t) = \arctan 2\left[\frac{\left(Dist[z]_{seg}(t) - Prox[z]_{seg}(t)\right)}{\left(Dist[y]_{seg}(t) - Prox[y]_{seg}(t)\right)}\right] \quad (17)$$

The $\arctan 2$ function determines in which of the four quadrants θ_{seg} lies and expresses the result as an angle in a range from -180° to +180°. However, 'discontinuities' in $\theta_{seg}(t)$ occur when adjacent time samples cross the ±180° line (Robertson and Caldwell, 2004), changing from large negative angles to large positive angles, or *vice versa*, in the process. This possibility was addressed by applying the condition that $\theta_{seg}(t)$ and $\theta_{seg}(t+1)$ had to be less than 180° apart, and making appropriate corrections to $\theta_{seg}(t+1)$ when this condition was violated. For example, if $\theta_{seg}(t)$ and $\theta_{seg}(t+1)$ were determined by Eq. (17) to be -179° and +178°, respectively, then $\theta_{seg}(t+1)$ was corrected to become -182°. Similarly, if $\theta_{seg}(t)$ and $\theta_{seg}(t+1)$ were determined by Eq. (17) to be +179° and -178°, respectively, then $\theta_{seg}(t+1)$ was corrected to become +182°. Hence, $\theta_{seg}(t)$ was not ultimately constrained to the range of -180° to +180° and discontinuities were avoided.

Segmental linear velocities ($cm[y']_{seg}$, $cm[z']_{seg}$) and accelerations ($cm[y'']_{seg}$, $cm[z'']_{seg}$) were determined using first order central difference equations (Miller and Nelson, 1973):

$$cm[y']_{seg}(t) = \frac{cm[y]_{seg}(t+\Delta t) - cm[y]_{seg}(t-\Delta t)}{2\Delta t},$$

$$cm[z']_{seg}(t) = \frac{cm[z]_{seg}(t+\Delta t) - cm[z]_{seg}(t-\Delta t)}{2\Delta t},$$

$$cm[y'']_{seg}(t) = \frac{cm[y]_{seg}(t+\Delta t) - 2cm[y]_{seg}(t) + cm[y]_{seg}(t-\Delta t)}{\Delta t^2}, \text{ and}$$

$$cm[z'']_{seg}(t) = \frac{cm[z]_{seg}(t+\Delta t) - 2cm[z]_{seg}(t) + cm[z]_{seg}(t-\Delta t)}{\Delta t^2} \quad (18)$$

where Δt is the inverse of the sampling frequency (f), the latter of which was 50 Hz for the kinematic data. Similarly, segmental angular velocities (ω_{seg}) and accelerations (α_{seg}) were calculated as follows:

$$\omega_{seg}(t) = \frac{\theta_{seg}(t+\Delta t) - \theta_{seg}(t-\Delta t)}{2\Delta t}, \text{ and}$$

$$\alpha_{seg}(t) = \frac{\theta_{seg}(t+\Delta t) - 2\theta_{seg}(t) + \theta_{seg}(t-\Delta t)}{\Delta t^2} \quad (19)$$

Because forward and backward difference equations were not used, the first and last displacement data points were removed when velocity or acceleration data were also required for objective function calculations.

4.4.3 Force Platform Data Processing

The manufacturer's instruction manual stated that data measured by the force platform were the forces and moments *applied* to the force platform, with

reference axes in the same directions as depicted in Fig 14, except with reversed polarities for the *X* and *Z* axes. Hence, ground *reaction* forces consistent with the global coordinate system adopted for this research were derived by reversing the polarity of antero-posterior (*y*) forces.

Force platform calibration data provided by the manufacturer stated that the origin of the platform was 0.0535 m directly below the centre of the top surface of the platform. Hence, the antero-posterior (*y*) coordinate of the centre of pressure (COP) of the GRF, as a function of time, was calculated as follows:

$$COP[y](t) = \frac{Mx(t)Mx_C + Mx_O - 0.0535\left(Fy(t)Fy_C + Fy_O\right)}{Fz(t)Fz_C + Fz_O} \tag{20}$$

where *Mx* is the measured moment about the force platform's *X* axis, and *Fy* and *Fz* are the antero-posterior and vertical components, respectively, of the measured GRF. Fz_C, Fz_O, Fy_C, Fy_O, Mx_C and Mx_O represent the dimension-specific force and moment calibration factor error and offset error terms. Values for these terms were assigned or estimated during the optimisation processes described in ensuing chapters.

The vertical and horizontal sagittal plane components of the whole body centre of mass acceleration ($CM''[z]_{IA}$ and $CM''[y]_{IA}$, respectively), as a function of time, were calculated from the GRF data as follows:

$$CM''[z]_{IA}(t) = \frac{Fz(t)\ Fz_C + Fz_O}{m_{WB}} + g$$

$$CM''[y]_{IA}(t) = \frac{Fy(t)\ Fy_C + Fy_O}{m_{WB}} \tag{21}$$

where m_{WB} is the whole body mass and g is the gravitational acceleration, which was -9.80 ms^{-2} for the location where the data were captured (viz. Melbourne, Australia).

For any given moment in time (t), the vertical and antero-posterior plane components of the whole body centre of mass velocity and displacement were calculated by numerical integration using the trapezoid rule as follows:

$$CM'[z]_{IA}(t) = \left(\sum_{\Delta t}^{t} \left[\left(CM''[z]_{IA}(t-\Delta t) + CM''[z]_{IA}(t) \right) \times \Delta t / 2 \right] \right) + CM'[z]_{IA}(0)$$

$$CM[z]_{IA}(t) = \left(\sum_{\Delta t}^{t} \left[\left(CM'[z]_{IA}(t-\Delta t) + CM'[z]_{IA}(t) \right) \times \Delta t / 2 \right] \right) + CM'[z]_{IA}(0) \times t + CM[z]_{IA}(0)$$

$$CM'[y]_{IA}(t) = \left(\sum_{\Delta t}^{t} \left[\left(CM''[y]_{IA}(t-\Delta t) + CM''[y]_{IA}(t) \right) \times \Delta t / 2 \right] \right) + CM'[y]_{IA}(0)$$

$$CM[y]_{IA}(t) = \left(\sum_{\Delta t}^{t} \left[\left(CM'[y]_{IA}(t-\Delta t) + CM'[y]_{IA}(t) \right) \times \Delta t / 2 \right] \right) + CM'[y]_{IA}(0) \times t + CM[y]_{IA}(0) \tag{22}$$

where Δt is the inverse of the sampling frequency (f) of the kinetic data; and $CM'[z]_{IA}(0)$, $CM'[y]_{IA}(0)$, $CM[z]_{IA}(0)$ and $CM[y]_{IA}(0)$ represent the respective dimension-specific components of the initial velocity and displacement of the whole body centre of mass. Values for these terms were assigned or estimated during the optimisation processes described in ensuing chapters.

5. ZPZP TECHNIQUES FOR ESTIMATING CM KINEMATICS DURING STANCE

ZPZP techniques based on those reported by Zatsiorsky and Duarte (2000) were developed and assessed during the experiment described in this chapter, due to their potential to produce accurate determinations of the initial antero-posterior CM displacement and velocity conditions (viz. $CM[y]_{IA}(0)$ and $CM'[y]_{IA}(0)$) for posturographic applications. If successful in this regard, these methods might also produce accurate $CM_{IA}(t)$ trajectory throughout a given trial, which is the ultimate objective of this experiment. This chapter includes a description of the research design (section 5.1), including full descriptions of all the methods developed for this experiment (section 5.1.1), the parameters developed to assess them (section 5.1.2), and the research hypotheses and the statistical techniques used to test them (section 5.1.3). Then the results are presented (section 5.2) and discussed (section 5.3).

5.1 Research Design

5.1.1 The Modified ZPZP Methods

The basic ZPZP method reported by Zatsiorsky and Duarte (2000) was compared with several modified ZPZP methods, including three optimisation-augmented approaches. Comparisons between these methods were made after they were applied to quiet stance activities. The various methods were derived as follows:

- ***ZPZP1***: This method was essentially the original method of Zatsiorsky and Duarte (2000), described previously within pages 17 to 24. The force platform data were re-sampled at 40 Hz and low-pass filtered with a 4th order zero-lag phase Butterworth filter at a cut-off frequency of 8 Hz. Instants when $Fy(t) = 0$ were determined by linear interpolations between adjacent $Fy(t)$ data points of opposite polarity and IEPs were determined by similar linear interpolations between the two corresponding $COP[y](t)$ values. The trapezoid rule of numerical integration was applied.

Fig. 15 shows a representative plot of the antero-posterior force during a typical quiet stance trial as measured by the instrumentation used in this study, and how adding a term to compensate for a potential offset error in *Fy* measurements can alter the timing and even the number of IEP instants when the antero-posterior force measurement is zero. Subsequently, this may have a noticeable effect on the ZPZP method and the resultant $CM[y]_{IA}(t)$ calculations. An offset error may occur if there is a systematic error in *Fy* associated with the positioning of the subject on the force platform, and/or if random noise is present at the instant the force signal is zeroed prior to data collection. The offset term in Fig. 15, Fy_O, equals the negative of the mean *Fy* value for the entire trial (11.2 s duration), not just for the three second period shown.

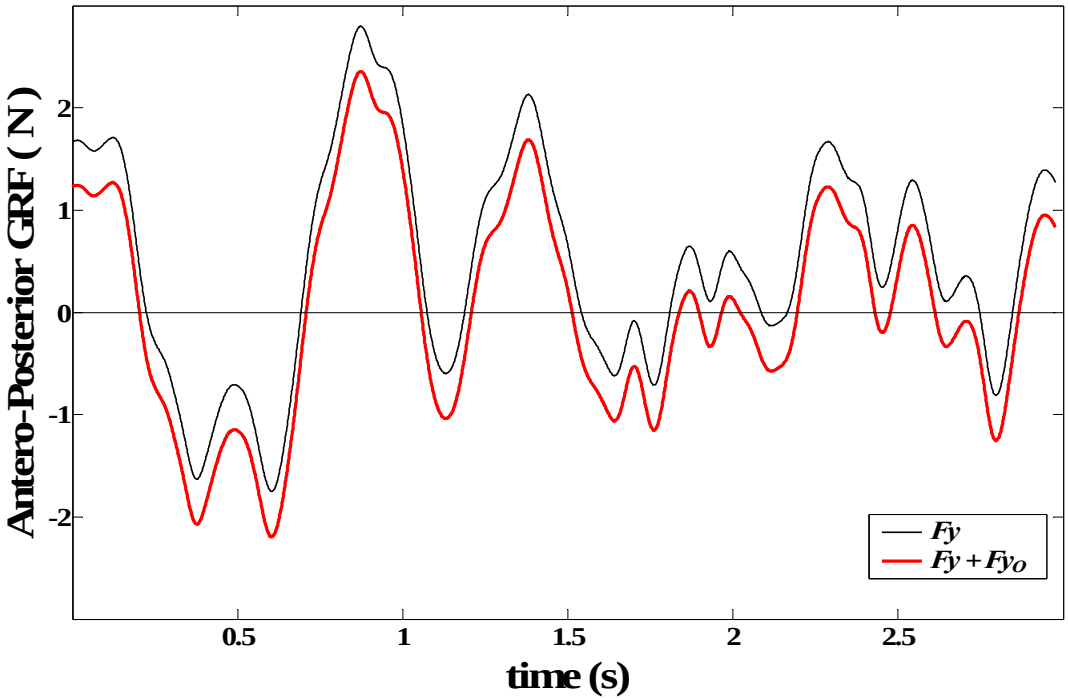

Figure 15. Demonstration of the potential effect on the timing and number of zero-force-crossings in a quiet stance trial elicited by adding an offset error term (Fy_O) to the antero-posterior GRF (Fy) measurements. Such a change may alter the ZPZP results. For example, there are 10 IEPs shown above in the original Fy measurements. However, with the inclusion of an error term, Fy_O = -0.45 N, the timing of those IEPs within the trial shifts and there are now an additional 4 IEPs.

Subtracting the average *Fy* value from all *Fy* measurements in a quasi-static trial may account well for an offset error and may improve the results produced by the ZPZP method. Hence, a second ZPZP variation was developed and assessed:

- ***ZPZP2***: As per *ZPZP1*, but with de-trended *Fy*(*t*). That is, the average *Fy* value over the entire trial was subtracted from each individual *Fy* value prior to applying the ZPZP algorithm.

ZPZP3 was designed to introduce more precise calculations to the ZPZP procedure than were used by Zatsiorsky and Duarte (2000):

- ***ZPZP3***: As per *ZPZP2*, but with all calculations conducted at the full temporal resolution afforded by the 1000 Hz data capture rate performed during this research.

All three aforementioned modified ZPZP methods were applied in the 'conventional' manner (*ZPZP1C*, *ZPZP2C* and *ZPZP3C*), with the ZPZP algorithm applied across each and every ZPZP interval, as mandated by *Step 6* (see page 17). Each method was also applied in an 'unconventional' way (*ZPZP1U*, *ZPZP2U* and *ZPZP3U*), with *Steps 1* to *5* of the ZPZP algorithm being applied only once across the entire interval spanned by the initial and final IEPs in the movement sequence, ignoring all intermediate IEPs. A logical argument exists for the unconventional approach: If the fundamental premise upon which the ZPZP methods are based is valid (viz. during stance, $CM[y]_{IA}(t)$ and $COP[y](t)$ coincide whenever the antero-posterior GRF is momentarily zero), then it should not be necessary to execute the ZPZP algorithm (see page 17) across each and every ZPZP interval in a movement sequence. That is, any ZPZP method that is not susceptible to other error sources should be able to be applied in the unconventional way, ignoring all intermediate IEPs, and still be capable of producing equivalent $COP[y](t)$ and $CM[y]_{IA}(t)$ values at not only the initial and final IEPs, but also at each and every intermediate IEP. In a pragmatic sense, force platform measurement errors may also need to be accounted for if the logical argument presented above is to be supported by empirical evidence. Hence, the following optimisation-augmented ZPZP method was developed and assessed:

- ***ZPZP4U**:* This method was applied in the unconventional manner, based on *ZPZP3U*. The difference was that *ZPZP4U* included a nonlinear optimisation approach, with design variables comprised of the dimensionally-relevant force and moment calibration factor and offset error terms (Fz_C, Fz_O, Fy_C, Fy_O, Mx_C and Mx_O). These design variables are inherent in Equations (20), (21) and (22), which were used to calculate all relevant $COP[y](t)$, $CM[y]_{IA}(t)$ and $CM'[y]_{IA}(t)$ values. The inclusion of the force platform error terms meant that *Fy* did not need to be de-trended and IEPs were identified at instants when $Fy(t)Fy_C + Fy_O = 0$, rather than when de-trended $Fy(t) = 0$. The iterative estimation of the design variables was designed to optimise $CM[y]_{IA}(t)$ across the intermediate IEPs. *ZPZP4U* involved applying the ZPZP algorithm (see page 17) in the unconventional manner. The design of the objective function was based on the premise that $COP[y](t)$ should equal $CM[y]_{IA}(t)$, not only at the initial and final IEPs (IEP_0 and IEP_n), as mandated by the ZPZP algorithm, but also at each and every intermediate IEP_i ($i = 1, \ldots, n - 1$). Hence, values for the design variables were sought that minimised the following objective function, which was defined as the mean of the absolute differences of all $n - 1$ intermediate IEP pairs of $COP[y](t_i)$ and $CM[y]_{IA}(t_i)$:

$$\frac{1}{n-1}\sum_{i=1}^{n-1}\left|CM[y]_{IA}(t_i) - COPy(t_i)\right| \qquad (23)$$

Linear interpolation was used between adjacent $CM[y]_{IA}(t_i)$ samples surrounding each IEP to find each $CM[y]_{IA}(t_i)$. An alternative approach was assessed, in which numerical integration was conducted over the interval

finishing at the linearly interpolated IEP, using the linearly interpolated *Fy* value at that time. Both methods were demonstrated to produce the same results to a precision of at least six decimal places, for both the 40 Hz and 1000 Hz data. Interpolation was less computationally intensive and therefore helped to improve the efficiency of the *ZPZP4U* optimisation algorithm. The mean, as opposed to the sum, of the absolute differences was chosen because the number of intermediate IEPs, n - 1, had the potential to vary, depending on the values of Fy_O and Fy_C.

As discussed on page 20, successive executions of the ZPZP algorithm applied to adjacent ZPZP intervals that share a common IEP_i at time t_i, will produce two potentially different CM velocity values at t_i. On the basis that two values representing the same kinematic quantity at the same instant should be equivalent, a second optimisation-augmented ZPZP method was developed and assessed:

- ***ZPZP5C***: Like *ZPZP4U*, this method incorporated a nonlinear optimisation approach and consisted of design variables for the force platform measurement error terms (Fz_C, Fz_O, Fy_C, Fy_O, Mx_C and Mx_O). Hence, IEPs were again identified at the instants when $Fy(t)Fy_C + Fy_O = 0$. Unlike *ZPZP4U,* this method involved applying the ZPZP algorithm in the conventional manner, based on *ZPZP3C*. The *ZPZP5C* objective function was based on the premise that, for each and every intermediate IEP_i ($i = 1, \ldots, n - 1$) in a movement sequence, the final CM velocity at the instant of IEP_i (viz. $CM'[y]_{IA}(t_i)$, calculated by numerical integration in *Step 5* of the i^{th} execution of the ZPZP algorithm for the i^{th} ZPZP interval) should equal the 'actual' initial CM velocity at the same instant t_i (viz. $V_0(t_i)$, calculated in *Step 4* of the $(i + 1)^{th}$

execution of the ZPZP algorithm for the $(i+1)^{th}$ ZPZP interval). Hence, values for the design variables were sought that minimised the *ZPZP5C* objective function, which was defined as the mean of the absolute differences of all n - 1 intermediate IEP pairs of $V_0(t_i)$ and $CM'[y]_{IA}(t_i)$:

$$\frac{1}{n-1}\sum_{i=1}^{n-1}\left|CM'[y]_{IA}(t_i)-V_0(t_i)\right| \tag{24}$$

where n is the total number of ZPZP intervals. The mean, as opposed to the sum, of the absolute differences was chosen because the total number of IEPs (n + 1) may vary, depending on the values of the force platform error terms.

Two nonlinear inequality constraints were developed and their application within *ZPZP4U* and *ZPZP5C* was assessed, based on the fact that the controlling COP excursions are greater in amplitude than CM displacement during quiet stance (Winter et al., 1996a). Hence, the minimum and maximum $CM[y]_{IA}(t)$ values within a period of quiet stance must have corresponding $COP[y](t)$ values that are lesser and greater, respectively. Hence, the nonlinear inequality constraints were applied as follows:

$$\max(CM[y]_{IA}(t)) - \max(COP[y](t_{maxCMy})) \le 0, \text{ and}$$
$$\min(COP[y](t_{minCMy})) - \min(CM[y]_{IA}(t)) \le 0 \tag{25}$$

where t_{maxCMy} is the time at which $\max(CM[y]_{IA}(t))$ occurred and t_{minCMy} is the time at which $\min(CM[y]_{IA}(t))$ occurred.

The closer that the initial estimates of the design variables are to the optimal values, the faster the optimisation algorithm will converge to the minimum (Vaughan et al., 1982a). Hence, all *ZPZP4U* and *ZPZP5C* optimisations were commenced with the best available estimates of the design variables, which consisted of $Mx_C = 1$, $Fy_C = 1$, $Fz_C = 1$, $Mx_O = 0$, $Fy_O = -\text{mean}(Fy(t))$ and $Fz_O = -m_{WB}*g/\text{mean}(Fz(t))$, where m_{WB} was the subject's mass as measured on precision scales (62.715 kg), $g = -9.80$ ms^{-2}, and mean($Fy(t)$) and mean($Fz(t)$) were the mean antero-posterior and vertical GRF, respectively, over all t within each trial.

Initially, broad linear bound constraints were applied for each design variable as described in Table 3. The bounds were broad in the sense that they were set beyond the error margins that were deemed realistically possible for the force platform used in this research. However, during preliminary testing of the algorithms, it was found that the Fz_O, Fz_C, Mx_O and Mx_C constraints often became active. That is, the optimisation solution would often slide to combinations of the prescribed upper and lower bounds for these design variables. Hence, sensitivity analyses were conducted to determine whether broadly feasible perturbations in any of these design variables, relative to similar perturbations in Fy_C and Fy_O, would result in significant changes to objective function values, and to $COP[y](t)$ and $CM[y]_{IA}(t)$ trajectories.

Table 3. The bound constraints initially applied to the proposed design variables, but later rejected, based on the sensitivity analyses (see Appendix A). Also shown are the initial estimates of the proposed design variables that were used for all ZPZP4U and ZPZP5C optimisations.

	Fy_O (N)	Fz_O (N)	Mx_O (Nm)	Fy_C Fz_C Mx_C
Lower Bound	-mean($Fy(t)$) - 5	$-m_{WB}*g$ - mean($Fz(t)$) - 10	-10	0.98
Initial Estimate	-mean($Fy(t)$)	$-m_{WB}*g$ - mean($Fz(t)$)	0	1.00
Upper Bound	-mean($Fy(t)$) + 5	$-m_{WB}*g$ - mean($Fz(t)$) + 10	10	1.02

Details of the sensitivity analyses are provided in Appendix A. In summary, relative to the changes evoked by feasible perturbations to Fy_O and Fy_C, feasible changes in all of the other design variables resulted in negligible change in the objective function values and the relativity of $COP[y](t)$ and $CM[y]_{IA}(t)$ trajectories. Hence, Fz_O, Fz_C, Mx_O and Mx_C were subsequently held constant at the initial estimate values described in Table 3. When only Fy_O and Fy_C were varied, the Fy_C bound constraint often became active. On this basis, and considering that the sensitivity analysis (Appendix A) also demonstrated negligible change in the objective function along the valley of the Fy_O-Fy_C-objective-function subspace, Fy_C was also held constant at a value of one for all subsequent optimisations.

Preliminary investigations also revealed the need to tighten the Fy_O bound-constraints described in Table 3 to ensure convergence within the feasible region, as defined by the nonlinear inequality constraints of Equations (25) (see

Appendix B). Thenceforth, Fy_O was restricted to values within the central 80% of the measured range of $Fy(t)$ values within each trial:

$$Fy_O < -\text{mean}(Fy(t)) + 0.4[\max(Fy(t)) - \min(Fy(t))], \text{ and}$$
$$Fy_O > -\text{mean}(Fy(t)) - 0.4[\max(Fy(t)) - \min(Fy(t))] \quad (26)$$

Another method based on the 'conventional' ZPZP approach was developed to assess whether allowing calculated $CM[y]_{IA}(t_i)$ and $COP[y](t_i)$ values to vary from each other at each IEP_i by up to 1 mm would improve the ZPZP method. Recognising that minimising Eq. (24) will not produce a perfect zero value, due to measurement and data filtering errors, it was hypothesised that allowing some acceptable tolerance to deviations from perfect coincidence of $CM[y]_{IA}(t_i)$ and $COP[y](t_i)$ values at each IEP_i would enable the minimised objective function value to be lowered further.

- ***ZPZP6C:*** This method was derived from the conventionally applied *ZPZP5C* method. The design variables consisted of *tolerances* (TOL) for each IEP in a given trial. For each IEP_i, $CM[y]_{IA}(t_i)$ was assigned the value of $COP[y](t_i) + TOL_i$, where TOL_i was bound-constrained to what was considered an acceptable range of ± 1 mm for quiet stance applications:

  $$-0.001 < TOL_i < +0.001 \quad (27)$$

  The number of design variables had the potential to vary if the force platform measurement error terms (in particular, Fy_C and Fy_O) were also included as design variables. Hence, the latter were held constant for *ZPZP6C* and the

design variables consisted only of the TOL variables. The *ZPZP6C* approach was applied to each trial twice: once with Fz_C, Fz_O, Fy_C, Fy_O, Mx_C and Mx_O assigned the same values as those pre-set or optimised during the *ZPZP4U* approach to the given trial, and once with the values pre-set or optimised during the *ZPZP5C* approach to the same trial. This allowed direct and valid comparisons between, respectively, the *ZPZP4U* and *ZPZP6C*, and the *ZPZP5C* and *ZPZP6C* optimised objective function results. The objective function for *ZPZP6C* was the same as that shown in Eq. (24). As outlined in the next section, *ZPZP6C* was hypothesised to be the best ZPZP method assessed in this experiment.

A reference table, summarising the different ZPZP methods assessed in this experiment, is presented in Table 4.

All optimisations were programmed in Matlab 6.5.1 (The Mathworks, Inc., Natick, MA., U.S.A.), using the 'fmincon' function. Several option parameters within this function (viz. TolFun, TolCon and TolX) were assigned a value of 0.000001 to ensure the objective function and the design variable solutions were defined to a sufficient level of precision and to ensure constraints were not violated.

Table 4. Summary of all the ZPZP methods assessed in this experiment. Methods with the suffix C denote 'conventional' methods, in which the ZPZP algorithm (see page 17) was applied in the conventional manner across each and every ZPZP interval, as per Zatsiorsky and Duarte (2000). Methods with the suffix U denote 'unconventional' methods, in which the ZPZP algorithm was applied in an unconventional manner once only across the entire interval spanned by the initial and final identified ZPs.

ZPZP Method(s)	**Description**
ZPZP1U, *ZPZP1C*	Essentially the original methodology of Zatsiorsky and Duarte (2000), with the exception that *ZPZP1U* was as described in the caption for unconventional methods. Force platform data was resampled at 40 Hz and low-pass filtered at a cut-off frequency of 8 Hz. ZPs and IEPs were determined by linear interpolation.
ZPZP2U, *ZPZP2C*	As per corresponding *ZPZP1*, but with de-trended $Fy(t)$.
ZPZP3U, *ZPZP3C*	As per corresponding *ZPZP2*, but 1000 Hz, not 40 Hz.
ZPZP4U	Optimisation ZPZP method based on *ZPZP3U*, except $Fy(t)$ values were optimised by the inclusion of a force platform offset error design variable Fy_O, rather than de-trended. Objective function: Eq. (23), page 141.
ZPZP5C	Optimisation ZPZP method based on *ZPZP3C*, except $Fy(t)$ values were optimised by the inclusion of a design variable Fy_O, rather than de-trended. Objective function: Eq. (24), page 143.
ZPZP6C	Optimisation ZPZP method based on *ZPZP5C*, but with the optimised Fy_O value from *ZPZP4U* or *ZPZP5C* used as a constant. The design variables were *tolerances* (TOL) for each IEP. Objective function: Eq. (24(24), page 143.

The effect of different 4th order zero-lag phase Butterworth low-pass filter cut-off frequencies (viz. 6, 8, 10, 12, 14, 16, 18, 20, 25 and 30 Hz) on the *ZPZP4U* and *ZPZP5C* objective function values was also assessed. Six stance trials ranging in duration from 11.0 to 12.3 s were used for the purposes of implementing and assessing the ZPZP methods. Various static head and neck flexion and extension orientations were adopted within each of these trials. In all other respects, a quiet stance posture was maintained.

5.1.2 ZPZP Method Comparisons

The conventional and unconventional applications of the modified ZPZP methods each presented a means by which they could be assessed. The two assessment parameters identified to evaluate the relative merits of the modified ZPZP methods were as follows.

- ***IEP Displacement Parameter (Eq. (23))***: This parameter enabled assessment of methods in which the ZPZP algorithm was applied in the unconventional way (i.e. only one application, between the first and last IEPs, ignoring all intermediate IEPs). Based on the premise used to define method *ZPZP4U*, (see pp. 140 - 141), the computation of Eq. (23), the mean of the absolute differences of all n - 1 intermediate IEP_i pairs of $COP[y](t_i)$ and $CM[y]_{IA}(t_i)$, was used as a measure of the relative performance of *ZPZP1U*, *ZPZP2U*, *ZPZP3U* and *ZPZP4U*. Though not part of the *ZPZP6C* objective function, it was also possible to evaluate Eq. (23) for this approach, and therefore possible to make a comparison between *ZPZP6C* and the unconventional ZPZP approaches. For all the other conventional ZPZP approaches, Eq. (23) would

be zero by design, thus making *IEP Displacement Parameter* inappropriate for those methods.

- ***IEP Velocity Parameter (Eq. (24))***: The second parameter enabled assessment of methods in which the ZPZP algorithm was applied in the conventional way (i.e. application across each and every adjacent pair of IEPs within the movement sequence). *IEP Velocity Parameter* was based on the same premise that was used to define *ZPZP5C* (see pp. 142 - 143). Eq. (24), the mean of the absolute differences of all n - 1 intermediate IEP pairs of $V_0(t_i)$ and $CM'[y]_{IA}(t_i)$, was computed and used as a measure of the relative performance of *ZPZP1C*, *ZPZP2C*, *ZPZP3C, ZPZP5C* and *ZPZP6C*. The *IEP Velocity Parameter* was not applied to the unconventional ZPZP methods because, for these methods, Eq. (24) was zero by design.

5.1.3 Hypotheses and Statistical Approaches

The following hypotheses for quiet stance trials were assessed:

Hypothesis 1: The respective unconventional ZPZP methods produce significantly different *IEP Displacement Parameter* values.

Hypothesis 2: The respective conventional ZPZP methods produce significantly different *IEP Velocity Parameter* values.

Hypothesis 3: *ZPZP6C* produces significantly lower *IEP Velocity Parameter* values than *ZPZP5C.*

Hypothesis 4: *ZPZP6C* produces significantly lower *IEP Displacement Parameter* values than *ZPZP4U.*

Hypothesis 5: The application of different cut-off frequencies to the force platform data (viz. 6, 8, 10, 12, 14, 16, 18, 20, 25 and 30 Hz) prior to executing the *ZPZP4U* method produces significantly different *IEP Displacement Parameter* values.

Hypothesis 6: The application of different cut-off frequencies to the force platform data (viz. 6, 8, 10, 12, 14, 16, 18, 20, 25 and 30 Hz) prior to executing the *ZPZP5C* method produces significantly different *IEP Velocity Parameter* values.

Hypotheses 1, 2, 5 and 6 were assessed using the two-tailed Friedman's one-way repeated-measures rank-order ANOVA tests[14]. For each test, *p*-levels were determined and reported; the research hypotheses were considered to be supported if *p* was less than 0.05. If Hypotheses 1 or 2 were found to be supported, then plots showing the median and range of the *IEP Displacement Parameter* values (for Hypothesis 1) or *IEP Velocity Parameter* values (for Hypothesis 1) produced by each method were plotted to enable an assessment of which method or methods produced the best results. Because it was hypothesised *a priori* that *ZPZP6C* would produce the best overall results of any ZPZP optimisation method,

[14] A parametric repeated-measures ANOVA approach was considered inappropriate, due to the small sample size of only six trials and the possibility of a non-normally distributed population.

planned Wilcoxon matched pairs comparisons (two-tailed) were used to assess Hypotheses 3 and 4. These hypotheses were deemed to be supported if p was less than 0.05, which was considered justified considering that these tests were planned comparisons and that a relatively conservative nonparametric test was being applied to continuous data. Even more conservatively, two-tailed tests were applied to test what were directional hypotheses. Statistica 7.1 (Stat Soft, Inc., Tulsa, OK., U.S.A.) was used for the aforementioned statistical analyses. Qualitative assessment of the performance of all methods was also conducted by examining the plots of $COP[y](t)$, $CM[y]_{IA}(t)$ and $CM'[y]_{IA}(t)$ that resulted from the implementation of each method.

5.2 Results

Table 5 summarises the results of the two Friedman rank-order ANOVA tests that were conducted to assess Hypotheses 1 and 2. It shows that these hypotheses were strongly supported, with *p* values well below the 0.05 level. Plots showing the median and range of the minimised objective function values are depicted for the unconventional and conventional ZPZP methods in Figs. 16 and 17, respectively.

Table 5. Results of the Friedman rank-order ANOVA tests (N = 6) used to assess Hypotheses 1 and 2.

Hypothesis	**Methods Assessed**	**df**	**ANOVA χ^2**	***p***
1	*ZPZP1U*, *ZPZP2U*, *ZPZP3U*, *ZPZP4U*	3	13.4	0.00385
2	*ZPZP1C*, *ZPZP2C*, *ZPZP3C*, *ZPZP5C*, *ZPZP6C*	4	20.8	0.00035

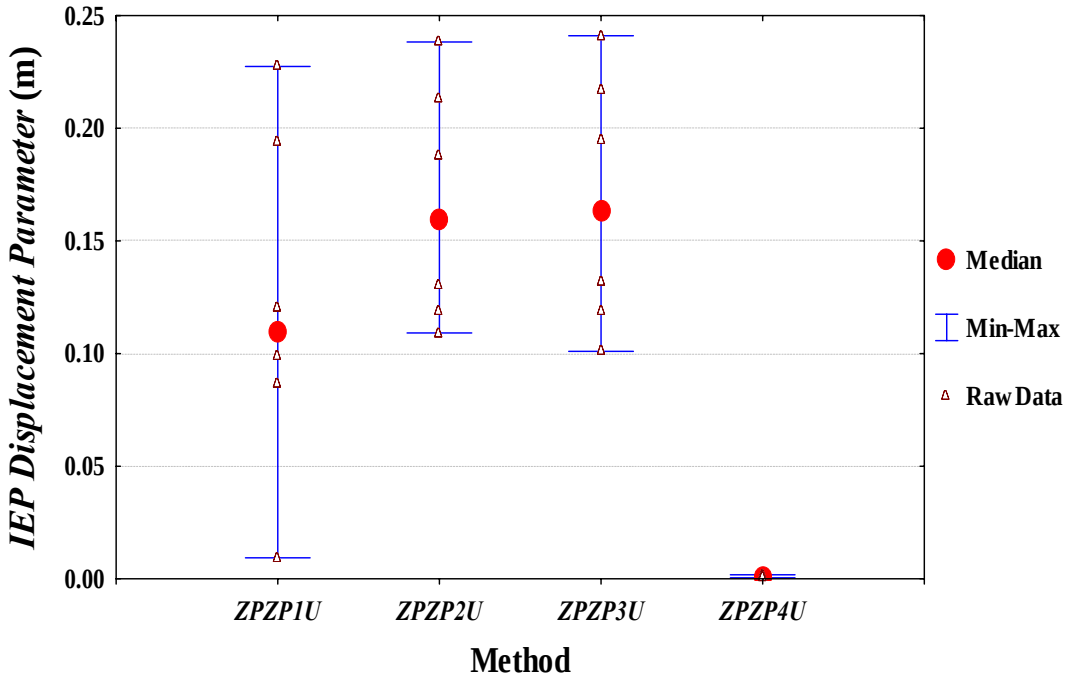

Figure 16. Range plot showing the median, range and raw data points of the IEP Displacement Parameter values across the six trials assessed in this research, for each of the unconventional ZPZP methods (ANOVA χ^2 [df = 3, N = 6] = 13.4, p = 0.00385).

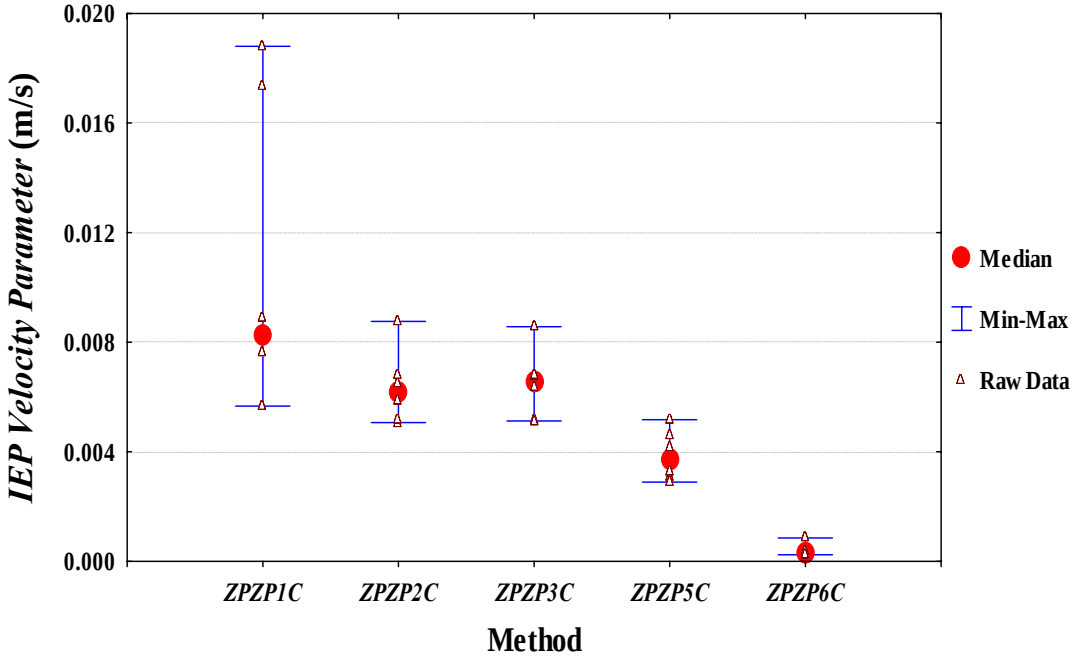

Figure 17. Range plot showing the median, range and raw data points of the IEP Velocity Parameter values across the six trials assessed in this research, for each of the conventional ZPZP methods (ANOVA χ^2 [df = 4, N = 6] = 20.8, p = 0.00035).

With respect to the unconventional ZPZP methods, the range plot in Fig. 16 clearly shows the superiority of the ZPZP optimisation approach (*ZPZP4U*) over all the other unconventional ZPZP methods. *ZPZP1U*, *ZPZPU2* and *ZPZP3U* resulted in median *IEP Displacement Parameter* values (Eq. (23)), across all six trials, of at least 0.11 m. The clearly unrealistic nature of such high values for quiet stance trials is supported by Figs. 18, 19 and 20 (methods *ZPZP1U*, *ZPZP2U* and *ZPZP3U*, respectively), which depict the plots of one indicative trial (trial '4463') of predicted $CM[y]_{IA}(t)$ lying well beyond the range of $COP[y](t)$. These plots demonstrate that the discrepancy between $CM[y]_{IA}(t)$ and $COP[y](t)$ at IEPs was as much as 0.25 m in the middle of these time series. The square markers in these figures indicate the IEPs at which the $CM[y]_{IA}(t)$ and $COP[y](t)$ plots are predicted to intersect.

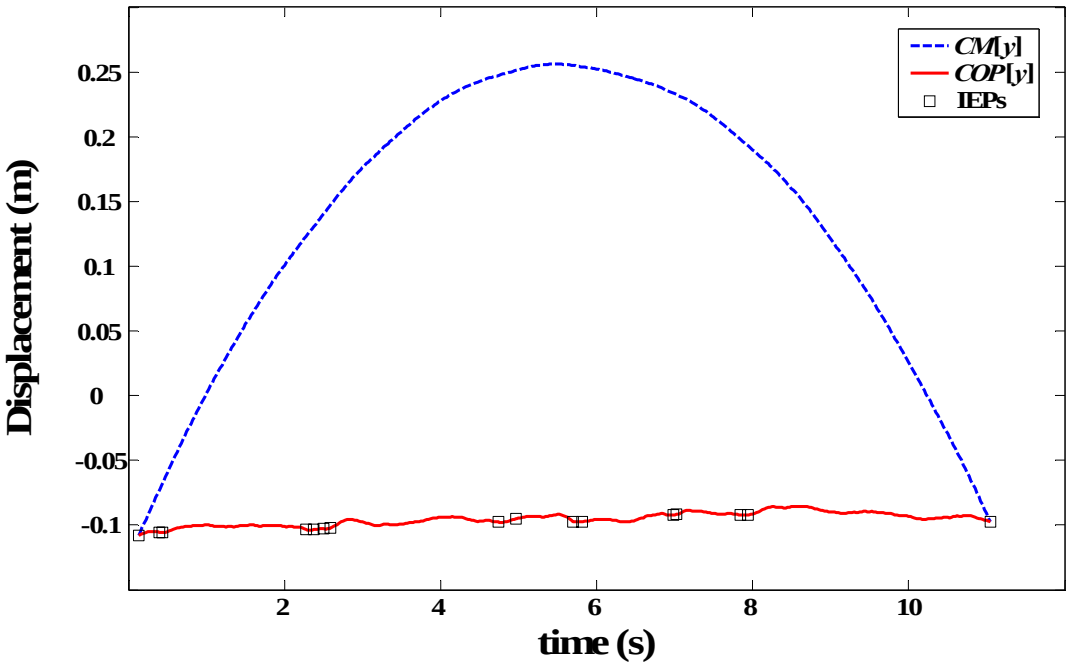

Figure 18. Plot of $CM[y]_{IA}(t)$ (blue dashed line) and $COP[y](t)$ (red solid line) with IEPs (squares), resulting from the ZPZP1U method (trial '4463'), indicating unrealistic $CM[y]_{IA}(t)$ estimates.

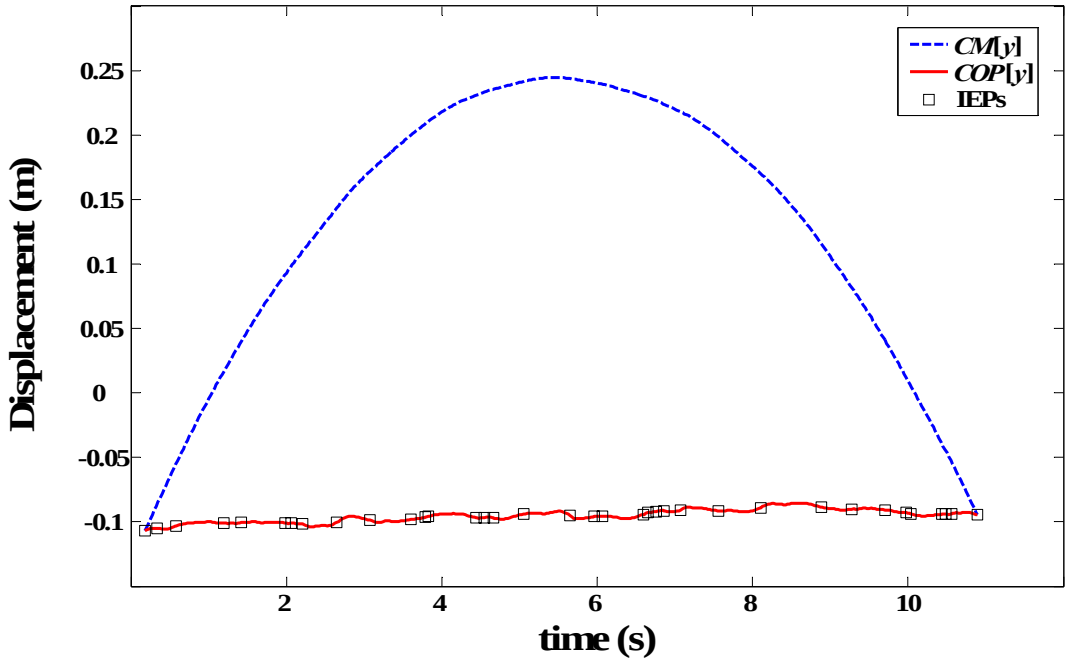

Figure 19. Plot of $CM[y]_{IA}(t)$ and $COP[y](t)$ with IEPs, resulting from the application of method ZPZP2U, again indicating unrealistic $CM[y]_{IA}(t)$ estimates. For this trial ('4463'), the inclusion of de-trended Fy in the ZPZP2U method has produced a greater number of IEPs, but negligible improvement towards what, in theory, should be the co-location of $CM[y]_{IA}(t)$ and $COP[y](t)$ at the IEPs.

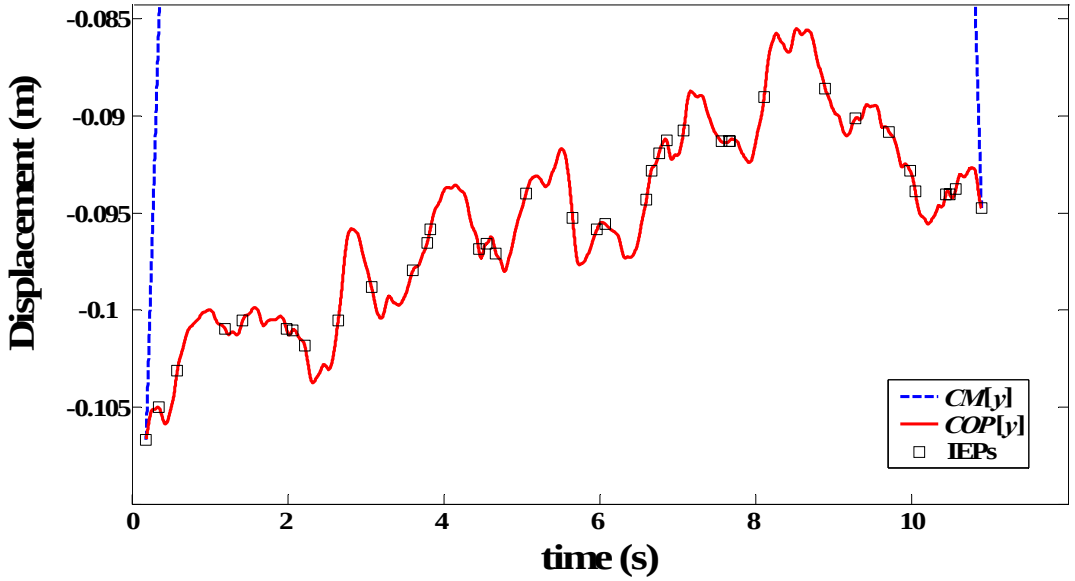

Figure 20. Plot of $CM[y]_{IA}(t)$ and $COP[y](t)$ with IEPs, resulting from method ZPZP3U (trial '4463'). The use of data sampled at 1000 Hz in ZPZP3U, as opposed to 40 Hz in ZPZP2U, made no discernable improvement (compared to Fig. 19). Hence, the scale of this plot was matched to that of the ZPZP4U plot in Fig. 22, thus permitting a more meaningful comparison of these two figures.

Even the 'best' case result for method *ZPZP1U* only occurred because so few IEPs existed in this case that the ZPZP interval was only defined over the 5.85 to 8.65 s interval of a 10.975 s trial (trial '4461'), which confined $CM[y]_{IA}(t)$ close enough to the vicinity of $COP[y](t)$ to produce an *IEP Displacement Parameter* value of only 0.009 m (Fig. 21). Note, this value is still very high compared with the values produced for all cases by *ZPZP4U* and Fig. 21 clearly shows the unrealistic nature of the $CM[y]_{IA}(t)$ trajectory relative to the $COP[y](t)$ plot.

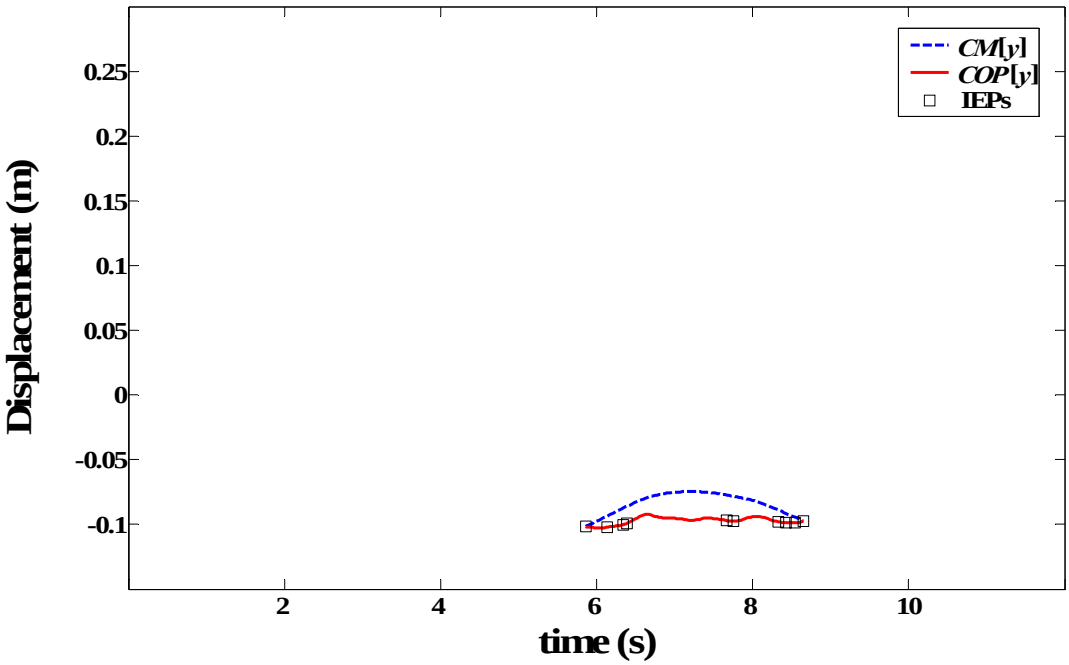

Figure 21. Plot of $CM[y]_{IA}(t)$ and $COP[y](t)$ with IEPs, resulting from the ZPZP1U method (trial '4461'), indicating better but still unrealistic $CM[y]_{IA}(t)$ estimates and an unrealistically short interval (t = 5.85 to 8.65 s) spanning the first and last IEPs.

ZPZP4U produced a median *IEP Displacement Parameter* (Eq. (24)) value of less than one millimetre. Fig. 22 shows the much more realistic $CM[y]_{IA}(t)$ and $COP[y](t)$ plots, for the same trial as the preceding figures, resulting from the application of *ZPZP4U*.

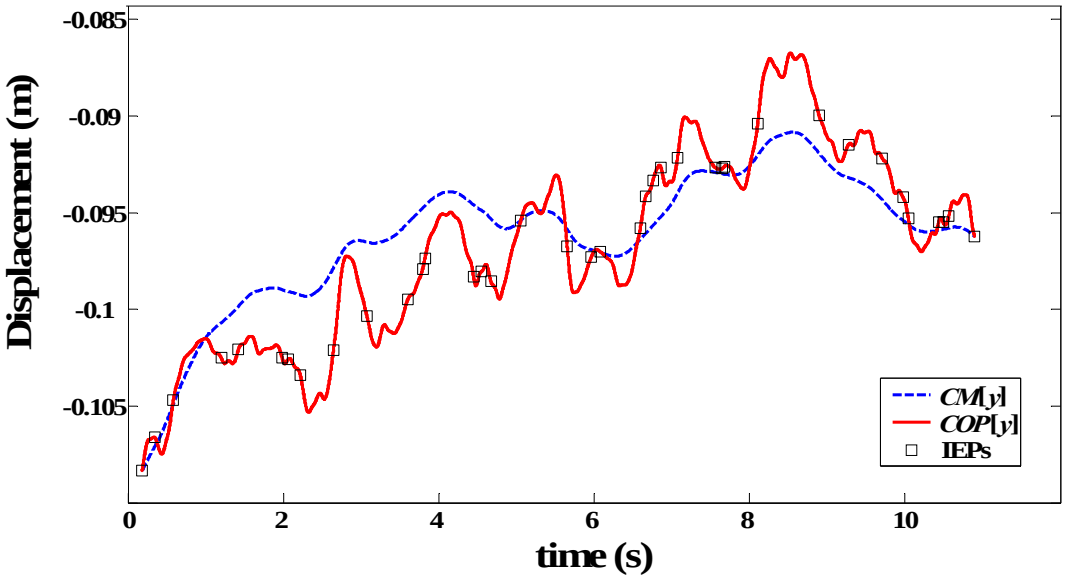

Figure 22. Plot of $CM[y]_{IA}(t)$ and $COP[y](t)$ with IEPs, resulting from method ZPZP4U (trial '4463'), showing more realistic, yet still somewhat unrealistic $CM[y]_{IA}(t)$ estimates, particularly during the 1 to 6 second period.

However, the $CM[y]_{IA}(t)$ plot still appears to be unrealistic, particularly where the $CM[y]_{IA}(t)$ excursions remained 'above' $COP[y](t)$ for an extended period of time during the 1 to 6 s period[15]. Generally though, *ZPZP4U* produced more realistic plots for the other five trials, as exemplified by Fig. 23. Fig. 24 shows the CM velocity plot, $CM'[y]_{IA}(t_i)$, for one trial subjected to the *ZPZP4U* method. As mandated by all the unconventional ZPZP approaches, the velocity function is smooth and continuous.

[15] Recall that $COP[y](t)$ must keep moving anteriorly and posteriorly with respect to $CM[y]_{IA}(t)$, to ensure maintenance of balance during quiet stance (Winter et al., 1996a).

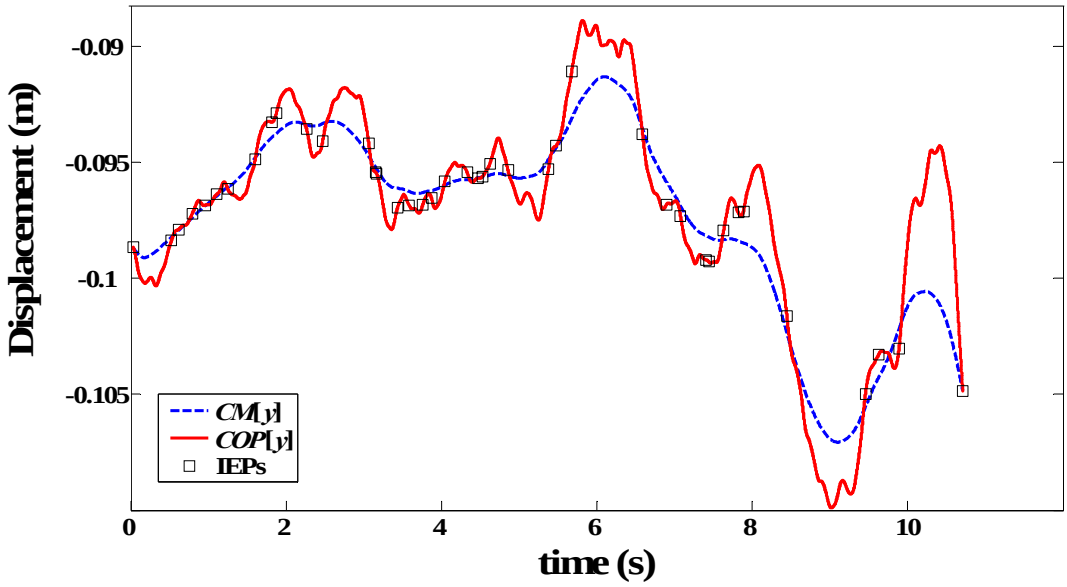

Figure 23. A more realistic plot of CM[y]$_{IA}$(t) relative to COP[y](t), resulting from the application of method ZPZP4U (trial '4462'). Note, relative to Fig. 22, the more inclusive nature of CM[y]$_{IA}$(t) within the surrounding COP[y](t) trajectory, and the closer approximation of CM[y]$_{IA}$(t) to the IEPs.

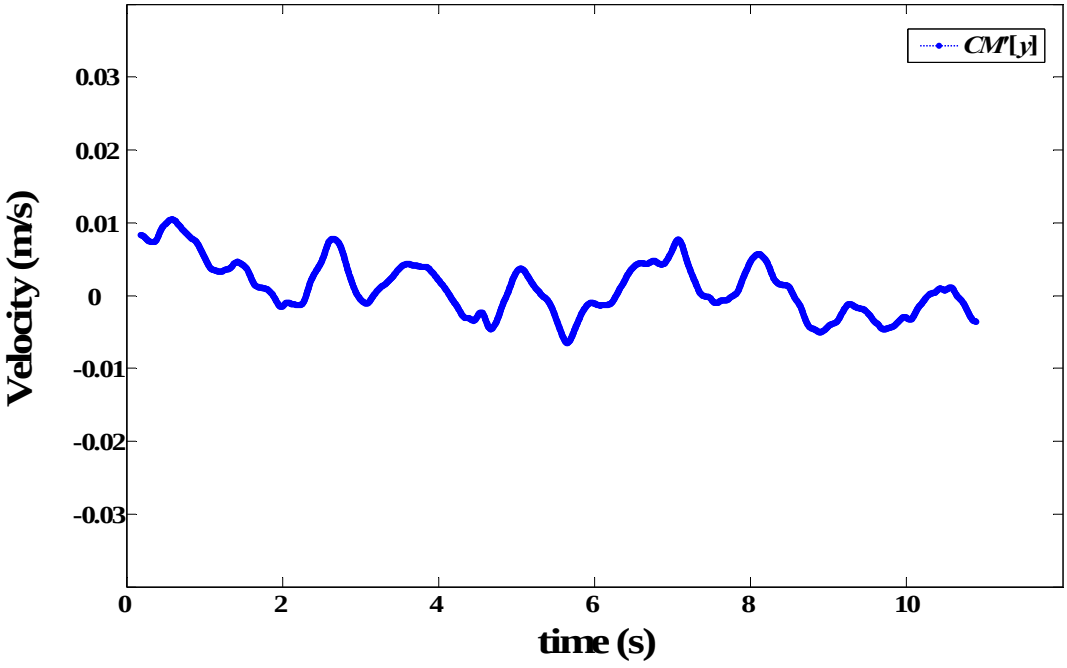

Figure 24. Plot of CM'[y]$_{IA}$(t) for trial '4463' (method ZPZP4U). As for all unconventional ZPZP methods, the velocity function is smooth and continuous. The values seem realistic for quiet stance, all being within a range of ±0.011 m/s.

With respect to the conventional ZPZP methods, the range plot in Fig. 17 (page 154) shows the superiority of the optimisation approaches *ZPZP5C* and *ZPZP6C* over the other conventional ZPZP methods. In particular, *ZPZP6C* produced median minimised objective function values (i.e. *IEP Velocity Parameters,* Eq. (23)), across all six trials, of less than 0.0004 ms^{-1}. *ZPZP1C* produced a much greater range of *IEP Velocity Parameter* values across the six trials, and *ZPZP6C* produced a much smaller range, compared with the ranges produced by *ZPZP2C*, *ZPZP3C* and *ZPZP5C*. Figs. 25 and 26 show the unrealistic results of applying *ZPZP1C* to a typical trial. Fig. 25 shows 'humps' in $CM[y]_{IA}(t)$ trajectory that stray well beyond the confines of the $COP[y](t)$ trajectory. The CM velocity plot, $CM'[y]_{IA}(t)$, shown in Fig. 26 is clearly not continuous at the IEPs, with discrepancies of up to 0.04 ms^{-1}. *ZPZP2C* improved $CM[y]_{IA}(t)$ and $COP[y](t)$ trajectories substantially, as depicted for one trial in Fig. 27, though some sharp turning points are noticeable at the IEPs. The presence of sharp turning points is confirmed by the $CM'[y]_{IA}(t)$ velocity discontinuities shown in Fig. 28, although they have decreased, relative to *ZPZP1C*, to less than 0.03 ms^{-1}. *ZPZP3C* produced essentially equivalent results to *ZPZP2C*, with no visually discernable differences between their respective displacement and velocity plots. Indeed, *IEP Velocity Parameter* ranges across all six trials, for methods *ZPZP2C* and *ZPZP3C*, were 0.0051 to 0.0088 ms^{-1} and 0.0051 to 0.0086 ms^{-1}, respectively.

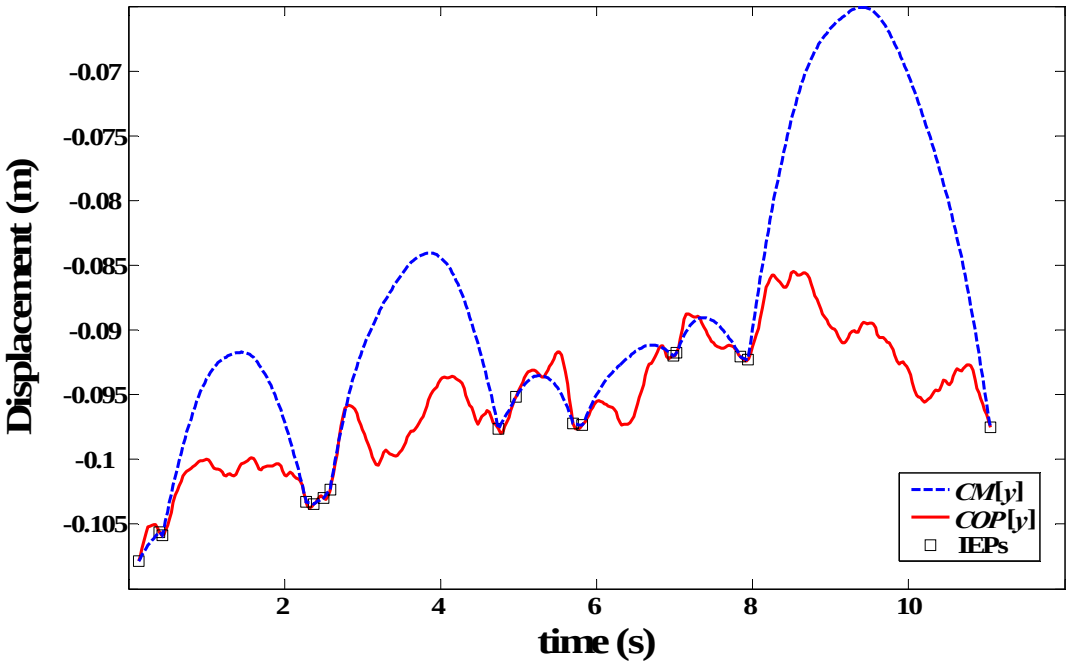

Figure 25. Plot of $CM[y]_{IA}(t)$ and $COP[y](t)$ with IEPs resulting from the application of method ZPZP1C (trial '4463'), indicating unrealistic $CM[y]_{IA}(t)$ 'humps'.

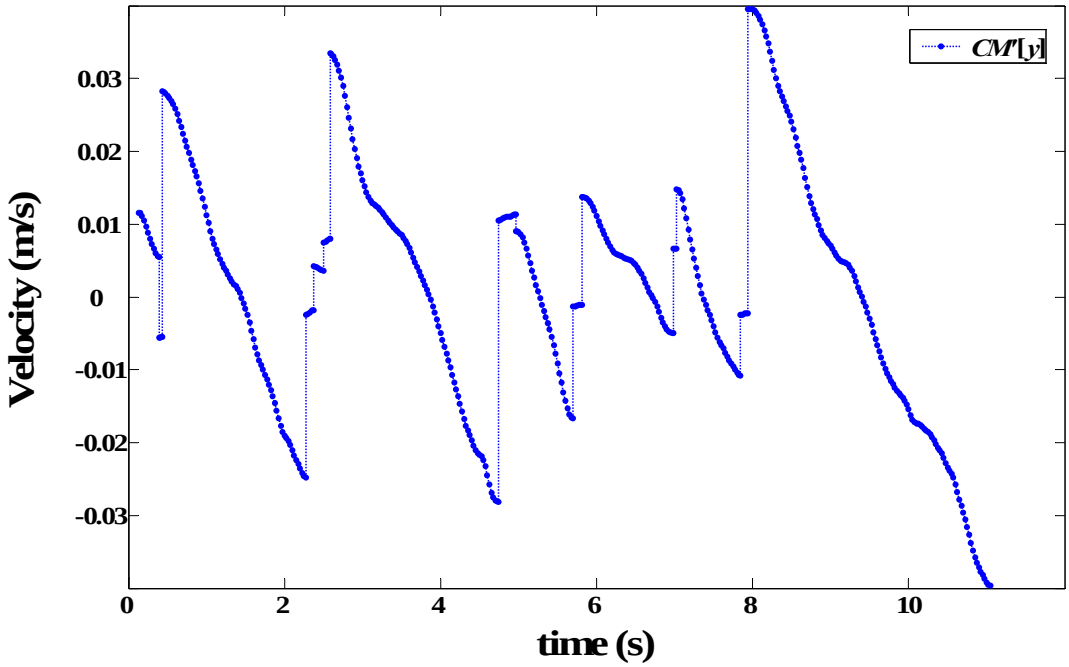

Figure 26. Plot of $CM'[y]_{IA}(t)$ for trial '4463' (method ZPZP1C). The velocity function is not continuous at the IEPs.

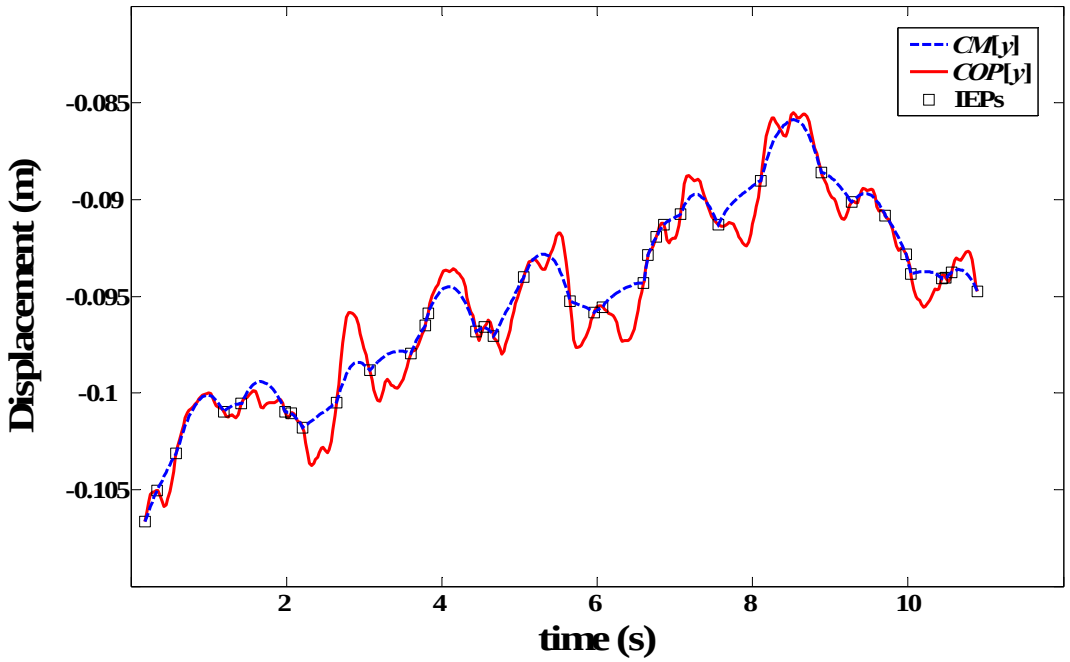

Figure 27. Plot of $CM[y]_{IA}(t)$ and $COP[y](t)$ with IEPs resulting from the ZPZP2C method. For this trial ('4463'), the inclusion of de-trended Fy in the ZPZP2C method has produced more IEPs and noticeable improvement in $CM[y]_{IA}(t)$ trajectory, although sharp turning points are apparent at some IEPs.

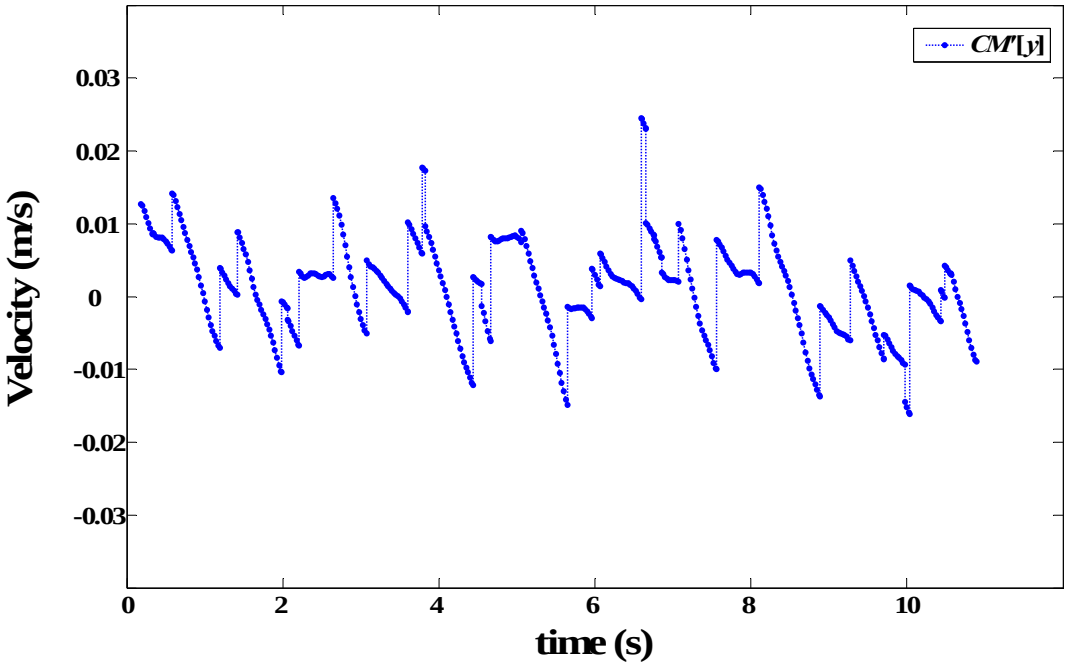

Figure 28. Plot of $CM'[y]_{IA}(t)$ for trial '4463' (method ZPZP2C). The velocity function was not continuous at the IEPs and it often had negative slope for several consecutive ZPZP intervals. The ZPZP3C method produced an essentially equivalent plot.

ZPZP5C produced a lower median minimised objective function value across all trials of 0.0037 ms^{-1}. This method produced relatively smooth $CM[y]_{IA}(t)$ trajectories, as evidenced by Fig. 29, although discontinuities in the first derivative are still visible in Fig. 30. However, $CM'[y]_{IA}(t)$ plots resultant from method *ZPZP5C* produced much smaller discrepancies at the IEPs than those produced by *ZPZP2C* and *ZPZP3C*.

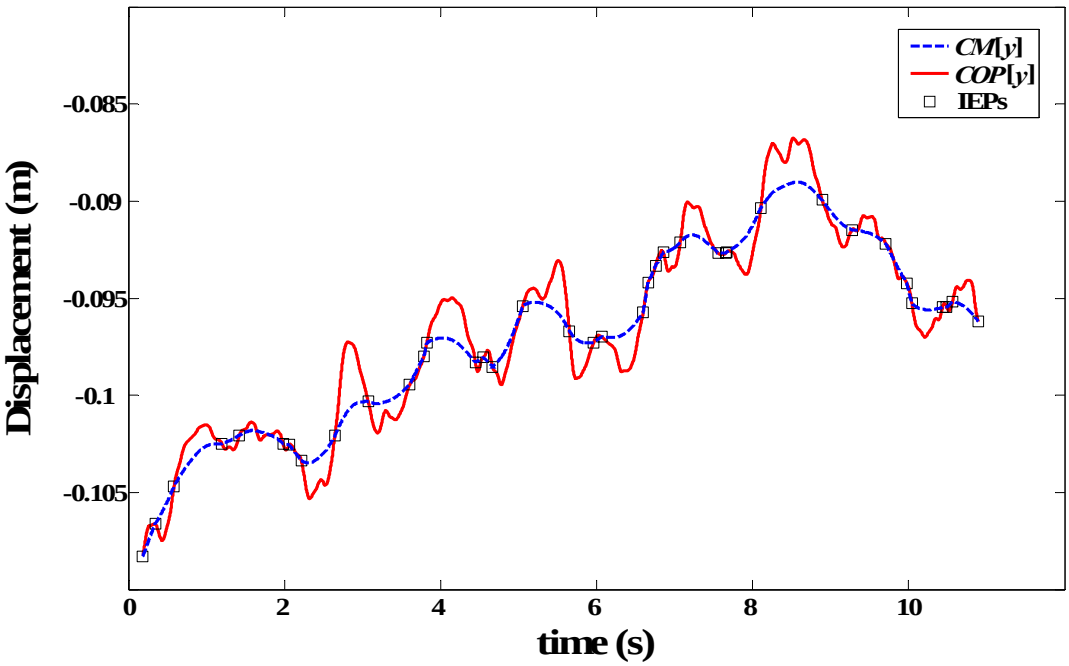

Figure 29. Plot of $CM[y]_{IA}(t)$ and $COP[y](t)$ with IEPs resulting from the ZPZP5C method (trial '4463'). ZPZP5C produced noticeable improvement in the smoothness of the $CM[y]_{IA}(t)$ trajectory, relative to ZPZP2C.

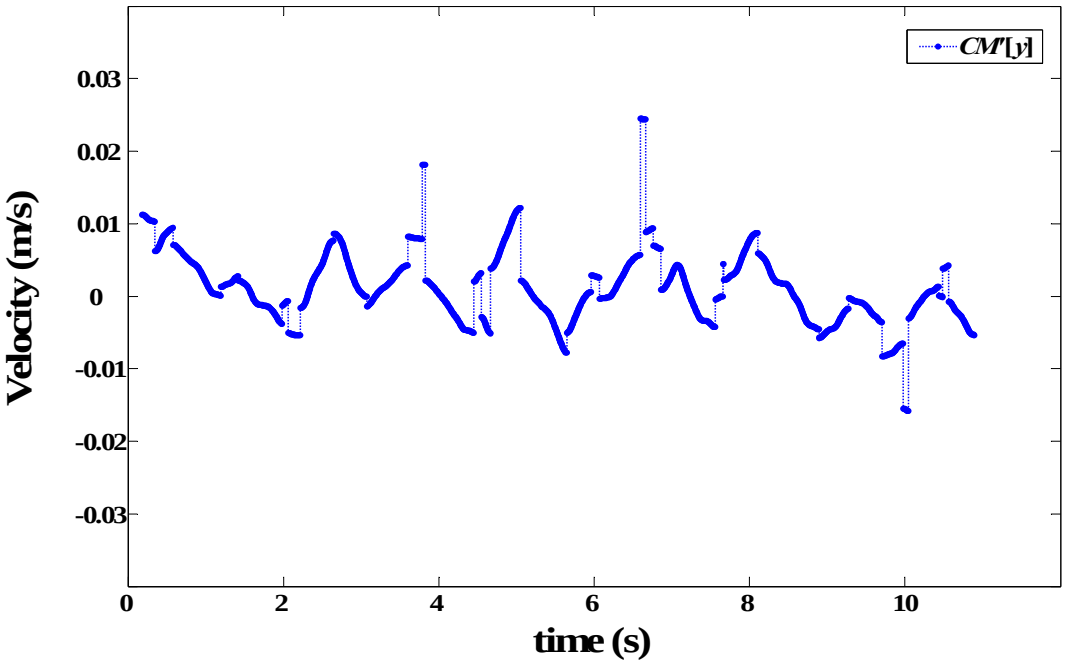

Figure 30. Plot of $CM'[y]_{IA}(t)$ for trial '4463' (method ZPZP5C). The velocity function is not continuous at the IEPs, but the discrepancies are less than those for methods ZPZP1C to ZPZP3C. Note also that the slope of $CM'[y]_{IA}(t)$ alternates between positive and negative from ZPZP interval to ZPZP interval.

ZPZP6C produced $CM[y]_{IA}(t)$ trajectories that were even smoother than those produced by *ZPZP5C*, albeit at the expense of $CM[y]_{IA}(t_i)$ and $COP[y](t_i)$ no longer coinciding precisely at each IEP_i (e.g. Fig. 31). However, by definition, $CM[y]_{IA}(t_i)$-$COP[y](t_i)$ discrepancies at each IEP_i did not exceed an absolute value of one millimetre. Introducing this tolerance reduced the median minimised objective function value across all trials to 0.0003 ms^{-1}. Of the six trials to which the *ZPZP6C* method was applied, bound constraints (Eq. (27)) only became active in two trials, and only twice in each of these two trials, out of a possible 38 and 39 bound constraints, respectively. Fig. 32 depicts the plot of $CM'[y]_{IA}(t)$ for one representative trial, showing few discontinuities that were discernable to the naked eye when the plot was drawn to the same scale as previous figures.

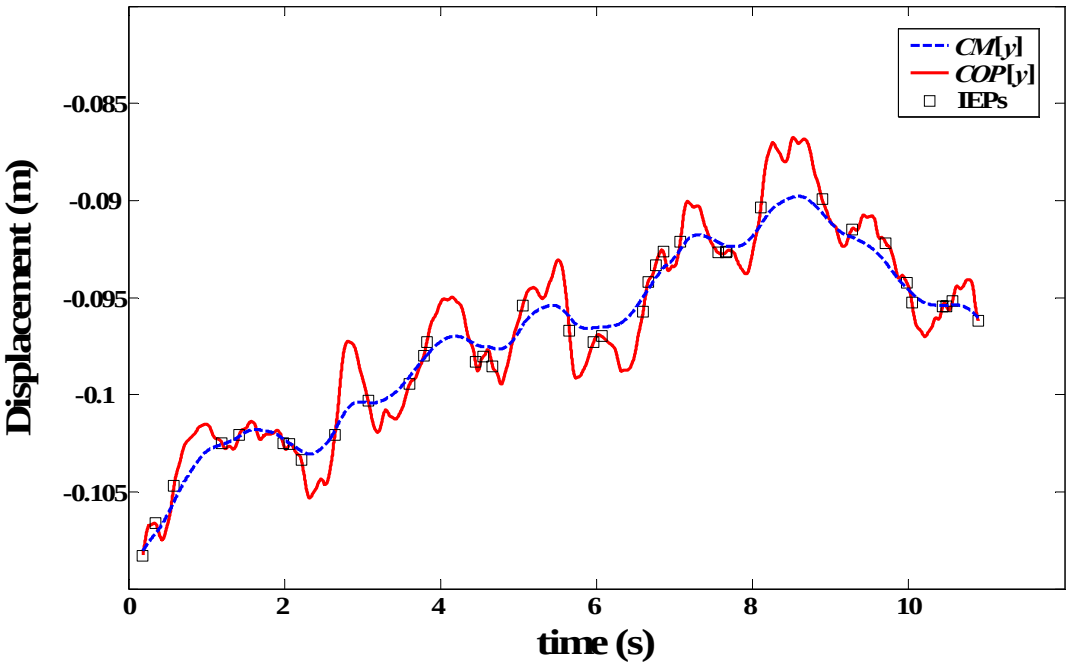

Figure 31. Plot of $CM[y]_{IA}(t)$ and $COP[y](t)$ with IEPs resulting from the ZPZP6C method (trial '4463'), which produced a noticeable improvement in the smoothness of the $CM[y]_{IA}(t)$ trajectory, relative to the ZPZP5C method.

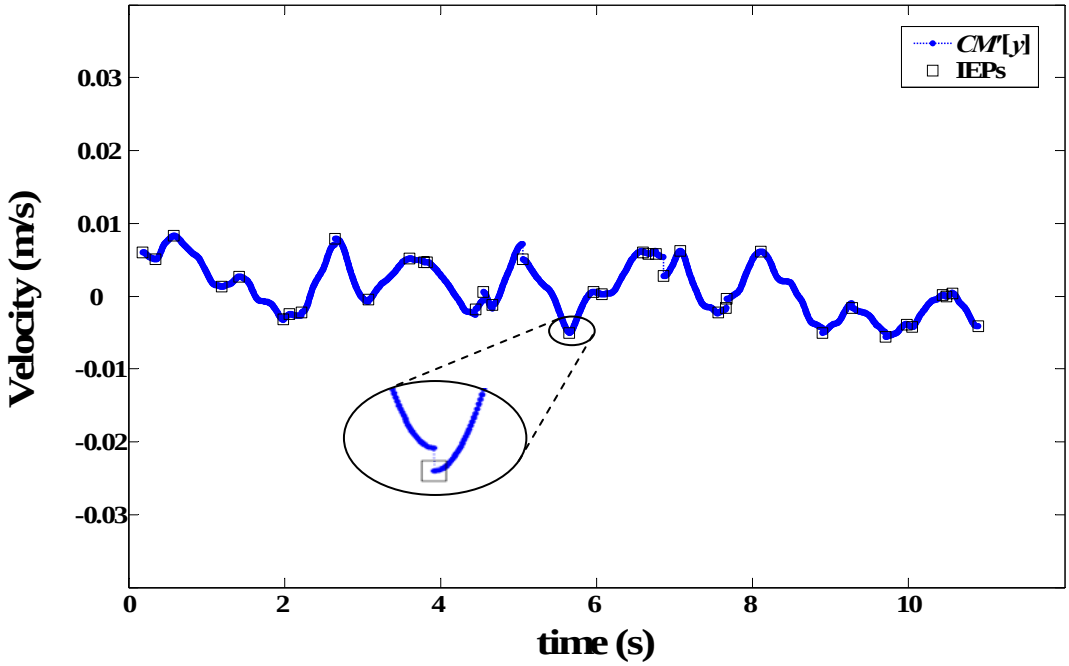

Figure 32. Plot of $CM'[y]_{IA}(t)$, with IEPs marked, for trial '4463' (method ZPZP6C). The inset magnification shows what would otherwise appear to be a continuous function at the given IEP. However, a small discrepancy still exists (0.00008 m/s). Although the velocity function is not continuous at the IEPs, the discrepancies are less than those for all other conventional ZPZP methods.

The results of the planned comparisons between *ZPZP5C* and *ZPZP6C*, and between *ZPZP4U* and *ZPZP6C*, are summarised in Table 6. Even using conservative nonparametric tests, the evidence supports Hypotheses 3 and 4. The range plots in Figs. 17 and 33 also show how *ZPZP6C* produces, respectively, significantly lower *IEP Velocity Parameter* values than *ZPZP5C*, and significantly lower *IEP Displacement Parameter* values than *ZPZP4U*. *ZPZP6C* also produced a smaller range of scores compared with each comparison method.

Table 6. Results of the Wilcoxon matched pairs tests (N = 6) used to assess Hypotheses 3 and 4.

Hypothesis	Methods Assessed	T	Z	*p*
3	*ZPZP5C*, *ZPZP6C*	0	2.201	0.028
4	*ZPZP4C*, *ZPZP6U*	0	2.201	0.028

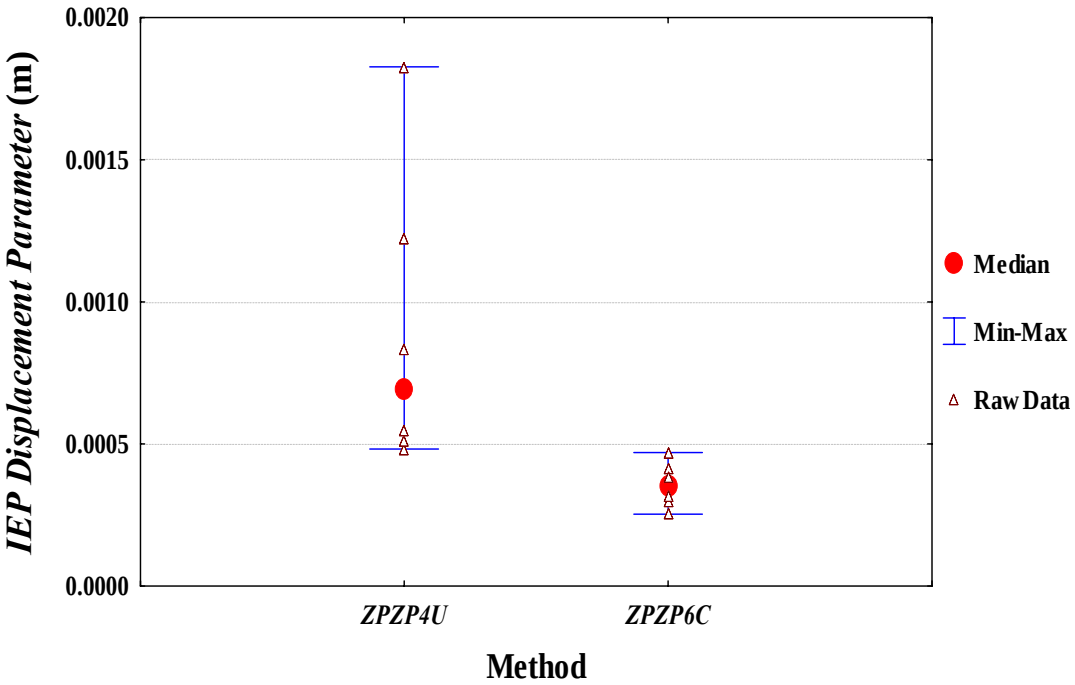

Figure 33. Range plot showing the median, range and raw data points of the IEP Displacement Parameter values across the six trials assessed in this research, for unconventional method ZPZP4U and conventional method ZPZP6C.

For all assessed trials, when the initial estimate of -mean(Fy) was adopted for the design variable Fy_O, both *ZPZP4U* and *ZPZP5C* converged to the local minimum within the feasible domain of their respective objective functions. The Fy_O bound constraint Eq. (26) never became active, even without the application of nonlinear constraint Eqs. (25). Whether or not nonlinear constraint Eqs. (25) were applied, Fy_O and the objective function solutions were the same to a precision of three and six decimal places, respectively. Hence, nonlinear constraint Eqs. (26) were never necessary for the trials optimised in this research.

Across the six trials and both the *ZPZP4U* and *ZPZP5C* optimisation methods, the optimised value of Fy_O ranged between 0.65 and 1.76 N. This range of values was deemed realistic for the force platform used in this research[16].

Table 7 summarises the results of the two Friedman rank-order ANOVA tests that were conducted to assess Hypotheses 5 and 6. It shows that only Hypothesis 6 was supported (p = 0.00001). Fig. 34 shows the plot of the median, range and raw data points of the minimised objective function values for the *ZPZP5C* method, when the supplied data were filtered at various cut-off frequencies.

[16] When a 633.75 N dead weight was placed in 26 different locations spread across the surface of the force platform, the Fy_O values that produced de-trended Fy signals averaged 0.65 N with a standard deviation of 0.95 N. Hence, the mean ± 3SD range of Fy_O values was -2.20 to 3.50 N.

Table 7. Results of the Friedman rank-order ANOVA tests (N = 6) used to assess Hypotheses 5 and 6.

Hypothesis	Cut-off Frequencies Assessed (Hz)	Method Used	df	ANOVA χ^2	*p*
5	6, 8, 10, 12, 14, 16, 18, 20, 25, 30	*ZPZP4U*	9	9.7	0.37912
6	6, 8, 10, 12, 14, 16, 18, 20, 25, 30	*ZPZP5C*	9	40.7	0.00001

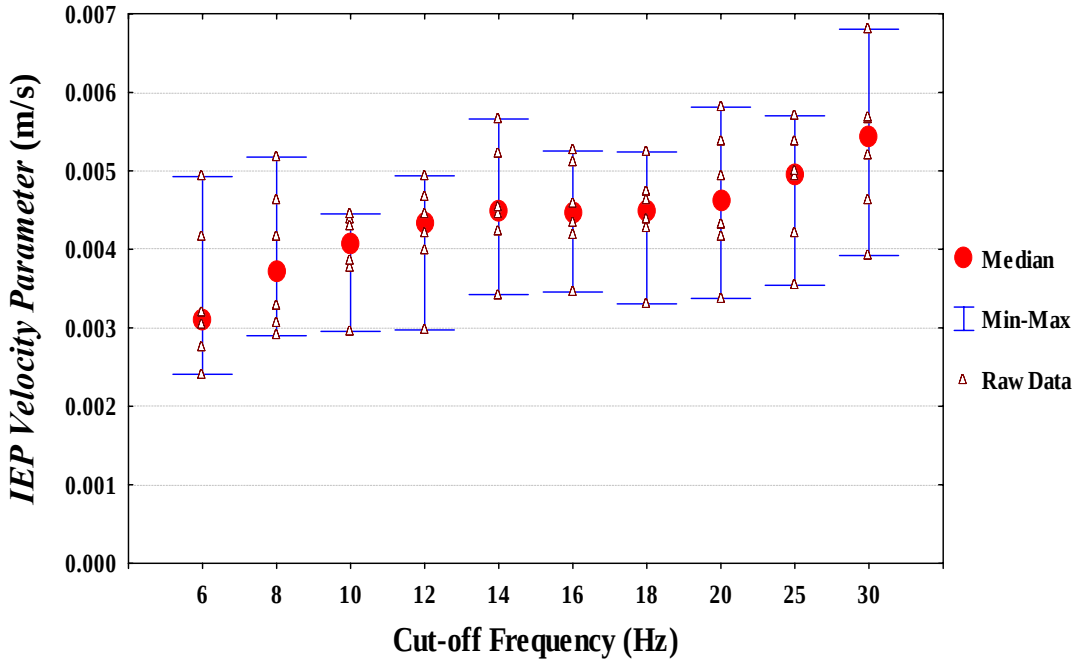

Figure 34. Range plot showing the median, range and raw data points of the IEP Velocity Parameter values for the ZPZP5C method, across the six trials assessed in this research, that resulted when the supplied data were smoothed at various cut-off frequencies (ANOVA χ^2 [df = 9, N = 6] = 40.7, p = 0.00001).

The reduction in cut-off frequency was also observed to decrease the number of identified IEPs. In particular, the number of zero-crossings (up to five) closely nearby each other (within 0.1 s ranges) were reduced with reductions in the

applied cut-off frequency and a reduction in the occurrence of jagged turning points in the $CM[y]_{IA}(t)$ plots was also observed (e.g. compare Figs. 35 and 36).

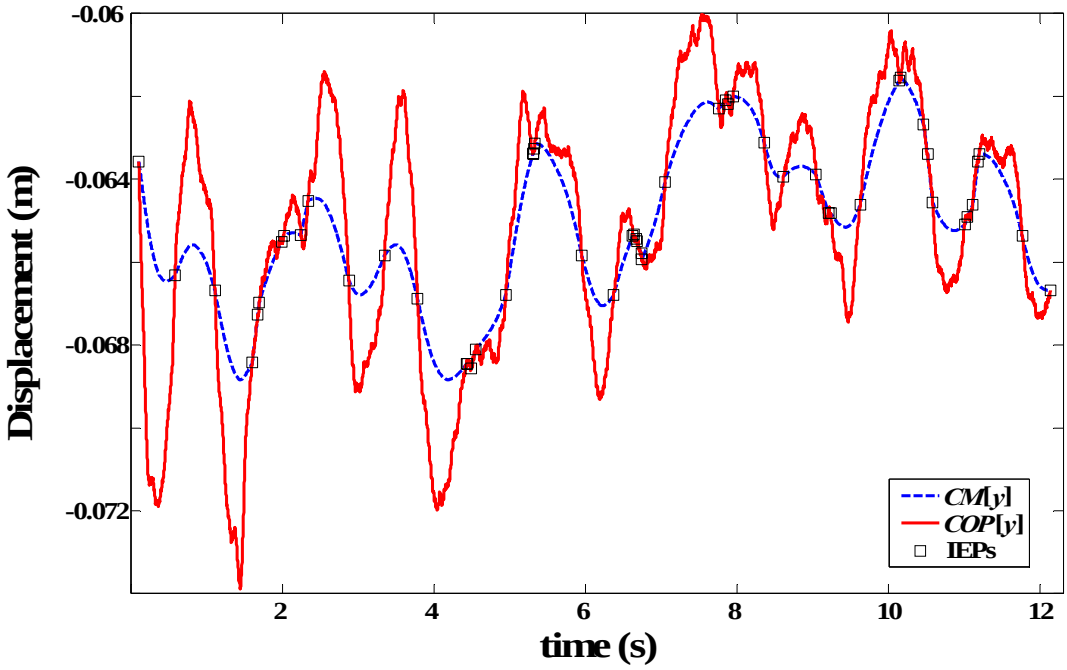

Figure 35. Plot of $CM[y]_{IA}(t)$ and $COP[y](t)$ with IEPs resulting from the ZPZP5C method (trial '4466') for force data low-pass filtered at 30 Hz.

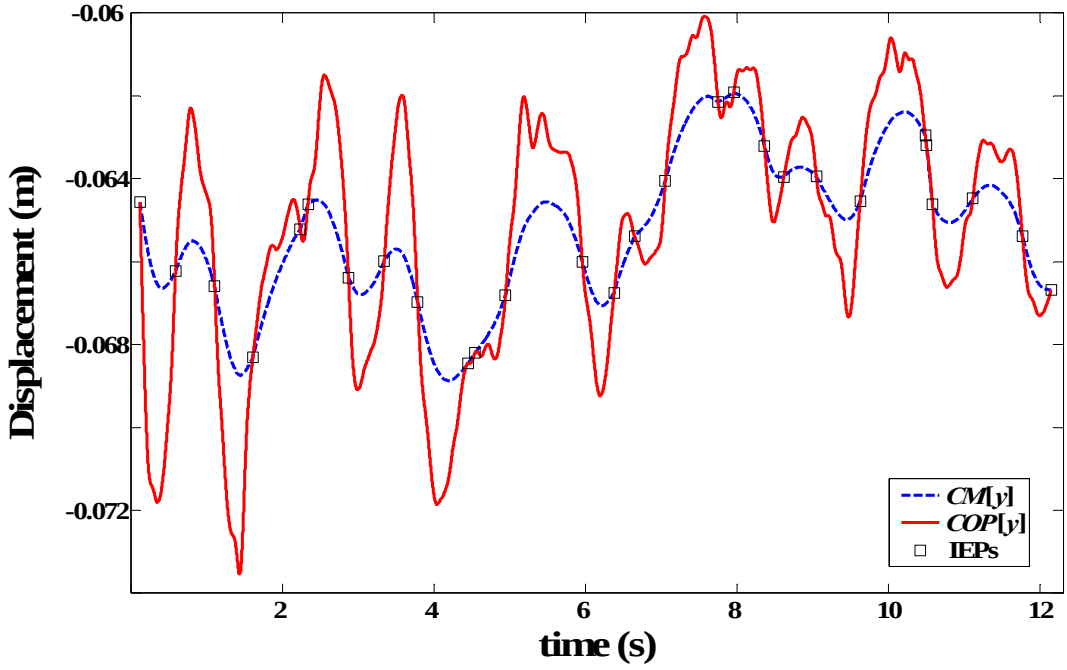

Figure 36. Plot of $CM[y]_{IA}(t)$ and $COP[y](t)$ with IEPs resulting from the ZPZP5C method (trial '4466') for force data low-pass filtered at 6 Hz.

5.3 Discussion

In this study, the performance of the ZPZP method of Zatsiorsky and Duarte (2000) was compared with several other conventional and unconventional derivations of this method, including optimisation approaches. This section explores the findings of the comparisons made between various methods. Firstly, the relative merits of the unconventional methods are discussed (section 5.3.1), followed by a similar discussion regarding the conventional methods (section 5.3.2). Then the effects of applying different sampling rates on the ZPZP methods are considered (section 5.3.3). This is followed by an appraisal of the different approaches for estimating the antero-posterior GRF offset error, Fy_O, covering the de-trended *Fy* and optimisation techniques (section 5.3.4). Next, the effects of applying different low-pass filter cut-off frequencies to the ZPZP methods are explored (section 5.3.5). Finally the theoretical bases, assumptions and relative performance of the unconventional and conventional ZPZP approaches are summarised (section 5.3.6) and the most promising method is identified, with suggestions for future improvements (section 5.3.7). The performance of the ZPZP methods developed in this study is also considered in the context of other CM kinematics determination methods commonly applied to quiet stance activities, and future research requirements are identified that will enable more objective comparisons of all such methods.

5.3.1 Unconventional ZPZP Methods

Evidence was found to strongly support Hypothesis 1; that is, significantly different *IEP Displacement Parameter* values were produced by different

unconventional ZPZP methods. Inspection of the range plot in Fig. 16 (page 154) supports the notion that the optimisation-based *ZPZP4U* method was superior to the other three unconventional ZPZP methods in producing not only much lower *IEP Displacement Parameter* values (in the case of *ZPZP4U*, minimised objective function values), but also a much smaller range in these values across the six assessed trials. All but one of the 18 cases for methods *ZPZP1U*, *ZPZP2U* and *ZPZP3U* resulted in IEP Displacement Parameter values of at least 0.086 m, which are clearly unrealistically high (see fig. 16, page 154). Indeed, the outlier (low value) for trial 4461 for method *ZPZP1U* was still unrealistic. Figs. 18, 19 and 20 (pp. 155-156) show how methods *ZPZP1U*, *ZPZP2U* and *ZPZP3U* produce similarly very unrealistic $CM[y]_{IA}(t)$ plots for a typical trial. In developing *ZPZP2U*, it was postulated that subtracting the mean *Fy* value from the *Fy* signal for quiet stance trials may account well for an anticipated offset error in *Fy* (Fy_O) and, therefore, improve the $CM[y]_{IA}(t)$ plots produced by the method. However, de-trending *Fy* (*ZPZP2U*) did not improve the basic unconventional ZPZP method (*ZPZP1U*), nor did increasing the sampling rate from 40 to 1000 Hz (*ZPZP3U*). The 11 to 12.3 s trials used in this research were not of long enough duration to produce mean *Fy* values that reflected the value of Fy_O accurately enough. For example, mean *Fy* was -1.508 N (implying Fy_O would be 1.508 N) in trial '4463' for method *ZPZP2U*, whereas the optimised Fy_O value was 1.479 N for method *ZPZP4U*.

In one sense, it is not surprising that *ZPZP4U* produced the lowest *IEP Displacement Parameter* values, considering that minimising an objective function equivalent to the *IEP Displacement Parameter* (Eq. (23)) is the

fundamental process performed by *ZPZP4U*. More importantly though, the practical outcome of applying method *ZPZP4U* was that it produced much more realistic $CM[y]_{IA}(t)$ trajectories relative to $COP[y](t)$ trajectory, compared with the other three unconventional ZPZP methods. This is exemplified by the trial shown for method *ZPZP4U* in Fig. 22 (page 158), compared with same trial for methods *ZPZP1U*, *ZPZP2U* and *ZPZP3U* shown in Figs. 18, 19 and 20, respectively (pages 155-156). However, $CM[y]_{IA}(t)$ trajectory relative to $COP[y](t)$ trajectory in Fig. 22 still appears to be somewhat unrealistic, particularly during the 1 to 6 second period, where the $CM[y]_{IA}(t)$ excursions remained 'above' the 'downward' turning points of the $COP[y](t)$ plot. Recall that the COP must keep moving anteriorly and posteriorly with respect to the CM position to ensure maintenance of balance during quiet stance (Winter et al., 1996a). This behaviour is not evident for the trial depicted in Fig. 22 during the 1 to 6 second period, although it was present in the plots for the other five trials (e.g. Fig. 23, page 159).

5.3.2 Conventional ZPZP Methods

The results provided strong support for Hypothesis 2; that is, significantly different *IEP Velocity Parameter* values were produced by different conventional ZPZP methods. The range plot in Fig. 17 (page 154) demonstrates that the optimisation-based *ZPZP5C* and *ZPZP6C* methods produced lower *IEP Velocity Parameter* values than *ZPZP1C, ZPZP2C* and *ZPZP3C*.

The inclusion of de-trended *Fy* (*ZPZP2C*) in the conventional ZPZP method was observed to produce more IEPs and noticeable improvement in $CM[y]_{IA}(t)$ trajectory, compared with *ZPZP1C*. Lafond et al. (2004) essentially de-trended

antero-posterior GRF data (*Fy*) by recording the signals from the unloaded force platform for 20 s before each experimental session and removing the mean of these signals from subsequently captured subject data. With respect to Lafond et al. (2004), Prince et al. (2005) stated, "we have noticed that the more often the anterior-posterior forces cross zero (i.e. during quiet standing), the better the results…" This observation is consistent with the findings of the current research for both conventional and unconventional ZPZP approaches (e.g. Fig. 66, page 345). Zatsiorsky and Duarte (2000) did not de-trend *Fy*. However, in collaboration with others, these researchers stated that they de-trended *Fy* in a more recent study (Mochizuki et al., 2006), though the effect of this approach could not be assessed from the results they presented.

Although *ZPZP2C* produced more realistic $CM[y]_{IA}(t)$ trajectories than *ZPZP1C*, jagged turning points were still apparent at some IEPs (e.g. Fig. 27, page 162). Similar phenomena are also evident in the one-legged stance data of King and Zatsiorsky (2002), reproduced in Fig. 37, with a magnified inset showing jagged turning points at the IEPs within the 18 to 19 s period. The jagged turning points observed in this study support the previous suspicion that the GLP-3 plot in Fig. 4 of King and Zatsiorsky (1997) shows similar jagged behaviour at the turning point corresponding to the IEP at $t \approx 0.8$ s (see Chapter 2, Fig. 3, page 22). Clearly, conventional applications of the ZPZP method, such as *ZPZP1C* and the methods of Zatsiorsky and King (1998) and Zatsiorsky and Duarte (1999), do not produce smooth $CM[y]_{IA}(t)$ functions at the IEPs, even if *Fy* is de-trended first (*ZPZP2C*, *ZPZP3C*).

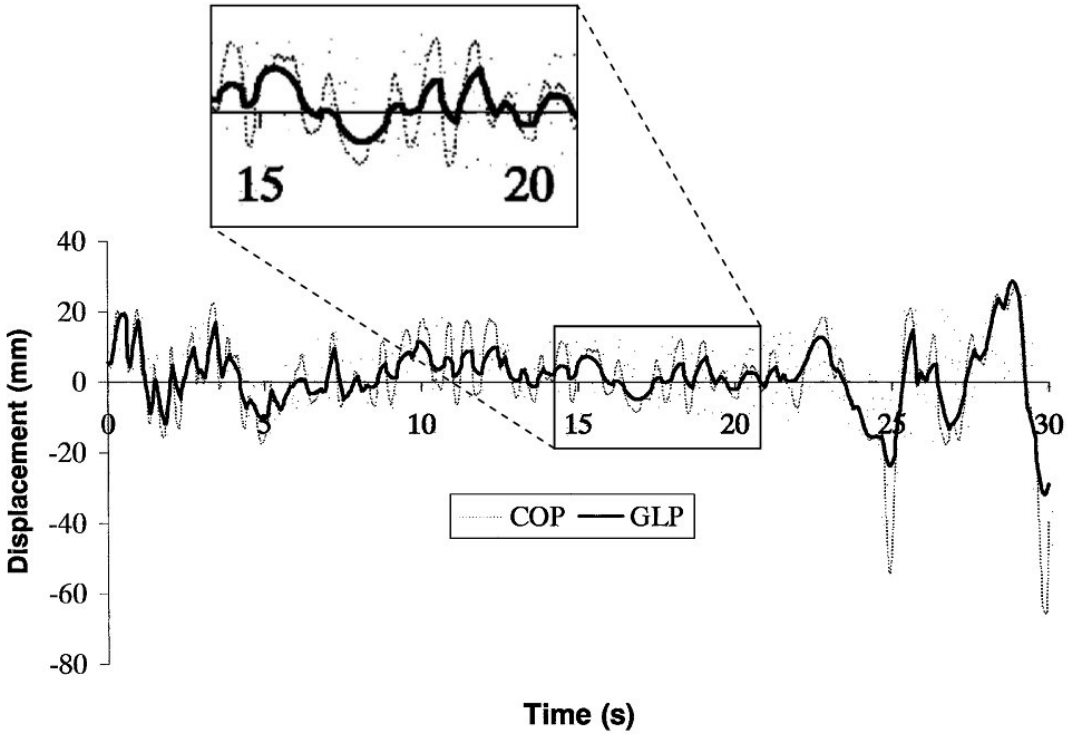

Figure 37. Plots of COP[*y*](*t*) *(labelled* COP*) and CM*[*y*]$_{IA}$(*t*) *(labelled* GLP*), reprinted and adapted from figure 5 of King and Zatsiorsky (2002), with permission of Elsevier. The inset magnification shows instances between approximately 18 to 19 s when the CM*[*y*]$_{IA}$(*t*) *plot is not smooth, inferring CM'*[*y*]$_{IA}$(*t*) *is not continuous at these points in time.*

Optimisation methods *ZPZP5C* and *ZPZP6C* produced lower *IEP Velocity Parameter* values than the other conventional approaches. This result was expected, considering that *ZPZP5C* and *ZPZP6C* were designed to decrease the average magnitude of the discontinuities in *CM'*[*y*]$_{IA}$(*t*) at the IEPs (i.e. to minimise the *IEP Velocity Parameter* value). Note also that the slope of the *CM'*[*y*]$_{IA}$(*t*) plot (i.e. the antero-posterior acceleration of the CM) in Fig. 30 (page 164) for *ZPZP5C* and in Fig. 32 (page 165) for *ZPZP6C* alternated between positive and negative from ZPZP interval to ZPZP interval, whereas it was often negative for many consecutive ZPZP intervals for methods *ZPZP2C* and *ZPZP3C* (cf. Fig. 28, page 162). This observation also supports the notion that *ZPZP5C*

and *ZPZP6C* produce more realistic results. This is because, according to the assumption upon which these methods are based, the antero-posterior component of the ground reaction force acting on the subject is zero at the IEPs (Zatsiorsky and King, 1998) and is in the process of changing from positive to negative or *vice versa* (Winter et al., 1996a).

5.3.3 Sampling Rate: 40 Hz *versus* 1000Hz

It is clear that a force platform sampling rate of 40 Hz produces essentially equivalent results to those produced with a sampling rate of 1000 Hz for both conventional and unconventional ZPZP methods. This finding validates the 40 Hz sampling rate used by Zatsiorsky and Duarte (2000). Data were not resampled at 20 Hz in the current study, so the appropriateness of the 20 Hz sampling rate used by Lafond et al. (2004) was not assessed. The finding regarding the sampling rate result is only applicable to quiet stance activities. In hindsight, a 40 Hz sampling rate could have been applied with methods *ZPZP4U*, *ZPZP5C* and *ZPZP6C* without significantly affecting the results. The speed of execution of all three methods, in particular *ZPZP6C*, would have been improved substantially by this refinement. Details of the relative speeds of these algorithms are discussed in section 5.3.7 on page 184.

5.3.4 Estimating Fy_O: De-trending *Fy versus* Optimisation Approaches

De-trending *Fy* appears to improve the conventional ZPZP approach, increasing the number of IEPs in the process, but does not appear to improve the

unconventional ZPZP approach. De-trending *Fy* does not always account adequately for the anticipated antero-posterior GRF offset error, Fy_O. The most significant finding was that optimisation ZPZP methods, whether from the conventional or unconventional category, outperformed all other ZPZP methods in their respective category. This supports the notion of the existence of an offset error Fy_O for each trial and that the optimisation approaches *ZPZP4U*, *ZPZP5C* and *ZPZP6C* were better able to account for it than the de-trending methods, and subsequently produce more realistic antero-posterior centre of mass displacement and velocity histories. As discussed in section 5.3.1, the 11 to 12.3 s trials used in this research were not of sufficient duration to produce mean antero-posterior GRF values that accurately accounted for the anticipated offset error in this signal.

The range of Fy_O values determined by both the *ZPZP4U* and *ZPZP5C* methods across all trials (viz. 0.65 to 1.76 N) may indicate systematic errors in *Fy* associated with the positioning of the subject on the force platform. The Fy_O values calculated for the dead weight spread across 26 different locations on the force platform (see footnote 16 on page 167) supports this notion. The position of the subject on the force platform was not controlled across the jumping trials and different locations were almost certainly adopted between trials during this experiment. The variation in Fy_O values between trials may also be associated with the force platform not being perfectly level or the origin of the force reference system within the force platform not being precisely as indicated by the manufacturers. If the subject is positioned on different places on the platform from trial to trial, this may lead to different calculations being made regarding the relative contribution that the load cells in each of the force platform's four corners

makes to the net force and moment components recorded for each dimension. It may also be that loads placed on different locations on the platform have different distortion effects on the platform and load cells, similar to those described by Schmiedmayer and Kastner (1999) for piezoelectric force platforms. The large dimensions of the platform used in this study may have increased the effects of such errors, compared with smaller platforms often used for posturographic analyses. Some of the differences in Fy_O values between trials can also be accounted for by the random noise in the *Fy* signals and the way in which signals were zeroed prior to each trial. The AMLAB software zeroed signals based on the instantaneous value at the time of zeroing, rather than using an average value over a pre-defined time period, as many other data acquisition software packages do. However, this explanation can only account for *Fy* offset errors of a magnitude less than 0.25 N, based on observed amplitudes of random noise for raw *Fy* signals recorded for the dead weight in this study. Finally, if the force platform signals contained very low frequency noise (< 0.15 Hz), as proposed by Zok et al. (2004), then Fy_O may have partially compensated for different manifestations of low frequency noise in different 11 to 12.3 s trials, thus also contributing to the different Fy_O values observed between trials. Such noise can be caused by temperature fluctuations, cross-talk among the different signals, and potential instrument nonlinearity not compensated for by the force platform calibration matrix (Zok et al., 2004), nor compensated for sufficiently by the Fy_O design variable.

5.3.5 Low-Pass Filtering of GRF Data: Effect of Cut-off Frequency

There was no evidence that significantly different *IEP Displacement Parameter* values result when different cut-off frequencies are applied to the force platform data (viz. 6, 8, 10, 12, 14, 16, 18, 20, 25 and 30 Hz) prior to executing the *ZPZP4U* method. That is, Hypothesis 5 was not supported by the results.

Hypothesis 6 was supported by a significant ANOVA χ^2 result ($p = 0.00001$). That is, evidence was found supporting the hypotheses that significantly different *IEP Velocity Parameter* values result when different cut-off frequencies are applied to the force platform data (viz. 6, 8, 10, 12, 14, 16, 18, 20, 25 and 30 Hz) prior to executing the *ZPZP5C* method. The trend evident in Fig. 34 (page 168) suggests that *ZPZP5C* objective function minimisation improves (i.e. *IEP Velocity Parameter* values decrease) as the cut-off frequency applied to the force platform data is reduced. The reduction in cut-off frequency was observed to decrease the number of identified ZPs. In particular, multiple (up to five) zero-crossings closely nearby each other (within 0.1 s ranges) associated with high frequency random noise in the force signals were diminished with reductions in the applied cut-off frequency. This was also observed to reduce the occurrence of jagged turning points in the $CM[y]_{IA}(t)$ plots (see Figs 35 and 36). It is possible that the TOL variables in *ZPZP6C* were able to compensate somewhat for any noise-related ZPs that may have remained after filtering the data at 8 Hz. The 8 Hz cut-off frequency applied to all methods in this study was used because all these methods were derived from the method of Zatsiorsky and Duarte (2000),

which involved data filtered at 8 Hz. Based on the current evidence, the 8 Hz cut-off frequency used in this study and by Zatsiorsky and Duarte (2000) and the 10 Hz cut-off used by Lafond et al. (2004) appear to be quite appropriate. At some point, he aforementioned benefits of reducing the cut-off frequency will be overcome by the effects of over-smoothing of the data, which will reduce the number of identified ZPs to unrealistically low levels and, possibly, also reducing the accuracy of their location in the time domain. The effects of cut-off frequencies lower than 6 Hz warrant further investigation.

5.3.6 Conventional *versus* Unconventional Optimised ZPZP Approaches

This study represents the first assessment of ZPZP methods for quiet stance[17] by means of qualitative interpretation of plots depicting the relationship between $COP[y](t)$ and $CM[y]_{IA}(t)$. When assessing dynamic balance and fundamental motor control problems in humans, this relationship is regarded as an important evaluation tool (Corriveau et al., 2000; Winter et al., 1996a; Winter et al., 1996b), so the benefit of such an assessment is of practical importance.

Recall that both the conventional and unconventional ZPZP methods are based on the assertion that, during stance, antero-posterior CM displacement and COP coincide whenever the antero-posterior GRF is momentarily zero (King and Zatsiorsky, 1997; Zatsiorsky and King, 1998). If this assertion is valid, then it

[17] Note that various static head and neck flexion and extension orientations were adopted within each of the assessed trials, as described previously, so they were not strictly quiet stance trials.

should not be necessary to execute the conventional ZPZP algorithm (see page 17) across each and every ZPZP interval during a quiet stance trial. That is, any ZPZP method that is not susceptible to other error sources should be capable of being applied in the unconventional way, ignoring all intermediate IEPs, and still be able to produce coinciding $COP[y](t_i)$ and $CM[y]_{IA}(t_i)$ values not only at the initial and final IEPs in the trial, but also at each and every intermediate IEP_i. Indeed, both approaches would produce identical results throughout the entire time series if both methods were free of modelling and measurement errors. The fact that this was not seen in practice for methods *ZPZP4U*, *ZPZP5C* and *ZPZP6C* suggests that errors existed.

Notwithstanding the presence of errors, the unconventional optimised ZPZP approach (*ZPZP4U*) has the advantage of producing perfectly smooth and continuous functions of CM displacement and velocity. Even though $COP[y](t_i)$ and $CM[y]_{IA}(t_i)$ did not coincide exactly at each intermediate IEP_i for this method, the median *IEP Displacement Parameter* (Eq. (24)) value across all six trials was less than one millimetre, and the relationship between the two plots appeared to be realistic for quiet stance in five of the six assessed trials (e.g. Fig. 23, page 159). The trial that produced the clearly unrealistic result in Fig. 22 (page 158), which included discrepancies of up to five millimetres at some of the IEPs, may have been at least partly due to very low frequency noise in the force platform signals, as proposed by Zok et al. (2004). Possible means of dealing with low frequency noise are discussed in the next section.

The inclusion of the nonlinear constraint Eqs. (25) (page 143) was not necessary for the cases examined in this research. However, their inclusion is recommended as an extra safeguard.

The development, demonstration and evaluation of a new technique dubbed the 'unconventional' ZPZP approach, is a distinguishing feature of this study. All previous researchers have only applied the ZPZP methods in the conventional, piecewise fashion across each and every pair of adjacent IEPs. Conspicuously, most of these studies have not published plots of both $CM[y]_{IA}(t)$ and $COP[y](t)$ for quiet stance, which would have allowed scrutiny of the performance of conventional ZPZP methods by means of qualitative assessment of the relationship between these two plots. Of the three studies that have done so, King and Zatsiorsky (1997) did not overlay $CM[y]_{IA}(t)$ and $COP[y](t)$ on the same axes, making qualitative assessment of the relationship between the two plots difficult; King and Zatsiorsky (2002) provided only a small-scale plot, making it hard to observe the desired relationship; and Lafond et al. (2004) did likewise, using a thick line to plot $CM[y]_{IA}(t)$ (see 'GLP' in Fig. 1, page 10), which may have had the inadvertent effect of disguising any jagged turning points that may have been inherent in their quiet stance data at the IEPs. Certainly, no previous study has acknowledged, let alone quantified, the discontinuities in $CM'[y]_{IA}(t)$ at the IEPs. The assessment methods presented in this study, including the qualitative assessment of $CM[y]_{IA}(t)$ plots *versus* $COP[y](t)$ plots and the continuity assessment of the $CM'[y]_{IA}(t)$ plots, have been demonstrated to be very effective in distinguishing between the relative merits of various ZPZP methods and have allowed the identification of the most promising method.

5.3.7 The Best Method, Future Improvements and Assessments

The most promising ZPZP method developed in this research was *ZPZP6C*. By design, the weakness of the unconventional optimised ZPZP approach *ZPZP4U* is the strength of the conventional optimised ZPZP approach *ZPZP5C*, and *vice versa*. Execution of *ZPZP5C* produces exact agreement between $COP[y](t_i)$ and $CM[y]_{IA}(t_i)$ at each IEP_i, however, it does not produce continuous functions of CM in the first derivative. *ZPZP6C* essentially provides a compromise solution between the conventional and unconventional approaches. The quantitative and qualitative results of this study suggest that it produces the best overall results. *ZPZP6C* produced significantly smaller discontinuities in the first derivative than *ZPZP5C* and significantly smaller discrepancies between $COP[y](t_i)$ and $CM[y]_{IA}(t_i)$ at each IEP_i than *ZPZP4U* (both $p = 0.028$). That is, the results support Hypotheses 3 and 4 and support the adoption of *ZPZP6C* over the other methods assessed. Ways of improving the qualitative assessment of ZPZP methods by better interpretation of the relationship between $COP[y](t)$ and $CM[y]_{IA}(t)$ plots, and ways of improving the *ZPZP6C* method itself, are now considered.

First consider the interpretation of the relationship between stance plots of $COP[y](t)$ and $CM[y]_{IA}(t)$. It has already been established that $COP[y](t)$ must keep moving anteriorly and posteriorly with respect to $CM[y]_{IA}(t)$ to ensure maintenance of balance during quiet stance (Winter et al., 1996a). This was the basis for constraint Eqs. (25) (i.e. the maximum $CM[y]_{IA}(t_i)$ range must be completely within the maximum $COP[y](t_i)$ range) and the qualitative assessment

of these curves in this study. Further improvements to the assessment criteria are possible, given the assumption that the antero-posterior component of the ground reaction force acting on the subject is zero at the IEPs (Zatsiorsky and King, 1998) and that it is in the process of changing from positive to negative or *vice versa* (Winter et al., 1996a). For each and every local maximum and local minimum $CM[y]_{IA}(t_i)$, the corresponding $COP[y](t_i)$ value should be greater or less, respectively. Further, any point of inflection in the $CM[y]_{IA}(t)$ curve should be present at, or very near to (if *ZPZP6C* TOL_i variables are included), an identified IEP. This is predicted by the Zatsiorsky and King (1998) assumption because, if $Fy = 0$, then the antero-posterior acceleration of the CM at such instants should also be zero. The double-derivative of $CM[y]_{IA}(t)$ represents the antero-posterior acceleration of the CM and this is equal to zero at points of inflection. Considering the plots of $COP[y](t)$ and $CM[y]_{IA}(t)$ resultant from the three optimised ZPZP methods assessed in this research (e.g. Figs. 22, 29 and 31), method *ZPZP6C* again appears to produce the best results in this regard (Fig. 31).

The existing *ZPZP6C* method allows for calculated $CM[y]_{IA}(t_i)$ and $COP[y](t_i)$ values to vary from each other at each IEP_i by up to 1 mm with the inclusion of variables termed TOL_i. The existence of TOL is, in itself, a violation of the main assumption upon which the method of King and Zatsiorsky (1997) is based, namely, that these parameters should coincide at each IEP_i. However, other assumptions of their model and method may not be strictly correct, so the inclusion of TOL may actually compensate quite well for these slight violations. For example, for their inverted pendulum model, they assumed that the feet didn't move and considered them to be solid bodies, and that the axis of ankle joint

rotation was fixed with respect to the force platform. It seems reasonable to suggest that these two assumptions may be violated by at least 1.0 mm in either direction. For example, the subject and his/her ankle joints might translate horizontally by ±1 mm or more throughout the full range of postural sway, while the soft plantar tissues of the feet remain in the same position on the force platform. However, this is only speculation in the absence of any evidence. The fact that so few of the TOL bound constraint Eq. (27) became active for the quiet stance activities seems to suggest that the 1.0 mm limit is generally acceptable, but that slightly greater tolerances may sometimes be necessary, for instance, when more unstable balance activities are assessed, such as one-legged stance. Fitting splines to the discrete values that constitute the $CM[y]_{IA}(t)$ plot resulting from the application of *ZPZP6C* would remove the small but remaining discontinuities in $CM'[y]_{IA}(t)$. The practical benefit of employing such a practice would need to be evaluated.

On a personal computer with a 2.0 GHz Intel® Pentium® (M) Processor and 1.50 GB of RAM, *ZPZP4U* and *ZPZP5C* took only a few seconds to converge, whereas *ZPZP6C* took almost two hours for one trial. No attempt was made during this study to make execution of the *ZPZP6C* code more time-efficient. It is predicted that substantial improvements would be possible if such an attempt was made. This would make it possible to apply *ZPZP6C* to trials much longer than 12 s. It might also be feasible to then execute a two-level optimisation process that involves a tabular optimisation at the outer level where only Fy_O is varied, but

allows optimal selection of the TOL_i variables at the inner level[18]. *ZPZP6C* might also be enhanced by implementing a multi-objective function of Eqs. (23) and (24). The optimal relative weighting of each equation in the multi-objective function would also need to be assessed.

As mentioned in the previous section, the force platform signals may have contained low frequency noise. When doubly integrated, the amplitude of any low frequency noise content is multiplied by the inverse of the square of that frequency and the effect is amplified as integration time increases (Zok et al., 2004). Zok et al. suggested that very low frequency noise can be in the form of "an offset, a drift, a sinusoid, or a less well-defined non-periodic signal." Any of the latter three, if present, might partially explain the result shown in Fig. 22 (page 158). It may be necessary to consider using a high-pass filter to remove low frequency noise.

Hof (2005) described a modification to the ZPZP method, part of which included high-pass filtering of the antero-posterior CM acceleration (Fy/m_{WB}), using a 0.2 Hz cut-off frequency. No results were provided to support the appropriateness or otherwise of its use for quiet stance, beyond stating that this method "performed about equally well" with the method of Zatsiorsky and King (1998). In defence of Hof (2005), this reference was only a letter to the editor regarding Lafond et al. (2004), Caron (2005) and Prince et al. (2005). However, Hof (2007)

[18] Recall that *ZPZP6C* only varied the TOL_i variables, with the pre-determined, *ZPZP5C*-optimised value of Fy_O.

has subsequently submitted findings of another study which relied on the methodology described in Hof (2005), objective and quantitative evaluations of which are yet to be published.

High-pass filtering was also used by Zok et al. (2004) for two IA approaches, though these approaches were not ZPZP methods. Zok et al. applied trial- and dimension-specific optimised cut-off frequencies ranging between 0.02 to 0.15 Hz to the force platform data obtained during a step ascent task. This strategy was based on power spectrum analyses of a dead weight of approximately 500 N on the force platform, sampled at 120 Hz for 200 s. After de-trending the vertical ground reaction force signal, thus removing the only true signal and leaving only noise in the recorded data, they reported that "considerable" power was present up to 0.1 Hz and "some" power was present up to 0.2 Hz. They did not mention how much power existed at other frequencies.

Assessing the noise content inherent in a force platform by analysing a de-trended dead weight signal (Zok et al., 2004) can be done with much greater confidence than determining the signal content of a human movement trial. The dilemma is to remove low frequency noise without removing significant signal content. Brief attempts to improve the performance of *ZPZP4U* for the trial presented in Fig. 22 (page 158) by high-pass filtering the antero-posterior GRF data first, only produced progressively worse results as the cut-off frequency was increased from very low values up to 0.2 Hz. This might suggest that significant low frequency signal content was being removed along with or rather than noise. Indeed, Duarte

and Zatsiorsky (2001) have observed long-term correlations in quiet stance COP data, which may indicate significant signal content at low frequencies.

Whether or not the changes in calculated $CM[y]_{IA}(t)$ trajectory invoked by the aforementioned alterations to the *ZPZP6C* method would be of any practical benefit needs future assessment. Morasso et al. (1999) pointed out that the difference between the $CM[y]_{IA}(t)$ and $COP[y](t)$ trajectories during quiet stance is "small but significant" and that study of this relationship is important for assessing balance control problems. The ability to distinguish subtle between-subject or within-subject changes in what is already a subtle relationship between $CM[y]_{IA}(t)$ and $COP[y](t)$ trajectories during quiet stance may assist our ability to discriminate between different subjects, pathologies and interventions during balance studies. Likewise, the changes in calculated $CM[y]_{IA}(t)$ trajectory produced by the previously suggested *ZPZP6C* modifications might represent practically significant improvements, even if they are small. Their influence on the usefulness of this technique warrants further investigation.

Comparisons of ZPZP and SK determinations of CM trajectory were deemed inappropriate for this experiment because of the head and neck movements associated with the otherwise quiet stance activities captured for this study. Zatsiorsky and King (1998) correctly pointed out that optical methods of CM estimation contain errors due to inaccurate estimates of BSPs and joint axis locations. Errors in head and neck segment BSPs and associated joint centre locations would have introduced errors into the SK determined CM trajectories for these activities. However, the limitations raised by Zatsiorsky and King

(1998) could be overcome in future evaluations of CM trajectory during quiet stance by conducting a *relative* rather than an *absolute* comparison of ZPZP-derived and SK-derived CM data. All the body segments superior to the ankle would have to be maintained as rigid as possible, relative to each other, throughout each trial. It would also be preferable for subjects to hold their breath throughout each trial in order to minimise thoracic mass distribution changes. Changes in *relative* CM position would then be due to sway, with minimal influence from BSP and joint centre estimate errors. This methodological approach would provide a valid reference CM trajectory for evaluating *ZPZP6C* modifications and other force platform based CM trajectory calculation methods.

5.3.8 Summary

The results of this experiment support the use of an optimised ZPZP method, *ZPZP6C*, over the conventional ZPZP method of Zatsiorsky and Duarte (2000) for determining anteroposterior CM kinematics during quiet stance. The antero-posterior GRF offset error term, Fy_O, was the only force platform calibration or offset error design variable that needed to be varied in order to optimise $CM[y]_{IA}(t)$ trajectory. The 'conventional' and 'unconventional' optimised ZPZP methods developed for this study both produced promising results. Conventional methods produce no discrepancies between $CM[y]_{IA}(t)$ and $COP[y](t)$ at the IEPs but they produce unrealistic discontinuities in $CM'[y]_{IA}(t)$. The opposite conflict applies to the unconventional methods, wherein $CM'[y]_{IA}(t)$ is continuous, by definition, but discrepancies exist between $CM[y]_{IA}(t)$ and $COP[y](t)$ at the IEPs. The *ZPZP6C* method represented a pragmatic compromise between these two approaches, recognising the presence of imperfect input data

and model assumptions. It reduced substantially the jagged points in the $CM[y]_{IA}(t)$ plots, compared with all the other 'conventional' ZPZP methods assessed in this research, thus also reducing substantially the magnitude of the discontinuities in $CM'[y]_{IA}(t)$ at the IEPs. It also significantly reduced the discrepancies between $CM[y]_{IA}(t)$ and $COP[y](t)$ at the IEPs, keeping them at or below one millimetre, by definition. Possibly most importantly, the practical outcome of applying method *ZPZP6C* was that it consistently produced the most realistic $CM[y]_{IA}(t)$ trajectory relative to $COP[y](t)$ trajectory. Further improvements to the *ZPZP6C* method might be possible by evaluating different band-pass cut-off frequencies for the force data and by fitting splines to the $CM[y]_{IA}(t)$ data after the optimisation process. Quiet stance trials with all segments superior to the ankle joint held rigid will allow the valid evaluation of these techniques in terms of *relative* CM displacement.

6. INTEGRATION APPROACH (IA) OPTIMISATION TECHNIQUES FOR ESTIMATING CM KINEMATICS DURING JUMPING ACTIVITIES

The methods developed in this experiment attempt to produce realistic determinations of *relative* $CM_{IA}(t)$ for transient dynamic activities commenced with a quasi-static stance phase, such as countermovement jumps, using only force platform data. Each method is based on different assumptions or interpretations about the expected behaviour of the CM during the quasi-static stance phase. All methods are based on the premise that estimated initial CM velocity conditions, determined to satisfy *relative* $CM_{IA}(t)$ expectations during the quasi-static stance phase, will also produce accurate *relative* $CM_{IA}(t)$ values throughout the countermovement and airborne phases when the IA approach is applied forwards beyond the quasi-static stance phase.

6.1 Research Design

6.1.1 The IA Optimisation Methods

Three core approaches to IA optimisation were developed for this study and compared over a series of jumping trials. The three core approaches are described in detail in section 6.1.1.1. In summary, an approach based on the method of Vanrenterghem et al. (2001) was applied in the vertical dimension (*Method A*); a

modified version of the Jaffrey et al. (2003) IA method was applied separately in both the antero-posterior and vertical dimensions (*Method B*); and a modification to the unconventional ZPZP approach described in the previous chapter was applied in the antero-posterior dimension (*ZPZP5U*). Two different definitions of quasi-static stance phase duration (*Max* and *2000*) were each applied to *Methods A* and *B*, thus creating uniquely defined variants *AMax*, *A2000*, *BMax* and *B2000*. The definition of *Max* involved using the maximum available quasi-static period, whereas the definition of *2000* involved using only a set 2000 ms period of quasi-static data preceding the dynamic, countermovement phase. The two definitions of the duration of the quasi-static stance phase are described in detail in section 6.1.1.2. All seven resultant methods are then summarised in section 6.1.1.3.

6.1.1.1 Definition of the Core IA Optimisation Approaches

- ***Modified Vanrenterghem et al. (2001) Approach (Method A)***:

  Vanrenterghem et al. (2001) reported using an "optimising loop" to find trial-specific whole body mass (m_{WB}) values that resulted in no net vertical displacement of the CM during the 2 s stance phase prior to jump initiation. They assumed the initial vertical velocity of the CM to be zero. The approach applied in this experiment varied from that of Vanrenterghem et al. (2001) insofar as m_{WB} was kept constant at the value measured pre-trial on precision scales (62.715 kg), and $CM'[z]_{IA}(0)$ was not assumed to be zero. $CM'[z]_{IA}(0)$ was considered a design variable in the optimisation process, as was Fz_O.

The objective function to be minimised was the absolute value of the net vertical displacement of the CM over the predefined quasi-static (*QS*) stance period ($t = t_{QSini}$ to t_{QSfin}) prior to countermovement initiation:

$$\left| CM[z]_{IA}(t_{QSfin}) - CM[z]_{IA}(t_{QSini}) \right| \tag{28}$$

$CM'[z]_{IA}(0)$ and Fz_O were bound-constrained to what were deemed to be conservatively realistic ranges, considering that Jaffrey et al. (2003) reported a value of 0.00352 ms^{-1} for $CM'[z]_{IA}(0)$, and quasi-static Fz values were contained within a 4 N range:

$$-0.005 < CM'[z]_{IA}(0) < 0.005 \tag{29}$$

$$\left(m_{WB} * g - \frac{1}{n}\left(\sum_{i=QSini}^{QSfin} Fz(t_i) \right) - 2 \right) < Fz_O < \left(m_{WB} * g - \frac{1}{n}\left(\sum_{i=QSini}^{QSfin} Fz(t_i) \right) + 2 \right) \tag{30}$$

where n represents the number of samples during the defined quasi-static phase preceding initiation of the countermovement phase of the jump.

- ***Modified Jaffrey et al. (2003) Approach (Method B)***: Jaffrey et al. (2003) minimised an objective function representing the sum of squared *relative* $CM[z]_{IA}(t)$ values during a two-second quasi-static stance phase prior to countermovement jump initiation. In this experiment, the objective function to be minimised was modified to represent the mean absolute difference of all individual quasi-static *relative* CM_{IA} values from the mean quasi-static value.

The IA optimisation of Jaffrey et al. (2003) aimed to minimise the deviation of quasi-static $CM[y]_{IA}(t)$ from $CM[y]_{IA}(0)$, whereas *Method B* was designed to minimise the deviation of quasi-static $CM[y]_{IA}(t)$ from mean quasi-static $CM[y]_{IA}(t)$. In both dimensions, $CM_{IA}(0)$ was assigned the value of zero and all subsequent $CM_{IA}(t)$ values throughout the trial were derived *relative* to this starting point. *Method B* was applied independently in both dimensions. Thus, the vertical and antero-posterior objective functions were, respectively:

$$\frac{1}{n}\sum_{j=QSini}^{QSfin}\left|CM[z]_{IA}(t_j)-\frac{1}{n}\sum_{i=QSini}^{QSfin}CM[z]_{IA}(t_i)\right|, \text{ and} \tag{31}$$

$$\frac{1}{n}\sum_{j=QSini}^{QSfin}\left|CM[y]_{IA}(t_j)-\frac{1}{n}\sum_{i=QSini}^{QSfin}CM[y]_{IA}(t_i)\right| \tag{32}$$

$CM'[z]_{IA}(0)$ and Fz_O were bound-constrained as per Eqs. (29) and (30). $CM'[y]_{IA}(0)$ and Fy_O were bound-constrained to what were deemed conservatively realistic ranges, based on the findings of the previous experiment (Chapter 5):

$$-0.02 < CM'[y]_{IA}(0) < 0.02 \tag{33}$$

$$\left(-\frac{1}{n}\sum_{i=QSini}^{QSfin}Fy(t_i)\ -\ 2\right) <\ Fy_O\ <\ \left(-\frac{1}{n}\sum_{i=QSini}^{QSfin}Fy(t_i)\ +\ 2\right) \tag{34}$$

Modified ZPZP Approach (ZPZP5U): Based on the results of the unconventional ZPZP method comparisons in the previous chapter, *ZPZP4U* was selected and further developed for application in the antero-posterior dimension for the jumping trials[19]. The basic procedure for implementing the *ZPZP4U* IA optimisation approach was outlined in section 5.1.1. It was modified slightly and named *ZPZP5U* for application to dynamic jumping activities. The modification involved introducing *tolerance* design variables for the initial and final IEPs (TOL_0 and TOL_{fin}). The consequence was that $CM[y]_{IA}(t_0)$ and $CM[y]_{IA}(t_{fin})$ were assigned the values of $COP[y](t_0) + TOL_0$ and $COP[y](t_{fin}) + TOL_{fin}$, respectively. The TOL design variables were bound-constrained to a range of ± 1.5 mm, as this was deemed an acceptable error for $CM[y]_{IA}(t)$ calculations during jumping applications. Fy_O was bound-constrained as per Eq. (26) and applied over only the quasi-static phase of the jump trials. $CM'[y]_{IA}(0)$, $CM[y]_{IA}(0)$, Fy_O, TOL_0 and TOL_{fin} values were calculated for the defined quasi-static period from t_0 to t_{fin} using the *ZPZP5U* optimisation method. *ZPZP5U* was equivalent to *ZPZP4U* in all other regards

---

[19] Conventional ZPZP methods were deemed inappropriate for IA applications that calculate CM kinematics beyond the quiet stance phase of an activity. For conventional ZPZP methods, the initial velocity calculated for the final ZPZP interval is only optimal for that small interval and not necessarily optimal for calculations beyond that interval. However, the initial velocity value selected for the *ZPZP4U* method is the best overall value for the entire quiet stance phase. Though it, too, may not be optimal for CM kinematics extrapolation beyond the ZPs, the assumption was made that *ZPZP4U* would be more appropriate than conventional ZPZP methods for producing an initial velocity estimate that is more appropriate for extrapolating CM kinematics beyond this phase.

(including the low-pass filtering of the force platform data at a cut-off frequency of 8 Hz), except as follows. In *ZPZP5U*, IEP_{fin} was defined as the *penultimate* IEP during the quasi-static phase. This was done to provide a safeguard against the potentially inaccurate identification of the end of the quasi-static phase by the researcher, thus ensuring the defined quasi-static phase did not cross over into the countermovement phase. Hence, the *ZPZP5U* method produced inter-trial quasi-static phases of variable duration that were similar, but not identical, to the *BMax* method applied in the antero-posterior [*y*] dimension. The unfiltered force platform data sampled at 1000 Hz, with the Fy_O offset term applied, was then used to calculate $CM[y]_{IA}(t)$ over the entire trial. The numerical integration process was commenced from the initial IEP (IEP_0) and was continued forwards beyond IEP_{fin}, throughout the flight phase of the jump and ceased just prior to landing.

All of the IA optimisation methods described above included a force offset error design variable in the relevant dimension, namely, Fy_O or Fz_O. These design variables are present in Equations (20), (21) and (22), which were used to determine all the relevant COP and CM kinematics and, subsequently, all objective function values. Force calibration error terms (Fy_C and Fz_C) were also considered potentially influential on all CM kinematics calculations. Tests of convergence and sensitivity analyses were conducted to assess the importance of these variables. The measures of relevance to the sensitivity analyses were the objective function values and, more critically, the change in antero-posterior and vertical CM displacement, because of the practical importance of the latter measures to jumping performance assessment. When Fy_O and Fy_C were allowed

to vary concurrently in the antero-posterior dimension objective functions, Fy_O bound constraint Eq. (34) never become active, whereas Fy_C constraints ($0.98 < Fy_C < 1.02$) became active in most cases, regardless of the initial estimate. The antero-posterior dimension objective functions were relatively much more sensitive to broadly feasible changes in Fy_O compared with changes in Fy_C. However, when Fy_O was allowed to vary and Fy_C was held constant at values ranging from 0.98 to 1.02, up to 5.3% changes in antero-posterior CM_{IA} range were produced (23 mm difference for the broad jump trial). At the same time, no change in the objective function values resulted. Hence, it was decided to exclude Fy_C from the set of design variables and set it to a constant value of one, which was assumed to be correct. Unlike Fy_C with respect to the antero-posterior objective functions, when Fz_O and Fz_C were allowed to vary concurrently in the vertical dimension objective functions, neither Fz_O nor Fz_C bound constraints became active. Once again, the objective functions were much more sensitive to changes in the offset variable than the calibration variable. For *Method B*, Fz_C always converged to the same value for all potentially feasible initial estimates ranging from 0.98 to 1.02. For *Method A*, Fz_C converged to within a range of 0.9997 to 1.0003 and there were no differences in objective function values across this range. However, there were differences in the range of vertical CM displacement during any given jump trial of up to 2.5% (15 mm) for *Method A*. There were no respective changes for *Method B*. These differences were not deemed negligible for *Method A* for the stated application. Hence, like Fy_C for the antero-posterior dimension objective functions, Fz_C was held constant at an assumed value of one for all IA optimisation methods applied in the vertical dimension. Mx_O and Mx_C were the other potentially relevant force platform

design variables inherent in Eq. (20). They were only relevant with respect to ZPZP calculations of *relative COP*[*y*](*t*) and $CM[y]_{IA}(t)$, but were found to be of negligible influence on these quantities during quiet stance (see Appendix A). Hence, they were held constant at values of one and zero, respectively, in all the objective functions developed for this experiment.

6.1.1.2 Variations of the Definition of Quasi-static Phase Duration

The criteria used to define the two quasi-static stance phase duration variations used in *Methods A* and *B* were based on criteria developed by Vanrenterghem et al. (2001). Their method involved three steps.

(1) The mean and standard deviation of the vertical GRF ($\overline{Fz}$ and SD, respectively) were calculated for the initial 2000 ms window of quasi-static stance data at the very start of the trial, spanning t_0 to t_{2000}.

(2) According to Vanrenterghem (2006), a five-point (5 ms) moving-average *Fz* value, $\overline{Fz}_5(t_k)$, was then calculated forwards in time, starting from $k = 2005$, such that:

$$\overline{Fz}_5(t_k) = \frac{1}{5}\sum_{i=k-4}^{k} Fz(t_i) \tag{35}$$

(3) The first value of t_k for which $\overline{Fz}_5(t_k)$ was outside the range of $\overline{Fz} \pm \text{SD}$ was defined as the commencement of the countermovement phase; the 2000 ms period immediately prior to this value of t_k was defined as the 2000 ms quasi-static phase for subsequent IA optimisation purposes.

Vanrenterghem et al. (2001) applied this method to theoretical data. However, in pilot testing for this study with empirical data, it was observed that the Vanrenterghem et al. (2001) approach often resulted in the defined 2000 ms quasi-static phase crossing into the countermovement phase, due to the insensitivity of the inequality criterion in step 3 to predict commencement of the countermovement phase. Obviously, the defined 2000 ms quasi-static phase should be in close proximity to the commencement of movement in order to minimise numerical integration drift errors. However, it also should not cross inadvertently into the countermovement phase because IA optimisation techniques based on *a priori* assumptions regarding quasi-static stance will be violated, rendering such techniques invalid. To achieve a compromise, three modifications to the method of Vanrenterghem et al. (2001) were introduced. Firstly, $\overline{Fz} \pm \mathrm{SD}$ was replaced with $\overline{Fz} \pm 0.1 \times \mathrm{SD}$ in step 3 as the new countermovement commencement identification criterion. Secondly, the five-sample (5 ms) forward-moving window was compared with a *forward-moving* 2000 ms window, rather than the *stationary* initial window of quasi-static data spanning t_0 to t_{2000}, until the new countermovement commencement identification criterion was satisfied. That is, both windows remained the same time interval apart as they were moved forward. Thirdly, this time interval, from the end of the 2000 ms window to the start of the 5 ms window, was set at 500 ms. In other words, starting from $k = 2505$, the first value of t_k for which $\overline{Fz}_5(t_k)$ was outside the range of $\overline{Fz}_{2000} \pm 0.1 \times \mathrm{SD}_{2000}$ was defined as the commencement of the countermovement phase, where:

$$\overline{Fz}_{2000}(t_k) = \frac{1}{2000}\sum_{i=k-2505}^{k-505} Fz(t_i) \tag{36}$$

and SD_{2000} was defined over the same range of i values.

Two definitions of the quasi-static phase were then established and assessed in this experiment.

- ***2000*:** The *2000* method quasi-static phase was defined as the 2000 ms period immediately prior to the aforementioned t_k value.
- ***Max*:** The *Max* method quasi-static phase was defined as the period from the start of the trial, t_0, to immediately prior to the aforementioned t_k value. This lead to inter-trial quasi-static phases of variable duration (up to 4.7 s in this research). It was postulated that the additional quasi-static data may produce different representations of the quasi-static baseline compared with the representation produced by only a 2000 ms data set.

6.1.1.3 Summary of the Seven Methods

Thus, with *ZPZP5U* applied in the antero-posterior dimension [*y*], *Method A* applied in the vertical dimension [*z*], *Method B* applied in both [*y*] and [*z*], and with two different quasi-static phase definitions applied to *Methods A* and *B*, a total of seven distinct methods of IA optimisation were developed and assessed in this experiment. Table 8 summarises the core approaches, the specific methods developed under each category, and the dimension and design variables relevant to each specific method's objective function.

Table 8. The three core approaches to IA optimisation developed and assessed in this experiment (column 1). Column 2 indicates each specific method formulated under each basic category, based on different definitions of the duration of the quasi-static stance phase. The dimension and the design variables relevant to each method's objective function are indicated in columns 3 and 4, respectively. Design variables TOL_0 and TOL_{fin} are defined in section 6.1.1.1 on page 194.

Core IA Optimisation Approaches	**Specific Methods**	**Relevant Dimension**	**Design Variables**
***Method A*:**	*AMax*[*z*]	[*z*]	Fz_O, $CM'[z]_{IA}(0)$
Modified Vanrenterghem et al. (2001)	*A2000*[*z*]	[*z*]	
***Method B*:**	*BMax*[*z*]	[*z*]	Fz_O, $CM'[z]_{IA}(0)$
Modified Jaffrey et al. (2003)	*B2000*[*z*]	[*z*]	
	BMax[*y*]	[*y*]	Fy_O, $CM'[y]_{IA}(0)$
	B2000[*y*]	[*y*]	
***ZPZP5U*:**	*ZPZP5U*[*y*]	[*y*]	Fy_O, TOL_0, TOL_{fin}
Modified unconventional ZPZP			

All optimisations were programmed in Matlab 6.5.1 (The Mathworks, Inc., Natick, MA., U.S.A.), using the 'fmincon' function. Several option parameters within this function (viz. TolFun, TolCon and TolX) were assigned a value of 0.00000001 to ensure the objective functions converged to the desired minima and to ensure constraints were not violated.

Five countermovement jumps and one broad jump were performed and used for this experiment. The countermovement jumps were commenced and completed near the centre of the force platform, whereas the broad jump was commenced near the posterior end and completed near the anterior end of the platform. All jumps were commenced with at least three seconds in the quasi-static posture depicted in Fig. 5. This posture was also maintained as rigidly as possible throughout the flight phase with respect to the arms, head and trunk.

6.1.2 Assessment of the IA Optimisation Methods

6.1.2.1 IA-SK RMS Parameters and Associated Hypotheses

The relative merits of the IA optimisation methods were assessed by comparing the CM displacement-time histories produced by these methods ($CM_{IA}(t)$) to that determined by SK analysis ($CM_{SK}(t)$). A sampling frequency of 1000 Hz was used for all IA calculations. These results were then synchronised with the motion capture data and resampled at 50 Hz to allow direct comparison with the SK calculations. All kinematic marker data were low-pass filtered using the GCV quintic spline software program written by van den Bogert (2000). Woltring (1995) reported that using quintic splines produced essentially equivalent results to those produced by applying a zero-lag phase 6^{th} order Butterworth filter. The GCV program (van den Bogert, 2000) allows the user to select the degree of spline smoothing in terms of the effective cut-off frequency of such a Butterworth filter, without producing the undesirable boundary problems often associated with Butterworth filters for the first and second derivatives of the smoothed signal. Data were filtered at an effective cut-off frequency of 3 Hz.

The assessment parameters were the RMS differences between *relative* $CM_{IA}(t)$ and *relative* $CM_{SK}(t)$ during what were deemed to be the valid phases of the jumps: the quasi-static stance and flight phases. The maintenance of an essentially quasi-rigid whole body posture by the subject during the quasi-static stance and flight phases enabled determination of $CM_{SK}(t)$ during these phases, *relative* to $CM_{SK}(t)$ at the commencement of the quasi-static stance phase, that was essentially independent of the applied set of BSPs[20]. Potential BSP errors, coupled with the reorientation of the segments relative to each other during the countermovement and propulsive phases of the jump, was assumed to invalidate any comparison of *relative* $CM_{SK}(t)$ and *relative* $CM_{IA}(t)$ calculations during these phases. Sensitivity analyses were conducted on the kinematic data to confirm these assertions. For example, changing the most influential BSP, $cm[L]_{Trunk}$, by 20% of the length of the Trunk segment, only changed *relative* $CM_{SK}(t)$ airborne values by a maximum of 0.2 mm, whereas the difference was as much as 8 mm at the minimum point of the countermovement. Consequently, the use of *relative* $CM_{SK}(t)$ as the comparison CM trajectory for *relative* $CM_{IA}(t)$, during the quasi-static stance and flight phases, was considered the most valid approach.. $CM[y]_{SK}(t)$ and $CM[z]_{SK}(t)$ were determined using Eqs. (16). The m_{seg} BSPs used for these equations were based on the regression equations of Clauser et al. (1969) and cm_{seg} BSPs were based on the mean values from the same study. The

[20] It should be noted that instructing the subject to maintain this posture during the airborne phase was a necessary strategy for this experiment, but only for the purposes of assessing the validity of IA methods using SK analysis. If any method can be validated using this strategy, then practical application of that method thereafter will be possible for less contrived activities that only require pre-jump quasi-static stance phases.

aforementioned sensitivity analyses demonstrated that possible errors inherent within the applied set of BSPs would have had negligible effect on the parameters used to assess the IA optimisation methods. Hence, no additional effort was deemed necessary to make the applied set of BSPs more subject-specific. The assessment parameters used to evaluate the relative merits of the vertical and antero-posterior IA optimisation methods were formulated as follows:

$$Quasi-static\ RMS\ CM[y]_{IA-SK} = \sqrt{\frac{1}{n}\left(\sum_{i=QSini}^{QSfin}\left(RelCM[y]_{IA}(t_i) - RelCM[y]_{SK}(t_i)\right)^2\right)} \quad (37)$$

$$Airborne\ RMS\ CM[y]_{IA-SK} = \sqrt{\frac{1}{n}\left(\sum_{i=ABini}^{ABfin}\left(RelCM[y]_{IA}(t_i) - RelCM[y]_{SK}(t_i)\right)^2\right)} \quad (38)$$

$$Quasi-static\ RMS\ CM[z]_{IA-SK} = \sqrt{\frac{1}{n}\left(\sum_{i=QSini}^{QSfin}\left(RelCM[z]_{IA}(t_i) - RelCM[z]_{SK}(t_i)\right)^2\right)} \quad (39)$$

$$Airborne\ RMS\ CM[z]_{IA-SK} = \sqrt{\frac{1}{n}\left(\sum_{i=ABini}^{ABfin}\left(RelCM[z]_{IA}(t_i) - RelCM[z]_{SK}(t_i)\right)^2\right)} \quad (40)$$

where t_{QSini} and t_{QSfin} are the times corresponding to the initial and final time samples in the quasi-static phase; t_{ABini} and t_{ABfin} are the times corresponding to the initial and final time samples in the airborne phase; and all $RelCM_{SK}$ and $RelCM_{IA}$ quantities are measures of CM displacement in the relevant dimension *relative to* $CM_{SK}(t_{QSini})$ and $CM_{IA}(t_{QSini})$, respectively.

Because the objective functions for the various IA optimisation methods were based on different quantities, they could not be compared directly. Instead, the quasi-static parameters provided the means for assessing the ability of the methods to produce realistic results in the phase associated with the objective functions, and the airborne parameters provided a means for assessing the performance of the methods in a phase of more practical importance to analyses of jumping performance outcome measures.

The following hypotheses regarding the application of the different IA optimisation methods to jumping trials were assessed:

Hypothesis 7: The respective IA optimisation methods applicable for calculating vertical CM displacement (viz. *AMax*[*z*], *A2000*[*z*], *BMax*[*z*] and *B2000*[*z*]) produce significantly different *Quasi-static RMS* $CM[z]_{IA\text{-}SK}$ *Parameter* values.

Hypothesis 8: The respective IA optimisation methods applicable for calculating vertical CM displacement (viz. *AMax*[*z*], *A2000*[*z*], *BMax*[*z*] and *B2000*[*z*]) produce significantly different *Airborne RMS* $CM[z]_{IA\text{-}SK}$ *Parameter* values.

Hypothesis 9: The respective IA optimisation methods applicable for calculating antero-posterior CM displacement (viz. *ZPZP5U*[*y*], *BMax*[*y*] and *B2000*[*y*]) produce significantly different *Quasi-static RMS* $CM[y]_{IA\text{-}SK}$ *Parameter* values.

Hypothesis 10: The respective IA optimisation methods applicable for calculating antero-posterior CM displacement (viz. *ZPZP5U*[*y*], *BMax*[*y*] and *B2000*[*y*]) produce significantly different *Airborne RMS CM*[*y*]$_{IA\text{-}SK}$ *Parameter* values.

Hypotheses 7, 8, 9 and 10 were tested using the two-tailed Friedman's one-way repeated-measures rank-order ANOVA[21]. For each test, *p*-levels were determined and reported; the research hypotheses were considered to be supported if *p* was less than 0.05. If significant differences between the methods were found, the relative performance of each method was subsequently considered by examining plots showing the median, range and raw data points of the parameters under investigation. Statistica 7.1 (Stat Soft, Inc., Tulsa, OK., U.S.A.) was used for the aforementioned statistical analyses.

6.1.2.2 Qualitative Assessment

Qualitative assessment of the performance of the antero-posterior methods was conducted by examining the resultant plots of *COP*[*y*](*t*), *CM*[*y*]$_{SK}$(*t*) and *CM*[*y*]$_{IA}$(*t*). Similarly, the performance of the vertical dimension methods was assessed by examining the plots of *CM*[*z*]$_{SK}$(*t*) and *CM*[*z*]$_{IA}$(*t*).

---

[21] Parametric repeated-measures ANOVA/MANOVA approaches were considered inappropriate, due to the small sample size of only six trials and the likelihood of a non-normally distributed population.

6.1.2.3 Practical Assessment Using Jump Performance Parameters.

Further analysis of the vertical dimension IA optimisation methods (viz. *AMax*[*z*], *A2000*[*z*], *BMax*[*z*] and *B2000*[*z*]) was conducted to assess whether they were sufficiently accurate for the common and practical application of determining various measures of jumping performance. The jump performance parameters used in this study included the parameters reported by Hatze (1998) as those most commonly used to characterise jumping performance:

- ***Height$_J$***, the jumping height, representing the increase in vertical CM displacement from take-off to the peak of CM flight trajectory
- ***Height$_P$***, the vertical distance over which the CM is displaced during the upward propulsive phase, representing the increase in vertical CM displacement from the minimum point in the countermovement to the point of take-off
- ***Work$_P$***, the vertical translational work done per kilogram of body mass in accelerating the CM upwards during the upward propulsive phase
- ***Max Power$_P$***, the maximum vertical translational power per kg of body mass during the upward propulsive phase
- ***Ave Power$_P$***, the average vertical translational power per kg of body mass for the upward propulsive phase.

$Height_J$ and $Height_P$ were derived directly from $RelCM[z]_{IA}(t)$ values at relevant points in time, as described above. Note that this method of calculating $Height_P$ produces equivalent results to the method reported by Hatze (1998) and the numerical integration method reported by Kibele (1998). With t_{Pini} and t_{Pfin} denoting the commencement and completion, respectively, of the upward

propulsive phase of the jump, the work done per kg of body mass and the maximum and average power per kg of body mass parameters were calculated as follows (Hatze, 1998):

$$Work_P = -g(Height_J + Height_P) \quad (41)$$

$$Max\ Power_P = \max[(Fz(t) + Fz_O) \times CM'[z]_{IA}(t) / m_{WB}], \text{ for all } t = t_{Pini} \text{ to } t_{Pfin} \quad (42)$$

$$Ave\ Power_P = Work_P / (t_{Pfin} - t_{Pini}) \quad (43)$$

6.1.2.4 Generic Parameter

Another parameter was also defined for comparing the vertical dimension IA optimisation methods, but not as a specific jump performance parameter:

- ***Peak Height***, the height of the CM at the peak of CM flight trajectory, relative to the height of the CM at the start of the pre-jump quasi-static phase. It is equivalent to $RelCM[z]_{IA}(t_{PH})$, which equals $CM[z]_{IA}(t_{PH}) - CM[z]_{IA}(t_{QSini})$, where t_{PH} is the time coinciding with the peak of CM flight and t_{QSini} is the time of commencement of the pre-jump quasi-static stance phase.

The *Peak Height* parameter was included to provide an assessment of $CM[z]_{IA}(t)$ trajectory that would be of more generic relevance to other, less transient activities to which these IA methods might be applicable in the future, such as sit-to-stand or weightlifting activities. Consider *Peak Height versus* $Height_J$. Both measure the CM height at the top of CM flight trajectory, but relative to different starting displacements (initial pre-jump quasi-static CM height *versus* CM height at

take-off, respectively) and over different durations (for this study, a median of approximately 4 s *versus* 0.25 s, respectively). The latter, temporal distinction, means that the cumulative influence of drift errors on $RelCM[z]_{IA}(t)$ calculations will be more pronounced in *Peak Height* measurements than in $Height_J$ measurements. Hence, the *Peak Height* parameter will provide some insight into the ability of the vertical dimension IA optimisation methods to produce accurate $CM[z]_{IA}(t)$ measures over longer periods of time than are captured by the jump performance parameters defined in section 6.1.2.3. The latter are restricted to much shorter durations within the upward propulsive (~0.35 s) and airborne (~0.25 s) phases.

6.1.3 Assessment of the Influence of $CM'[z]_{IA}(0)$, Fz_O and m_{WB}

To demonstrate the relative influence of design variables $CM'[z]_{IA}(0)$ and Fz_O on vertical dimension IA optimisation methods for countermovement jumps, selected perturbations were made to these variables for *Methods A2000*[*z*] and *B2000*[*z*], followed by an assessment of the changes these perturbations produced in the jump performance parameters defined in section 6.1.2.3 and in the more generically applicable parameter defined in section 6.1.2.4. The effect of including m_{WB} as a design variable instead of Fz_O, as per Vanrenterghem et al. (2001), was also assessed.

The solution to the original optimisation problem (i.e. with design variables Fz_O and $CM'[z]_{IA}(0)$; m_{WB} set constant to 62.715 kg) represented the 'baseline' condition (*Condition 1*). The '$CM'[z]_{IA}(0) = 0$' condition (*Condition 2*),

represented setting $CM'[z]_{IA}(0)$ constant to zero[22], as has been common practice by previous researchers (e.g. Kibele, 1998; Vanrenterghem et al., 2001), and Fz_O constant to its originally optimised value for comparative purposes. The 'Fz_O + 1 N' condition (*Condition 3*) represented setting $CM'[z]_{IA}(0)$ constant to its originally optimised value and setting Fz_O constant to its originally optimised value plus a 1 N perturbation[23]. The 'Optimised m_{WB}' condition (*Condition 4*) represented including m_{WB} in the set of design variables and setting Fz_O to a constant value of zero, as per Vanrenterghem et al. (2001).

For each trial and each method, the changes (Δ) in *Peak Height*, $Height_J$, $Height_P$, $Work_P$, $Max\ Power_P$ and $Ave\ Power_P$ produced by the application of *Conditions 2*, *3* and *4*, relative to *Condition 1*, were determined. Hence, for $i = 2$ to *4*, the changes produced by applying *Condition i* were calculated as follows:

$$\begin{aligned}
\Delta\, Peak\ Height_{(Condition\ i)} &= Peak\ Height_{(Condition\ i)} - Peak\ Height_{(Condition\ 1)} \\
\Delta\, Height_{J\,(Condition\ i)} &= Height_{J\,(Condition\ i)} - Height_{J\,(Condition\ 1)} \\
\Delta\, Height_{P\,(Condition\ i)} &= Height_{P\,(Condition\ i)} - Height_{P\,(Condition\ 1)} \\
\Delta\, Work_{P\,(Condition\ i)} &= Work_{P\,(Condition\ i)} - Work_{P\,(Condition\ 1)} \\
\Delta\, Max\ Power_{P\,(Condition\ i)} &= Max\ Power_{P\,(Condition\ i)} - Max\ Power_{P\,(Condition\ 1)} \\
\Delta\, Ave\ Power_{P\,(Condition\ i)} &= Ave\ Power_{P\,(Condition\ i)} - Ave\ Power_{P\,(Condition\ 1)}
\end{aligned} \tag{44}$$

---

[22] This represented a maximum perturbation in $CM'[z]_{IA}(0)$ of 1.6 mms^{-1} across all trials and methods.

[23] A 1 N perturbation represented a 9.1% to 11.4% change in the originally optimised Fz_O values across all trials and methods.

6.1.4 Identification and Zeroing of Airborne Phase GRF Values

The digitised GRF signals did not return precisely to zero when the subject jumped off the surface of the platform, as shown in Fig. 38. Apart from an inherent offset error in the data, the curvilinear nature of the plot in Fig. 38 suggests the presence of other artefacts in the signals, possibly produced by the AMLAB real-time analogue anti-alias low-pass filter and/or hysteresis in the force platform electronics. Regardless of the cause, criteria were established to define when take-off and landing occurred, during which time all force platform signals throughout the flight phase were set to zero. Zeroing the signals prevents a time-dependent cumulative error being introduced to numerically integrated calculations. The criterion adopted for take-off identification was to find the first instant (t_i) in the force platform data in the vicinity of take-off, for which $Fz(t_i) - Fz(t_{i+1}) < 3$ N and $Fz(t_{i+1}) - Fz(t_{i+2}) < 3$ N. All force platform signals for $t \geq t_i$, during the flight phase, were then assigned zero values. Touch-down (t_{TD}), the exclusive end of the airborne phase, was identified by finding the first Fz sample that was greater than the maximum Fz value from the previous 200 ms period, and that is also not followed by another Fz value that is less than the said maximum.

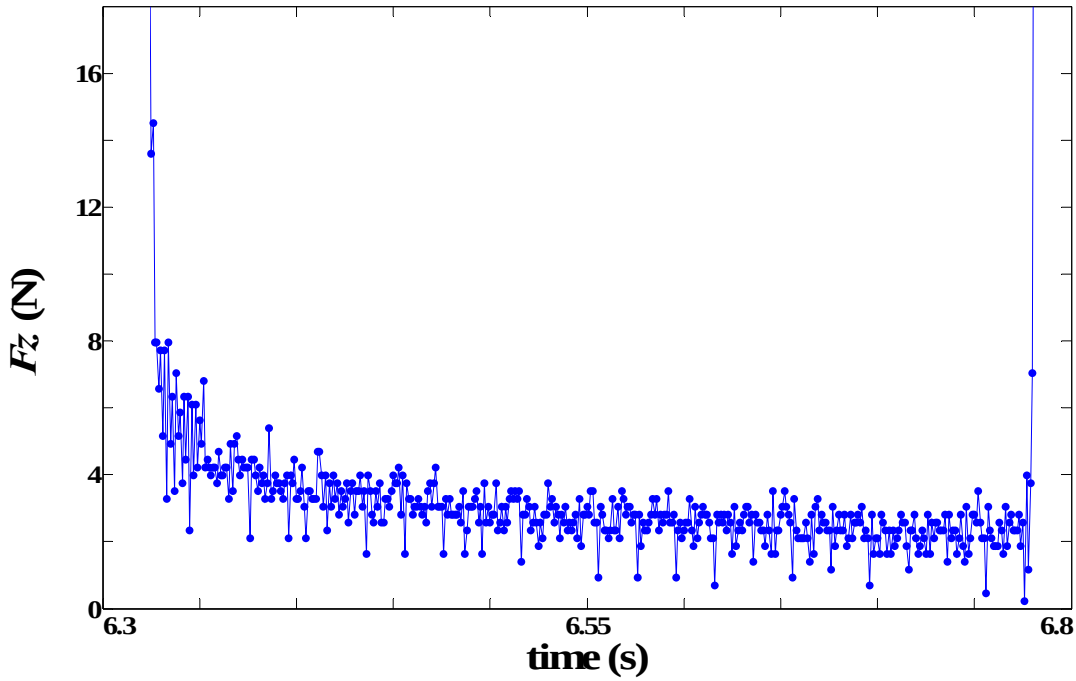

Figure 38. Record of Fz versus time from just prior to the commencement of the airborne phase until just after the completion of the airborne phase of a typical trial captured in this study. Note that Fz does not return to zero during the airborne phase.

6.2 Results

The median and range of quasi-static phase durations across all trials, for each of the IA optimisation methods of variable duration, are shown in Table 9. All such methods have mean durations greater than 3.2 s, or 1.2 s longer than the set 2 s quasi-static duration of the *2000* methods.

Table 9. Median and range values for the duration of the quasi-static phase for all variable-duration methods (N= 6). By definition, the other methods (A2000[*z*]*, B2000*[*z*] *and B2000*[*y*]*) all had quasi-static phases with a set duration of 2000 ms.*

Methods	**Median (ms)**	**Range (ms)**
AMax[*z*], *BMax*[*z*]	3077	2035 – 4698
BMax[*y*]	3518	2179 – 4766
ZPZP5U[*y*]	4030	2240 - 4370

6.2.1 Vertical Dimension Methods

There were no significant differences demonstrated between the performances of any of the vertical dimension IA optimisation methods with respect to their ability to predict quasi-static or airborne *relative CM*$[z]_{IA}(t)$. That is, Hypotheses 7 and 8 were not supported by the results. Table 10 shows the results of the two Friedman rank-order ANOVA tests conducted to assess Hypotheses 7 and 8.

Table 10. Results of the Friedman rank-order ANOVA tests (N = 6) used to assess the vertical IA optimisation methods (Hypotheses 7 and 8).

Hypothesis	Assessment Parameter	Methods Assessed	df	ANOVA χ^2	*p*
7	*Quasi-static RMS* $CM[z]_{IA\text{-}SK}$	*AMax*[*z*], *A2000*[*z*], *BMax*[*z*], *B2000*[*z*]	3	2.6	0.45749
8	*Airborne RMS* $CM[z]_{IA\text{-}SK}$	*AMax*[*z*], *A2000*[*z*], *BMax*[*z*], *B2000*[*z*]	3	2.0	0.57241

All four vertical dimension methods produced lower *Quasi-static RMS* $CM[z]_{IA\text{-}SK}$ *Parameter* values (Eq. (39)) than *Airborne RMS* $CM[z]_{IA\text{-}SK}$ *Parameter* values (Eq. (40)), as is clearly evident from the range plots in Fig. 39.

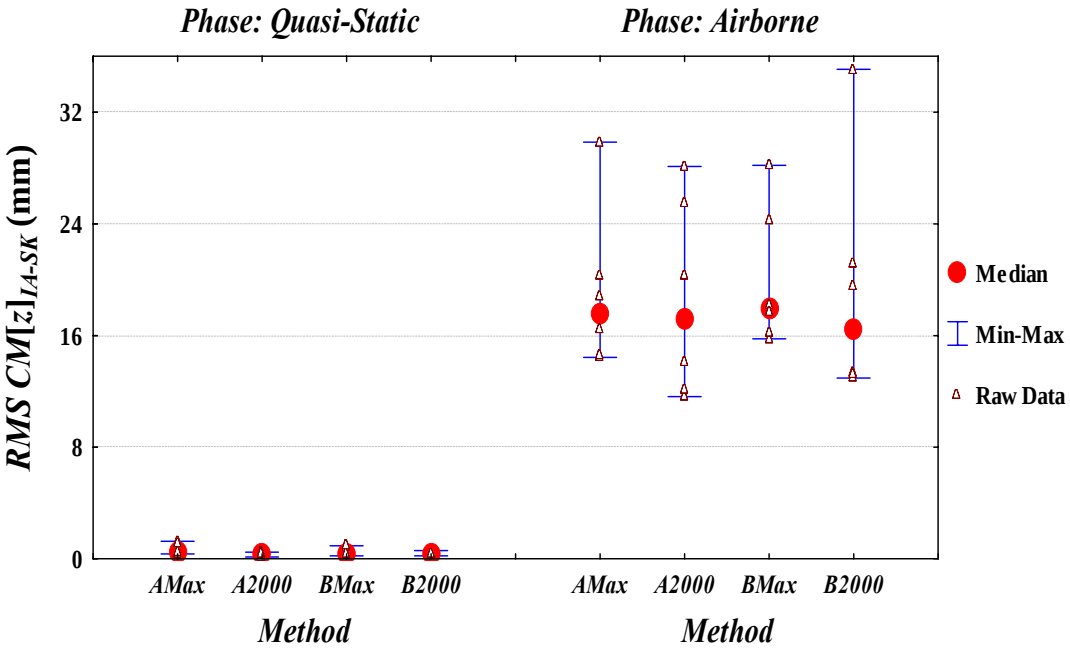

Figure 39. Range plots of Quasi-static and Airborne RMS $CM[z]_{IA\text{-}SK}$ *Parameter values (Eq. (39) and Eq. (40), respectively) across six trials assessed in this research, for each of the four vertical dimension IA optimisation methods, illustrating the relationship between relative* $CM[z]_{IA}$ *and* $CM[z]_{SK}$ *values is significantly closer during the quasi-static phase compared to the airborne phase.*

Fig. 40 shows the plots of *relative* $CM[z]_{IA}(t)$ for a typical countermovement jump (trial '5208'). Only *Methods AMax* and *BMax* are shown due to the similarity of the *A2000* and *B2000* plots for this trial on the scale presented in this figure. If the latter plots had also been included, the only discernable difference, on this scale, would have been the reduced duration of the quasi-static phase to 2 s.

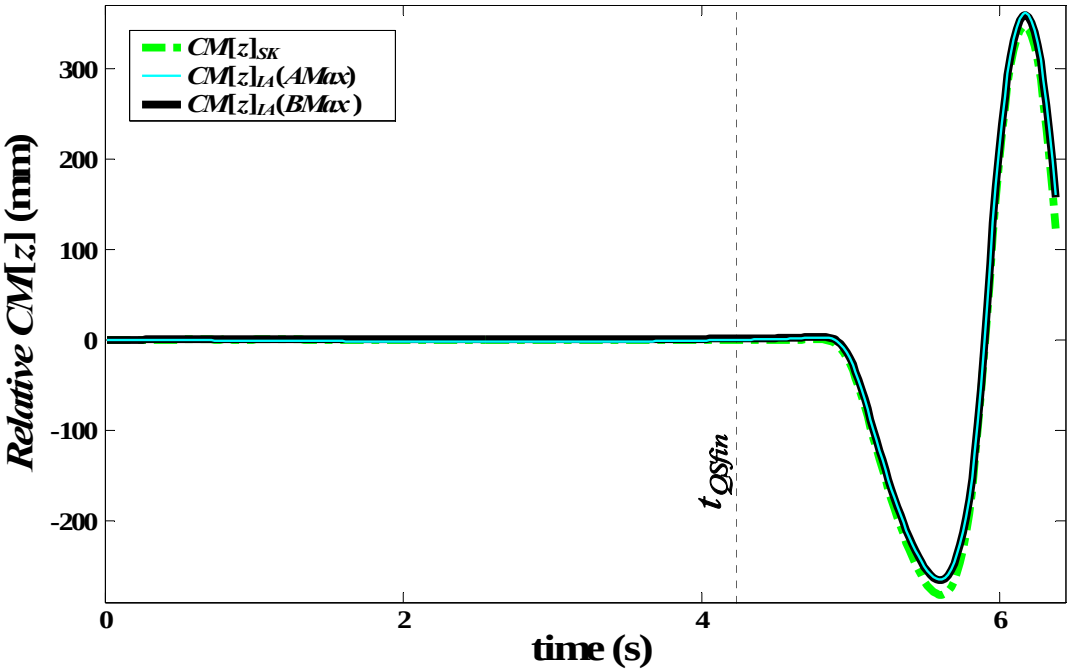

Figure 40. Plots of relative $CM[z]_{IA}(t)$ *and relative* $CM[z]_{SK}(t)$ *for a typical countermovement jump (trial '5208'). Only IA optimisation Methods AMax and BMax are shown up to and including the airborne phase. The end of the defined quasi-static phase is indicated (*t_{QSfin}*).*

For the same trial, the airborne phase *relative* $CM[z]_{IA}(t)$ plots and the *relative* $CM[z]_{SK}(t)$, plot for all four vertical dimension methods, are shown on the re-scaled graph in Fig. 41. Although the plots of *relative* $CM[z]_{IA}(t)$ look very similar on the scale shown in Fig. 40, and despite the statistically insignificant between-methods findings, the re-scaled airborne phase plots in Fig. 41 highlight the actual differences in *Peak Height* produced by the different methods.

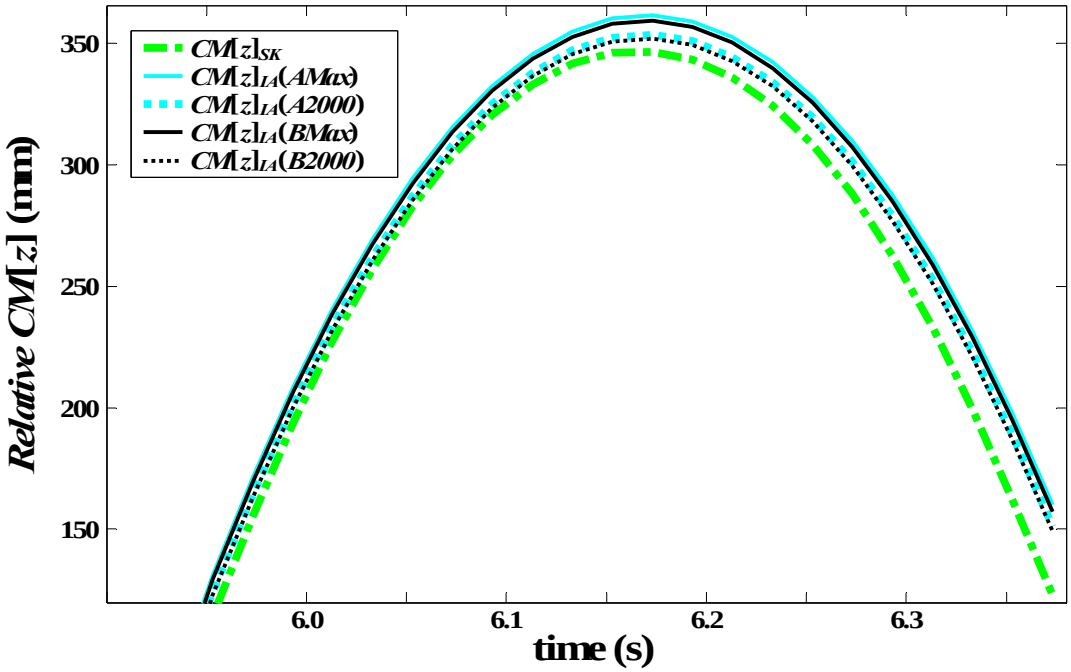

Figure 41. Plots of relative $CM[z]_{IA}(t)$ and relative $CM[z]_{SK}(t)$ for the airborne phase of the same trial as Fig. 40 (trial '5208'). All four vertical dimension IA optimisation methods are shown, with A2000 and B2000 $CM[z]_{IA}(t)$ plots offset relative to the AMax and BMax plots (the offset procedure is explained on page 218 and the rationale for its application is depicted clearly in Fig. 42. Peak Height differences between IA methods of up to 9.2 mm are depicted, with 14.9 mm between the SK method and Method AMax.

All vertical dimension IA optimisation methods consistently estimated *Peak Height* values greater than those calculated by the SK method in each of the six trials, regardless of whether they produced *relative* $CM[z]_{IA}(t)$ values greater or less than *relative* $CM[z]_{SK}(t)$ values in the initial part of the countermovement phase. Across all trials and all IA optimisation methods, differences between IA- and SK-calculated *Peak Height* ranged from 5.2 mm (1.4% of the relevant IA method's calculated *Peak Height*) to 30.9 mm (9.8%). However, from trial-to-trial, differences in *Peak Height* between the four IA optimisation methods varied somewhat less, ranging between 3.2 mm (0.9% of IA-calculated *Peak Height* for the given trial) and 15.1 mm (4.8%).

Tables 11 and 12 show all jump performance parameters for all trials and the maximum differences across all four vertical dimension IA methods for each parameter and each trial. Compared with the more transient jump performance parameters defined in section 6.1.2.3 produced differences between the four IA methods that were much smaller. There was a maximum of only 0.7% difference among all four vertical dimension methods for any of the jump performance parameters across all 6 trials. For instance, this equated to a maximum difference of 2.5 mm for $Height_P$.

Table 11. Jump performance parameters $Height_J$ and $Height_P$ that resulted from the application of each of the vertical dimension IA methods for all six trials, and the maximum between-method differences expressed in absolute terms (mm) and as a percentage (%) of the maximum parameter value produced for that trial (the bolded result in the relevant row). It is evident that no particular method consistently produced the largest or smallest values across all trials.

	***AMax*[*z*]**	***A2000*[*z*]**	***BMax*[*z*]**	***B2000*[*z*]**	**Maximum Difference**	
***Height*$_J$ (mm)**					**mm**	**(%)**
'5208'	**261.8**	260.6	261.2	260.3	1.5	0.6%
'5209'	224.5	225.2	224.9	**226.1**	1.6	0.7%
'5210'	227.6	**228.0**	227.1	226.8	1.2	0.5%
'5211'	271.9	271.6	**272.3**	271.4	0.9	0.3%
'5212'	**259.7**	259.2	259.6	259.3	0.5	0.2%
'5217'	258.0	258.3	**259.0**	**259.0**	1.0	0.4%
***Height*$_P$ (mm)**					**mm**	**(%)**
'5208'	**365.0**	363.3	364.1	362.9	2.1	0.6%
'5209'	344.4	345.6	345.0	**346.9**	2.5	0.7%
'5210'	341.2	**342.0**	340.4	339.8	2.2	0.6%
'5211'	395.4	395.0	**395.9**	394.7	1.2	0.3%
'5212'	**355.0**	354.3	354.8	354.5	0.7	0.2%
'5217'	493.6	494.0	**495.4**	495.3	1.8	0.4%

Table 12. Jump performance parameters $Work_P$, Max $Power_P$ and Ave $Power_P$ that resulted from the application of each of the vertical dimension IA methods for all six trials, and the maximum between-method differences expressed in absolute terms (J/kg or W/kg) and as a percentage (%) of the maximum parameter value produced for that trial (the bolded result in the relevant row). It is evident that no particular method consistently produced the largest or smallest values across all, or even most trials for these parameters.

	***AMax*[z]**	***A2000*[z]**	***BMax*[z]**	***B2000*[z]**	**Maximum Difference**	
***Work*$_P$ (J/kg)**					**J/kg**	**(%)**
'5208'	**6.14**	6.11	6.13	6.11	0.03	0.5%
'5209'	5.57	5.59	5.58	**5.61**	0.04	0.7%
'5210'	5.57	**5.59**	5.56	5.55	0.04	0.7%
'5211'	7.37	7.37	**7.39**	**7.39**	0.02	0.3%
'5212'	6.54	6.53	**6.55**	6.53	0.02	0.3%
'5217'	**6.02**	6.01	**6.02**	6.01	0.01	0.2%
***Max Power*$_P$ (W/kg)**					**W/kg**	**(%)**
'5208'	**47.43**	47.31	47.37	47.29	0.14	0.3%
'5209'	43.46	43.53	43.50	**43.62**	0.16	0.4%
'5210'	45.42	**45.46**	45.37	45.33	0.13	0.3%
'5211'	47.75	47.73	**47.79**	47.70	0.09	0.2%
'5212'	**48.02**	47.98	**48.02**	47.99	0.04	0.1%
'5217'	46.37	46.40	**46.47**	**46.47**	0.10	0.2%
***Ave Power*$_P$ (W/kg)**					**W/kg**	**(%)**
'5208'	**18.12**	18.09	18.08	18.07	0.05	0.3%
'5209'	**15.66**	15.63	15.64	15.60	0.06	0.4%
'5210'	**14.01**	14.00	**14.01**	13.98	0.03	0.2%
'5211'	18.85	18.83	**18.87**	18.86	0.04	0.2%
'5212'	18.70	18.73	18.70	**18.74**	0.04	0.2%
'5217'	17.41	17.43	**17.44**	**17.44**	0.03	0.2%

Fig. 42 shows the plots for the same trial as depicted in Figs. 40 and 41, but re-scaled to cover only the quasi-static phase and the early part of the countermovement phase. This figure helps to explain why an offsetting procedure was applied to the *A2000* and *B2000 relative* $CM[z]_{IA}(t)$ plots in Figs. 41, 42 and 43. Because the *Max* and *2000* methods produce different $CM[z]_{IA}(t_{QSini})$ values, the *A2000* and *B2000 relative* $CM[z]_{IA}(t)$ plots have been adjusted with respect to the *AMax* and *BMax* plots to enable a valid graphical comparison of all the $CM[z]$ plots. This was done by offsetting the *A2000* and *B2000 relative* $CM[z]_{IA}(t)$ plots by a value of $-CM[z]_{SK}(t_{QSini\ (2000)})$, represented graphically below by the difference between the horizontal axis and the horizontal dotted line below it.

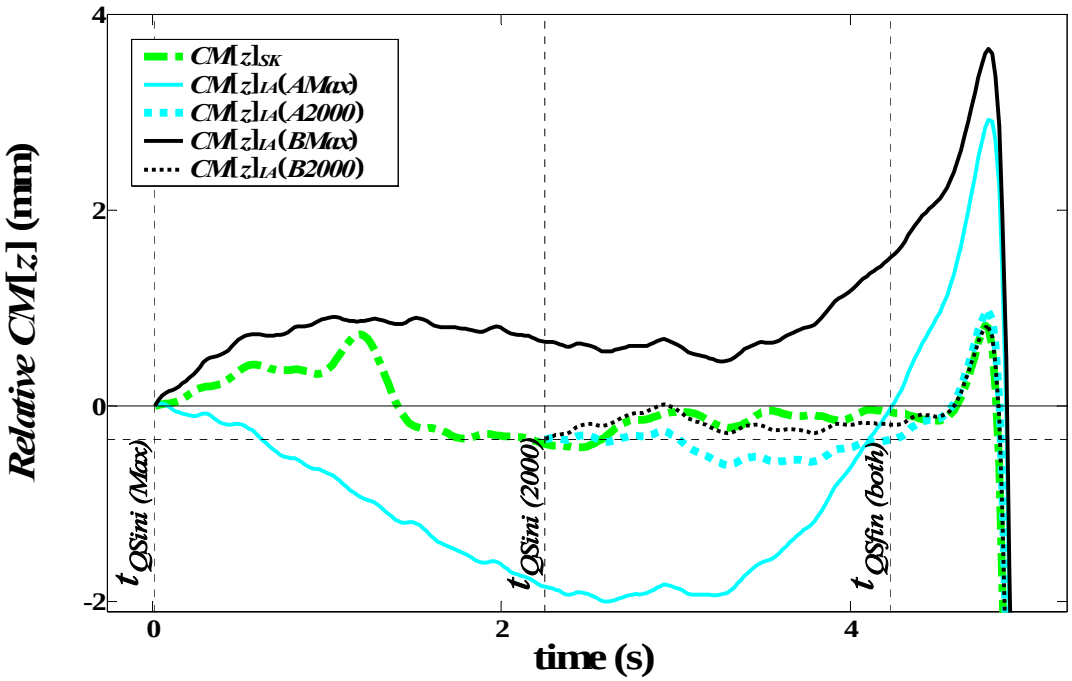

Figure 42. Plots of relative $CM[z]_{IA}(t)$ *and relative* $CM[z]_{SK}(t)$ *for the quasi-static phase and the start of the countermovement phase of trial '5208'. The A2000 and B2000 relative* $CM[z]_{IA}(t)$ *plots are adjusted with respect to the AMax and BMax plots, as described in the above text, to enable a valid graphical comparison. The start of the quasi-static phases, as defined by the Max and 2000 methods, and the end of the quasi-static phase, which has a common definition in both methods, are shown here as* $t_{QSini\ (Max)}$, $t_{QSini\ (2000)}$ *and* $t_{QSfin\ (both)}$, *respectively.*

Fig. 43 shows a zoomed-in section of the same plots from the same trial as the preceding figures, but this time showing the airborne and landing phases. The *relative* $CM[z]_{SK}(t)$ plot shows the expected behaviour in the landing phase, with the plot returning to an essentially stable value of zero. Contrastingly, all the IA optimisation methods produced *relative* $CM[z]_{IA}(t)$ values that drifted away from the known quasi-static ending. This observation led to the development of further analysis aimed to produce a better understanding of the observed drift (see Section 6.2.4).

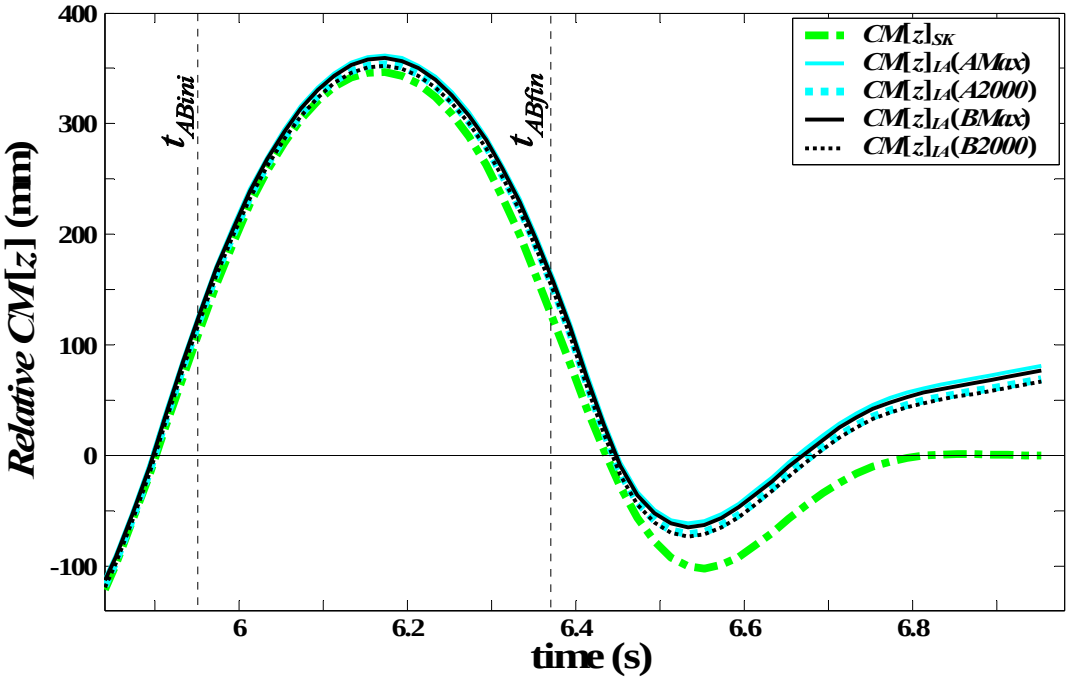

Figure 43. Plots of relative $CM[z]_{IA}(t)$ *and relative* $CM[z]_{SK}(t)$ *for the airborne and landing phases of the same trial as Figs. 40, 41 and 42 (trial '5208'). The A2000 and B2000 relative* $CM[z]_{IA}(t)$ *plots are adjusted with respect to the AMax and BMax plots, as described on page 218. The start and finish of the airborne phase are indicated by* t_{ABini} *and* t_{ABfin}*, respectively.*

In the example depicted in Figs. 40, 41, 42 and 43, the *2000* methods produced better matches with the SK method results in the quasi-static and early

countermovement phases than did the *Max* methods. Subsequently, they produced better results in the airborne phase (Fig. 41). For each trial, the method that most closely matched the SK method in the late quasi-static and early countermovement phase was consistently also the method that performed better in the airborne phase. However, as the statistical results suggested, different methods performed better in different trials, with no trends evident in what was a small sample.

The $CM'[z]_{IA}(0)$ bound constraint (Eq. (29)) never became active for any of the vertical dimension IA optimisation methods, with values always confined within the range of ±3 mm. The Fz_O bound constraint (Eq. (30)) never became active either. Across the six trials and the four vertical dimension IA optimisation methods, the optimised value of Fz_O ranged between -10.97 and -8.75 N. This range of values was deemed realistic for the force platform used in this research[24].

6.2.2 Antero-Posterior Dimension Methods

Table 13 shows the results of the two Friedman rank-order ANOVA tests that were conducted to assess the performance of the antero-posterior dimension IA optimisation methods (Hypotheses 9 and 10). There were no significant differences demonstrated between the performances of any of the antero-posterior dimension IA optimisation methods with respect to their ability to predict airborne

[24] When a 633.75 N dead weight was placed in 26 different locations spread across the surface of the force platform, the Fz_O values that produced de-trended Fz signals averaged -11.98 N with a standard deviation of 1.61 N. Hence, the mean ± 3SD range of Fz_O values was -16.81 to -7.15 N.

relative CM[*y*]$_{IA}$(*t*). However, there was strong evidence ($p < 0.01$) to suggest that differences existed between the methods with respect to the quasi-static phase.

Table 13. Results of the Friedman rank-order ANOVA tests (N = 6) used to assess the antero-posterior IA optimisation methods (Hypotheses 9 and 10).

Hypothesis	**Assessment Parameter**	**Methods Assessed**	**df**	**ANOVA χ^2**	***p***
9	*Quasi-static RMS CM*[*y*]$_{IA\text{-}SK}$	*ZPZP5U*[*y*], *BMax*[*y*], *B2000*[*y*]	2	10.3	0.00570
10	*Airborne RMS CM*[*y*]$_{IA\text{-}SK}$	*ZPZP5U*[*y*], *BMax*[*y*], *B2000*[*y*]	2	2.3	0.31140

Fig. 44 shows the range plots of the three antero-posterior dimension IA optimisation methods for the *Quasi-static RMS CM*[*y*]$_{IA\text{-}SK}$ *Parameter* (Eq. (37)) data across all trials, clearly showing that the *ZPZP5U* method produced the best results (i.e. the lowest RMS values).

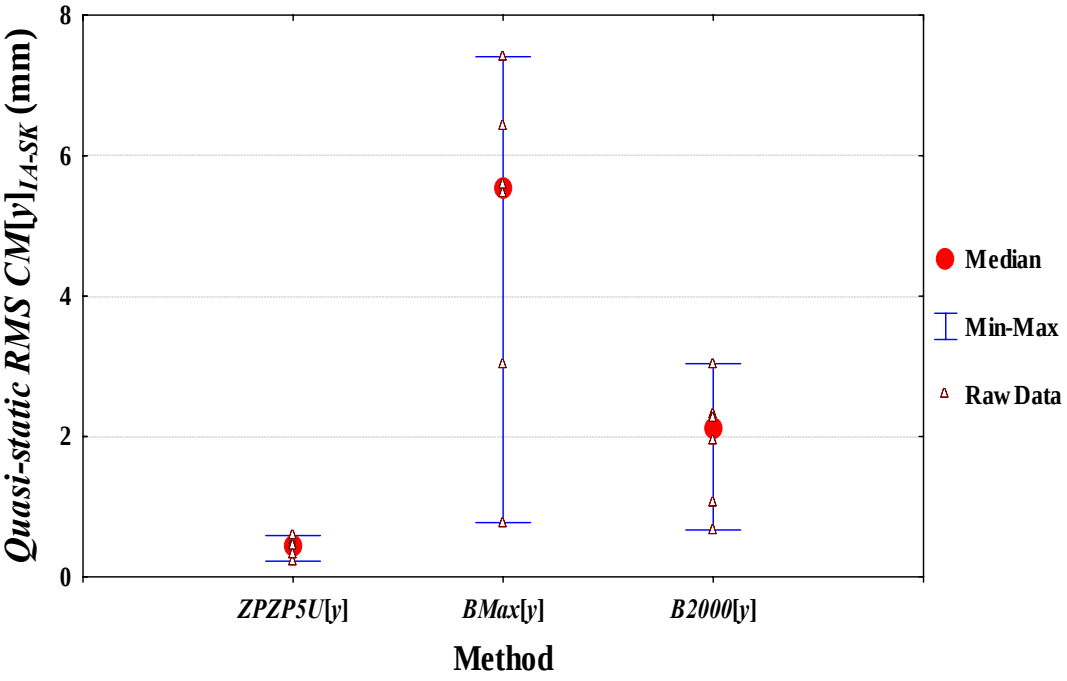

Figure 44. Range plot showing the median, range and raw data points of the Quasi-static RMS $CM[y]_{IA\text{-}SK}$ Parameter values (Eq. (37)) across the six trials assessed in this research, for the three antero-posterior dimension IA optimisation methods (ANOVA χ^2 [df = 2, N = 6] = 10.3, p = 0.00570).

The finding that *ZPZP5U* produced the best results is exemplified by comparing the respective *relative* $CM[y]_{IA}(t)$ plots of the three antero-posterior dimension IA optimisation methods to the *relative* $CM[y]_{SK}(t)$ plot for a typical trial (trial '5210'), as shown in Fig. 45. The *ZPZP5U relative* $CM[y]_{IA}(t)$ plot is accompanied by the *relative* $COP[y]$ plot and the location of the associated IEPs. Because the *ZPZP5U* and *B2000* methods produce different initial trial start times and, therefore, different initial $CM[y]_{IA}$ values, the *ZPZP5U* and *B2000 relative* $CM[y]_{IA}(t)$ plots have been adjusted with respect to the *BMax* plot to enable a valid graphical comparison. This was done by offsetting the *ZPZP5U* and *B2000 relative* $CM[y]_{IA}(t)$ plots by values of $-CM[y]_{SK}(t_{QSini\ (ZPZP5U)})$ and $-CM[y]_{SK}(t_{QSini\ (B2000)})$, respectively.

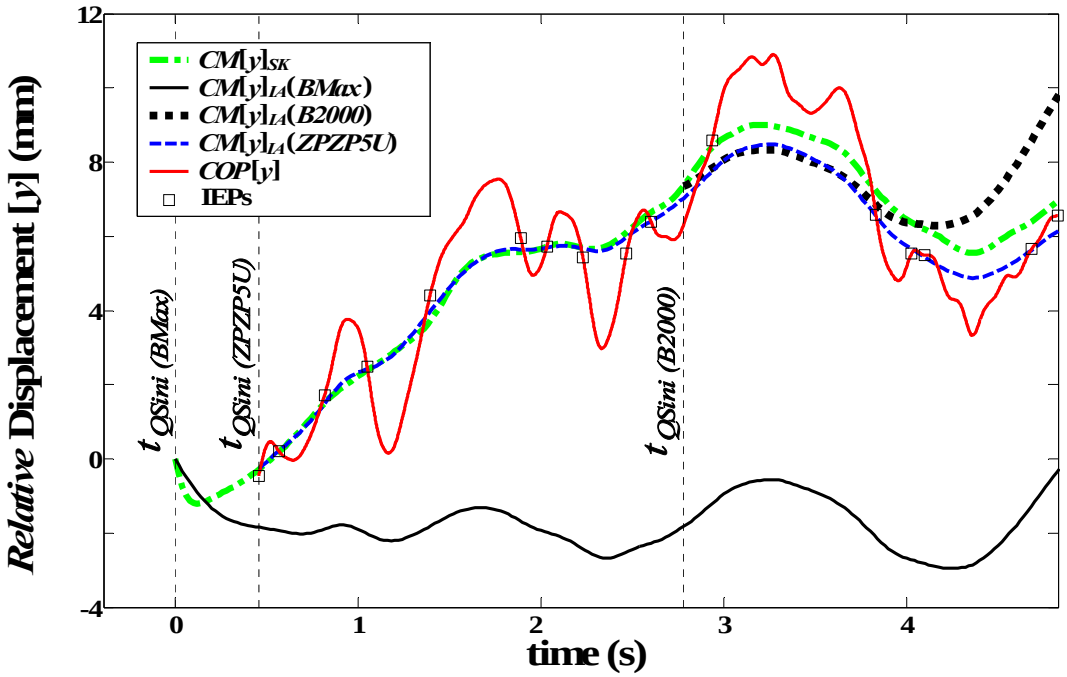

Figure 45. Plots of relative CM[y]$_{IA}$(t), relative CM[y]$_{SK}$(t) and relative COP[y](t) for the quasi-static phase for trial '5210'. All three antero-posterior [y] dimension IA optimisation methods are shown, with the relative COP[y](t) plot and the ZPZP5U and B2000 relative CM[y]$_{IA}$(t) plots adjusted with respect to the BMax plot, as described on page 222, to enable a valid graphical comparison. The start of the quasi-static phases, as defined by the BMax, B2000 and ZPZP5U methods, are shown here as $t_{QSini\ (BMax)}$, $t_{QSini\ (B2000)}$ and $t_{QSini\ (ZPZP5U)}$, respectively.

Fig. 46 shows the same *relative CM*[y]$_{IA}$(t) plots, but this time re-scaled for the entire quasi-static, countermovement and airborne phases. It demonstrates that, for this particular trial, the method that performed best in the quasi-static phase (*ZPZP5U*) was not the best performer in the airborne phase. Despite the fact that *BMax* performed most poorly of all three methods in the quasi-static phase for the trial depicted in Fig. 46, it was the best performer in the airborne phase for this particular trial.

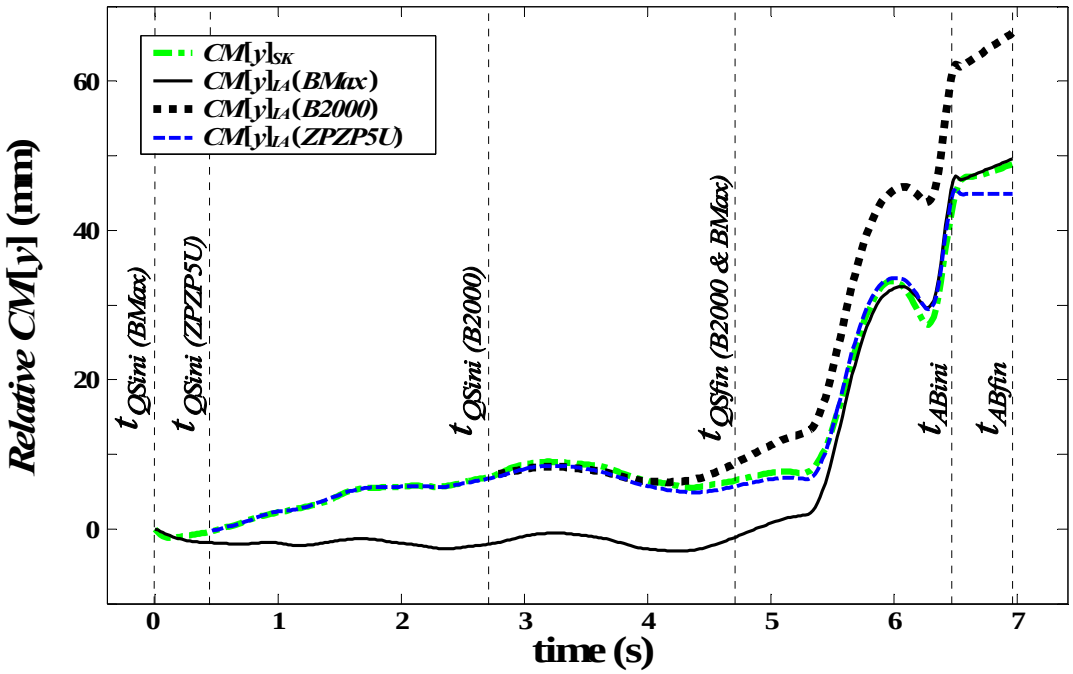

Figure 46. Plots of relative CM[y]$_{IA}$(t) and relative CM[y]$_{SK}$(t) for the quasi-static, countermovement and airborne phases for the same trial as depicted in Fig. 45 (trial '5210'). The ZPZP5U and B2000 relative CM[y]$_{IA}$(t) plots are adjusted with respect to the BMax plot, as described on page 222, to enable a valid graphical comparison. $t_{QSini\ (BMax)}$, $t_{QSini\ (B2000)}$ and $t_{QSini\ (ZPZP5U)}$ denote the start of the quasi-static phases, as defined by the three antero-posterior [y] methods. The end of the quasi-static stance phase (t_{QSfin}) is also shown, as are the start and finish of the airborne phase (t_{ABini} and t_{ABfin}).

The TOL_{ini} and TOL_{fin} design variable bound constraints (Eq. (33)) never became active for the *ZPZP5U* method. Values for all trials were between ±1 mm, except for a single case for TOL_{ini} of 1.27 mm. The $CM'[y]_{IA}(0)$ bound constraint (Eq. (33)) never became active, with all $CM'[y]_{IA}(0)$ values falling within a range of ±15 mm. The Fy_O bound constraint (Eq. (34)) never became active either. Across all six trials and the three antero-posterior dimension IA optimisation

methods, the optimised value of Fy_O ranged between -1.69 and 1.83 N, which was deemed realistic for the force platform used in this research[25].

6.2.3 The Influence of $CM'[z]_{IA}(0)$, Fz_O and m_{WB}

The influence of selected perturbations of design variables $CM'[z]_{IA}(0)$ and Fz_O on various jump performance parameters and one generic parameter was assessed for *Methods A2000*[*z*] and *B2000*[*z*]. Table 14 summarises the changes in selected jump performance parameters caused by setting $CM'[z]_{IA}(0)$ to zero, as described in section 6.1.3 (i.e. *Condition 2*). The maximum, mean and SD across all six trials for each of *Methods A2000*[*z*] and *B2000*[*z*] are reported for $\Delta\, Height_{J\ (Condition\ 2)}$, $\Delta\, Height_{P\ (Condition\ 2)}$, $\Delta\, Work_{P\ (Condition\ 2)}$, $\Delta\, Max\ Power_{P\ (Condition\ 2)}$ and $\Delta\, Ave\ Power_{P\ (Condition\ 2)}$, both in absolute terms and, except for SD, as a percentage of the relevant parameter value derived from the originally optimised solutions (i.e. *Condition 1*). The magnitude of $CM'[z]_{IA}(0)$ did not exceed 0.9 mms^{-1} for all but one of the originally optimised trials (*Condition 1*) for *Methods A2000*[*z*] and *B2000*[*z*]; it was 1.6 mms^{-1} for one trial for *Method B2000*[*z*]. Setting these values to zero for *Condition 2* produced negligible change in all of the jump performance parameters (i.e. never more than a 0.2% change).

---

[25] When a 633.75 N dead weight was placed in 26 different locations spread across the surface of the force platform, the Fy_O values that produced de-trended *Fy* signals averaged 0.65 N with a standard deviation of 0.95 N. Hence, the mean ± 3SD range of Fy_O values was -2.20 to 3.50 N.

Table 14. For Methods A2000[z] and B2000[z], the maximum, mean and SD of the changes (Δ) in the jump performance parameters $Height_J$, $Height_P$, $Work_P$, $Max\ Power_P$ and $Ave\ Power_P$ (all defined in section 6.1.2.3) across all trials, produced by setting $CM'[z]_{IA}(0)$ to zero (Condition 2). These changes are expressed in absolute terms (mm, J/kg or W/kg) and, except for SD, as percentages (%) of the parameter values derived from the originally optimised solutions (Condition 1). Negative values denote reductions.

Condition 2: 'CM'[z]$_{IA}$(0) = 0'		***A2000[z]***		***B2000[z]***	
Δ *Height$_J$* (*Condition 2*)		**mm**	**(%)**	**mm**	**(%)**
	Max	-0.09	0.0%	-0.34	-0.1%
	Mean	-0.07	0.0%	-0.09	0.0%
	SD	0.02		0.18	
Δ *Height$_P$* (*Condition 2*)		**mm**	**(%)**	**mm**	**(%)**
	Max	-0.16	0.0%	-0.62	-0.2%
	Mean	-0.11	0.0%	-0.14	0.0%
	SD	0.05		0.31	
Δ *Work$_P$* (*Condition 2*)		**J/kg**	**(%)**	**J/kg**	**(%)**
	Max	0.00	0.0%	-0.01	-0.2%
	Mean	0.00	0.0%	0.00	0.0%
	SD	0.00		0.00	
Δ *Max Power$_P$* (*Condition 2*)		**W/kg**	**(%)**	**W/kg**	**(%)**
	Max	-0.01	0.0%	-0.04	-0.1%
	Mean	-0.01	0.0%	-0.01	0.0%
	SD	0.00		0.02	
Δ *Ave Power$_P$* (*Condition 2*)		**W/kg**	**(%)**	**W/kg**	**(%)**
	Max	-0.01	0.0%	-0.03	-0.2%
	Mean	0.00	0.0%	-0.01	0.0%
	SD	0.00		0.02	

Table 15 summarises the changes in selected jump performance parameters caused by the perturbations to Fz_O, as described in section 6.1.3 (i.e. *Condition 3*). The results indicate clearly that perturbing Fz_O by 1 N[26] produced much larger changes in the calculated jump performance parameters than applying *Condition 2*, with maximum differences across all trials ranging between 4% and 11% for the five jump performance parameters. For example, the maximum change in $Height_P$ across all six trials was 37.7 mm, which represented an 11.0% increase in $Height_P$ for *Condition 3*, compared with *Condition 1*.

[26] A 1 N perturbation represented a 9.1% to 11.4% change in the originally optimised Fz_O values across all trials and methods.

Table 15. For Methods A2000[z] and B2000[z], the maximum, mean and SD of the changes (Δ) in the jump performance parameters $Height_J$, $Height_P$, $Work_P$, Max $Power_P$ and Ave $Power_P$ (all defined in section 6.1.2.3) across all trials, produced by perturbing the originally optimised Fz_O value by +1 N (Condition 3). These changes are expressed in absolute terms (mm, J/kg or W/kg) and, except for SD, as percentages (%) of the parameter values derived from the originally optimised solutions (Condition 1). Negative values denote reductions.

Condition 3: 'Fz_O + 1 N'		***A2000*[z]**		***B2000*[z]**	
Δ *$Height_J$* (*Condition 2*)		**mm**	**(%)**	**mm**	**(%)**
	Max	20.5	9.0%	20.2	8.9%
	Mean	15.8	6.4%	15.8	6.4%
	SD	2.8		2.7	
Δ *$Height_P$* (*Condition 2*)		**mm**	**(%)**	**mm**	**(%)**
	Max	37.7	11.0%	36.9	10.9%
	Mean	25.2	6.7%	25.1	6.6%
	SD	7.6		7.3	
Δ *$Work_P$* (*Condition 2*)		**J/kg**	**(%)**	**J/kg**	**(%)**
	Max	0.57	10.2%	0.56	10.1%
	Mean	0.40	6.5%	0.40	6.5%
	SD	0.10		0.10	
Δ *Max $Power_P$* (*Condition 2*)		**W/kg**	**(%)**	**W/kg**	**(%)**
	Max	2.10	4.6%	2.08	4.6%
	Mean	1.51	3.3%	1.51	3.3%
	SD	0.32		0.31	
Δ *Ave $Power_P$* (*Condition 2*)		**W/kg**	**(%)**	**W/kg**	**(%)**
	Max	0.72	4.1%	0.72	4.1%
	Mean	0.04	0.2%	0.04	0.1%
	SD	0.42		0.42	

Table 16 summarises the changes in the jump performance parameters caused by including m_{WB} as a design variable whilst holding Fz_O constant at zero, as described in section 6.1.3 (i.e. *Condition 4*). Optimising m_{WB} and setting Fz_O to zero produced changes in the calculated jump performance parameters, with maximum differences across all trials ranging between 1.7% and 5.0% for the five jump performance parameters. For example, in absolute terms across all six trials, the maximum decrease in $Height_P$ produced for *Method A2000*[*z*] was 13.7 mm.

Table 16. For Methods A2000[z] and B2000[z], the maximum, mean and SD of the changes (Δ) in the jump performance parameters $Height_J$, $Height_P$, $Work_P$, $Max\ Power_P$ and $Ave\ Power_P$ (all defined in section 6.1.2.3) across all trials, produced by including m_{WB} as a design variable and setting Fz_O to zero (Condition 4). These changes are expressed in absolute terms (mm, J/kg or W/kg) and, except for SD, as percentages (%) of the parameter values derived from the originally optimised solutions (Condition 1). Negative values denote reductions.

***Condition 4:* 'Optimised m_{WB}'**		***A2000*[z]**		***B2000*[z]**	
Δ $Height_J$ (*Condition 2*)		**mm**	**(%)**	**mm**	**(%)**
	Max	-11.9	-5.0%	-9.0	-3.5%
	Mean	-10.6	-4.2%	-7.7	-3.1%
	SD	1.3		0.7	
Δ $Height_P$ (*Condition 2*)		**mm**	**(%)**	**mm**	**(%)**
	Max	-13.7	-3.7%	-8.6	-1.7%
	Mean	-10.2	-2.7%	-6.0	-1.6%
	SD	2.5		1.3	
Δ $Work_P$ (*Condition 2*)		**J/kg**	**(%)**	**J/kg**	**(%)**
	Max	-0.25	-4.2%	-0.17	-2.3%
	Mean	-0.20	-3.3%	-0.13	-2.2%
	SD	0.04		0.02	
Δ $Max\ Power_P$ (*Condition 2*)		**W/kg**	**(%)**	**W/kg**	**(%)**
	Max	-1.59	-3.5%	-1.23	-2.6%
	Mean	-1.39	-3.0%	-1.11	-2.4%
	SD	0.15		0.08	
Δ $Ave\ Power_P$ (*Condition 2*)		**W/kg**	**(%)**	**W/kg**	**(%)**
	Max	-0.51	-2.9%	-0.41	-2.3%
	Mean	-0.40	-2.3%	-0.37	-2.2%
	SD	0.08		0.04	

Table 17 summarises the changes in the generic parameter *Peak Height* (defined in section 6.1.2.4) produced by applying *Conditions 2*, *3* and *4* (defined in section 6.1.36.1.4). For each of *Conditions 2*, *3* and *4*, the effects on the generic parameter were clearly greater than the effects on the jump performance displacement parameters $\Delta\, Height_P$ and $\Delta\, Height_J$ reported in Tables 14, 15 and 16.

Table 17. For Methods A2000[z] and B2000[z], the maximum, mean and SD of the changes (Δ) in the generic parameter Peak Height (defined in section 6.1.2.4) across all trials, produced by setting $CM'[z]_{IA}(0)$ to zero (Condition 2), perturbing the originally optimised Fz_O value by +1 N (Condition 3), and including m_{WB} as a design variable and setting Fz_O to zero (Condition 4). These changes are expressed in absolute terms (mm) and, except for SD, as percentages (%) of the parameter values derived from the originally optimised solutions (Condition 1). Negative values denote reductions.

		***A2000*[z]**		***B2000*[z]**	
		mm	**(%)**	**mm**	**(%)**
Δ *Peak Height* **(*Condition 2*)**	**Max**	-2.3	-0.7%	-9.5	-2.9%
('$CM'[z]_{IA}(0) = 0$')	**Mean**	-1.4	-0.4%	-2.1	-0.6%
	SD	0.7		4.4	
Δ *Peak Height* **(*Condition 3*)**	**Max**	292.1	84.1%	284.9	85.8%
('Fz_O + 1 N')	**Mean**	170.5	47.5%	169.3	47.5%
	SD	66.5		63.9	
Δ *Peak Height* **(*Condition 4*)**	**Max**	-56.5	-16.3%	-11.2	-2.9%
('Optimised m_{WB}')	**Mean**	-31.6	-8.8%	-9.4	-2.6%
	SD	14.1		0.9	

6.2.4 Additional Analysis of Drift

The observation that the IA optimisation methods produced *relative* $CM_{IA}(t)$ values that drifted away from the known quasi-static ending led to the conduct of further analysis not originally planned nor described in the research design section of this chapter. This additional analysis was designed to categorise any observed drift as either linear or quadratic in nature and was only possible for trials containing a post-jump quasi-static stance phase. Such data were only available from four of the six trials (viz. three of the countermovement jumps: trials '5209', '5211', '5212'; and the broad jump: trial '5217'), so these trials are presented as case studies. The additional analysis is now defined, followed by presentation of the results for *Methods B2000*[*z*] and *ZPZP5U*[*y*].

Firstly, for each trial, for all t in each dimension, $CM_{IA}(t)$ was subtracted from $CM_{SK}(t)$. These quantities were then numerically differentiated using first order central difference equations (Miller and Nelson, 1973), as per Eqs. (18). The resultant first derivatives, $CM'_{SK\text{-}IA}(t)$, represent $CM'_{IA}(t)$ relative to $CM'_{SK}(t)$. The first derivative was chosen for the following figures because it more clearly depicts the linear or quadratic nature of any drift errors that were detected, as described below. Only the pre- and post-jump quasi-static stance phase sections of the $CM'_{SK\text{-}IA}(t)$ plot are meaningful in terms of describing the drift. This is because the SK method of determining $CM(t)$ is prone to errors during the countermovement, propulsive and landing phases due to potential BSP errors coupled with the reorientation of the segments relative to each other during these phases. For example, Fig. 47 shows $CM'[z]_{SK\text{-}IA}(t)$ plotted against the right vertical axis for trial '5209'. *Relative* $CM[z]_{SK}(t)$ and *relative* $CM[z]_{IA}(t)$ produced

by *Method B2000* are plotted against the left vertical axis for reference. For the reasons just described, the plot of $CM'[z]_{SK\text{-}IA}(t)$ is clearly erratic during the dynamic phases (shaded) making it impossible to identify drift trends during these phases.

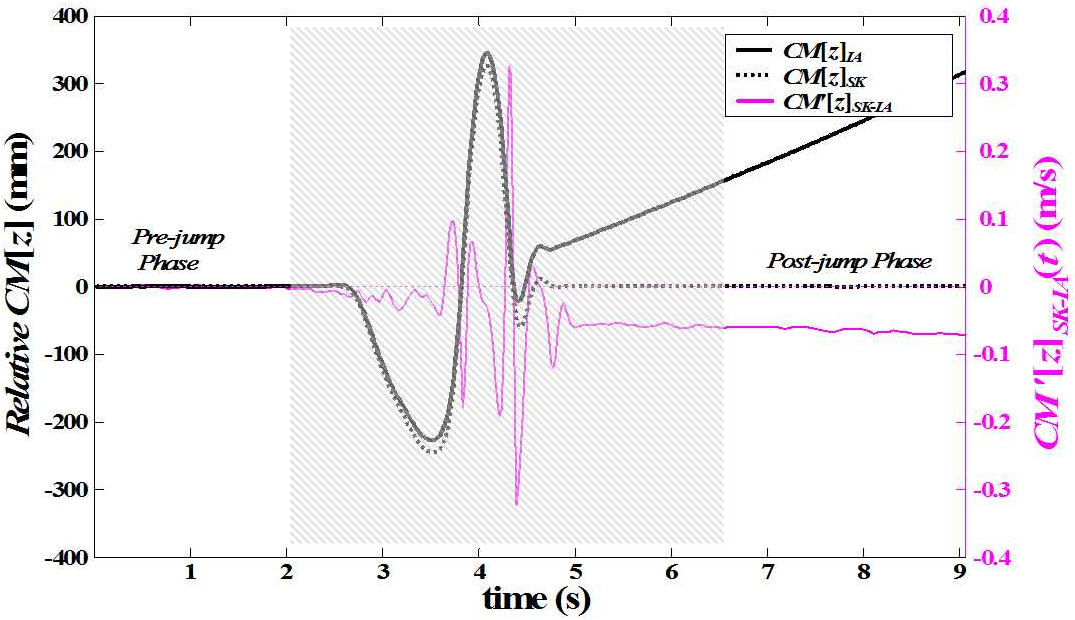

Figure 47. Plots of relative $CM[z]_{SK}(t)$, relative $CM[z]_{IA}(t)$ and $CM'[z]_{SK\text{-}IA}(t)$ for Method B2000[z] (trial '5209'). This full-scale graph shows the relatively erratic behaviour of the $CM'[z]_{SK\text{-}IA}(t)$ plot during the dynamic phases of the trial (shaded) and its relative consistency during the pre- and post-jump quasi-static phases.

Whereas the behaviour of $CM'[z]_{SK\text{-}IA}(t)$ is relatively erratic during the dynamics phases, it is relatively linear during the quasi-static phases[27]. Hence, linear regression lines were fitted separately to the $CM'[z]_{SK\text{-}IA}(t)$ data of the pre-jump

[27] The slight fluctuations in $CM'[z]_{SK\text{-}IA}(t)$ during the quasi-static phases are most likely explained by differentiation-induced amplification of the noise that is inherent in the $CM[z]_{SK}(t)$ component of this quantity.

and post-jump quasi-static phases. Table 18 summarises the gradients of these regression lines across the four relevant trials for *Methods B2000*[*z*] and *ZPZP5U*[*y*]. It can be seen that the gradient was very close to zero for all the pre-jump quasi-static phases, being equal to or less than 0.0008 in magnitude in all such cases. In only one case (trial '5211'; *ZPZP5U*[*y*]) was the magnitude of the post-jump gradient equal to or less than the magnitude of the gradient of the corresponding pre-jump gradient. All the other post-jump gradients were within a range of 1.8 to 100 times greater than the magnitudes of the corresponding pre-jump gradients.

Table 18. Gradients of the linear regression lines fitted to the $CM'_{SK\text{-}IA}(t)$ data separately for the pre- and post-jump quasi-static (QS) phases across the four relevant trials for Methods B2000[*z*] *and ZPZP5U*[*y*].

Trial	***B2000*[*z*]**		***ZPZP5U*[*y*]**	
	Pre-jump QS	***Post-jump QS***	***Pre-jump QS***	***Post-jump QS***
'5209'	-0.0008	-0.0052	-0.0003	-0.0029
'5211'	0.0005	-0.0017	0.0006	-0.0001*
'5212'	0.0000	-0.0041	0.0006	-0.0011
'5217'	-0.0007	-0.0050	0.0003	0.0288

* Magnitude of the post-jump gradient is less than the magnitude of the pre-jump gradient.

Fig. 48 shows $CM'[z]_{SK\text{-}IA}(t)$ for trial '5209', for the vertical dimension method *B2000*[*z*]. Figs. 49 to 51 show $CM'[y]_{SK\text{-}IA}(t)$ for trials '5212', '5211' and '5217', respectively, for the horizontal dimension method *ZPZP5U*[*y*]. The scale of the right vertical axes of the subsequent figures have been zoomed in to improve the resolution of the $CM'_{SK\text{-}IA}(t)$ plots during the relevant quasi-static phases, and the

dynamic phases have been dimmed to draw the reader's attention to the more meaningful quasi-static phases. In all of these figures, the $CM'_{SK\text{-}IA}(t)$ plot was essentially linear along the horizontal axis during the pre-jump quasi-static stance phase[28], suggesting essentially no drift effect was present in this early phase for all trials, as expected. However, between-trials differences in the nature of post-jump drift were evident within the post-jump quasi-static stance phases for the *ZPZP5U*[*y*] method.

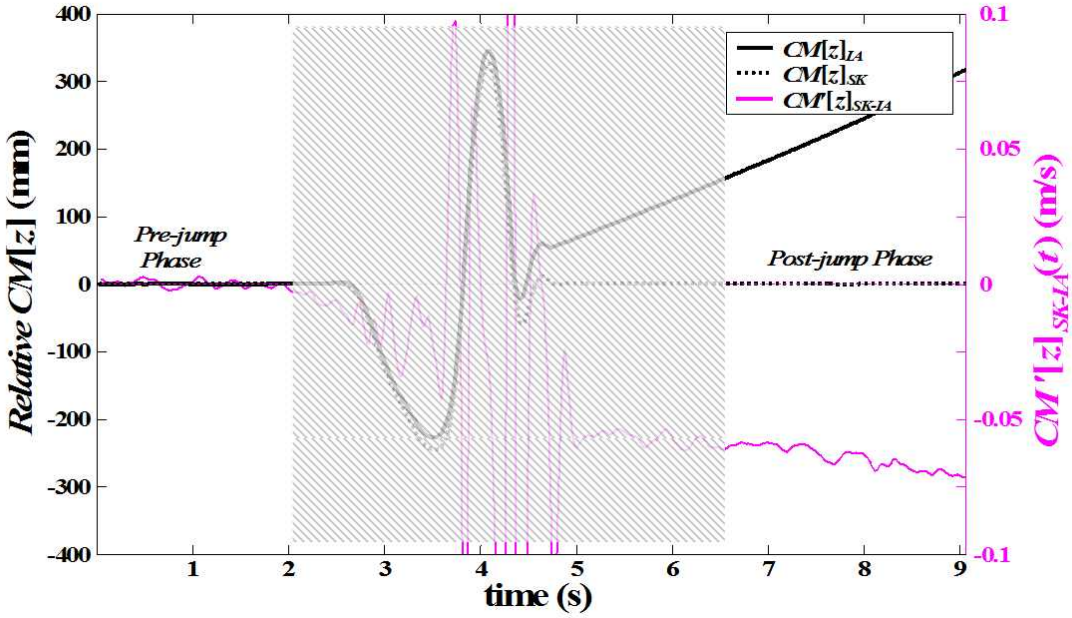

Figure 48. Zoomed plot of $CM'[z]_{SK\text{-}IA}(t)$ for Method B2000[z] (trial '5209'), concentrating on the unshaded, pre- and post-jump quasi-static stance phases. A linear regression line fitted to the post-jump quasi-static phase data (not shown) had a gradient of -0.0052, suggesting the presence of a quadratic drift, with respect to t, in post-landing $CM[z]_{IA}(t)$ calculations. Trials '5211', '5212' and '5217' produced similar results.

[28] The magnitudes of gradient of linear regression lines fitted to $CM'_{SK\text{-}IA}(t)$ in the pre-jump quasi-static phase for all trials were all ≤ 0.0008.

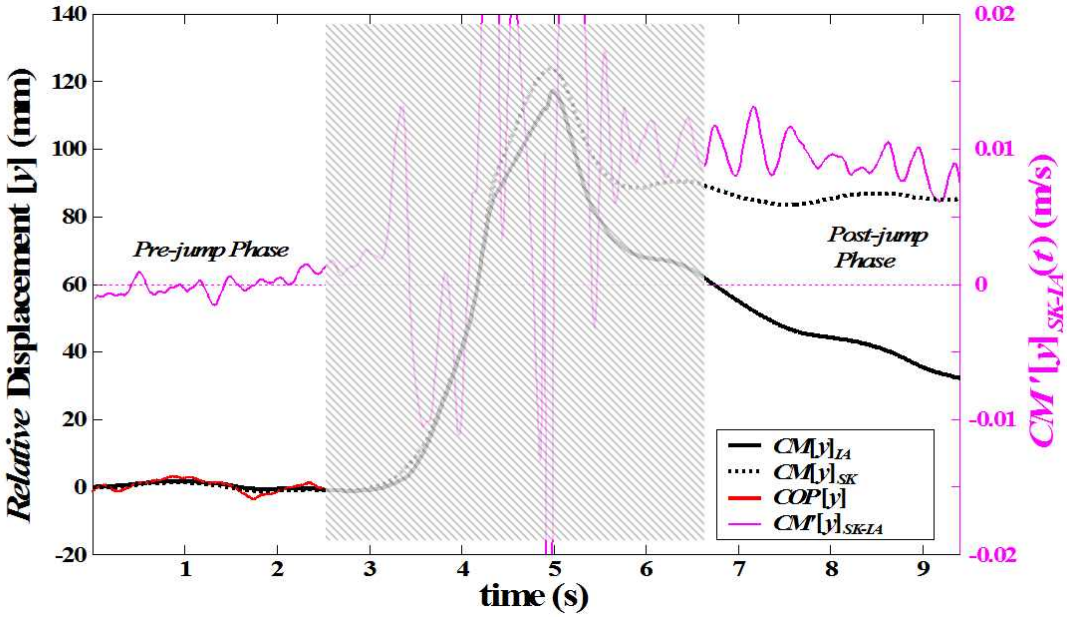

Figure 49. Zoomed plot of CM'[y]$_{SK\text{-}IA}$(t) for Method ZPZP5U[y] (trial '5212'), concentrating on the unshaded, pre- and post-jump quasi-static stance phases. A linear regression line fitted to the post-jump quasi-static phase data (not shown) had a gradient of -0.0011, suggesting the presence of a subtle quadratic drift, with respect to t, in post-landing CM[y]$_{IA}$(t) calculations. Trials '5209' and '5217' produced similar results but with progressively more pronounced quadratic drifts (see also Fig. 51 for trial '5217').

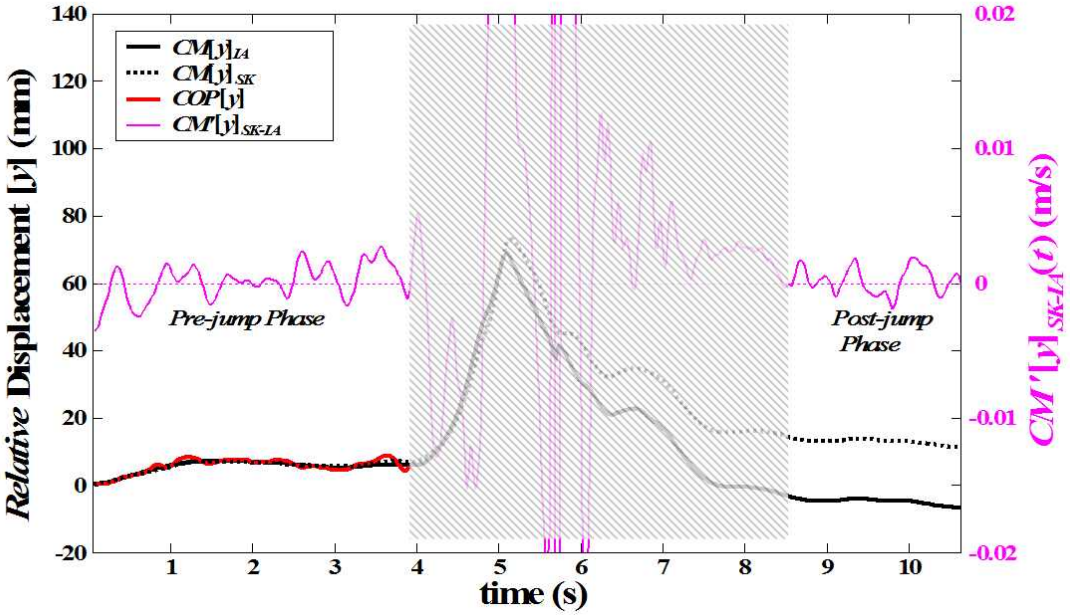

Figure 50. Zoomed plot of CM'[y]$_{SK\text{-}IA}$(t) for Method ZPZP5U[y] (trial '5211'), concentrating on the unshaded, pre- and post-jump quasi-static stance phases. A linear regression line fitted to the post-jump quasi-static phase data had an essentially negligible gradient of -0.0001 and a mean value, essentially, of zero, suggesting the presence of no drift or, possibly, a subtle linear or quadratic drift, with respect to t, in post-landing CM[y]$_{IA}$(t) calculations.

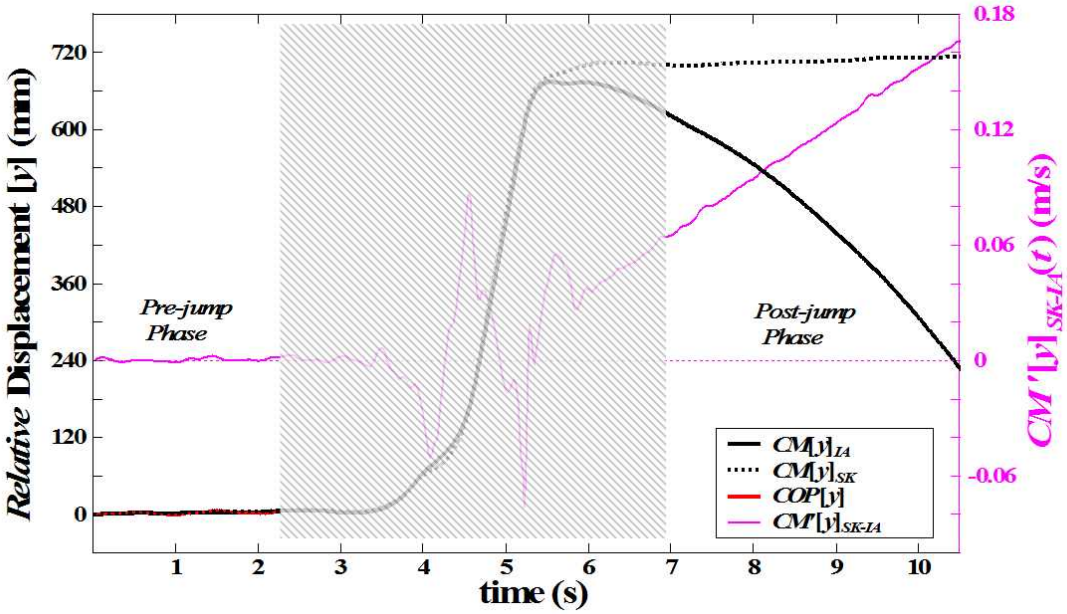

Figure 51. Plot (not zoomed in) of CM'[y]$_{SK\text{-}IA}$(t) for Method ZPZP5U[y] (trial '5217'), concentrating on the unshaded, pre- and post-jump quasi-static stance phases. A linear regression line fitted to the post-jump quasi-static phase data had a gradient of 0.0288, suggesting the presence of a quadratic drift, with respect to t, in post-landing CM[y]$_{IA}$(t) calculations. This plot was not zoomed to the same scale as the previous two figures due to the comparatively large gradient of CM'[y]$_{SK\text{-}IA}$(t). A larger scale was also required for the left axis because this trial was the broad jump.

For all trials for *Method B2000* (e.g. trial '5209'; Fig. 48) and all trials except trial '5211' for the *ZPZP5U*[*y*] method (e.g. trials '5212' and '5217'; Figs. 49 and 51), linear regression lines fitted to the post-jump quasi-static stance phase of the $CM'_{SK\text{-}IA}(t)$ plot had non-zero gradients. This suggests that the drift was essentially quadratic, with respect to time, in these cases. In the other case (viz. trial '5211'; Fig. 50), the regression line fitted to the post-jump quasi-static phase $CM'[y]_{SK\text{-}IA}(t)$ data had an essentially zero gradient and an essentially zero mean value, suggesting that essentially no drift in $CM[y]_{IA}(t)$ calculations occurred in this phase, for this case. Clearly though, from the discrepancy between the

relative $CM[y]_{SK}(t)$ *and relative* $CM[y]_{IA}(t)$ values at the commencement of the post-jump quasi-static phase, drift had occurred during the dynamic phases, but the drift did not continue during the post-jump quasi-static phase, which is evidenced by both the $CM'[y]_{SK\text{-}IA}(t)$ plot in Fig. 50, and the essentially parallel paths of *relative* $CM[y]_{SK}(t)$ *and relative* $CM[y]_{IA}(t)$ throughout this final phase.

6.3 Discussion

The IA optimisation approaches developed for this experiment were designed for application to transient dynamic activities (viz. jumps) that were preceded by a period of quasi-static stance. All methods attempted to optimise quasi-static CM trajectory, with each method based on a unique set of assumptions about CM behaviour during the quasi-static stance phase. Movement phase CM trajectory was then predicted by forward application of the integration approach (IA), using the relevant set of optimised design variables. Hence, these methods can be described as extrapolative techniques. This experiment assessed the ability of several extrapolative IA optimisation methods to determine relative vertical and/or antero-posterior CM trajectory. This section reviews the performance of these methods in theoretical and practical terms, identifies and provides explanations for current methodological limitations, and makes recommendations for future research.

It will be demonstrated that, for all methods, extrapolated airborne phase CM values were susceptible to cumulative drift errors. These errors were generally quadratic in nature, with respect to time, and were probably caused by force platform measurement errors that were not accounted for in each method's objective function. Further, it will be shown most of the methods developed for this experiment (viz. *ZPZP5U*) were based on flawed assumptions regarding the behaviour of the CM during quasi-static stance. However, these errors and flawed assumptions were of negligible practical significance (no more than 0.7% difference) when the four vertical dimension methods developed for this

experiment were applied to countermovement jumps for the purpose of calculating several parameters commonly used in jump performance analyses (described in section 6.1.2.3). If the application of IA methods is to be valid for CM trajectory estimation relative to a quasi-static starting point, better accounting for all sources of cumulative drift error through better modelling of force platform structural and measurement response characteristics will be required, even for activities as transient as countermovement jumps.

The practice of assuming the initial vertical velocity of the CM to be zero for the application of IA methods (e.g. Kibele, 1998; Vanrenterghem et al., 2001) was demonstrated to be generally acceptable for determining the jump performance parameters commonly calculated during jump analyses (Hatze, 1998). With the magnitude of the optimised $CM'[z]_{IA}(0)$ values not exceeding 1.6 mms^{-1} for all the originally optimised trials (*Condition 1*) for *Methods A2000*[*z*] and *B2000*[*z*], setting these values to zero (*Condition 2*) produced negligible change in all of the jump performance parameters (i.e. never more than a 0.2% change; less than 2 mm for the displacement jump performance parameters). Optimising subject mass on a trial-by-trial basis, as practised previously by Kibele (1998) and Vanrenterghem et al. (2001), was shown to produce practically significant changes in *relative* $CM[z]_{IA}(t)$ by the end of the airborne phase of up to 16.3% or 56.5 mm, and practically significant errors in some jump performance parameters of up to 5.0%. Even when the true mass of the subject was used, a perturbation of only 1 N in the vertical ground reaction force measured by the force platform used in this study was demonstrated to produce very large changes in *relative* $CM[z]_{IA}(t)$ at *Peak Height* of up to 292 mm (84%) and changes in the jump

performance parameters of up to 11% (e.g. 37 mm for $Height_P$). If there is doubt about the accuracy or currency of the force platform's calibration, then the use of an optimised force offset term, Fz_O, is recommended when IA methods are applied to countermovement jump analyses. An accurate determination of the subject's mass on precision scales is also recommended.

6.3.1 Relative Performance of the Methods

The statistical results did not reveal that any IA optimisation method in either dimension out-performed all others during the airborne phase. With the exception of the *ZPZP5U* approach in the antero-posterior dimension, the statistical results did not demonstrate that any method out-performed any other during the pre-jump quasi-static phase either. Statistical power was limited by the small sample size in this experiment, and possibly because of the variable between-trials duration of the quasi-static phase defined by the *ZPZP5U* and *Max* approaches. Notwithstanding these limitations, closer inspection of the *relative* $CM_{IA}(t)$ data produced by the seven methods sheds some light on the statistical outcomes produced and the relative merits of the methods.

6.3.1.1 Vertical Dimension Methods

All vertical dimension IA optimisation methods consistently (i.e. in all six trials) estimated *Peak Height* values greater than those calculated by the SK method by between 5.2 mm and 30.9 mm, regardless of whether they produced *relative* $CM[z]_{IA}(t)$ values greater or less than *relative* $CM[z]_{SK}(t)$ values in the initial part of the countermovement phase. At least two explanations for this finding are possible. Firstly, the posture during the airborne phase may have been sufficiently

different to that of the quasi-static phase to produce, in the presence of BSP estimate errors, the observed differences in IA and SK peak relative jump height. This explanation was ruled out based on the sensitivity analyses conducted for this experiment (see page 202). An alternative explanation is that one or more systematic errors existed that caused cumulative drift error in *relative* $CM[z]_{IA}(t)$ calculations.

The latter explanation is supported by the steadily increasing discrepancy between *relative* $CM[z]_{IA}(t)$ and the *relative* $CM[z]_{SK}(t)$ for all methods, as time progressed during the airborne and landing phases, and is illustrated for an indicative trial in Fig. 43 (page 219). This trend was observed consistently across all trials, irrespective of whether they produced *relative* $CM[z]_{IA}(t)$ values greater or less than *relative* $CM[z]_{SK}(t)$ values in the initial part of the countermovement phase. Indeed, Fig. 48 (page 235) also exemplifies that the increasing difference between *relative* $CM[z]_{IA}(t)$ and *relative* $CM[z]_{SK}(t)$ in the post-landing quasi-static stance phase is due to changes in *relative* $CM[z]_{IA}(t)$ and not changes in *relative* $CM[z]_{SK}(t)$. This is because *relative* $CM[z]_{SK}(t)$ was observed to return to an expected quasi-static condition, whereas *relative* $CM[z]_{IA}(t)$ continued to diverge from $CM[z]_{SK}(t)$. This was observed for all vertical dimension IA methods applied across all trials. Cumulative drift error also explains why *Airborne RMS* $CM[z]_{IA\text{-}SK}$ *Parameter* values were always greater than corresponding *Quasi-static RMS* $CM[z]_{IA\text{-}SK}$ *Parameter* values (see Fig. 39, page 213). Fig. 48 (page 235) and the gradients of the regression lines fitted to $CM'[z]_{SK\text{-}IA}(t)$ (Table 18, page 234), confirm the presence of drift error and demonstrate its quadratic nature, with respect to time.

From trial-to-trial, differences in *Peak Height* between the four IA optimisation methods only varied by 3.2 mm to 15.1 mm, compared with IA-SK *Peak Height* differences of 5.2 mm to 30.9 mm. This is consistent with a finding of non-significant differences between the four vertical dimension IA methods with respect to the *Airborne RMS* $CM[y]_{IA\text{-}SK}$ *Parameter* (Hypothesis 8). Different vertical dimension IA optimisation methods were observed to produce the smallest *Airborne RMS* $CM[y]_{IA\text{-}SK}$ *Parameter* values in different trials. However, for any given trial, the SK *Peak Height* value was always less than *Peak Height* values determined for all the four vertical dimension IA methods. This suggests that there was a source of drift error that was:

- common to all four vertical dimension IA methods, and
- of greater influence on airborne relative $CM[z]_{IA}(t)$ calculations than any method-specific error introduced by false assumptions inherent in any of the four objective functions.

Potential sources of this drift error will be explored in section 6.3.4.

The fact that the less transient, generic parameter, *Peak Height*, was shown to vary by as much as 15.1 mm between these four methods, demonstrates that not all of the respective premises upon which the four methods' objective functions are based can be correct. *Method A* assumes there is no net change in quasi-static phase $CM[z]_{IA}(t)$ (see Eq. (31)) and the objective function of *Method B* was designed to minimise the mean absolute difference of all quasi-static *relative* $CM[z]_{IA}(t)$ values about the mean quasi-static *relative* $CM[z]_{IA}(t)$ value (see Eq. (32)). Inspection of all trial $CM[z]_{SK}(t)$ plots demonstrated that, in reality,

these conditions were not observed for any of the methods (e.g. see Fig. 42). Hence, no single vertical dimension IA optimisation method can be recommended for determining *Peak Height* or other, less transient $CM[z]_{IA}(t)$ values, if sub-centimetre accuracy is required.

Notwithstanding the preceding comments, the maximum difference between the four vertical dimension IA methods was never more than 0.7% when the more transient jump performance parameters were calculated (e.g. 2.5 mm for $Height_P$). Hence, for practical purposes, *Methods AMax*, *A2000*, *BMax* and *B2000* were demonstrated to produce essentially equivalent jump performance parameter values for countermovement jumps. Less time transpires during the upward propulsive and airborne phases (~0.6 s), compared with the time elapsed between t_{QSini} and *Peak Height* (~2.6 s to 5.4 s in the current experiment), resulting in less influence of the cumulative drift error on jump performance parameter calculations. That is, the drift error accumulated within *relative* $CM[z]_{IA}(t)$ by the time the countermovement minimum point is reached, is essentially removed when $Height_P$ is calculated; the only drift error in this parameter is that which accumulates over the relatively short time period that transpires during the upward propulsive phase (~0.35 s).

SK-determined vertical CM displacement range (i.e. peak height relative to the countermovement minimum point) was no more than an absolute difference of 5.1 mm (0.8%) from the same range determined by any of the four IA methods for five of the six trials, and was 10.2 mm (1.8%) less for the other trial (viz. trial '5210'). Recall that errors in SK-determined vertical CM displacement at the

countermovement minimum point, due to BSP errors, were predicted to be up to 8 mm (see page 202). Considering these potential errors in the SK method, the SK- and IA-determined ranges were found to be sufficiently similar to suggest that *Methods AMax*, *A2000*, *BMax* and *B2000* can predict vertical CM displacement range for countermovement jumps to essentially the same degree of accuracy as the SK method. Indeed, these methods might be more accurate than the 50 Hz SK method used in this research, due to the higher temporal resolution of the captured force platform data.

Hence, all four vertical dimension IA methods developed for this research can be used to calculate accurately (i.e. within 0.7%) the more transient (i.e. up to ~0.35 s) jump performance parameters defined in section 6.1.2.3. However, the influence of drift errors on *relative* $CM[z]_{IA}(t)$ calculations will increase with time, making the application of these methods to calculating *relative* $CM[z]_{IA}(t)$ over longer duration activities progressively more inappropriate. Indeed, if sub-centimetre accuracy is required, then even the calculation of *Peak Height* cannot be recommended, despite this parameter being calculated over a time period as small as 2.6 s after a 2 s quasi-static stance phase.

6.3.1.2 Antero-Posterior Dimension Methods

Further evidence supporting the presence of drift error, not accounted for within the objective functions, is provided by the graphical results of the antero-posterior dimension methods. Consider the relative performance of the three antero-posterior dimension methods during the quasi-static and airborne phases of the trial depicted in Figs. 45 and 46 (pages 223 and 224, respectively).

Clearly, the *BMax*[*y*] and *B2000*[*y*] objective functions produced relatively inaccurate representations of *relative CM*[*y*]$_{IA}$(*t*) during the quasi-static phase, whereas *ZPZP5U*[*y*] produced *relative CM*[*y*]$_{IA}$(*t*) values that matched *relative CM*[*y*]$_{SK}$(*t*) values much more closely. Indeed, for all trials, the SK approach demonstrated that quasi-static phase antero-posterior CM displacement was not reproduced well by *Method B*. The initial and final IEPs identified in the *ZPZP5U*[*y*] method provide two valid and specific reference points within the objective function that the objective functions of *BMax*[*y*] and *B2000*[*y*] lack. The latter two methods rely on more generalised and somewhat flawed assumptions about CM trajectory during the pre-jump quasi-static stance phase. That is, the antero-posterior quasi-static CM trajectory, in reality, does not fulfil the criterion of a minimised Eq. (32). Hence, *ZPZP5U*[*y*] is the only one of the antero-posterior dimension methods assessed in this experiment that is worthy of further consideration.

Notwithstanding the contrast between the relative merits of the antero-posterior dimension methods' objective functions, Fig. 46 demonstrates that the good performance of the *ZPZP5U*[*y*] method in the quasi-static phase did not necessarily always carry over to the airborne phase and that the poorest performing method in the quasi-static phase (viz. *BMax*[*y*]) performed best in the airborne phase. A plausible explanation for these observations is that another source, or other sources, of drift error existed that were not accounted for by any of the objective functions, which made the forward prediction of antero-posterior CM kinematics beyond the pre-jump quasi-static stance phase inaccurate for all the methods investigated, including the *ZPZP5U*[*y*] method. Potential sources of

drift error beyond the pre-jump quasi-static phase will be discussed in section 6.3.4.

Between the three antero-posterior IA optimisation methods, differences in *relative* CM displacement at the end of the airborne phase (i.e. *relative* $CM[y]_{IA}(t_{ABfin})$) were 2.6% of the antero-posterior displacement range for the broad jump trial and as much as 27.3% for the countermovement jumps, for which antero-posterior displacement range was as low as 49.1 mm. None of the antero-posterior IA optimisation methods consistently predicted *relative* $CM[y]_{IA}(t)$ accurately during the airborne phase. The fact that $ZPZP5U[y]$, invariably the best-performing method during the quasi-static phase, did not perform consistently better than the other methods during the airborne phase, shows that another source or sources of drift error had practically significant effects on *relative* $CM[y]_{IA}(t)$ during the airborne phase, thus confounding forward prediction of *relative* $CM[y]_{IA}(t)$ beyond the pre-jump quasi-static phase. Potential sources of drift error beyond the pre-jump quasi-static phase will be discussed in section 6.3.4.

Hence, application of the current antero-posterior dimension methods to estimating *relative* $CM[y]_{IA}(t)$ during countermovement jumps and other, less transient activities, is not recommended. Application of $ZPZP5U[y]$ to countermovement jumps and activities of longer duration shows the most promise, but it will require better accounting for all sources of cumulative drift error.

Conventional ZPZP methods (see section 5.1.1) were assumed to be inappropriate for these dynamic activity applications because they only involve 'interpolating' between adjacent pairs of close-proximity IEPs. The initial velocity selected for the final ZPZP interval is only optimal for that particular interval. On the contrary, the unconventional ZPZP method developed for this study (*ZPZP5U*[*y*]), like all the previous unconventional ZPZP methods (see section 5.1.1), chooses the best initial velocity value for a single, consolidated ZPZP interval that spans the entire quasi-static stance phase. Therefore, *ZPZP5U*[*y*] was assumed, on theoretical grounds, to be more appropriate than conventional ZPZP methods such as *ZPZP6C*, for extrapolating beyond the quasi-static stance phase. Due to time constraints, *ZPZP6C* was not assessed in this experiment. Future work remains necessary to test the relative merits of *ZPZP5U versus ZPZP6C* for jumping and other dynamic activities commenced with a quasi-static stance phase.

6.3.2 Quasi-static Phase Duration: *Max versus 2000*

The methods used in this study produced pre-jump quasi-static stance phases ranging in duration from 2 to 4.8 s. No benefit from using quasi-static stance phase durations greater than 2 s was demonstrated in this study. It is possible that pre-jump quasi-static stance phases of duration greater than 5 s would reduce the errors associated with the assumptions of *Methods A* and *B*, although any other inherent drift errors would be exacerbated by numerical integration processes over a longer period of time. No researchers have addressed this issue to date; Vanrenterghem et al. (2001) and Jaffrey et al. (2003) used a 2 s window and Kibele (1998) used only a 0.3 s duration.

6.3.3 The Influence of $CM'[z]_{IA}(0)$, Fz_O and m_{WB}

The influence of practically relevant perturbations of design variables $CM'[z]_{IA}(0)$ and Fz_O on the calculation of transient jump performance parameters $\Delta\, Height_J$, $\Delta\, Height_P$, $\Delta\, Work_P$, $\Delta\, Max\ Power_P$ and $\Delta\, Ave\ Power_P$ was assessed for *Methods A2000*[*z*] and *B2000*[*z*]. The effect on the calculation of the relatively less transient, generic parameter Δ *Peak Height* was also assessed. The effect of including m_{WB} as a design variable whilst setting Fz_O constant to zero was also determined for all of these parameters.

The optimised value of $CM'[z]_{IA}(0)$ did not exceed a magnitude of 0.9 mms^{-1} for the originally optimised trials (*Condition 1*), except for one trial (viz. trial '5210') for which the value was 1.6 mms^{-1} for *Method B2000*[*z*]. Setting these values to zero for *Condition 2* produced negligible reductions in *Peak Height* (3.5 mm; 0.9% of *Peak Height*), except for the 1.6 mms^{-1} case, for which the reduction was 9.5 mm (2.9%). However, for all trials and both methods, the change elicited in the jump performance parameters did not exceed 0.2% (e.g. 0.62 mm for $\Delta\, Height_P$). Previous researchers have assumed $CM'[z]_{IA}(0)$ to be zero when applying IA methods to countermovement jumps (e.g. Kibele, 1998; Vanrenterghem et al., 2001). The findings of this study suggest that this assumption had a negligible effect on the calculation of the jump performance parameters. An error in estimated or assumed $CM'[z]_{IA}(0)$ introduces a linear drift error to $CM[z]_{IA}(t)$ calculations. Clearly, this error will become more influential as time passes, so it is recommended that $CM'[z]_{IA}(0)$ be included as a design variable in vertical dimension IA optimisation methods. If only the jump

performance parameters defined in section 6.1.2.3 are to be calculated, then $CM'[z]_{IA}(0)$ can be assumed to be zero for countermovement jump analyses.

Of much greater relative influence was the effect of perturbing Fz_O by 1 N. This represented a perturbation, across all trials and methods, of 9.1% to 11.4% of the Fz_O values originally optimised under *Condition 1*. Such 1 N perturbations resulted in very large, practically significant changes not only in *Peak Height*, but also in the less sensitive jump performance parameters. For example, the maximum change in $Height_P$ across all six trials was 37.7 mm, which represented an 11.0% increase in $Height_P$ for *Condition 3*, compared with *Condition 1*. It is best practice to calibrate a force platform prior to collecting experimental data. Although the force platform had been in use for several years, only the calibration matrix originally supplied by the force platform manufacturer was applied. No recalibration was performed for the current study in order to demonstrate the benefits of including and optimising force offset error terms. However, in hindsight, it would have been advantageous to recalibrate the device and instate a known offset error, in order to test the effectiveness and validity of the force offset optimisation process. Originally optimised Fz_O values obtained for the six trials assessed in this experiment ranged between -10.97 and -8.75 N. The validity of these values was supported by the analysis of a dead weight of known mass on the same force platform (see footnote 24, page 220). Calibration should not be assumed and should be stated explicitly in research articles if it has been carried out. Whether or not calibration is carried out, the inter-trial variation in Fz_O, for which explanations are offered in the following section, and the large influence of small perturbations to this variable, suggests that any IA analysis of a

countermovement jump will benefit from the application of an IA optimisation process that includes Fz_O as a design variable. Only Jaffrey et al. (2003) and Rabuffetti and Baroni (1999) have previously included an offset error design variable in a method designed to calculate countermovement jump CM trajectory. In the case of Rabuffetti and Baroni (1999), m_{WB} was also included as a design variable, though m_{WB} clearly does not change from trial-to-trial in reality.

Including m_{WB} as a design variable whilst setting Fz_O constant to zero (*Condition 4*) in the current study led to reductions of up to 16.3% (56.5 mm) in *Peak Height* and a maximum change of 5.0% in jump performance parameters (e.g. 11.9 mm change in Δ *Height*$_J$). As was also evident from the data presented by Jaffrey et al. (2003), the change elicited in m_{WB} by applying *Condition 4* compensated well for the forced change in Fz_O to zero, but this change was clearly unrealistic. m_{WB} was not the only unrealistic parameter produced by this approach. The $CM[z]'_{IA}(0)$ bound constraint Eq. (29) also became active at 0.005 ms^{-1} for two of the trials subjected to *Method A2000*[z]. Clearly, any methods of CM trajectory estimation for countermovement jumps that permit trial-specific variations to m_{WB} (e.g. Kibele, 1998; Rabuffetti and Baroni, 1999; Vanrenterghem et al., 2001) are unrealistic on theoretical grounds. Further, this experiment has demonstrated that this approach can produce practically significant errors in jump performance parameters, *Peak Height* and less transient *relative* $CM[z]_{IA}(t)$ values. Hence, it is recommended that m_{WB} should be measured on precision scales and that an IA optimisation method that includes Fz_O as a design variable should be employed when estimating countermovement jump CM trajectory.

6.3.4 Potential Sources of Drift Error

The presence of one or more sources of drift error in IA-calculations of $CM[z]_{IA}(t)$ have been established. It has also been demonstrated that the drift is usually quadratic in nature, with respect to time. Any offset error in the force measurements not accounted for by Fy_O or Fz_O would manifest itself in the CM trajectory data as a quadratic drift, due to the double integration process inherent in IA optimisation methods. Attempts are now made to identify potential sources of the drift error.

The different optimal force offset variable values that were determined for each trial ranged from -1.69 to 1.83 N for Fy_O, and from -10.97 to -8.75 N for Fz_O. One explanation for this finding is that there are systematic errors in Fy and Fz that are dependent on foot position on the force platform. The different force values recorded for the 633.75 N dead weight positioned on different positions on the force platform (see footnotes 24 and 25 on pages 220 and 225, respectively) also support this assertion. Furthermore, during the downward and early upward propulsive phases of each jump trial, during which foot position remained unaltered, the antero-posterior COP was observed to translate approximately 60 mm, compared with only about 20 mm during the quasi-static phase. As COP varies, the force platform and load cell in each corner will experience slightly different distortions, similar to those described by Bobbert and Schamhardt (1990) and Schmiedmayer and Kastner (1999) for piezoelectric force platforms. Hence, different foot pressure distribution profiles within the quasi-static, countermovement, and propulsive phases, and within the quasi-static phase itself, will result in force offset error terms that vary somewhat during these phases.

However, the optimised quasi-static phase Fy_O and Fz_O values derived in this study represented constant offsets across the quasi-static phase, that were then utilised forwards in subsequent phases. Consequently, Fy_O and Fz_O values could have been sub-optimal for forward application to the propulsive and airborne phases, thus introducing cumulative drift error to *relative* $CM_{IA}(t)$ calculations during these phases.

Upon landing in a different location on the platform, a different force offset error term and, therefore, a quadratic drift error, will be introduced for the final stages of the trial. However, only a single, constant value was modelled and optimised in each dimension within the IA optimisation methods developed in this study. The regression line fitted to the post-jump quasi-static phase $CM'[y]_{SK\text{-}IA}(t)$ data of trial '5211' in Fig. 50 had an essentially zero gradient and an essentially zero mean value, suggesting that essentially no drift in $CM[y]_{IA}(t)$ calculations occurred in this phase for this trial. This was the only observed occasion when the drift was not quadratic in nature, with respect to time. This suggests that the force offset error variable defined and optimised for the pre-jump quasi-static stance phase was also quite representative of the force offset error during the post-jump quasi-static stance phase. $CM[y]_{IA}(t)$ *and* $CM[y]_{SK}(t)$ followed parallel paths but approximately 200 mm apart during this phase (see Fig. 50). This suggests that the actual force offset error must have varied during the intermediate dynamic phases. That is, it was different to the Fy_O value optimised for this trial over the pre-jump quasi-static stance phase.

The only other studies to have included a force offset error term per dimension studied were Rabuffetti and Baroni (1999) and Jaffrey et al. (2003). No IA optimisation study to date has applied multiple force offset error terms per dimension to a time series. Future research should commence by assessing whether or not it is sufficient to simply include different optimised force offset error terms for each ground-based phase of the activity (e.g. pre-jump quasi-static stance, countermovement, propulsive, landing and post-jump quasi-static phases). The inclusion of a post-landing quasi-static phase of at least 2 seconds duration is also recommended. This would ensure both pre- and post-jump quasi-static phase information could be used to refine relative CM displacement estimates during the intermediate phases. Whether or not these additional modelling processes are necessary for the methods established in this research depends upon the level of accuracy required for any given practical application. Based on the results of this experiment, these additional modelling processes are not necessary for estimating the jump performance parameters defined in section 6.1.2.3. However, these potential enhancements may result in the IA optimisation methods proposed in this research becoming valid predictors of *relative* $CM[z]_{IA}(t)$ and $CM[y]_{IA}(t)$ over less transient periods of time. If not, more complex modelling of force platform structural properties and how they are influenced by foot and COP position may be required (e.g. Bobbert and Schamhardt, 1990; Schmiedmayer et al., 1999).

6.3.5 Summary

When IA methods are applied to countermovement jump analyses, the use of an optimised force offset term, Fz_O, is recommended if there is any doubt about the accuracy or currency of the force platform's calibration. It has been demonstrated

that the inclusion of an optimally selected force offset error term during IA calculations of CM trajectory will improve these calculations. Vertical dimension IA optimisation methods that include Fz_O and $CM'[z]_{IA}(0)$ as design variables are recommended over methods that assume the initial velocity of the CM is zero and that no force offset errors exist. However, assuming $CM'[z]_{IA}(0)$ to be zero is acceptable for determining the jump performance parameters defined in section 6.1.2.3. Whole body mass, m_{WB}, should be measured on precision scales and supplied as a constant to the IA optimisation process. Optimising m_{WB} is unsound on theoretical grounds and was demonstrated to be detrimental to IA-determined estimates of CM trajectory for countermovement jumps (producing errors of up to 16.3% in *relative* $CM[z]_{IA}(t)$ by the end of the airborne phase) and even to the more transient jump performance parameters used in this experiment (up to 5.0% errors).

None of the vertical dimension IA optimisation methods developed for this experiment (viz. *AMax*, *A2000*, *BMax* and *B2000*) can be recommended for determining *Peak Height* or other *relative* $CM[z]_{IA}(t)$ values beyond the quasi-static stance phase, if sub-centimetre accuracy is required. It was demonstrated that there was a source of drift error common to all vertical dimension IA methods that was of greater influence on airborne *relative* $CM[z]_{IA}(t)$ calculations than that produced by any between-method objective function differences. The influence of a drift error in these methods on *relative* $CM[z]_{IA}(t)$ calculations becomes progressively worse as time passes, thus preventing the valid application of these methods to other, longer duration activities. The drift error was usually quadratic in nature, with respect to time.

Application of the current antero-posterior dimension IA methods to *relative* $CM[y]_{IA}(t)$ calculations beyond the pre-jump quasi-static stance phase for countermovement jumps is not recommended. However, application of *ZPZP5U*[*y*] to countermovement jumps and activities of longer duration shows some promise, based on the good performance of this method during the pre-jump quasi-static stance phase. Nevertheless, even this method requires better accounting for all potential sources of cumulative drift error. Future work is also required to test the relative merits of *ZPZP5U*[*y*] *versus ZPZP6C*[*y*] for dynamic activities preceded by a quasi-static stance phase.

Variable errors in *Fy* and *Fz* measurements that are dependent on COP position and foot pressure distribution patterns on the force platform are suspected to be the main remaining sources of drift error in IA optimisation method CM trajectory calculations. Theoretical and empirical measurement approaches, aimed at understanding force platform distortion characteristics and the subsequent effects on measured signals, may lead to better modelling of the error sources in force platform measurements. These additional modelling processes may represent the improvement required to make IA optimisation methods valid predictors of *relative* CM trajectory not only for countermovement jumps, but also for activities of longer duration.

Notwithstanding the preceding conclusions, the vertical dimension IA optimisation methods developed for this experiment (viz. *AMax*, *A2000*, *BMax* and *B2000*) are all appropriate for determining the more transient jump

performance parameters commonly calculated in jumping assessments (as defined in section 6.1.2.3). This is because all the vertical dimension IA optimisation methods were demonstrated to produce essentially equivalent (within 0.7% of each other) jump performance parameter values for countermovement jumps, due to the decreased influence of drift error over this relatively short time period (viz. only ~0.35 s). These methods were also demonstrated to be as accurate as the SK method for determining another transient parameter, the vertical CM displacement range from the minimum countermovement point to the peak of flight.

7. COMBINED DYNAMICS AND OPTIMISATION TECHNIQUES FOR ESTIMATION OF BSPS

The experiment described in this chapter involved applying nonlinear optimisation techniques to minimise various objective functions based on different dynamics equations. Design variables were comprised of force platform error terms and BSPs. The aims were to improve dynamics solutions whilst also determining subject-specific BSPs. Although not a sufficient condition, it is at least a necessary condition that feasible and realistic force platform error terms and BSPs result from the combined optimisation and dynamics techniques developed in this experiment, if the aims of this experiment are to be achieved. Previously, the only study to estimate all the sagittal plane BSPs of a living subject by combined dynamics and optimisation techniques was conducted by Vaughan et al. (1982a), who reported some unrealistic BSP values. Approaches assessed in this experiment were developed from the method of Vaughan et al. (1982a). The effect of different degrees of kinematic data filtering on the dynamics solutions and design variable values was also assessed.

7.1 Research Design

7.1.1 The Combined Dynamics and Optimisation Methods

7.1.1.1 Movement Activities and Trial Formulation

Apart from the general description provided in section 4.3.4, the movement activities performed by the subject for this experiment were designed to produce angular and translational movement of all segments relative to each other, including some high acceleration movements of the smaller, more distal limb segments (up to 350 rad/s^2 for the Foot segments and 300 rad/s^2 for the Lower Arm segments). The subject balanced on one foot for each captured trial. Squats were conducted for the contact limb, while segmental accelerations were imposed on the trunk and the free extremity segments, with linear and angular motion relative to all other segments. The data from several trials were then added in series to produce combined trials for analysis purposes, ensuring each combined trial involved the comprehensive movement patterns described above for all segments. Unlike Vaughan et al. (1982a), who only collected data for three transient activities (viz. a jump, a kick and a running step), long duration combined trials were established for this experiment in an attempt to provide much more information to aid the optimisation processes in finding optimal dynamics solutions, governed by feasible and realistic design variable values. Four combined trials were constructed, ranging in duration from 52 to 83 s. The data of which the combined trials were comprised were clearly not continuous at the junctions between the sub-trials. However, this posed no problem with respect to acceleration derivations because all acceleration calculations were conducted within the sub-trials prior to combining them; and after sub-trials were combined,

trial objective function computations were all based on the summation of squared differences between discrete, time-matched pairs of calculations.

7.1.1.2 Design Variables and Constraints

The design variables for this experiment were comprised of 52 BSPs, as described in section 4.4.1.3, and several force platform measurement offset error terms. The BSPs were each segment's mass (m_{seg}), the longitudinal and perpendicular components of the segmental centre of mass ($cm[L]_{seg}$ and $cm[P]_{seg}$) and the principal segmental moments of inertia about the subject's transverse axis through each segment's centre of mass (I_{seg}). The force platform measurement offset error terms were the offset error terms for the measured vertical and antero-posterior components of the GRF (viz. Fy_O and Fz_O, respectively). Separate Fy_O and Fz_O design variables were established for each sub-trial within each combined trial, considering the trial-to-trial variation in these parameters that was established in the previous chapter (viz. -1.69 N < Fy_O < 1.83 N and -10.97 N < Fz_O < -8.75 N). The number of Fy_O and Fz_O design variables established for a given combined trial equalled the number of sub-trials for that combined trial, and varied from five to nine across the four combined trials[29]. Also on the basis of results from the previous chapter, the initial values assigned to the force offset design variables were zero for Fy_O and -10 for Fz_O, with respective bound-constrained ranges set conservatively at -14 to -6 N and -3 to +3 N.

[29] Henceforth, the four combined trials are referred to simply as 'the trials', with the variable number of trials used to construct the combined trials are referred to as 'the sub-trials'.

Initial values assigned to each of the BSP design variables at the commencement of the optimisation process are listed in Tables 19 and 20, as are the respective bound constraints. No distinction is made between left and right limb segments in these tables because bilateral limb segment BSP equivalency was assumed in this study, as was the case for Vaughan et al. (1982a). This was formalised in the optimisation problem as a set of four equality constraints per limb segment (for *seg* = Foot, Shank, Thigh, Upper Arm and Lower Arm):

$$\begin{aligned} m_{seg}\,(\text{Left}) &= m_{seg}\,(\text{Right}) \\ cm[L]_{seg}\,(\text{Left}) &= cm[L]_{seg}\,(\text{Right}) \\ cm[R]_{seg}\,(\text{Left}) &= cm[R]_{seg}\,(\text{Right}) \\ I_{seg}\,(\text{Left}) &= I_{seg}\,(\text{Right}) \end{aligned} \tag{45}$$

The initial m_{seg} values were based on the regression equations of Clauser et al. (1969)[30]. For each segment, the three regression equations based on various anthropometric measurements were utilised. The mean result from all three regression equations was used as the initial design variable value for each m_{seg} BSP. For the limb segments, the mean of the results from both limbs was used. The trunk segment defined by Clauser et al included the neck, so an adjustment was made to account for this difference. The mean neck volume value, calculated from the four different regression equations of McConville et al. (1980) for neck

[30] All necessary anthropometric measurements were collected from the subject.

Table 19. The initial values and lower and upper bound constraints applied to each of the m_{seg} and I_{seg} BSP design variables included in the optimisations. Each segment's mass (m_{seg}) is expressed as a proportion of whole body mass (m_{WB}) and the principal segmental moments of inertia about the subject's transverse axis through each segment's centre of mass (I_{seg}) are expressed in kgm^2.

BSP	Initial Value	Lower Bound	Upper Bound
m_{Foot}	0.0146	0.0110	0.0183
m_{Shank}	0.0482	0.0361	0.0602
m_{Thigh}	0.1063	0.0797	0.1329
$m_{Lower\ Arm}$	0.0245	0.0184	0.0306
$m_{Upper\ Arm}$	0.0268	0.0201	0.0335
m_{Head}	0.0711	0.0533	0.0889
m_{Neck}	0.0151	0.0113	0.0188
m_{Trunk}	0.4730	0.3547	0.5912
I_{Foot}	0.0034	0.0025	0.0042
I_{Shank}	0.0368	0.0276	0.0460
I_{Thigh}	0.1078	0.0809	0.1348
$I_{Lower\ Arm}$	0.0211	0.0158	0.0264
$I_{Upper\ Arm}$	0.0087	0.0065	0.0108
I_{Head}	0.0225	0.0169	0.0281
I_{Neck}	0.0016	0.0012	0.0020
I_{Trunk}	0.8758	0.6569	1.0948

Table 20. The initial values and lower and upper bound constraints applied to each of the segmental centre of mass BSP design variables. Each segment's longitudinal and perpendicular segmental centres of mass ($cm[L]_{seg}$ and $cm[P]_{seg}$) are expressed as proportions of segment length.

BSP	Initial Value	Lower Bound	Upper Bound
$cm[L]_{Foot}$	0.400	0.200	0.600
$cm[L]_{Shank}$	0.379	0.179	0.579
$cm[L]_{Thigh}$	0.399	0.199	0.599
$cm[L]_{Lower\ Arm}$	0.480	0.280	0.680
$cm[L]_{Upper\ Arm}$	0.493	0.293	0.693
$cm[L]_{Head}$	0.200	0	0.400
$cm[L]_{Neck}$	0.300	0.100	0.500
$cm[L]_{Trunk}$	0.429	0.229	0.629
$cm[P]_{Foot}$	-0.060	-0.260	0.140
$cm[P]_{Shank}$	-0.060	-0.160	0.040
$cm[P]_{Thigh}$	0	-0.100	0.100
$cm[P]_{Lower\ Arm}$	0	-0.100	0.100
$cm[P]_{Upper\ Arm}$	0	-0.100	0.100
$cm[P]_{Head}$	0	-0.200	0.200
$cm[P]_{Neck}$	0	-0.200	0.200
$cm[P]_{Trunk}$	0	-0.100	0.100

volume, and the mean density value for the head and neck of the cadavers measured by Dempster (1955), were used to estimate the mass of the subject's neck. This value was subtracted from the trunk mass value already determined using the equation of Clauser et al. (1969). Once all the individual segmental mass BSPs had been estimated, they were all adjusted slightly by the same factor to ensure the sum of these parameters equalled one. The initial estimates of the segmental moments of inertia were calculated from the regression equations of McConville et al. (1980)[31]. For each segment, the height-weight regression equation, and the three regression equations based on other anthropometric measurements, were all utilised. Ultimately, the mean result from all four regression equations was used as the initial design variable value for each I_{seg} BSP. For the limb segments, the mean of the results from both limbs was used. The initial $cm[L]_{seg}$ BSPs were based on the mean values of the cadavers from the study by Clauser et al. (1969); adjustments were made to some of these values, reflecting the different segmental end-point definitions between Clauser et al. and this study. Because Clauser et al. did not define a neck segment, $cm[L]_{Neck}$ was estimated based on the author's assessment of Fig. 11. The $cm[P]_{seg}$ BSPs were assigned initial values of zero, except for $cm[P]_{Foot}$ and $cm[P]_{Shank}$, which were assigned a value of -0.06, based on the author's assessment of Fig. 11.

It is recognised that segment definitions varied between this study and the different studies used to define the initial BSP design variable values adopted for this study. However, with the exception of the need to account for a separate neck

[31] All necessary anthropometric measurements were collected from the subject.

segment, the adopted initial estimates were deemed acceptable because they were only starting points for an optimisation process aimed at improving these BSP estimates. Further, conservatively broad bound constraints (see Tables 19 and 20) were imposed on all BSPs to ensure the true values would all be within the feasible space of the optimisation problem. One of the anticipated benefits of the combined dynamics and optimisation method of BSP estimation is that optimised BSP estimates will be specific to the actual marker placements and specific joint and segment definitions to which the process is applied. They will be subject-specific and even testing-session-specific to some degree, and modelling will not be constrained or limited by the joint and segment definitions of other BSP estimation methods.

The other constraint employed by Vaughan et al. (1982a) and common to all objective functions in this experiment was the equality constraint requiring the sum of all segmental masses (m_{seg}) to equal the whole body mass (m_{WB}):

$$\left(\sum_{seg=1}^{13} m_{seg} \right) - m_{WB} = 0 \tag{46}$$

7.1.1.3 The First Three Dynamics-Based Objective Functions

The objective functions developed for this experiment were based on one or more of the following principles of dynamics and their application to multi-body systems:

- Newtonian principles that the net external force and torque acting on the whole body equal the rates of change of the linear and angular momentum of the whole body, respectively
- Inverse Dynamics Approach (IDA) for calculating net joint and segmental end-point forces and moments.

The Newtonian principles regarding the rates of change of linear and angular momentum can be described by the following three equations, comprised of two sagittal plane component equations for the linear principle and one equation for the angular principle. At any time *t*:

$$Fy(t) + Fy_O = \left(\sum_{seg=1}^{13} m_{seg} \ddot{y}_{seg}(t) \right) \tag{47}$$

$$Fz(t) + Fz_O = \left(\sum_{seg=1}^{13} m_{seg} \left(\ddot{z}_{seg}(t) + g \right) \right) \tag{48}$$

$$Tx(t) = \left(\sum_{seg=1}^{13} I_{seg} \alpha_{seg}(t) \right) + \left(\sum_{seg=1}^{13} \vec{r}_{seg}(t) \times m_{seg} \ddot{\vec{r}}_{seg}(t) \right) \tag{49}$$

where $\ddot{y}_{seg}$ and $\ddot{z}_{seg}$ are the horizontal and vertical linear accelerations of the segmental centre of mass, respectively; *Fy*, Fy_O, *Fz* and Fz_O are, respectively, the horizontal and vertical components of the measured GRF and their respective force offset error terms; *g* is gravitational acceleration; α_{seg} is the segmental angular acceleration; $\vec{r}_{seg}$ is the position vector of the segmental centre of mass in the global coordinate system; $\ddot{\vec{r}}_{seg}$ is the second derivative of $\vec{r}_{seg}$; and *Tx* is the

net external torque acting on the whole body with respect to the global coordinate system origin. *Tx* is comprised of the torques produced by the whole body weight force acting at the CM, and the GRF acting at the COP, with respect to the global coordinate system origin:

$$Tx(t) = [CMy(t)][m_{WB}g] + [COPy(t)][Fz(t) + Fz_O] \quad (50)$$

where *CMy* and *COPy* represent the horizontal coordinates of the CM and COP position vectors in the global coordinate system. Although only represented by Fy_O and Fz_O in the preceding four equations, it has already been stated (see section 7.1.1.1) that separate force offset error terms were established for each sub-trial within each of the four trials used in this experiment.

Apart from not incorporating force offset error terms, Vaughan et al. (1982a) used Eqs. (47), (48) and (49) as equality constraints in their optimisation approach. In reality, precise equalities would not have been attained by Vaughan et al. (1982a) due to the presence of noise in their experimental data. However, the degree to which they relaxed these equality constraints was not reported. During pilot testing for the current experiment, it was found that the degree to which it was necessary to relax these constraints made them ineffective as equality constraints. Hence, when utilised in the current experiment, the sum of squared differences (*SSD*) of the terms in each of Eqs. (47), (48) and (49) were incorporated into various objective function formulations and minimised instead:

$$SSDy = \sum_{t=1}^{t=n} \left(\left(Fy(t) + Fy_O \right) - \left(\sum_{seg=1}^{13} m_{seg} \ddot{y}_{seg}(t) \right) \right)^2 \tag{51}$$

$$SSDz = \sum_{t=1}^{t=n} \left(\left(Fz(t) + Fz_O \right) - \left(\sum_{seg=1}^{13} m_{seg} \left(\ddot{z}_{seg}(t) + g \right) \right) \right)^2 \tag{52}$$

$$SSDx = \sum_{t=1}^{t=n} \left(Tx(t) - \left(\sum_{seg=1}^{13} I_{seg} \alpha_{seg}(t) \right) - \left(\sum_{seg=1}^{13} \vec{r}_{seg}(t) \times \ m_{seg} \ddot{\vec{r}}_{seg}(t) \right) \right)^2 \tag{53}$$

where n is the total number of time samples. Note that all m_{seg}, $cm[L]_{seg}$ and $cm[P]_{seg}$ BSP design variables are present in Eqs. (51) and (52), and Eq. (53) contains all the BSPs, including the I_{seg} BSPs. Fy_O design variables were not represented in Eqs. (51) and (53) and Fz_O design variables were not present in Eq. (52).

For many practical applications, IDA calculations are only conducted 'bottom-up' or 'top-down' (see page 92 for definitions) and often only to the most proximal joint of the limb(s) in which calculations were commenced. For example, gait analysis usually only involves bottom-up IDA calculations and often only up to the hip joints. Only for an application requiring two separate calculations of these quantities at each joint, such as validation of a model (e.g. de Looze et al., 1992) or a BSP estimation method (e.g. Vaughan et al., 1982a), does a bi-directional (i.e. bottom-up and top-down) IDA analysis proceed throughout the entire body. For such applications, especially when left and right limbs are defined separately, the top-down and bottom-up terminology is somewhat misleading. Entire body IDA calculations do not actually commence from any single extremity. Rather,

they commence from the distal ends of all but one extremity (see Fig. 52). Calculations then proceed proximally along these extremities towards the trunk and can be termed 'Distal-to-Proximal' (DP) IDA calculations. They then proceed 'through the trunk' and distally along the remaining extremity, terminating at the distal end-point of that extremity's distal segment. Hence, these latter calculations can be termed 'Proximal-to-Distal' (PD) IDA calculations.

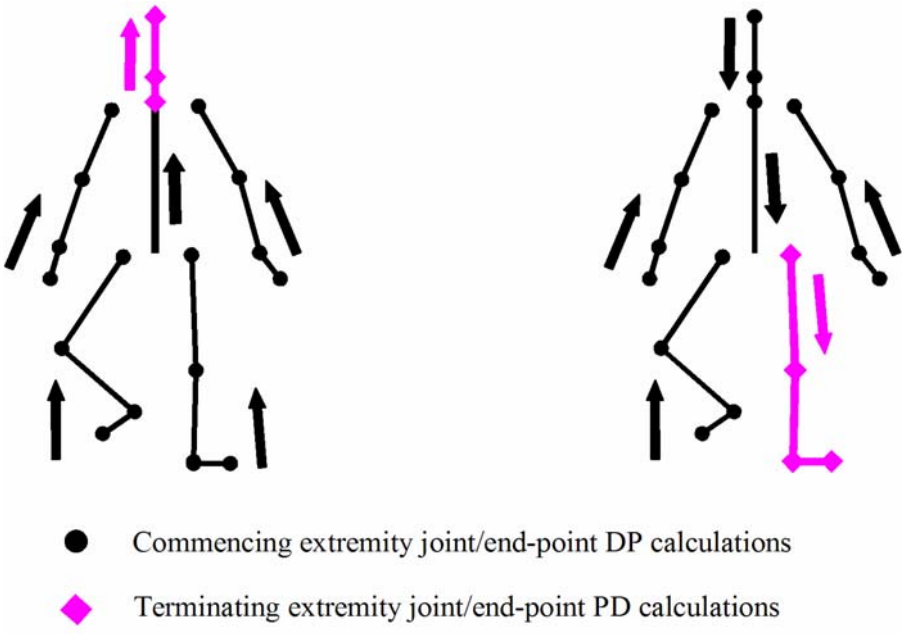

Figure 52. Two of the possible five orders of progression of entire body IDA calculations for the model used in this research. Arrows indicate the directions in which the IDA calculations proceed. The left figure illustrates how an IDA commencing with Distal-to-Proximal (DP) calculations for the limbs leads to Proximal-to-Distal (PD) net force and moment calculations for the trunk-neck joint, the head-neck joint and the vertex of the head. The right figure shows how commencing with DP calculations for the non-supported 'extremities' leads to PD net force and moment calculations for the hip, knee and ankle joints and the distal end of the support leg. Once IDA calculations have been conducted through the entire body using all five possible orders of progression (i.e. one terminating at each of the five 'extremities'), a pair of PD and DP net forces and moments has been calculated for all joints and distal segment end-points.

The 2-D equations for calculating the net force and moment acting at a joint using IDA are well documented (e.g. Whittlesey and Robertson, 2004). Fig. 53 represents a free body diagram of a segment and the net joint forces and moments acting on that segment at both its ends. An IDA to calculate the net external force and moment acting on a segment at one end-point of a segment (i.e. the terminating end of the analysis, *Term*) requires the segmental kinematics and inertial characteristics, and the values of the net external force and moment acting on the other end-point of the segment (i.e. the commencing point of the analysis, *Comm*) to be known *a priori*. For the distal end-points of each extremity, the external force and moment acting at *Comm* have already been measured or are known to be zero. At each joint, the external force and moment acting at *Comm* are equal and opposite to the equivalent quantities calculated by an IDA of the preceding segment's *Term* point.

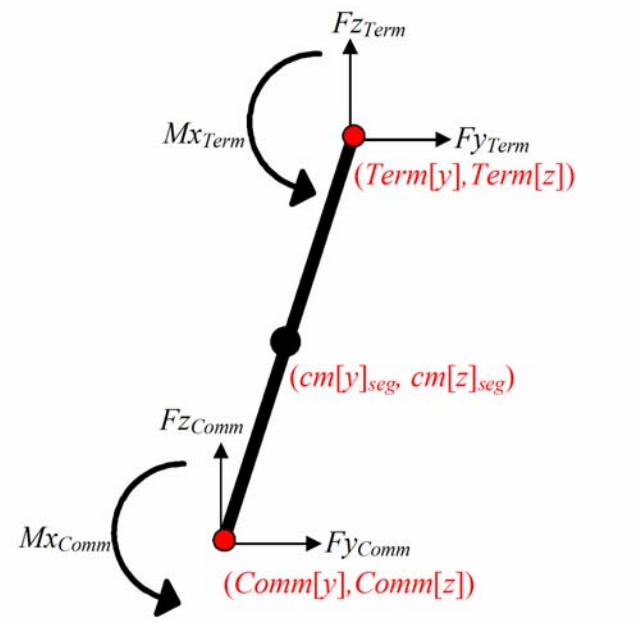

Figure 53. A free body diagram of a segment and the 2-D components of the net joint forces (Fy and Fz) and the moments (Mx) acting on the segment at both its commencing and terminating end-points of the IDA (viz. Comm and Term). The 2-D position coordinates of Comm and Term and of the segmental centre of mass are bracketed and shown in red.

The calculation of the 2-D net external force and moment acting at *Term* is achieved by solving the following three scalar equations:

$$Fy_{Term} = m_{seg}cm[y'']_{seg} - Fy_{Comm} \tag{54}$$

$$Fz_{Term} = m_{seg}cm[z'']_{seg} - Fz_{Comm} - m_{seg}g \tag{55}$$

$$\begin{aligned} Mx_{Term} = I_{seg}\alpha_{seg} &- Mx_{Comm} \\ &- Fy_{Comm}(cm[z]_{seg} - Comm[z]) - Fz_{Comm}(Comm[y] - cm[y]_{seg}) \\ &- Fy_{Term}(cm[z]_{seg} - Term[z]) - Fz_{Term}(Term[y] - cm[y]_{seg}) \end{aligned} \tag{56}$$

These equations were used for all IDA calculations, except for the Trunk segment. The equations for the PD IDA calculations of the five Trunk segment end-points were similar to Eqs. (54), (55) and (56). However, for each of the Trunk segment's five *Term* end-points, there were four *Comm* end-points and associated known net forces and moments, rather than the one, as shown in the preceding equations and figure.

For a DP IDA, point *Comm* is the distal joint or end-point of the segment being analysed and point *Term* is the proximal joint, whereas, if a PD IDA is conducted, *Comm* represents the proximal joint and *Term* represents the distal joint or end-point of the segment in question. Fig. 54 shows free body diagrams of both segments of a two-segment system. It illustrates how both DP and PD IDA calculations are possible at the joint linking both segments.

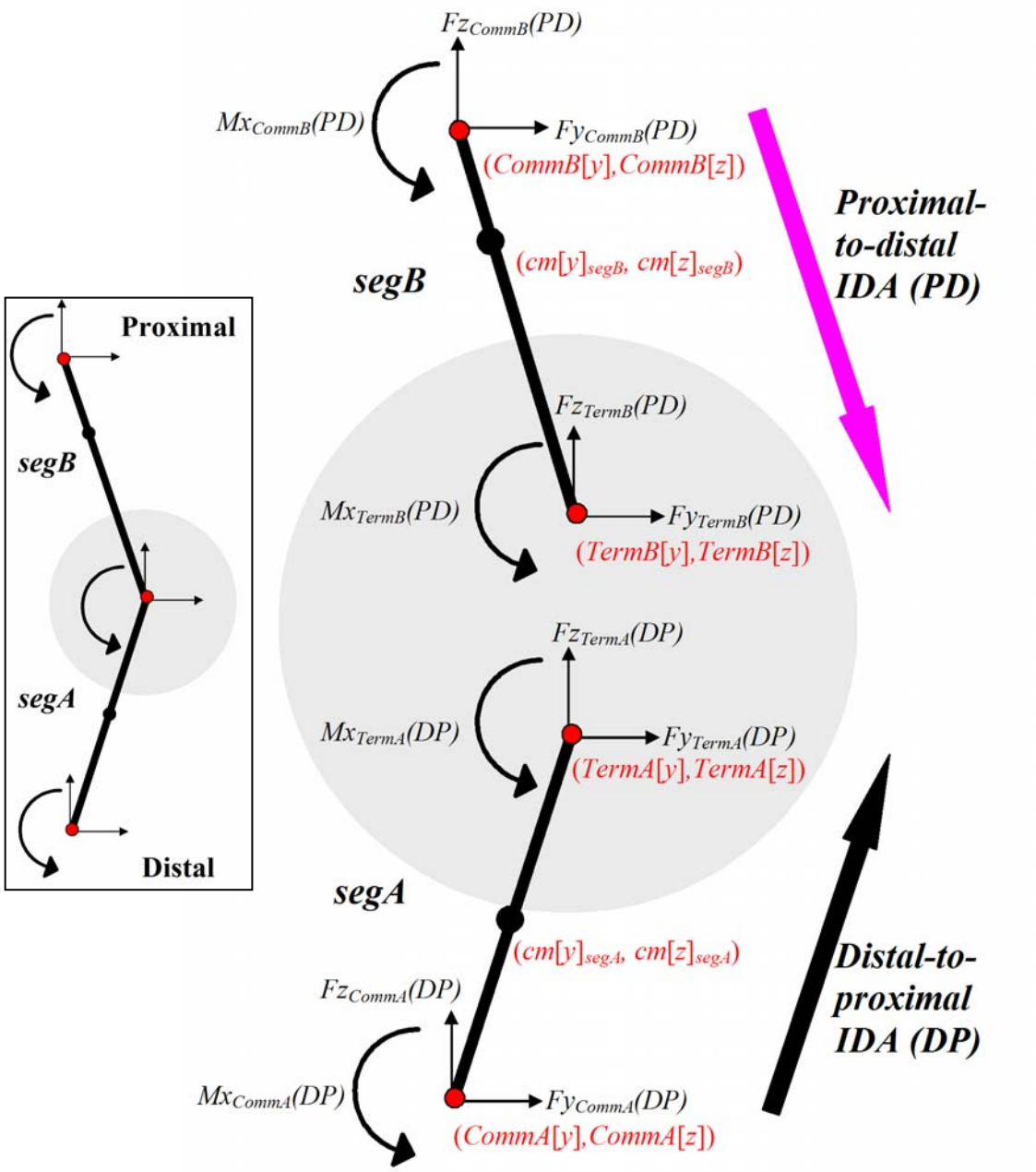

Figure 54. A two-segment system (left box), linked at the joint inside the grey circle. The main part of the figure, showing the free body diagrams of both segments, illustrates the bi-directional (DP and PD) IDA calculations possible at the joint linking both segments. $Fy_{TermA}(DP)$, $Fz_{TermA}(DP)$ *and* $Mx_{TermA}(DP)$ *are the net external force and moment acting at point TermA, as determined by a DP IDA of segA.* $Fy_{TermB}(PD)$, $Fz_{TermB}(PD)$ *and* $Mx_{TermB}(PD)$ *are the net external force and moment acting at point TermB, as determined by a PD IDA of segB. For a theoretically perfect system, these kinetic quantities are equal and opposite. That is,* $Fy_{TermA}(DP) + Fy_{TermB}(PD)$, $Fz_{TermA}(DP) + Fz_{TermB}(PD)$ *and* $Mx_{TermA}(DP) + Mx_{TermB}(PD)$ *should all equal zero.*

For a perfect, errorless simulation of a system of rigid segments linked by frictionless joints, DP and PD solutions at any given joint or distal segment end-point will be equal but opposite in value. For example, in Fig. 54, $Fy_{TermA}(DP) = -Fy_{TermB}(PD)$, $Fz_{TermA}(DP) = -Fz_{TermB}(PD)$ and $Mx_{TermA}(DP) = -Mx_{TermB}(PD)$. However, for real human movement data, due to errors that include (but are not restricted to) BSP estimate errors, a residual will exist between the DP and PD calculations of the net force and moment at each joint and distal segment end-point. After DP and PD IDA analyses have proceeded through the entire body, the DP-PD residuals of the net moment and force acting at the distal joint (*J*) or the distal end-point (*EP*) of segment *A*, can be represented by the following scalar equations:

$$\hat{M}x_J = Mx_{CommA}(DP) - Mx_{TermA}(PD);\ \hat{M}x_{EP} = Mx_{CommA}(DP) - Mx_{TermA}(PD) \quad (57)$$

$$\hat{F}y_J = Fy_{CommA}(DP) - Fy_{TermA}(PD);\quad \hat{F}y_{EP} = Fy_{CommA}(DP) - Fy_{TermA}(PD) \quad (58)$$

$$\hat{F}z_J = Fz_{CommA}(DP) - Fz_{TermA}(PD);\quad \hat{F}z_{EP} = Fz_{CommA}(DP) - Fz_{TermA}(PD) \quad (59)$$

where $\hat{M}x_J$, $\hat{F}y_J$ and $\hat{F}z_J$ are the DP-PD residuals of, respectively, the net moment and the horizontal and vertical components of the net force acting at the distal joint of segment *A*. In the specific case where segment *A* is the distal segment of any of the extremities, $\hat{M}x_{EP}$, $\hat{F}y_{EP}$ and $\hat{F}z_{EP}$ are the DP-PD residuals of, respectively, the net moment and the horizontal and vertical components of the net force acting at the distal end-point of segment *A*. Note that, for any given segment, m_{seg}, $cm[L]_{seg}$ and $cm[P]_{seg}$ BSP design variables are present in Eqs. (57)

and (58), and all four segmental BSPs, including I_{seg}, are represented in Eq. (59). The force offset design variables are also present via their involvement in the DP IDA calculations of the contact Foot segment. Minimising these residuals in an optimisation process may lead to realistic estimates of the BSP design variables.

In addition to the limb extremities, Jaffrey et al. (2002) noted that the head can be considered the distal segment of a fifth 'extremity' for IDA purposes. This allows additional DP-PD residuals to be calculated and incorporated into IDA-based objective functions used to estimate BSPs. It is unclear whether some or all of the available DP-PD residuals should be included in an IDA-based objective function or which ones are most important. Hence, this experiment compared IDA-based objective functions comprised of all joint and distal segment end-point net force and moment DP-PD residuals with selected single point DP-PD residuals. The contact Foot distal end-point and the contact limb Hip joint were chosen for this purpose. The first three objective functions were defined as follows:

IDA_{Foot}: The objective function based only on the net force and moment DP-PD residuals of the distal end of the contact Foot segment was designed to be similar to the approach reported by Vaughan et al. (1982a).

IDA_{Hip}: The Hip joint objective function was also for the contact leg and was designed to see if the increased DP IDA error propagation and decreased PD IDA error propagation at this more proximal location had any systematic effect on BSP estimation performance.

IDA_{All}: The objective function based on all joints and distal segment end-points was assessed to see if the provision of more system information produced better BSP estimation performance.

As discussed previously on page 268, the IDA-based approaches developed in this experiment differed from the approach of Vaughan et al. (1982a) because force offset error terms were included and equality constraint Eqs. (47), (48) and (49) could not be utilised. Hence, Eqs. (51), (52) and (53) were incorporated into the IDA-based objective functions. Based on the preceding definitions, and from Eqs. (57), (58) and (59), the first three IDA-based objective functions are summarised as follows:

$$\mathrm{IDA}_{Foot} = \frac{1}{n}\left[\left(\sum_{t=1}^{t=n}\left(\left(\hat{F}y(t)_{EP(Ball)}\right)^2 + \left(\hat{F}z(t)_{EP(Ball)}\right)^2 + \left(\hat{M}x(t)_{EP(Ball)}\right)^2\right)\right) + SSDy + SSDz + SSDx\right] \tag{60}$$

$$\mathrm{IDA}_{Hip} = \frac{1}{n}\left[\left(\sum_{t=1}^{t=n}\left(\left(\hat{F}y(t)_{J(Hip)}\right)^2 + \left(\hat{F}z(t)_{J(Hip)}\right)^2 + \left(\hat{M}x(t)_{J(Hip)}\right)^2\right)\right) + SSDy + SSDz + SSDx\right] \tag{61}$$

$$\mathrm{IDA}_{All} = \frac{1}{17n}\left[\sum_{t=1}^{t=n}\left(\sum_{J=1}^{J=12}\left(\left(\hat{F}y(t)_{J}\right)^2 + \left(\hat{F}z(t)_{J}\right)^2 + \left(\hat{M}x(t)_{J}\right)^2\right) + \sum_{EP=1}^{EP=5}\left(\left(\hat{F}y(t)_{EP}\right)^2 + \left(\hat{F}z(t)_{EP}\right)^2 + \left(\hat{M}x(t)_{EP}\right)^2\right)\right) + SSDy + SSDz + SSDx\right] \tag{62}$$

where t represents a time sample and n is the total number of time samples. The additional denominator factor of 17 in Eq. (62) accounts for the 12 joints and the distal end-points of the five extremities at which DP-PD residuals were calculated, thus, normalising all three objective function outputs.

Another IDA-based objective function was also devised. It utilised additional information identified while the code developed for this experiment was being validated using noiseless simulation data. Before defining the fourth objective function, the code development and validation processes and relevant observations are described first.

7.1.1.4 Code Development, Validation and Observations

All optimisations were programmed in Matlab 6.5.1 (The Mathworks, Inc., Natick, MA., U.S.A.), using the 'fmincon' function. Several option parameters within this function (viz. TolFun, TolCon and TolX) were assigned a value of 0.000001 to ensure the objective functions converged to the desired minima and to ensure constraints were not violated.

The bi-directional (DP and PD) inverse dynamics code written for this experiment was developed from the distal-to-proximal (i.e. bottom-up) 2-D lower limb inverse dynamics code provided, with permission, by van den Bogert (1996b). Prior to expanding the code to cover all joints and segment end-points in the 13-segment model used in this research, a three-segment, single lower limb DP-PD version was validated using the noiseless lower limb gait simulation data provided by van den Bogert (1996a).

Using the validated code and the simulation data, an additional observation was made. As expected, when all the m_{seg}, $cm[L]_{seg}$ and $cm[P]_{seg}$ design variable values were correct, one or several incorrect I_{seg} BSPs produced non-zero DP-PD net moment residuals at each joint and end-point. However, these residuals were also observed to be equivalent at all joints and end-points for any given set of incorrect I_{seg} values. Hence IDA_{All_2}.was developed.

7.1.1.5 The Fourth Dynamics-Based Objective Function

IDA_{All_2}: Essentially, if all the other design variable values are correct, any given set of incorrect I_{seg} values will produce non-zero, but equivalent, DP-PD net moment residuals at each joint and end-point. Therefore, minimising the difference between all combinations of pairs of joint and endpoint DP-PD net moment residuals might help produce better m_{seg}, $cm[L]_{seg}$ and $cm[P]_{seg}$ BSPs, as long as concurrent attempts are made to minimise all DP-PD net force and moment residuals by applying Eq. (62). Hence, the additional term in IDA_{All_2}, reflecting this finding, is the mean of the squared differences of all 136 unique combinations of pairs of joint (J) and end-point (EP) DP-PD net moment residuals:

$$\mathrm{IDA}_{All\_2} = \frac{1}{17n}\left[\begin{array}{l}\sum_{t=1}^{t=n}\left(\begin{array}{l}\sum_{J=1}^{J=12}\left(\left(\hat{F}y(t)_J\right)^2+\left(\hat{F}z(t)_J\right)^2+\left(\hat{M}x(t)_J\right)^2\right)+\\ \sum_{EP=1}^{EP=5}\left(\left(\hat{F}y(t)_{EP}\right)^2+\left(\hat{F}z(t)_{EP}\right)^2+\left(\hat{M}x(t)_{EP}\right)^2\right)\end{array}\right)+\\ SSDy+SSDz+SSDx\end{array}\right]+$$

$$\frac{1}{136n}\left[\sum_{t=1}^{t=n}\left(\begin{array}{l}\sum_{J_A=1}^{J_A=12}\left(\sum_{J_B=J_A+1}^{J_B=12}\left(\hat{M}x(t)_{J_A}-\hat{M}x(t)_{J_B}\right)^2\right)+\\ \sum_{EP_A=1}^{EP_A=5}\left(\sum_{EP_B=EP_A+1}^{EP_B=5}\left(\hat{M}x(t)_{EP_A}-\hat{M}x(t)_{EP_B}\right)^2\right)+\\ \sum_{EP=1}^{EP=5}\left(\sum_{J=1}^{J=12}\left(\hat{M}x(t)_{EP}-\hat{M}x(t)_J\right)^2\right)\end{array}\right)\right] \quad (63)$$

where subscripts *A* and *B* simply represent different nested summation iterations.

7.1.2 Kinematic Data Filtering: Assessed Conditions

The effect of filtering the displacement data used in this experiment at different cut-off frequencies was also assessed. All kinematic marker data used in this experiment were low-pass filtered using the GCV quintic spline software program written by van den Bogert (2000). Initially, the Generalised Cross-Validation (GCV) option in this program was used to filter all data. This is an automatic cut-off frequency determination method, which enabled an independent and objective determination of the degree of smoothing for each marker in each dimension. This initial set of kinematic data, subsequently used in the optimisation processes in this experiment, was termed '*GCV* '.

Giakas and Baltzopoulos (1997a) reported that, when comparing several automatic cut-off frequency determination methods, GCV quintic splines

produced the best results for smoothed gait displacement data. However, results for the first and second derivatives were noisy. Giakas and Baltzopoulos (1997b) reported that cut-off frequencies lower than those considered optimal for displacement data produced better results for the first and second derivatives of the gait data they analysed. Compared with cut-off frequencies considered to be optimal for the gait displacement data, they reported that lower cut-off frequencies (0.46 ± 0.28 Hz and 0.86 ± 0.36 Hz less, for velocity and acceleration data, respectively) produced the best results for the derivatives. Although based on gait data, the findings of Giakas and Baltzopoulos motivated an assessment of the effect of different degrees of kinematic data filtering on the optimisation approaches assessed in this experiment.

The other filtering conditions developed and assessed in this experiment (viz. *90%GCV*, *80%GCV* and *70%GCV*) represented incrementally lower cut-off frequencies (for each marker in each dimension) than those produced by *GCV*. For each of these conditions, the cut-off frequency required for each marker in each dimension was calculated by multiplying the GCV cut-off frequency for that signal by the relevant percentage, and then rounding the result to the nearest 0.25 Hz. Rounding to the nearest 0.25 Hz was implemented for the following pragmatic reasons. The GCV program of van den Bogert (2000) is only capable of determining different cut-off frequencies for each marker when it is invoked in the GCV mode. When a predetermined cut-off frequency is supplied by the user using the 'cut-off frequency' option, it is applied to all identified markers for that execution of the program. To smooth each marker in each dimension for each trial, at predetermined trial- and marker-specific cut-off frequencies, would have

required execution of the program once for every marker in each dimension, for every trial and for every specific cut-off frequency. For this experiment, it was deemed necessarily expedient and acceptable to smooth all markers for all trials at predefined 0.25 Hz increments, thus requiring much fewer manually executed GCV program executions (fewer by a factor exceeding 50). It was also for pragmatic reasons that cut-off frequencies were not rounded down in cases when the GCV cut-off frequency for a given marker was already less than 0.25 Hz. Not rounding down was only required, across all conditions, for less than 5% of markers and was always for markers at or below the knee of the stance limb.

To produce the *90%GCV*, *80%GCV* and *70%GCV* kinematic data sets, the 'cut-off frequency' option in van den Bogert's (2000) GCV software was invoked, which allows the amount of smoothing applied by the splines to be controlled explicitly by the user. The cut-off frequency option in van den Bogert's (2000) program, GCV.exe, produces results with quintic splines that are essentially equivalent to those produced by a 6^{th} order zero-lag phase Butterworth filter with the same cut-off frequency (Woltring, 1995), though without the end-point errors produced by Butterworth filters (see p. 129). Matlab 6.5.1 code (The Mathworks, Inc., Natick, MA., U.S.A.) was developed to access the appropriate data in the files produced by GCV.exe with the 'cut-off frequency' option, and subsequently to construct the *90%GCV*, *80%GCV* and *70%GCV* data sets.

7.1.3 Assessment of the Objective Functions, Force Offset Error Terms, BSP Estimates and Degree of Filtering

The performance of the four IDA-based objective functions was assessed in terms of the objective function values and the number of non-feasible force offset error and BSP design variable values that resulted after optimisation. With only four trials of data available to assess the application of four objective functions and four degrees of filtering, it was not deemed to be appropriate to perform multifactorial statistical hypothesis testing. Nor was it practically feasible to capture, process and optimise any more data, considering the labour-intensive processes involved in the conduct of this research, as described in the general methodology for this research (Chapter 4) and the research design section for this experiment (section 7.1). Hence, analysis was restricted to descriptive techniques.

It is necessary to establish that feasible and realistic force platform error terms and BSPs result from the combined optimisation and dynamics techniques developed in this experiment before consideration can even be given to whether or not the estimated subject-specific BSPs are valid. Based on the results of Vaughan et al. (1982a), who reported several active bound constraints and, therefore, non-feasible BSPs, the analysis of the objective functions in this experiment, in terms of resultant design variable values, focussed on how many of the optimised force offset error and BSP bound constraints became active. Because the number of Fy_O and Fz_O design variables varied from trial-to-trial (see section 7.1.1.1), the percentage of total Fy_O and Fz_O design variables per trial that became active was

to be reported, rather than the absolute number of active force offset bound constraints.

Minimised objective function values were also compared. The first three objective functions, IDA_{Foot}, IDA_{Hip} and IDA_{All}, were normalised with respect to the number of calculated DP-PD residuals. Although the factor of 136 in the denominator of the second component in Eq. (63) weighted the contribution of this component more appropriately in the IDA_{All_2} objective function relative to its other component, it did not make the IDA_{All_2} objective function values directly comparable to the values of the other three objective functions. Hence, only the relative performance of IDA_{Foot}, IDA_{Hip} and IDA_{All} was compared in terms of resultant objective function values.

The four different degrees of filtering applied to the trial kinematic data were assessed by comparing, for each objective function, the minimised objective function values and the resultant number of bound constraints that became active.

7.2 Results

7.2.1 Objective Function Values

Fig. 55 shows the relative performance of IDA_{Foot}, IDA_{Hip} and IDA_{All} in terms of objective function values that resulted for each of the four trials in each of the four filtering scenarios. Trials C and D involved movement activities executed at close to maximum volitional angular accelerations with respect to the extremities (e.g. up to 350 rad/s^2 for the Foot segments and 300 rad/s^2 for the Lower Arm segments), whereas Trials A and B were conducted significantly below maximum volitional acceleration (e.g. up to 200 rad/s^2 for the Foot segments and 100 rad/s^2 for the Lower Arm segments). IDA_{Hip} produced the lowest minimised objective function values for all four trials under all filtering conditions, except for Trial B filtered at *GCV*, and IDA_{Foot} produced the highest values.

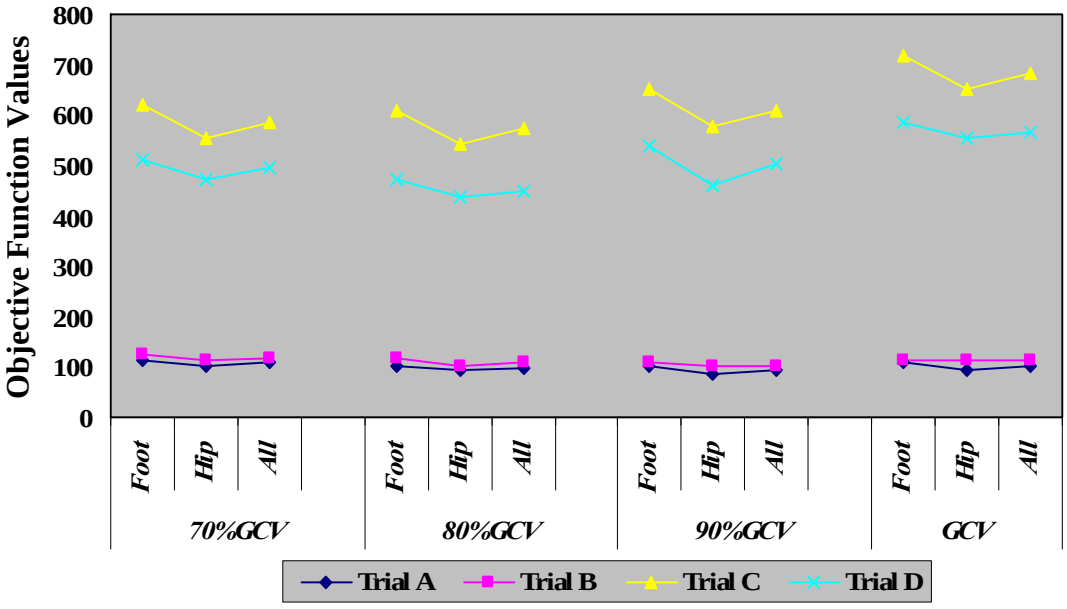

Figure 55. The minimised objective function values of objective functions IDA_{Foot}, IDA_{Foot} and IDA_{All} (Foot, Hip and All, respectively), under each of the four kinematic data filtering conditions (70%GCV, 80%GCV, 90%GCV and GCV).

Fig. 56 shows the indicative DP-PD net moment residuals at all of the joints and extremity distal end-points, prior to and after the application of IDA_{All}, for a typical low acceleration trial (Trial A, *70%GCV*) and a typical high acceleration trial (Trial D, *70%GCV*). As expected, this figure demonstrates how the optimisation process reduced the DP-PD residuals when the objective function was minimised. The figure also illustrates other consistent findings for IDA_{All}. High acceleration trials (Trials C and D) produced greater DP-PD residuals than low acceleration trials (Trials A and B) and, with the consistent exception of the Shoulder joints, DP-PD residuals decreased on each extremity at more proximal joints.

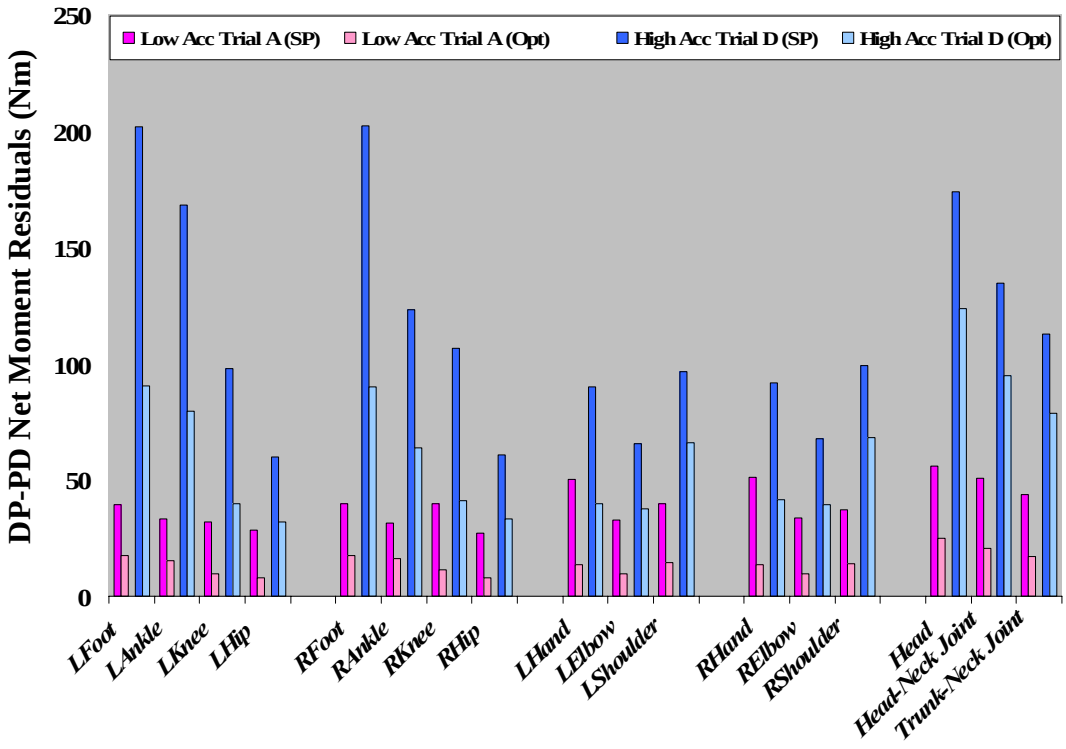

Figure 56. DP-PD net moment residuals (mean values across entire trial) at each of the joints and at each extremity distal segment end-point, prior to and after the application of IDA_{All} (Starting Point – SP, and Optimised - Opt, respectively), for a typical low acceleration trial (Low Acc Trial A; 70%GCV) and a typical high acceleration trial (High Acc Trial D; 70%GCV).

7.2.2 BSP and Force Offset Error Term Estimates

None of the force offset design variable bound constraints became active for any of the four objective functions or any of the four filtering conditions. All Fy_O values ranged from -0.65 to +2.02 N, which was within the constrained bounds of -3 to +3 N for these design variables. All Fz_O values ranged from -13.16 to -7.23 N, which was within their constrained bounds of -14 to -6 N. In contrast, the bound constraints of many of the 32 BSPs became active. Fig. 57 shows that approximately 50% of the BSP bound constraints became active in most trials, for almost all objective functions and all filtering conditions.

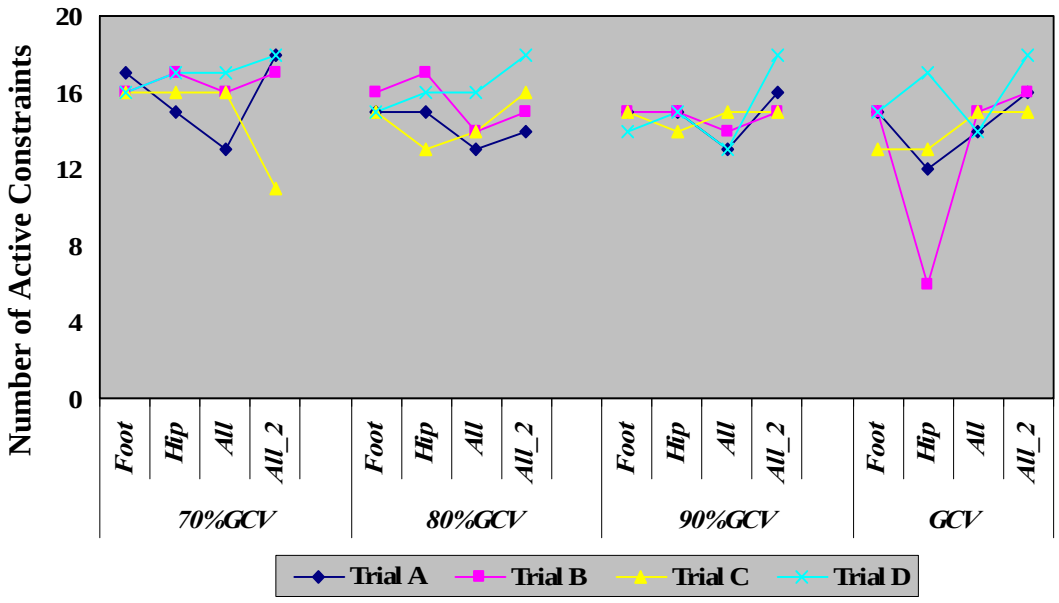

Figure 57. The number of active BSP bound constraints for objective functions IDA_{Foot}, IDA_{Foot}, IDA_{All} and IDA_{All_2} (Foot, Hip, All and All_2, respectively), under each of the four kinematic data filtering conditions (70%GCV, 80%GCV, 90%GCV and GCV).

Fig. 58 shows the percentage of the 64 cases (i.e. 4 trials × 4 objective functions × 4 filtering conditions) for which each BSP's lower and upper bound constraints became active. Only nine (28%) of the BSP lower and upper bound constraint pairs never became active during this experiment. Conversely, the upper bounds of m_{Thigh} and $I_{Upper\ Arm}$, and the lower bound of I_{Neck} invariably became active, with another 10 bound constraints becoming active in over 50% of cases. When bound constraints did not become active, BSP values were generally realistic, with the exception of m_{Trunk} and $cm[L]_{Thigh}$. When feasible, m_{Trunk} and $cm[L]_{Thigh}$ were always in the lowest 11% (i.e. < 0.381) and 18% (i.e. < 0.271) of their respective bound-constrained ranges. Although other BSP values were generally realistic when their respective bound constraints did not become active, the values often varied broadly across their respective feasible regions from trial-to-trial.

Generally speaking, the estimated $cm[L]_{seg}$ and $cm[P]_{seg}$ BSP values were more often feasible (72% and 82% of BSP-cases, respectively) and realistic than estimated m_{seg} and I_{seg} BSP values (39% and 23% of BSP-cases, respectively). Whenever an m_{seg} bound constraint became active, it was always restricted to the upper bound, except for cases of an active m_{Trunk} bound constraint, which only ever became active at the lower bound. Conversely, one of the $cm[L]_{seg}$, one of the $cm[P]_{seg}$ and six of the seven I_{seg} bound constraints became active at the lower bound in some cases and the upper bound in some others.

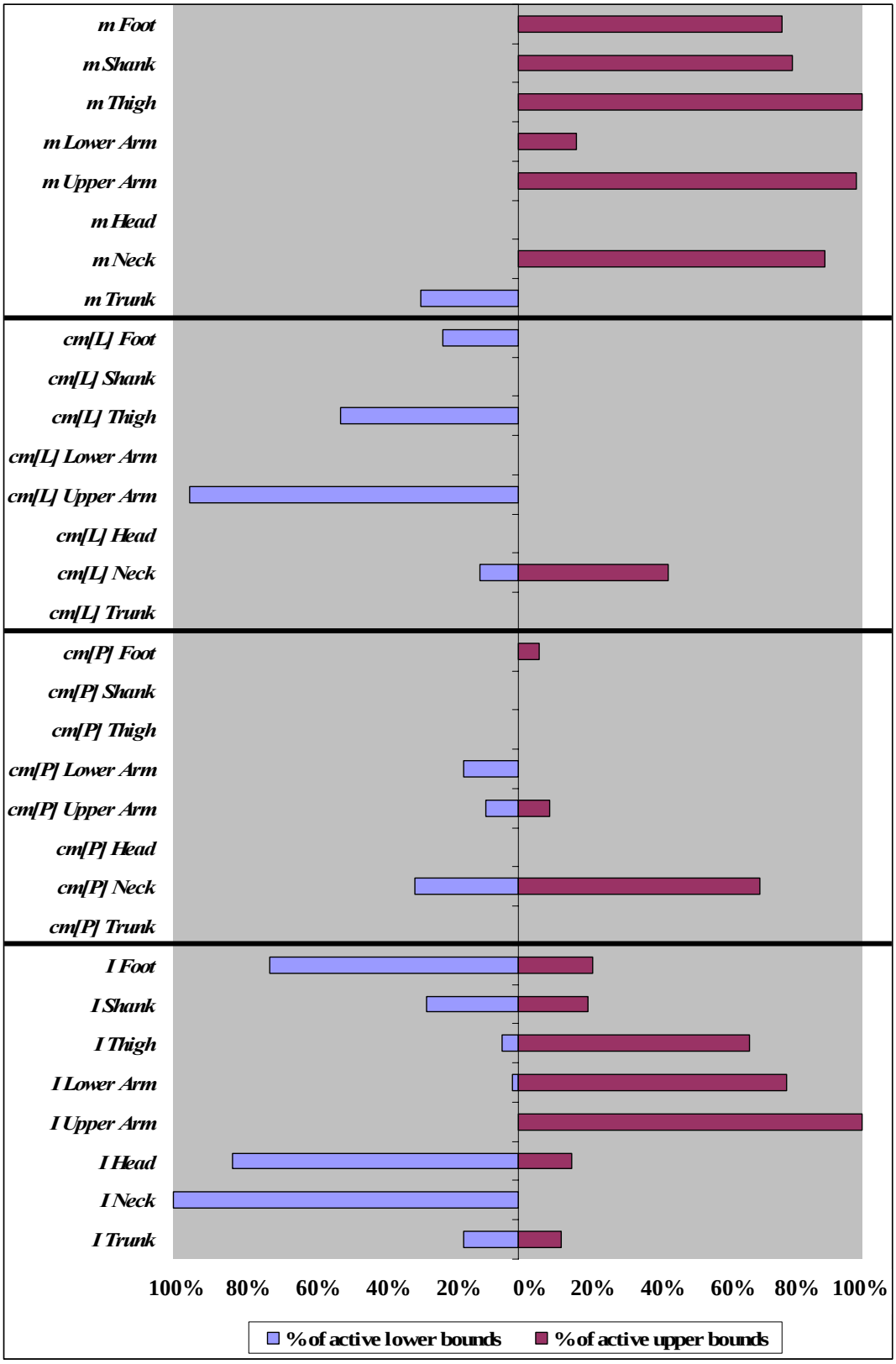

Figure 58. The percentage of all 64 cases (i.e. 4 trials × 4 objective functions × 4 filtering conditions) for which each BSP's lower and upper bound constraints became active.

7.2.3 Filtering Approaches

For Trials A and B, and Trials C and D, respectively, Figs. 59 and 60 show the minimised objective function values for each of the objective functions assessed in this research under each of the four kinematic data filtering conditions. Although there were only four trials, minimised objective functions were consistently lowest at either *80%GCV* or *90%GCV* and consistently greatest at either *70%GCV* or *GCV*. However, this did not coincide with a consistent improvement in the number of feasible BSP estimates for the *80%GCV* or *90%GCV* conditions, as indicated in Fig. 61. Indeed, there was no evident trend towards any particular filtering condition producing fewer non-feasible BSP estimates than any other filtering condition.

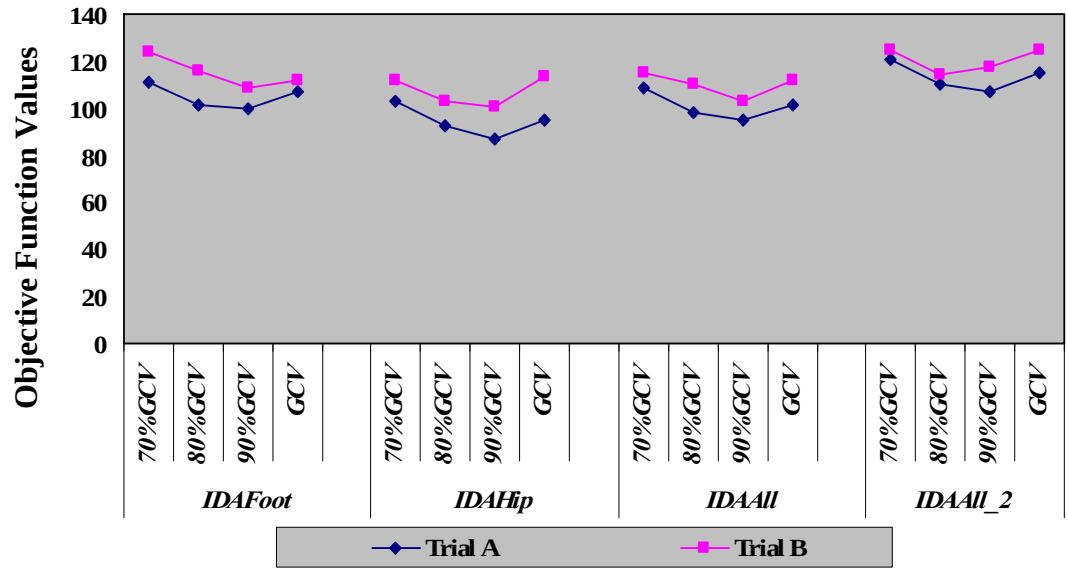

Figure 59. The minimised objective function values of objective functions IDA_{Foot}, IDA_{Hip}, IDA_{All} and IDA_{All_2} (Foot, Hip, All and All_2, respectively) for trials A and B, under each of the four kinematic data filtering conditions (70%GCV, 80%GCV, 90%GCV and GCV).

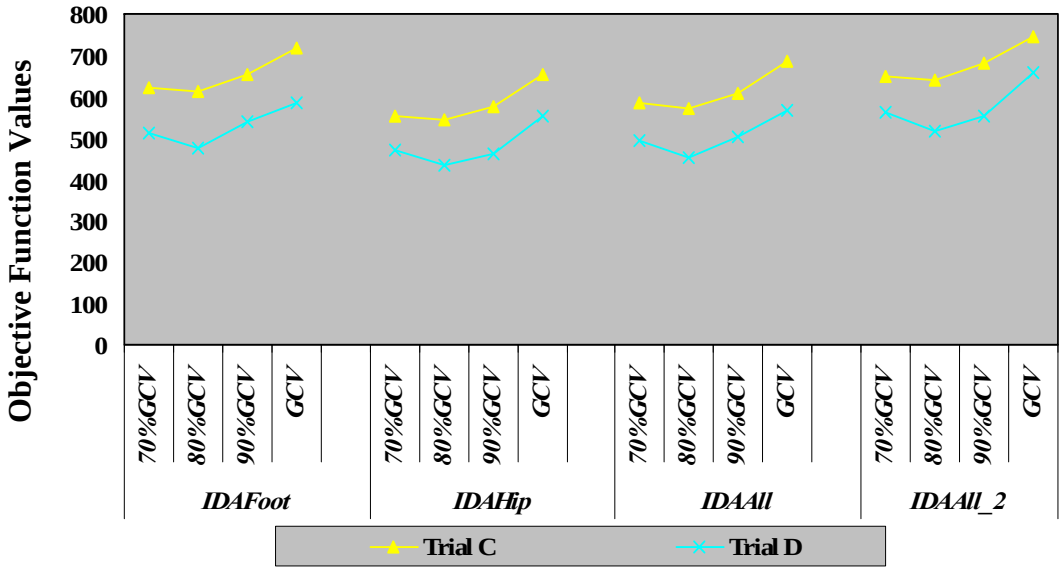

Figure 60. The minimised objective function values of objective functions IDA_{Foot}, IDA_{Hip}, IDA_{All} *and* IDA_{All_2} *(Foot, Hip, All and All_2, respectively) for trials C and D, under each of the four kinematic data filtering conditions (70%GCV, 80%GCV, 90%GCV and GCV).*

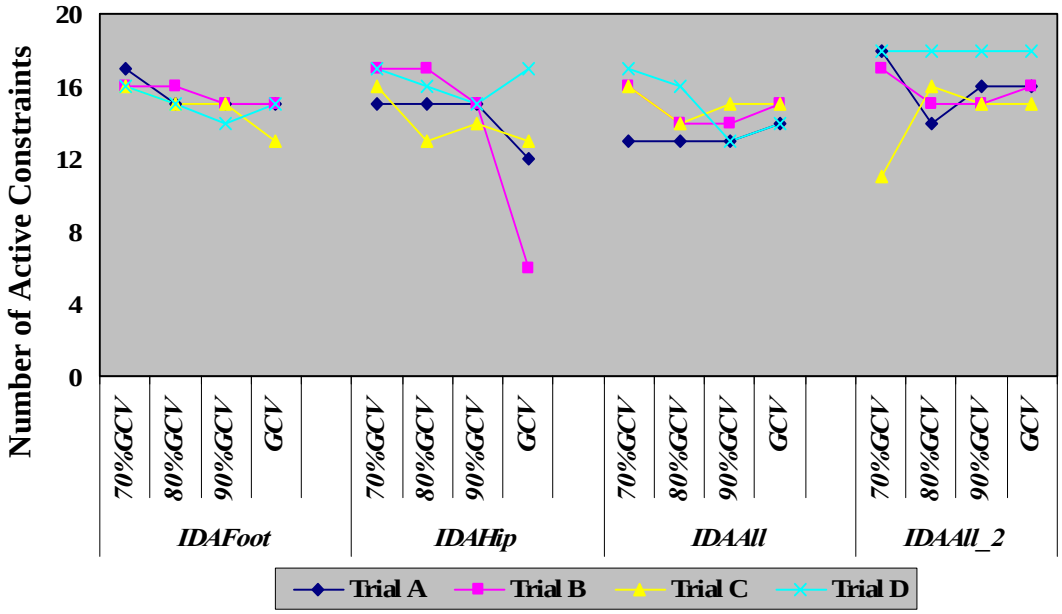

Figure 61. The number of active BSP bound constraints for the four kinematic data filtering conditions (70%GCV, 80%GCV, 90%GCV and GCV), for each of the objective functions (IDA_{Foot}, IDA_{Foot}, IDA_{All} *and* IDA_{All_2}*).*

7.3 Discussion

This experiment demonstrated the application of various IDA-based objective functions to produce estimates of force platform offset error terms and subject-specific BSPs under different kinematic data filtering conditions. This section discusses the performance of these methods in terms of the objective function and design variable values produced, and comparisons are made to studies with similar methodologies conducted by other researchers. Potential methodological limitations are also identified and recommendations for future research are made.

7.3.1 Objective Function Values

IDA_{Hip} produced the lowest and IDA_{Foot} produced the highest optimised objective function values for 15 of the 16 trial-filtering condition combinations. IDA_{All} produced values between the aforementioned single-point approaches, reflecting the mean of all segment end-points and joints, both distal and proximal. Although only two single-point IDA approaches were assessed in this research, the smaller DP-PD residuals at the Hip joint suggest that the net error propagation to the Hip joint by DP and PD IDA calculations may be less than the net error propagation throughout the entire body to the distal end-point of the Foot. That is, relative to IDA_{Foot}, IDA_{Hip} increases DP IDA error propagation and decreases PD IDA error propagation, but the net discrepancy at more proximal joints, such as the Hip joint, may be less than that at a distal limb segment end-point, such as the Foot segment. Challis (1996) and Pezzack and Norman (1981) have also suggested that IDA error propagation may be cumulative and, therefore, more pronounced at

the final link in the chain. In general, Fig. 56 supports this concept, although the Shoulder was the exceptional joint. The reason for the exception might have been due to the simplified representation of the Shoulder joint centre used in this experiment. Another possible explanation is that the propagation of a net moment error from a preceding joint may, in some cases, actually cancel out some of the error at an adjacent joint (Challis, 1996). However, the reason for the Shoulder joint exception remains unclear.

The current research produced different net residuals at each end-point and joint (e.g. Fig. 56). Vaughan (1980) asserted that any of the distal segment end-point residuals could be used because of the over-determined nature of the posed IDA problem, and that the choice of this point should not change the resulting set of BSPs. However, this was not the case in the current experiment, which produced different BSP estimates for each of the objective functions (IDA_{Foot}, IDA_{Hip} and IDA_{All}). There is no evidence to assert that any of the objective functions assessed in this experiment consistently improved dynamics solutions more than any other. Hence, it is recommended that all joint and distal segment end-point DP-PD residuals be assessed in future IDA-based objective function formulations, both collectively (viz. IDA_{All}) and individually, and that the relative influence of all DP-PD residuals should be assessed.

For Trials C and D, the extremities were accelerated at close to maximum volitional angular accelerations, whereas Trials A and B were conducted significantly below maximum volitional acceleration. Trials C and D produced minimised objective function values five to six times greater than those produced

for Trials A and B (Fig. 55). The higher acceleration terms in Trials C and D were the only objective function input parameters for which the magnitude changed appreciably during Trials C and D, so they clearly contributed to the greater DP-PD residuals observed within the objective functions for Trials C and D (e.g. Fig. 56). The more prevalent wobbling of soft tissues in Trials C and D and, hence, the violation of the rigid body model (Pain and Challis, 2006), may have contributed to the increased DP-PD residuals, but this could not be confirmed nor quantified based on the results produced by this experiment. As discussed in the review of literature (Chapter 2), the sensitivity of DP-PD residuals to BSP errors should be relatively more significant for open-loop activities during which limb segments undergo relatively large accelerations, such as throwing (Pearsall and Costigan, 1999), kicking (Ganley and Powers, 2004b) and those executed in Trials C and D. Although the inclusion of higher acceleration activities for the distal, less massive segments theoretically should have produced better BSP estimates for these segments, the results of this experiment showed no clear improvement in this regard. This suggests that concomitant and confounding errors may have been present. However, the source or sources of such errors remains unclear.

7.3.2 Filtering Approaches

Notwithstanding that there were only four trials in this experiment, minimised objective functions were consistently lowest at either *80%GCV* or *90%GCV* and consistently greatest at either *70%GCV* or *GCV*. This result for *80%GCV* and *90%GCV* matches well with the findings of Giakas and Baltzopoulos (1997b), albeit for 3-D gait data in their case. They reported that cut-off frequencies

0.86 ± 0.36 Hz lower than those they considered to be optimal for their displacement data, produced the best results for the second derivative. Considering the range of mean cut-off frequencies that they considered optimal for their marker displacement data was 3.7 Hz to 8.2 Hz, a reduction of 0.86 Hz to these figures represents a range of 76.8% to 89.5% of the original cut-off frequencies considered optimal for their displacement data. However, the consistent production of the lowest objective function values by either *80%GCV* or *90%GCV* in the current experiment was not matched by a consistent improvement in the number of feasible BSP estimates for the same filtering conditions, as indicated in Fig. 61. Indeed, no trend was evident towards any particular filtering condition producing less non-feasible BSP estimates than any other filtering condition. In this experiment, for any given marker and dimension, both the displacement data and derived acceleration data supplied to the optimisation process were based on marker data filtered at the same cut-off frequency. It may have been preferable to use marker displacement data filtered at *GCV* and acceleration data derived from marker data filtered at *80%GCV* or *90%GCV*. However, as Giakas and Baltzopoulos (1997b) pointed out, "there might be cases in which consistence is needed between position, velocity and acceleration." This "consistence" was deemed more appropriate in the current experiment, considering that both displacement and acceleration data were required concurrently for all objective function calculations. Concurrent application of marker position data filtered in one way with acceleration data derived from the same marker data but filtered a different way, was deemed inappropriate. Retrospective inspection of the data indicated that filtering at *80%GCV* never reduced displacement values by more than 0.4% (0.3 mm)

compared with *GCV*, whereas acceleration signals were sometimes reduced by up to 20%. Further work is required to identify the most appropriate filtering strategies for combined dynamics and optimisation techniques of BSP estimation. This is important because estimated joint moments are highly sensitive to uncertainties in acceleration data (Cahouet et al., 2002; Pezzack and Norman, 1981).

7.3.3 Force Offset Error Term Design Variables

No Fy_O or Fz_O bound constraints became active for any of the objective function and filtering condition combinations. All Fy_O values ranged from -0.65 to +2.02 N and all Fz_O values ranged from -13.16 to -7.23 N, all of which represent feasible and realistic values[32]. Additional testing demonstrated that the components of the objective functions based on Newtonian principles regarding the rate of change of linear momentum were primarily responsible for the feasible Fy_O and Fz_O design variable values. That is, when Eqs. (51) and (52) were removed from the objective functions, many Fy_O and Fz_O bound constraints became active. Further, more BSP bound constraints also became active under these conditions. The inclusion of force offset error term design variables by Vaughan et al. (1982a) may have reduced the number of active BSP bound

[32] As indicated in previous chapters, when a 633.75 N dead weight was placed in 26 different locations spread across the surface of the force platform, the Fz_O values that produced de-trended *Fz* signals averaged -11.98 N with a standard deviation of 1.61 N. Hence, the mean ± 3SD range of Fz_O values was -16.81 to -7.15 N. Similarly, the Fy_O values that produced de-trended *Fy* signals averaged 0.65 N with a standard deviation of 0.95 N. Hence, the mean ± 3SD range of Fy_O values was -2.20 to 3.50 N.

constraints in their study. Based on the results of the current experiment, the retention of Eqs. (51) and (52) and the inclusion of force offset error term design variables is recommended for future development of these BSP estimation techniques.

7.3.4 BSP Estimates

There was no indication that any of the four IDA-based objective functions assessed in this experiment produced better BSP estimates than any other. Indeed, all four objective functions produced many realistic and unrealistic BSP estimates in most trials, for all the objective functions and all the filtering conditions. Vaughan et al. (1982a) applied an objective function very similar to IDA_{Foot}, which also resulted in non-feasible BSPs, albeit, substantially fewer. They speculated that possible reasons for non-feasible BSPs included inaccurate kinematic data measurements and invalid modelling assumptions.

As discussed in Chapter 2 (pages 84-85), Fregly and Reinbolt (2004) extended the work of Vaughan et al. (1982a) to a 3-D method. They used a nonlinear optimisation technique similar to Vaughan et al. (1982a) to estimate all BSPs by minimising residual pelvis loads. By modifying experimental gait data, they produced noiseless synthetic data that satisfied the dynamics equations precisely. Then, after perturbing all the BSPs randomly by ±50% from their known values, their optimisation approach was able to reproduce the original synthetic BSP values with "essentially zero pelvis residual loads". However, when they added noise to their synthetic data set, some non-feasible BSPs resulted, as was the case in the current study and the study of Vaughan et al. (1982a). Fregly and Reinbolt

(2004) did not identify which segmental BSPs were non-feasible, however, like Vaughan et al. (1982a), they suggested that a significant limiting factor responsible for inaccurate BSP results was erroneous kinematic input data.

Recently, Reinbolt et al. (2007) published a full paper extending the work first reported by Fregly and Reinbolt (2004). In the most recently reported study, they estimated joint parameter values (viz. joint axis positions and orientations in body segments) and BSPs by optimising IDA calculations derived, again, from synthetic gait data with added noise. Firstly, they varied the joint parameters and then the BSPs to optimise the IDA calculations. They found that joint parameter values could be found accurately from noisy kinematic data but that this was not the case for BSP values, though many of the BSP values were realistic. Interestingly, they did not use BSP bound constraints. Rather, they included terms in their IDA-based objective function that applied an increasing penalty as BSP values varied away from their starting point estimates. These terms constrained the BSPs somewhat artificially and may have affected the effectiveness of the IDA terms in the objective function. Reinbolt et al. (2007) also tried varying joint parameter and BSP values simultaneously and found that small additional variations to joint parameter and BSP values produced large reductions in residual forces and torques at the pelvis (46% and 62%, respectively). They also conducted Monte Carlo analyses to evaluate how errors in joint parameter and BSP values affected IDA calculations. Errors in the joint parameter values but not the BSP values were found to have a significant effect on lower-extremity IDA joint torques for the synthetic gait data, suggesting that BSP

estimation in isolation from joint parameter estimation may be an ill-posed problem.

The findings of Reinbolt et al. (2007) and Fregly and Reinbolt (2004) suggested that inaccurate BSP estimates may be due to modelling and kinematic errors. In the context of this possible explanation, further consideration is now given to the current study, and the work of Vaughan (1980) in his doctoral dissertation and also published by Vaughan et al. (1982a).

7.3.5 Comparison of the Current Research with Vaughan (1980) and Vaughan et al. (1982a)

The motion capture procedure used for the current research involved relatively low resolution stereophotogrammetry. The resolution of the recorded digital video was only 720×576 pixels. Furthermore, it was recorded from the composite video image from the analogue CCTV cameras, which only had 430 lines of horizontal resolution. Digitising was done automatically by recording the position of markers pre-placed on the subject's body. On the other hand, Vaughan (1980) used cinematography and reported that the 14×19 cm images were manually digitised, by subjective estimation of joint centres, using a device with a resolution of 0.025 mm. Clearly though, the resolution of the device is greater than the precision of the human digitiser's subjective estimates of joint centres.

In the current research, the laboratory dimensions facilitated the setting up of the cameras with telephoto lenses at least 13.5 m from the subject, whereas Vaughan (1980) had to place their camera only 4.5 m from their subject, necessitating the use of a 10 mm wide-angle lens, which caused "considerable" image distortion. This led Vaughan (1980) to introduce lens distortion correction procedures. Although lens distortion had much less influence in the current research, the application of distortion correction procedures may have improved the quality of the kinematic data. The video data were captured at 50 Hz for the current research, whereas Vaughan et al. (1982a) filmed at 100 Hz. A capture rate higher than 50 Hz in the current experiment may have improved the accuracy of the acceleration calculations derived from the displacement data (Pagnacco et al., 1997), but this remains unclear. Regardless, only 50 Hz video equipment was available. Whether the cinematographic approach of Vaughan et al. (1982a) or the video and automatic digitising approach conducted for the current research produced more accurate raw kinematic data also remains unclear.

Quintic spline smoothing techniques were employed in this research and that of Vaughan et al. (1982a) for the kinematic data. For the current research, the Generalised Cross-Validation approach was used to estimate automatically and objectively the optimal effective low-pass cut-off frequencies for the kinematic data. Vaughan (1980) manually selected what he deemed to be the best smoothing parameters for his quintic spline smoothing process by completing a methodical, incremental assessment of the smoothing parameters separately for every marker signal in both dimensions. He stated, "While this might at first seem a tedious and time-consuming task, it was considered necessary since the

success of the study depended heavily on the accuracy of the kinematic data." The findings of Reinbolt et al. (2007) and Fregly and Reinbolt (2004), reported in section 7.3.4, support Vaughan's statement and actions. Alonso et al. (2005) suggested that spline-based methods are usually more appropriate for filtering signals of different signal-to-noise ratios than other traditionally-used filtering methods in biomechanics research. However, they pointed out that traditionally-used methods are not suited for smoothing non-stationary signals such as human motion with ground impacts. Because the activities measured for this experiment and that of Vaughan et al. (1982a) did not involve transient impacts, splines were appropriate in both cases.

Della Croce et al. (2005) recently provided a thorough review of the problems associated with joint centre estimation. The methods applied in this research and by Vaughan et al. (1982a) were two-dimensional and much less sophisticated than many of the methods summarised by Della Croce et al. (2005). Della Croce et al. (2005) reported that even the more sophisticated methods still lack the desired degree of accuracy for many biomechanical applications. Considering the encouraging BSP estimates reported by Vaughan et al. (1982a), the modelled joint centres and segment end-points used in this research were kept similar to those employed by Vaughan et al. (1982a) so that meaningful comparisons would be possible. However, postulating that Vaughan et al. (1982a) may have introduced significant limitations by defining the trunk segment end-points simply as the mid-hip and mid-shoulder points, the more complex definition of the Trunk segment developed for the current research (section 4.4.1.1) was expected to produce relatively favourable results with respect to the number of feasible BSP

estimates. This was particularly anticipated because Vaughan et al. (1982a) had not attempted to prevent their subject from flexing or curving his trunk during the measured activities, whereas, the subject in the present research was instructed to maintain a straight and rigid trunk. Pezzack and Norman (1981) explained that changes in apparent trunk length introduced by the more simplistic trunk definition, predominately due to shoulder elevation, introduce errors in cm_{Trunk} linear displacement and acceleration. They argued that because m_{Trunk} is the greatest component of whole body mass, even small inaccuracies in cm_{Trunk} linear kinematics could produce large errors in IDA-calculated net forces and moments at the Hip and Shoulder joints. Somewhat surprisingly, the expected benefit of the trunk model definition introduced for the current research was not forthcoming.

Several researchers have highlighted the significant influence joint centre errors can have on IDA-calculated net joint moments (e.g. Davis, 1992; Desjardins et al., 1998; Holden and Stanhope, 1998; Nagano et al., 2000). Such errors would have been present in both the current research and that of Vaughan et al. (1982a). The automatic digitising approach adopted in the current research was a time-management necessity, given the long duration of the trials. Although it was a somewhat objective method, it was affected by subjective marker placement and subsequent skin movement artefacts and out-of-sagittal-plane motion. Whether the no-marker, subjective manual digitising approach adopted by Vaughan et al. (1982a) overcame these issues to some extent is not clear. However, the bilateral recording approach in the current experiment would seem to be preferable to the unilateral approach used by Vaughan et al. (1982a), when considering the

difficulty of manually digitising obscured Hip and Shoulder joint centres accurately on the far side of the subject.

Another potential source of confounding error is the possibility of an error in measuring the location of the COP in the force platform reference system and the subsequent location of the COP within the global coordinate system (i.e. the kinematic coordinate system). McCaw and De Vita (1995) reported that IDA calculations of net joint moments changed by up to 7% when a 5 mm mismatch was introduced between the force platform and camera coordinate system origins. Similarly, Heiss and Pagnacco (2002) asserted that errors in COP appreciably increase the difference between the rate of change of angular momentum of the whole body and the net external moment acting on it (Eqs. (49) and (50)). Silva and Ambrosio (2004) found that IDA net joint moment calculations for gait analysis were "very sensitive" to errors in COP and "less sensitive" to errors in segmental mass BSPs. Chockalingam et al. (2002) indicated there was a decrease in accuracy of COP calculations as COP moves away from the centre of the platform. However, this was not an issue for the current research because the subject was always standing on one foot very close to the centre of the platform. A limitation of the current study is that the match between the kinetic and kinematic origins was not tested empirically. Future work should enable measurement of the match between the kinetic and kinematic origins. The inclusion of kinematic-kinetic origin offset error term design variables should also be considered.

Other differences between the two studies were the different trial durations and types of movement activities performed by the subjects. The movement activities devised by Vaughan et al. (1982a) included powerful propulsive ground contact phases as well as airborne phases. They were comprised of the propulsive and airborne phases of a running stride and a long-jump leap, and an American football punt kicking motion without a ball. For the current research, deliberate movements were executed to ensure that all segments underwent linear and angular changes relative to each other at different degrees of acceleration. All the high acceleration movements executed by the subject in the current research were conducted by non-contact extremities, whilst one lower limb remained in contact with the ground at all times. Because the Foot segment of the contact limb always remained in contact with the ground, contact limb accelerations and, possibly, trunk accelerations would not have reached the magnitudes of those in the study of Vaughan et al. (1982a). The running, jumping and kicking activities were very short duration activities. Much longer duration movement trials were used for the current research. The movement patterns executed in the current study were also carefully designed to be essentially planar in the sagittal plane, thus minimising errors associated with the 2-D model. Review of the pictorial representations of the movements assessed by Vaughan et al. (1982a) suggests that they would have produced more out-of-plane motion than the movements assessed in the current study. It was anticipated that longer trials of this nature might have produced exclusively feasible BSP estimates, or at least more feasible results than were achieved by Vaughan et al. (1982a), but this did not eventuate.

Ultimately, all combined dynamics and optimisation methods of BSP estimation will be somewhat limited by the nature of the applied model. Hatze (2002b) stated succinctly that the inverse dynamical behaviour of a mathematic model "is profoundly different from that of the source system." The 2-D inverse dynamics analyses conducted in the current research and by Vaughan et al. (1982a) were based on the assumption of the model being comprised of rigid bodies linked by frictionless joints. Clearly, this is not true in reality. Pain and Challis (2001) reported an example of the location of the centre of mass of the lower leg moving 1.7 cm more proximally when the triceps surae muscles went from a relaxed state to a contracted state causing plantar flexion. The idea of attributing different inertial properties to the rigid and non-rigid (wobbling mass) components of segments has also been proposed (e.g. Pain and Challis, 2006; Pierrynowski et al., 1983); this might be more important for activities with ground impacts than for the activities conducted during the current research and the work of Vaughan et al. (1982a). Clearly, a modelling paradox always exists: the more complex a model, the more potential it has to improve the biomechanical representation of human movement Hatze (2002a), but this will necessarily be at the expense of the relative ease of model utility and the relative economy of computational requirements. A compromise is often necessary in reality. For example, Kingma et al. (1996b) reported that trunk mass and centre of mass were the BSPs with the strongest influence on the dynamics quantities they calculated in their study, effectively supporting the notion that the trunk be prioritised for remodelling. The main modifications to the model of Vaughan et al. (1982a) that were applied in the current research were attempts to improve the representation of the Trunk end-point definitions and the introduction of two-component cm_{seg} BSPs.

7.3.6 Rationale for Future Research

Although the results of this experiment were quite disappointing in terms of BSP estimation, many potentially confounding error sources were considered in the previous section, several of which could be reduced using more contemporary data capture techniques. Further, there are other good reasons for pursuing estimation of BSPs via combined dynamics and optimisation techniques. One particular advantage of these techniques was also identified by Challis (1996) with respect to some geometric models. The experimenter is free to define the segments and segment boundaries that best suit his/her proposed study. One is not restricted to the definitions originally used by the researcher who developed the applied estimation technique. If they can be improved sufficiently, combined dynamics and optimisation techniques will also produce subject-specific BSP estimates. Such techniques are only dependent on information directly related to the subject in question.

Most current BSP estimation methods only estimate one set of discrete BSP values, based on a single body posture, or even completely independently of body posture. Any such BSP estimation method probably would not consistently outperform all others during dynamics comparisons of different movement sequences. For example, Kingma et al. (1996b) found that different lifting activities were capable of producing net moment residuals that were 'minimised' by different BSP estimation methods. In order for a BSP estimation method to consistently outperform all others during dynamics comparisons of different movement sequences, it would need to account for the effect on BSPs of the

specific movement pattern to be analysed. Possibly the only methods that can do this to any degree are the combined dynamics and optimisation techniques that use an actual movement sequence of the individual to estimate the BSPs. Combined dynamics and optimisation techniques will be movement-specific, recognising that the inertial properties of the segments vary with different segment orientations and joint angles, due to the changing distribution of soft tissues across the model-defined segment boundaries during movement (Hatze, 2002b).

7.3.7 Recommendations for Future Research

If all of the benefits of the combined dynamics and optimisation methods of estimating BSPs discussed in the previous section are to be realised, then additional technique improvements need to be implemented and evaluated. With the contemporary, high resolution digital cameras now more readily available in biomechanics laboratories, 3-D reconstruction of marker data will result in sub-millimetre accuracy of actual marker displacements and will improve acceleration calculations (Della Croce et al., 2005). The high resolution and accuracy of these cameras also means that markers can be placed on anatomical locations quite close to each other and still be accurately discerned from each other. This allows marker placements at locations that are less prone to skin movement artefacts. Thus, the method can be applied to 3-D movement activities or reduced to a 2-D analysis and BSP prediction method if the movements are constrained, essentially, to the sagittal plane. However, even in the latter case, the process will be enhanced by the initial capture and 3-D reconstruction of the marker data.

If and when combined dynamics and optimisation techniques are able to produce a complete set of feasible BSPs from real experimental data, the next question will be regarding whether the produced results accurately reflect the subject's true BSPs. Rather than making mere comparisons with other methods and stating that the results are in general agreement with other accepted methods, the dynamics approach will enable the same subject to repeat the same movement patterns with additional mass strapped onto one or more segments. If the resultant BSP estimates accurately reflect the artificial inertial changes, then significant progression will have been made towards validating such methods. This potential means of validating the method on a specific, living subject and for a specific movement pattern is appealing.

7.3.8 Summary

This experiment presented methods of optimising inverse dynamics analyses and representations of the rate of change of whole body linear and angular momentum by selecting optimal force measurement offset error term values and optimal BSPs. Although feasible force offset error terms were invariably produced, results were generally poor with respect to BSP estimation, with approximately 50% of all BSP bound constraints becoming active under almost all experimental conditions. The reason for the fewer active bound constraints reported by Vaughan et al. (1982a), compared with the current experiment, remains unclear. Modelling assumptions and kinematic data capture errors were probably the main reasons for the unrealistic outcomes in both studies. The combined dynamics and optimisation methods developed in this research may yet prove to be valid,

versatile and relatively non-invasive subject-specific BSP estimation methods if further methodological improvements can be developed. The use of contemporary, high-resolution and accurate motion capture systems may help improve future methods. The retention of Eqs. (51) and (52) and the inclusion of force offset error term design variables is recommended.

8. CONCLUSION

The overall objective of this research was to improve the representation of sagittal plane whole body dynamics using nonlinear optimisation techniques. The broad aims were to assess various IA optimisation approaches for determining CM kinematics solely from force platform data; and to assess the effectiveness of various IDA-based optimisation techniques in terms of their ability to estimate subject-specific BSPs.

In the first study, ZPZP IA optimisation methods were developed for posturographic analyses based on relative CM displacement calculations. These methods were described as interpolative techniques because they only calculate CM displacement between known points of COP displacement that are hypothesised to coincide with, or be within 1 mm of, time-matched CM horizontal displacement. The results supported the use of method *ZPZP6C*, over the conventional ZPZP method of Zatsiorsky and Duarte (2000), for determining anteroposterior CM kinematics during quiet stance. Both the 'conventional' and 'unconventional' ZPZP optimisation methods developed for this research produced promising results. Conventional methods produced no discrepancies between antero-posterior CM and COP trajectory at the IEPs but produced unrealistic discontinuities in antero-posterior CM velocity. The opposite trade-off applied to the unconventional methods. In these cases, antero-posterior CM velocity was continuous, but discrepancies existed between antero-posterior CM and COP trajectory at the IEPs. The *ZPZP6C* method represents a pragmatic compromise between these two approaches, recognising the presence of imperfect

input data and model assumptions. This method might be improved by fitting splines to the optimised antero-posterior CM trajectory data. Future attempts to validate such methods for quiet stance applications should involve comparisons with segmental kinematic determination of CM trajectory in which all segments superior to the ankle joint are held rigid.

In the second study, various methods of IA optimisation were applied in both the antero-posterior and vertical dimensions to transient dynamic activities (i.e. jumps) that were preceded by a period of quasi-static stance. In these methods, the design variables consisted of the initial CM velocity and force platform error terms. Such methods were described as extrapolative techniques because they attempted to predict CM trajectory forwards into the dynamic phases of the jump based on predictions about CM trajectory during the quasi-static phase only. None of these methods was recommended for determining relative CM trajectory for points beyond the pre-jump quasi-static stance phase for countermovement jumps, if sub-centimetre accuracy is required. The influence of a drift error in these methods becomes progressively worse as time passes, thus preventing the valid application of these methods to other, longer duration activities. Vertical dimension IA optimisation methods that include Fz_O and initial vertical CM velocity as design variables are recommended over methods that assume both of these parameters to be zero. However, assuming the latter parameter to be zero produced acceptably accurate estimates of jump performance parameters commonly calculated in jumping assessments (Hatze, 1998), including CM jump height, work and power. This was because of the decreased influence of drift error over this relatively short time period (viz. ~0.35 s). These methods

were also demonstrated to be as accurate as the segmental kinematic method for determining the vertical displacement range of the CM from the minimum countermovement point to the peak of flight. Optimising whole body mass is unsound on theoretical grounds and was demonstrated to be detrimental to IA-determined estimates of CM trajectory for countermovement jumps. Whole body mass should be measured on precision scales and supplied as a constant to the IA optimisation process. Time-variable errors in *Fy* and *Fz* measurements that are dependent on COP position and foot pressure distribution patterns on the force platform are suspected to be the main remaining sources of drift error in IA optimisation method calculations of CM trajectory. Theoretical and empirical measurement approaches may lead to a better understanding of force platform distortion characteristics and the subsequent effects these have on measured signals. In turn, this may lead to better modelling of the error sources in force platform measurements.

The third study presented combined dynamics and optimisation methods based on inverse dynamics calculations and representations of the rate of change of whole body linear and angular momentum. The objective functions included force offset error terms and BSPs as the design variables and the intention was to estimate subject-specific BSPs. Although feasible force offset error terms were always produced, many non-feasible and unrealistic BSP estimates resulted from almost all experimental conditions. The use of contemporary, high-resolution and accurate motion capture systems may help improve these BSP estimation techniques. Eqs. (51) and (52) and force offset error term design variables should be retained in future developments of these techniques.

In summary, the main findings of this research were as follows:

- ZPZP IA optimisation methods developed in this research showed considerable potential for calculating CM trajectory independent of kinematic data collection, particularly the interpolative method *ZPZP6C* for quiet stance and balance applications.
- When applied in the vertical dimension to jumping activities, the extrapolative ZPZP IA optimisation methods produced acceptably accurate estimates of jump performance parameters commonly used for jumping assessments (Hatze, 1998), including CM jump height, work and power.
- The combined dynamics and optimisation methods developed in this research, based on IDA calculations, produced many non-feasible and unrealistic BSP estimates.
- All the optimisation methods developed in this research benefited from the inclusion of force platform measurement offset error design variables.

REFERENCES

Primary References

Ackland, T. R., Blanksby, B. A., Bloomfield, J., 1988a. Inertial characteristics of adolescent male body segments. Journal of Biomechanics 21, 319-327.

Ackland, T. R., Henson, P. W., Bailey, D. A., 1988b. The uniform density assumption: its effect upon the estimation of body segment inertial parameters. International Journal of Sport Biomechanics 4, 146-155.

Allum, J. H. J., Young, L. R., 1976. The relaxed oscillation technique for the determination of the moment of inertia of limb segments. Journal of Biomechanics 9, 21-25.

Alonso, F. J., Del Castillo, J. M., Pintado, P., 2005. Application of singular spectrum analysis to the smoothing of raw kinematic signals. Journal of Biomechanics 38, 1085-1092.

Andrews, J., Mish, S., 1996. Methods for investigating the sensitivity of joint resultants to body segment parameter variations. Journal of Biomechanics 29, 651-654.

Arampatzis, A., Gao, J., Bruggemann, G.-P., 1997. Influences of inertial properties on joint resultants. In Abstracts of the XVIth Congress of the International Society of Biomechanics. Tokyo University, Tokyo.

Australian Radiation Protection and Nuclear Safety Agency, 2002. Recommendations for limiting exposure to ionizing radiation (1995) (Guidance note [NOHSC:30022(1995)]). Radiation Protection Series Publication No. 1.

Barbier, F., Allard, P., Guelton, K., Colobert, B., Godillon-Maquinghen, A. P., 2003. Estimation of the 3-D center of mass excursion from force-plate data during standing. IEEE Transactions on Neural Systems and Rehabilitation Engineering 11, 31-37.

Benda, B. J., Riley, P. O., Krebs, D. E., 1994. Biomechanical relationship between center of gravity and center of pressure during standing. IEEE Transactions on Rehabilitation Engineering 2, 3-10.

Bobbert, M. F., Schamhardt, H. C., 1990. Accuracy of determining the point of force application with piezo-electric force plates. Journal of Biomechanics 23, 705-710.

Bouisset, S., Pertuzon, E., 1968. Experimental determination of the moments of inertia of limb segments. In Proceedings of the First International Seminar on Biomechanics 1967. Karger, Zurich.

Box, M. J., Davies, D., Swann, W. H., 1969. Non-Linear Optimization Techniques. Oliver and Boyd, Edinburgh.

Brooks, C., Jacobs, A., 1975. The gamma mass scanning technique for inertial anthropometric measurement. Medicine and Science in Sports 7, 290-294.

Brooks, C. M., 1973. Validation of the gamma mass scanner for determination of center of gravity and moment of inertia of biological tissue. M.S. thesis, Pennsylvania State University, University Park.

Cahouet, V., Luc, M., David, A., 2002. Static optimal estimation of joint accelerations for inverse dynamics problem solution. Journal of Biomechanics 35, 1507-1513.

Cappozzo, A., 1983. The forces and couples in the human trunk during level walking. Journal of Biomechanics 16, 265-277.

Cappozzo, A., Berme, N., 1990. Subject-specific segmental inertia parameter determination - a survey of current methods. In: Berme, N., Cappozzo, A. (Eds.), Biomechanics of Human Movement: Applications in Rehabilitation, Sports and Ergonomics. Bertec, Worthington, pp. 179-185.

Caron, O., 2005. Comments about the article titled: Comparison of three methods to estimate the center of mass during balance assessment, written by D. Lafond, M. Duarte, F. Prince (37 (2004) 1421-1426). Journal of Biomechanics 38, 1737-1738.

Caron, O., Faure, B., Brenière, Y., 1997. Estimating the centre of gravity of the body on the basis of the centre of pressure in standing posture. Journal of Biomechanics 30, 1169-1171.

Cavagna, G. A., 1975. Force platforms as ergometers. Journal of Applied Physiology 39, 174-9.

Cavanagh, P. R., Gregor, R. J., 1974. The quick-release method for estimating the moment of inertia of the shank and foot. In: Nelson, R. C., Moorehouse, C. A. (Eds.), Biomechanics IV. University Park Press, University Park, pp. 524-530.

Challis, J. H., 1996. Accuracy of human limb moment of inertia estimations and their influence on resultant joint moments. Journal of Applied Biomechanics 12, 517-530.

Challis, J. H., 1999. Precision of the estimation of human limb inertial parameters. Journal of Applied Biomechanics 15, 418-428.

Challis, J. H., Kerwin, D. G., 1992. Calculating upper limb inertial parameters. Journal of Sports Sciences 10, 275-284.

Challis, J. H., Kerwin, D. G., 1996. Quantification of the uncertainties in resultant joint moments computed in a dynamic activity. Journal of Sports Sciences 14, 219-231.

Chandler, R. F., Clauser, C. E., McConville, J. T., Reynolds, H. M., Young, J. W., 1975. Investigation of the Inertial Properties of the Human Body. Technical Report AMRL-TR-74-137, Wright-Patterson Air Force Base, Ohio.

Chen, S.-C., Shieh, H.-R., Lu, T.-W., Tseng, C.-H., 2003. An optimization-based model for the estimation of segmental inertial properties. In Proceedings of the International Society of Biomechanics XIXth Congress. University of Otago, Dunedin.

Cheng, C.-K., Chen, H.-H., Chen, C.-S., Lee, C.-L., Chen, C.-Y., 2000. Segment inertial properties of Chinese adults determined from magnetic resonance imaging. Clinical Biomechanics 15, 559-566.

Chester, V. L., Jensen, R. K., 1998. Changes in segment inertias and hip angular impulses during the swing phase of the first three months of independent walking. In Proceedings of the North American Congress on Biomechanics. University of Waterloo, Waterloo.

Chiari, L., Della Croce, U., Leardini, A., Cappozzo, A., 2005. Human movement analysis using stereophotogrammetry: Part 2: Instrumental errors. Gait and Posture 21, 197-211.

Chiu, L. Z. F., Salem, G. J., 2005. Net joint moment calculation errors during weightlifting: Dempster versus DEXA. In Proceedings of the 4th Meeting of the Southern California Conference on Biomechanics. California State University, Fullerton.

Chockalingam, N., Giakas, G., Iossifidou, A., 2002. Do strain gauge force platforms need in situ correction? Gait and Posture 16, 233-237.

Clarys, J. P., Marfell-Jones, M. J., 1986. Anatomical segmentation in humans and the prediction of segmental masses from intra-segmental anthropometry. Human Biology 58, 771-782.

Clauser, C. E., McConville, J. T., Young, J. W., 1969. Weight, Volume and Center of Mass of Segments of the Human Body. Technical Report AMRL-TR-69-70, Wright-Patterson Air Force Base, Ohio.

Conforto, S., Schmid, M., Camomilla, V., D'Alessio, T., Cappozzo, A., 2001. Hemodynamics as a possible internal mechanical disturbance to balance. Gait and Posture 14, 28-35.

Contini, R., 1972. Body segment parameters, Part II. Artificial Limbs 16, 1-19.

Corriveau, H., Hebert, R., Prince, F., Raiche, M., 2000. Intrasession reliability of the "center of pressure minus center of mass" variable of postural control in the healthy elderly. Archives of Physical Medicine and Rehabilitation 81, 45-48.

Crowe, A., Schiereck, P., de Boer, R. W., Keessen, W., 1993. Characterization of gait of young adult females by means of body centre of mass oscillations derived from ground reaction forces. Gait and Posture 1, 61-68.

Dainis, A., 1980. Whole body and segment centre of mass determination from kinetic data. Journal of Biomechanics 13, 647-651.

Davis, B. L., 1992. Uncertainty in calculating joint movements during gait. In Proceedings of the VIIIth Meeting of the European Society of Biomechanics. La Sapienza University, Rome.

de Leva, P, 1993. Validity and accuracy of four methods for locating the center of mass of young male and female athletes. In Abstracts of the XIVth Congress of the International Society of Biomechanics. Paris.

de Leva, P., 1996a. Adjustments to Zatsiorsky-Seluyanov's segment inertia parameters. Journal of Biomechanics 29, 1223-1230.

de Leva, P., 1996b. Joint center longitudinal positions computed from a selected subset of Chandler's data. Journal of Biomechanics 29, 1231-1233.

de Looze, M. P., Kingma, I., Bussmann, J. B. J., Toussaint, H. M., 1992. Validation of a dynamic linked segment model to calculate joint moments in lifting. Clinical Biomechanics 7, 161-169.

Della Croce, U., Leardini, A., Chiari, L., Cappozzo, A., 2005. Human movement analysis using stereophotogrammetry: Part 4: assessment of anatomical landmark misplacement and its effects on joint kinematics. Gait and Posture 21, 226-237.

Dempster, W. T., 1955. Space Requirements of the Seated Operator. Technical Report AMRL-55-159, Wright-Patterson Air Force Base, Ohio.

Desjardins, P., Plamondon, A., Gagnon, M., 1998. Sensitivity analysis of segment models to estimate the net reaction moments at the L5/S1 joint in lifting. Medical Engineering and Physics 20, 153-158.

Dillon, M. P., Barker, T. M., McDonald, M. D., 1999. Modelling of body segment parameters for partial foot amputees. In Abstracts of the XVIth Congress of the International Society of Biomechanics. Calgary.

Directorate-General for the Environment of the European Commission, 2000. Referral guidelines for imaging. Radiation Protection Report 118, European Commission.

Dixon, D. L., Dugdale, L. M., 1988. An Introduction to Clinical Imaging. Churchill Livingstone, London.

Donelan, J. M., Kram, R., Kuo, A. D., 2002. Simultaneous positive and negative external mechanical work in human walking. Journal of Biomechanics 35, 117-24.

Dowling, J. J., 2003. Author's response. Journal of Biomechanics 36, 1407-1408.

Drillis, R., Contini, R., Bluestein, M., 1964. Body segment parameters: a survey of measurement techniques. Artificial Limbs 8, 44-66.

Duarte, M., 2005. Personal Communication to M. A. Jaffrey.

Duarte, M., Zatsiorsky, V. M., 2001. Long-range correlations in human standing. Physics Letters A 283, 124-128.

Durkin, J. L., 1998. The prediction of body segment parameters using geometric modelling and dual photon absorpsiometry. MSc. thesis, McMaster University.

Durkin, J. L., Dowling, J. J., 2003. Analysis of body segment parameter differences between four human populations and the estimation errors of four popular mathematical models. Journal of Biomechanical Engineering 125, 515-22.

Durkin, J. L., Dowling, J. J., Andrews, D. M., 2002. The measurement of body segment inertial parameters using dual energy X-ray absorptiometry. Journal of Biomechanics 35, 1575-1580.

Duval-Beaupere, G., Robain, G., 1987. Visualization on full spine radiographs of the anatomical connections of the centres of the segmental body mass supported by each vertebra and measured in vivo. International Orthopaedics 11, 261-9.

Eames, M. H. A., Cosgrove, A., Baker, R., 1999. Comparing methods of estimating the total body centre of mass in three dimensions in normal and pathological gaits. Human Movement Science 18, 637-646.

Eng, J. J., Winter, D. A., 1993. Estimation of the horizontal displacement of the total body centre of mass: considerations during standing activities. Gait and Posture 1, 141-144.

Erdmann, W. S., 1997. Geometric and inertial data of the trunk in adult males. Journal of Biomechanics 30, 679-688.

Ertaud, J. Y., Savatier, X., Schmidt, W., Thomine, J. M., Dujardin, F. H., 1999. Multivision determination of the volume of human body segments and implementation of a dynamic model.

Fenn, W. O., Brody, H., Petrilli, A., 1931. The tension developed by human muscles at different velocities of shortening. American Journal of Physiology 97, 1-14.

Fregly, B. J., Reinbolt, J. A., 2004. Estimation of body segment parameters from three-dimensional gait data using optimization. In Proceedings of the Eighth International Symposium on the 3D Analysis of Human Movement. Tampa, FL.

Ganley, K. J., Powers, C. M., 2004a. Anthropometric parameters in children: a comparison of values obtained from dual energy x-ray absorptiometry and cadaver-based estimates. Gait and Posture 19, 133-140.

Ganley, K. J., Powers, C. M., 2004b. Determination of lower extremity anthropometric parameters using dual energy X-ray absorptiometry: the influence on net joint moments during gait. Clinical Biomechanics 19, 50-56.

Gard, S. A., Miff, S. C., Kuo, A. D., 2004. Comparison of kinematic and kinetic methods for computing the vertical motion of the body center of mass during walking. Human Movement Science 22, 597-610.

Giakas, G., Baltzopoulos, V., 1997a. A comparison of automatic filtering techniques applied to biomechanical walking data. Journal of Biomechanics 30, 847-850.

Giakas, G., Baltzopoulos, V., 1997b. Optimal digital filtering requires a different cut-off frequency strategy for the determination of the higher derivatives. Journal of Biomechanics 30, 851-855. Erratum: Journal of Biomechanics 30, 1003.

Giakas, G., Stergioulas, L. K., Vourdas, A., 2000. Time-frequency and filtering of kinematic signals with impacts using the Wigner function: accurate estimation of the second derivative. Journal of Biomechanics 33, 567-574.

Halliday, D., Resnick, R., 1978. Physics Parts 1 & 2 Combined. Wiley, New York.

Hanavan, E. P., 1964. A Mathematical Model of the Human Body. Technical Report AMRL-64-102, Wright-Patterson Air Force Base, Ohio.

Hatze, H., 1975. A new method for the simultaneous measurement of the moment of inertia, the damping coefficient and the location of the centre of mass of a body segment *in situ*. European Journal of Applied Physiology 34, 217-226.

Hatze, H., 1980. A mathematical model for the computational determination of parameter values of anthropomorphic segments. Journal of Biomechanics 13, 833-843.

Hatze, H., 1998. Validity and reliability of methods for testing vertical jumping performance. Journal of Applied Biomechanics 14, 127-140.

Hatze, H., 2002a. Fundamental issues, recent advances, and future directions in myodynamics. Journal Electromyography and Kinesiology 12, 447-54.

Hatze, H., 2002b. The fundamental problem of myoskeletal inverse dynamics and its implications. Journal of Biomechanics 35, 109-115.

Hausdorff, J.M., Purdon, P.L., Peng, C.-K., Ladin, Z., Wei, J.Y., Goldberger, A.L., 1996. Fractal dynamics of human gait: Stability of long-range correlations in stride interval fluctuations. Journal of Applied Physiology 80, 1448-1457.

Hay, J. G., Wilson, B. D., Dapena, J., Woodworth, G. G., 1977. Computational technique to determine the angular momentum of a human body. Journal of Biomechanics 10, 269-277.

Hedoux, P., Pinti, A., Waterlain, E., Kemoun, G., Boluix, B., 2000. Comparaison of center of mass positions of lower body segments obtained from M.R.I. and geometric models. In Abstracts of the XIth Congress of the Canadian Society for Biomechanics. University of Montréal, Montréal.

Heiss, D. G., Pagnacco, G., 2002. Effect of center of pressure and trunk center of mass optimization methods an the analysis of whole body lifting mechanics. Clinical Biomechanics 17, 106-115.

Hinrichs, R. N., 1985. Regression equations to predict segmental moments of inertia from anthropometric measurements: an extension of the data of Chandler et al. Journal of Biomechanics 18, 621-624.

Hinrichs, R. N., 1990. Adjustments to the segment centre of mass proportions of Clauser et al. (1969). Journal of Biomechanics 23, 949-951.

Hof, A. L., 2005. Comparison of three methods to estimate the center of mass during balance assessment (Letter to the editor). Journal of Biomechanics 38, 2134-2135.

Hof, A. L., 2007. The equations of motion for a standing human reveal three mechanisms for balance. Journal of Biomechanics 40, 451-457.

Hof, A. L., Gazendam, M. G. J., Sinke, W. E., 2005. The condition for dynamic stability. Journal of Biomechanics 38, 1-8.

Holden, J. P., Stanhope, S. J., 1998. The effect of variation in knee centre location estimates on net knee joint moments. Gait and Posture 7, 1-6.

Huang, H. K., Suarez, F. R., 1983. Evaluation of cross-sectional geometry and mass density distributions of humans and laboratory animals using computerized tomography. Journal of Biomechanics 16, 821-832.

Hui, X., Xiuyuan, Z., Xuanliang, D., Donghong, H., Qin, L., Hong, L., Jingmin, L., Wei, L., 1999. A research on the body center of mass of Chinese adults. International Journal of Industrial Ergonomics 23, 129-133.

Iida, H., Yamamuro, T., 1987. Kinetic analysis of the center of gravity of the human body in normal and pathological gaits. Journal of Biomechanics 20, 987-995.

International Society of Geodesy, 1971. Geodetic Reference System 1967. International Society of Geodesy, Paris.

Jaffrey, M. A., Best, R. J., Wrigley, T. V., 1998. Estimation of an individual's body segment parameters using kinematic data of the individual while airborne. In Abstracts of the 2nd Australia and New Zealand Society of Biomechanics Conference. University of Auckland, Auckland.

Jaffrey, M. A., Best, R. J., Wrigley, T. W., 2003. Calculating CMJ height by double integration of the ground reaction force: accurate subject mass measurement is more valid than using a mass correction factor. In Proceedings of the International Society of Biomechanics XIXth Congress. University of Otago, Dunedin.

Jaffrey, M., Best, R., Wrigley, T., 2002. Predicting body segment parameters with a 2-D whole-body inverse dynamics objective function. In Proceedings of the 4th Australasian Biomechanics Conference. La Trobe University, Melbourne.

Jensen, R. K., 1976. Model for body segment parameters. In: Komi, P.V. (Ed.), Biomechanics V-B. University Park, Baltimore, pp. 380-386.

Jensen, R. K., 1978. Estimation of the biomechanical properties of three body types using a photogrammetric method. Journal of Biomechanics 11, 349-358.

Jensen, R. K., 1986. Body segment mass, radius and radius of gyration properties in children. Journal of Biomechanics 19, 355-368.

Jensen, R. K., 1989. Changes in segment inertia proportions between 4 and 20 years. Journal of Biomechanics 22, 529-536.

Jensen, R. K., Doucet, S., Treitz, T., 1996. Changes in segment mass and mass distribution during pregnancy. Journal of Biomechanics 29, 251-256.

Jensen, R. K., Fletcher, P., 1993. Body segment moments of inertia of the elderly. Journal of Applied Biomechanics 9, 287-305.

Jensen, R. K., Fletcher, P., 1994. Distribution of mass to the segments of elderly males and females. Journal of Biomechanics 27, 89-96.

Jensen, R. K., Nassa, G., 1988. Growth of segment principal moments of inertia between four and twenty years. Medicine and Science in Sports and Exercise 20, 594-604.

Jensen, R. K., Treitz, T., Sun, H., 1997. Prediction of infant segment inertias. Journal of Applied Biomechanics 13, 287-299.

Karlsson, A., Lanshammar, H., 1997. Analysis of postural sway using inverted pendulum model and force plate data. Gait and Posture 5, 198-203.

Kerwin, D. G., 1986. A force platform determination of angular momentum. In Proceedings of the Sports Biomechanics Study Group. British Association Of Sports Science, Leeds Polytechnic.

Kibele, A., 1998. Possibilities and limitations in the biomechanical analysis of countermovement jumps: a methodological study. Journal of Applied Biomechanics 14, 105-117.

King, D. L., Zatsiorsky, V. M., 1997. Extracting gravity line displacement from stabilographic recording. Gait and Posture 6, 27-38.

King, D. L., Zatsiorsky, V. M., 2002. Periods of extreme ankle displacement during one-legged standing. Gait and Posture 15, 172-179.

Kingma, I., de Looze, M. P., Toussaint, H. M., Klinjnsma, H. G., Bruijnen, T. B. M., 1996a. Validation of a full body 3-D dynamic linked segment model. Human Movement Science 15, 833-860.

Kingma, I., Toussaint, H. M., Commissaris, D. A. C. M., Hoozemans, M. J. M., Ober, M. J., 1995. Optimizing the determination of the body centre of mass. Journal of Biomechanics 28, 1137-1142.

Kingma, I., Toussaint, H. M., de Looze, M. P., van Dieën, J. P., 1996b. Segment inertial parameter evaluation in two anthropometric models by application

of a dynamic linked segment model. Journal of Biomechanics 29, 693-704.

Krabbe, B., Farkas, R., Baumann, W., 1997. Influence of inertia on intersegment moments of the lower extremity joints. Journal of Biomechanics 30, 517-519.

Kuo, A. D., 1998. A least-squares estimation approach to improving the precision of inverse dynamics computations. Journal of Biomechanical Engineering 120, 148-159.

Kwon, Y.-H., 1996. Effects of the method of body segment parameter estimation on airborne angular momentum. Journal of Applied Biomechanics 12, 413-430.

Lafond, D., Duarte, M., Prince, F., 2004. Comparison of three methods to estimate the center of mass during balance assessment. Journal of Biomechanics 37, 1421-1426.

Larivière, C., Gagnon, D., 1999a. The influence of trunk modeling in 3D biomechanical analysis of simple and complex lifting tasks. Clinical Biomechanics 14, 449-461.

Larivière, C., Gagnon, D., 1999b. The L5/S1 joint moment sensitivity to measurement errors in dynamic 3D multisegment lifting models. Human Movement Science 18, 573-587.

Lebiedowska, M. K., Polisiakiewicz, A., 1997. Changes in the lower leg moment of inertia due to child's growth. Journal of Biomechanics 30, 723-728.

Lee, C. R., Farley, C. T., 1998. Determinants of the center of mass trajectory in human walking and running. Journal of Experimental Biology 201, 2935-44.

Lenzi, D., Cappello, A., Chiari, L., 2003. Influence of body segment parameters and modeling assumptions on the estimate of center of mass trajectory. Journal of Biomechanics 36, 1335-1341.

Lephart, S. A., 1984. Measuring the inertial properties of cadaver segments. Journal of Biomechanics 17, 537-543.

Levin, O., Mizrahi, J., 1996. An iterative model for estimation of the trajectory of center of gravity from bilateral reactive force measurements in standing sway. Gait and Posture 4, 89-99.

Liu, Y. K., Wickstrom, J. K., 1973. Estimation of the inertial property distribution of the human torso from segmented cadaveric data. In: Kenedi, R. M. (Ed.), Perspectives in Biomedical Engineering. pp. 203-213.

MacKinnon, C. D., Winter, D. A., 1993. Control of whole body balance in the frontal plane during human walking. Journal of Biomechanics 26, 633-644.

Martin, P. E., Mungiole, M., Marzke, M. W., Longhill, J. M., 1989. The use of magnetic resonance imaging for measuring segmental inertia properties. Journal of Biomechanics 22, 367-376.

Masani, K., Popovic, M.R., Nakazawa, K., Kouzaki, M., Nozaki, D., 2003. Importance of Body Sway Velocity Information in Controlling Ankle Extensor Activities during Quiet Stance. Journal of Neurophysiology 90, 3774-3782.

Matsuo, A., Fukunaga, T., Uchino, S., 1991. Estimation of volume, density, mass and location of CG by means of MRI method. In Abstracts of the XIIIth International Congress on Biomechanics. University of Western Australia, Perth.

McCaw, S. T., De Vita, P., 1995. Errors in alignment of center of pressure and foot coordinates affect predicted lower extremity torques. Journal of Biomechanics 28, 985-988.

McConville, J. T., Churchill, T. D., Kaleps, I., Clauser, C. E., Cuzzi, J., 1980. Anthropometric Relationships of Body and Body Segment Moments of Inertia. Technical Report AFAMRL-TR-80-119, Wright-Patterson Air Force Base, Ohio,

McKinon, W., Hartford, C., Di Zio, L., van Schalkwyk, J., Veliotes, D., Hofmeyr, A., Rogers, G., 2004. The agreement between reaction-board measurements and kinematic estimation of adult male human whole body centre of mass location during running. Physiological Measurement 25, 1339-54.

Miller, D. I., Morrison, W. E., 1975. Prediction of segmental parameters using the Hanavan human body model. Medicine and Science in Sports 7, 207-212.

Miller, D. I., Nelson, R. C., 1973. The biomechanics of sport; a research approach. Lea & Febiger, Philadelphia.

Mochizuki, L., Duarte, M., Amadio, A. C., Zatsiorsky, V. M., Latash, M. L., 2006. Changes in postural sway and its fractions in conditions of postural instability. Journal of Applied Biomechanics 22, 51-60.

Morasso, P. G., Spada, G., Capra, R., 1999. Computing the COM from the COP in postural sway movements. Human Movement Science 18, 759-767.

Mungiole, M., Martin, P. E., 1990. Estimating segmental inertial properties: comparison of magnetic resonance imaging with existing methods. Journal of Biomechanics 23, 1039-1046.

Nagano, A., Gerritsen, K., Fukashiro, S., 2000. A sensitivity analysis of the calculation of mechanical output through inverse dynamics: a computer simulation study. Journal of Biomechanics 33, 1313-1318.

Nigg, B. M., 1999. Inertial properties of the human or animal body. In: Nigg, B. M., Herzog, W. (Eds.), Biomechanics of the Musculo-skeletal System. Wiley, New York, pp. 376-399.

Norton, J., Donaldson, N., Dekker, L., 2002. 3D whole body scanning to determine mass properties of legs. Journal of Biomechanics 35, 81-86.

Pagnacco, G., Oggero, E., Morr, D. R., Berme, N., 1997. Oversampling data acquisition to improve resolution of digitized signals. Biomedical Sciences Instrumentation 34, 137-42.

Pai, Y.-C., 1997. Center of mass velocity-position predictions for balance control. Journal of Biomechanics 30, 347-354.

Pain, M. T. G., Challis, J. H., 2001. High resolution determination of body segment inertial parameters and their variation due to soft tissue motion. Journal of Applied Biomechanics 17, 326-334.

Pain, M. T. G., Challis, J. H., 2006. The influence of soft tissue movement on ground reaction forces, joint torques and joint reaction forces in drop landings. Journal of Biomechanics 39, 119-124.

Papa, E., Cappozzo, A., 1999. A telescopic inverted-pendulum model of the musculo-skeletal system and its use for the analysis of the sit-to-stand motor task. Journal of Biomechanics 32, 1205-1212.

Pataky, T. C., Zatsiorsky, V. M., Challis, J. H., 2003. A simple method to determine body segment masses *in vivo*: reliability, accuracy and sensitivity analysis. Clinical Biomechanics 18, 364-368.

Pavol, M. J., Owings, T. M., Grabiner, M. D., 2002. Body segment inertial parameter estimation for the general population of older adults. Journal of Biomechanics 35, 707-712.

Pearsall, D. J, Reid, G., 1994. The study of human body segment parameters in biomechanics: an historical review and current status report. Sports Medicine 18, 126-140.

Pearsall, D. J., Costigan, P. A., 1999. The effect of segment parameter error on gait analysis results. Gait and Posture 9, 173-183.

Pearsall, D. J., Reid, J. G., Livingstone, L. A., 1996. Segmental inertial parameters of the human trunk as determined from computed tomography. Annals of Biomedical Engineering 24, 198-210.

Pearsall, D. J., Reid, J. G., Ross, R., 1994. Inertial properties of the human trunk of males determined from magnetic resonance imaging. Annals of Biomedical Engineering 22, 692-706.

Peyton, A. J., 1986. Determination of the moment of inertia of limb segments by a simple method. Journal of Biomechanics 19, 405-410.

Pezzack, J. C., Norman, R. W., 1981. A validation of the joint reaction force and resultant moment output of an "n" link plane motion model of the human. In: Biomechanics VII-A. University Park Press, Baltimore, pp. 260-266.

Pierrynowski, M. R., Tupling, S. J., Wilson, C. D., 1983. Variation in inertial parameters of the human thigh and leg segments during human locomotion. Canadian Journal of Applied Sport Sciences 8, 208.

Plagenhoef, S., 1971. Patterns of Human Motion. Prentice-Hall, Englewood Cliffs.

Plagenhoef, S., Evans, F. G., Abdelnour, T., 1983. Anatomical data for analyzing human motion. Research Quarterly for Exercise and Sport 54, 169-178.

Plamondon, A., Gagnon, M., Desjardins, P., 1996. Validation of two 3-D segment models to calculate the net reaction forces and moments at the L_5/S_1 joint in lifting. Clinical Biomechanics 11, 101-110.

Prince, F., Lafond, D., Duarte, M., 2005. Author's response. Journal of Biomechanics 38, 1738-1740.

Rabuffetti, M., Baroni, G., 1999. Validation protocol of models for centre of mass estimation. Journal of Biomechanics 32, 609-613.

Reid, J. G, Jensen, R. K., 1990. Human body segment inertia parameters: a survey and status report. Exercise and Sport Sciences Reviews 18, 225-241.

Reid, J. G., 1984. Physical properties of the human trunk as determined by computed tomography. Archives of Physical Medicine and Rehabilitation 65, 246-250.

Reinbolt, J. A., Haftka, R. T., Chimielewski, T. L., Fregly, B. J., 2007. Are patient-specific joint and inertial parameters necessary for accurate inverse dynamics analyses of gait? IEEE Transactions on Biomedical Engineering 54, 782-793.

Robertson, D. G. E., Caldwell, G. E., 2004. Planar Kinematics. In: Robertson, D. G. E., Caldwell, G. E., Hamill, J., Kamen, G., Whittlesey, S. N. (Eds.), Research Methods in Biomechanics. Human Kinetics, Champaign, pp. 9-34.

Rodrigue, D., Gagnon, M., 1983. The evaluation of forearm density with axial tomography. Journal of Biomechanics 16, 907-913.

Saini, M., Kerrigan, D., Thirunarayan, M., Duff-Raffaele, M., 1998. The vertical displacement of the center of mass during walking: a comparison of four measurement methods. Journal of Biomechanical Engineering 120, 133-139.

Schmiedmayer, H.-B., Kastner, J., 1999. Parameters influencing the accuracy of the point of force application determined with piezoelectric force plates. Journal of Biomechanics 32, 1237-1242.

Schmiedmayer, H.-B., Peham, C., Kastner, J., 1999. Errors in the COP determined with force plates depend on the load distribution - Experimental results. In Abstracts of the XVIth Congress of the International Society of Biomechanics. Calgary.

Schneider, K., Zernicke, R. F., 1992. Mass, center of mass, and moment of inertia estimates for infant limb segments. Journal of Biomechanics 25, 145-148.

Schultz, R., Oberrgefell, L., Rizer, A., Albery, C., Anderson, B., 1997. Comparison of measured and predicted human whole-body inertial properties. In Proceedings of the 41st Stapp Car Crash Conference. Society of Automotive Engineers, Warrendale.

Shimba, T., 1984. An estimation of center of gravity from force platform data. Journal of Biomechanics 17, 53-60.

Silva, M. P. T., Ambrosio, J. A. C., 2004. Sensitivity of the results produced by the inverse dynamic analysis of a human stride to perturbed input data. Gait and Posture 19, 35-49.

Sprigings, E. J., Burko, D. B., Watson, L. G., Laverty, W. H., 1987. An evaluation of three segmental methods used to predict the location of the total-body CG for human airborne movements. Journal of Human Movement Studies 13, 57-68.

Stijnen, V. V., Willems, E. J., Spaepen, A. J., Peeraer, L., van Leemputte, M., 1983. A modified release method for measuring the moment of inertia of the limbs. In: Matsui, H., Kobayashi, K. (Eds.), Biomechanics VIII-B. Human Kinetics, Champaign, pp. 1138-1143.

Sun, H., 1992. Body segment growth curves during infancy. PhD. thesis, Laurenthian University of Sudbury, Canada.

Tesio, L., Civaschi, P., Tessari, L., 1985. Motion of the center of gravity of the body in clinical evaluation of gait. American Journal of Physical Medicine 64, 57-70.

Tesio, L., Lanzi, D., Detrembleur, C., 1998a. The 3-D motion of the centre of gravity of the human body during level walking. I. Normal subjects at low and intermediate walking speeds. Clinical Biomechanics 13, 77-82.

Tesio, L., Lanzi, D., Detrembleur, C., 1998b. The 3-D motion of the centre of gravity of the human body during level walking. II. Lower limb amputees. Clinical Biomechanics 13, 83-90.

Thirunarayan, M. A., Kerrigan, D. C., Rabuffetti, M., Della Croce, U., Saini, M., 1996. Comparison of three methods for estimating vertical displacement of center of mass during level walking in patients. Gait and Posture 4, 306-314.

van den Bogert, A. J., 1996a. all.frc, all.fmg, all.mom and all.kin. Data. Available from http://isbweb.org/data/invdyn/index.html (URL active as of 02 Nov 2007).

van den Bogert, A. J., 1996b. idynopt.m, idynfun.m, inv2d.m and cross2d.m. Software. Available from http://isbweb.org/data/invdyn/index.html (URL active as of 02 Nov 2007).

van den Bogert, A. J., 2000. gcv.exe. Software. Available from http://isbweb.org/software/sigproc.html (URL active as of 02 Nov 2007).

Vanrenterghem, J., 2006. Personal Communication to M. A. Jaffrey.

Vanrenterghem, J., De Clercq, D., Van Cleven, P., 2001. Necessary precautions in measuring correct vertical jumping height by means of force plate measurements. Ergonomics 44, 814-8.

Vaughan, C. L., 1980. An optimization approach to closed loop problems in biomechanics. PhD. thesis, University of Iowa.

Vaughan, C. L., Andrews, J. G., Hay, J. G., 1982a. Selection of body segment parameters by optimization methods. Journal of Biomechanical Engineering 104, 38-44.

Vaughan, C. L., Hay, J. G., Andrews, J. G., 1982b. Closed loop problems in biomechanics. Part I - A classification system. Journal of Biomechanics 15, 197-200.

Vint, P. F., Hinrichs, R. N., 1996. Endpoint error in smoothing and differentiating raw kinematic data: an evaluation of four popular methods. Journal of Biomechanics 29, 1637-42.

Webber, C., 1995. Dual photon transmission measurements of bone mass and composition during growth. In: Blimkie, C., Bar-Or, O. (Eds.), New Horizons in Pediatric Exercise Science. Human Kinetics, Champaign, pp. 57-76.

Wei, C., Jensen, R., K., 1995. The application of segment axial density profiles to a human body inertia model. Journal of Biomechanics 28, 103-108.

Weinbach, A. P., 1938. Contour maps, center of gravity, moment of inertia and surface area of the human body. Human Biology 10, 356-371.

Whitsett, C. E., 1963. Some Dynamic Response Characteristics of Weightless Man. Technical Report AMRL-TDR-63-18, Wright-Patterson Air Force Base, Ohio.

Whittle, M., 1997. Three-dimensional motion of the center of gravity of the body during walking. Human Movement Science 16, 347-355.

Whittlesey, S. N., Robertson, D. G. E., 2004. Two-Dimensional Inverse Dynamics. In: Robertson, D. G. E., Caldwell, G. E., Hamill, J., Kamen, G., Whittlesey, S. N. (Eds.), Research Methods in Biomechanics. Human Kinetics, Champaign, pp. 103-124.

Winter, D. A., 1990. Biomechanics and Motor Control of Human Movement. Wiley, New York.

Winter, D. A., Prince, F., Frank, J. S., Powell, C., Zabjek, K. F., 1996a. Unified theory regarding A/P and M/L balance in quiet stance. Journal of Neurophysiology 75, 2334-2343.

Winter, D. A., Prince, F., Patla, A., 1996b. Interpretation of COM and COP balance control during quiet standing. Gait and Posture 4, 174-175.

Woltring, H. J., 1985. On optimal smoothing and derivative estimation from noisy displacement data in biomechanics. Human Movement Science 4, 229-245.

Woltring, H. J., 1986. A FORTRAN package for generalized cross-validatory spline smoothing and differentiation. Advances in Engineering Software 8, 104-113.

Woltring, H. J., 1995. Smoothing and differentiation techniques applied to 3-D data. In: Allard, P., Stokes, I., Blanchi, J.-P. (Eds.), Three-dimensional analysis of human movement. Human Kinetics, Champaign, pp. 79-99.

Wrigley, A. T., Albert, W. J., Deluzio, K. J., Stevenson, J. M., 2005. Differentiating lifting technique between those who develop low back pain and those who do not. Clinical Biomechanics 20, 254-263.

Yeadon, M., Atha, J., Hales, F. D., 1990. The simulation of aerial movement IV. A computer simulation model. Journal of Biomechanics 23, 85-89.

Yeadon, M. R., 1990a. The simulation of aerial movement I. The determination of orientation angles from film data. Journal of Biomechanics 23, 59-66.

Yeadon, M. R., 1990b. The simulation of aerial movement II. A mathematical inertia model of the human body. Journal of Biomechanics 23, 67-74.

Yeadon, M. R., 1990c. The simulation of aerial movement III. The determination of the angular momentum of the human body. Journal of Biomechanics 23, 75-83.

Yochum, T. R., Rowe, L. J., 1987. Essentials of Skeletal Radiology, Volume 1. Williams and Wilkins, Baltimore.

Young, J. W., Chandler, R. F., Snow, C. C., Robinette, K. M., Zehner, G. F., Lofberg, M. S., 1983. Anthropometric and Mass Distribution Characteristics of the Adult Female. Revised. Technical Report FAA-AM-83-16, Federal Aviation Administration Civil Aeromedical Institute, Oklahoma City.

Zatsiorsky, V. M., 2002a. Inertial Properties of the Human Body. In: Zatsiorsky, V. M. (Ed.), Kinetics of Human Motion. Human Kinetics, Champaign, pp. 265-364.

Zatsiorsky, V. M., 2002b. Kinetics of Human Motion. Human Kinetics, Champaign.

Zatsiorsky, V. M., 2003. Measuring body segment parameters: x-ray versus gamma scanning. Letter to the editor. Journal of Biomechanics 36, 1405-1406.

Zatsiorsky, V. M., Duarte, M., 1999. Instant equilibrium point and its migration in standing tasks: rambling and trembling components of the stabilogram. Motor Control 3, 28-38.

Zatsiorsky, V. M., Duarte, M., 2000. Rambling and trembling in quiet standing. Motor Control 4, 185-200.

Zatsiorsky, V. M., King, D. L., 1998. An algorithm for determining gravity line location from posturographic recordings. Journal of Biomechanics 31, 161-164.

Zatsiorsky, V. M., Seluyanov, V. N., Chugunova, L. G., 1990a. In vivo body segment inertial parameters determination using a gamma-scanner method. In: Berme, N., Cappozzo, A. (Eds.), Biomechanics of Human Movement: Applications in Rehabilitation, Sports and Ergonomics. Bertec, Worthington, pp. 186-202.

Zatsiorsky, V. M., Seluyanov, V. N., Chugunova, L. G., 1990b. Methods of Determining Mass-Inertial Characteristics of Human Body Segments. In:

Chernyi, G. G., Regirer, S. A. (Eds.), Contemporary Problems of Biomechanics. Mir Publishers/CRC Press, Moscow/Boston, pp. 272-291.

Zatsiorsky, V., Seluyanov, V., 1983. The mass and inertia characteristics of the main segments of the human body. In: Matsui, H., Kobayashi, K. (Eds.), Biomechanics VIII-B. Human Kinetics, Champaign, pp. 1152-1159.

Zatsiorsky, V., Seluyanov, V., 1985. Estimation of the mass and inertia characteristics of the human body by means of the best predictive regression equations. In: Winter, D. A., Norman, R. W., Wells, R. P., Hayes, K. C., Patla, A. E. (Eds.), Biomechanics IX-B. Human Kinetics, Champaign, pp. 233-239.

Zheng, Z., 1990. A new method to determine inertial parameters of the segments of the human body. In Proceedings of the 11th Asian Games Scientific Congress. Beijing.

Zok, M., Mazza, C., Della Croce, U., 2004. Total body centre of mass displacement estimated using ground reactions during transitory motor tasks: application to step ascent. Medical Engineering & Physics 26, 791-798.

Secondary References

Barter, J. T., 1957. Estimation of the Mass of Body Segments. Technical Report WADC-TR-57-260, Wright-Patterson Air Force Base. [In Cappozzo and Berme (1990)].

Bernstein, N. A., Salzgeber, O. A., Pavlenko, P. P., Gurvich, N. A., 1936. *Determination of location of the centres of gravity and mass of the limbs of the living human body* (in Russian), All-Union Institute of Experimental Medicine, Moscow. [In Drillis et al. (1964) and Pearsall and Reid (1994)].

Braune, W., Fischer, O., 1889. Über den Schwerpunkt des menschlichen Körpers, mit Rücksicht auf die Austrustung des deutschen Infanteristen.

Abhanlugen der Mathematische-Physichen Klasse der Köninglich-Säshsischen Gesellschaft der Wissenschaften 15, 561-672. [In Reid and Jensen (1990) and Pearsall and Reid (1994)].

Braune, W., Fischer, O., 1892. Bestimung der Tragheitsmomente des meschlichen Körpers und seiner Glieder. Abhanlugen der Mathematische-Physichen Klasse der Köninglich-Säshsischen Gesellschaft der Wissenschaften 18, 409-492. [In Reid and Jensen (1990) and Pearsall and Reid (1994)].

Casper, R. M., Jacobs, A.M., Kennedy, E. S., McMaster, I. B., 1971. On the use of gamma ray images for determination of body segment parameters. In Proceedings of the Quantitative Imagery in Biomedical Sciences Conference. Houston, Texas. [In Reid and Jensen (1990)].

Fischer, O., 1906. Theoretische Grundlagen für eine Mechanick der lebenden Körper mit speziellen Anwendungen auf die Menschen. B. G. Teubner, Berlin. [In Pearsall and Reid (1994)].

Harless, E., 1860. Die statisclten momente der menschlichen gliedmassen. Akademie der Wissenschaften 8, 69-96, 257-294. [In Drillis et al. (1964), Pearsall and Reid (1994) and Reid and Jensen (1990)].

Meeh, C., 1895. Volummessungen des menschlichen Körpers und seiner einzelnen Teile in den verschidenen Altersstufen. Ztschr. für Biologie 13,

125-147. [In Dempster (1955), Drillis et al. (1964) and Pearsall and Reid (1994)].

Tieber, J. A., Lindemuth, R. W., 1965. An Analysis of the Inertial Properties and Performance of the Astronaut Maneuvering System. M.S. thesis, U.S. Air Force Institute of Technology, Wright-Patterson Air Force Base, Ohio. [In Chandler et al. (1975)].

Appendix A: The Sensitivity of the *ZPZP4U* and *ZPZP5C* Objective Functions and other Parameters to Perturbations of the Design Variables

The proposed design variables for methods *ZPZP4U* and *ZPZP5C* were comprised of the dimensionally-relevant force and moment calibration factor and offset error terms (Fz_C, Fz_O, Fy_C, Fy_O, Mx_C and Mx_O). Sensitivity analyses of the respective objective functions and the calculated $COP[y](t_i)$ and $CM[y]_{IA}(t_i)$ trajectories to feasible perturbations in the proposed design variables were conducted in the context of quiet stance trials. Consideration was then given to removing (i.e. setting to constant values) any proposed design variable that was observed to have relatively negligible influence on the aforementioned functions and trajectories.

Firstly, sensitivity analyses were conducted by subjecting all 15 unique pairs of the proposed design variables to 2-D tabulation optimisations of the *ZPZP4U* objective function, which allowed the subsequent plotting of 3-D surface maps of the objective function with respect to the broadly feasible subspace of each pair of design variables. This involved evaluating the objective function at small, discrete intervals across the broadly feasible ranges (defined in Table 3, p. 145) of both design variables in the pair. For each unique pair, the other four design variables were held constant at the initial estimates described in Table 3 (p. 144). Representative examples of the results are provided in Figs. 62, 63, 64 and 65. Only feasible values, with respect to Eqs. (25), were plotted.

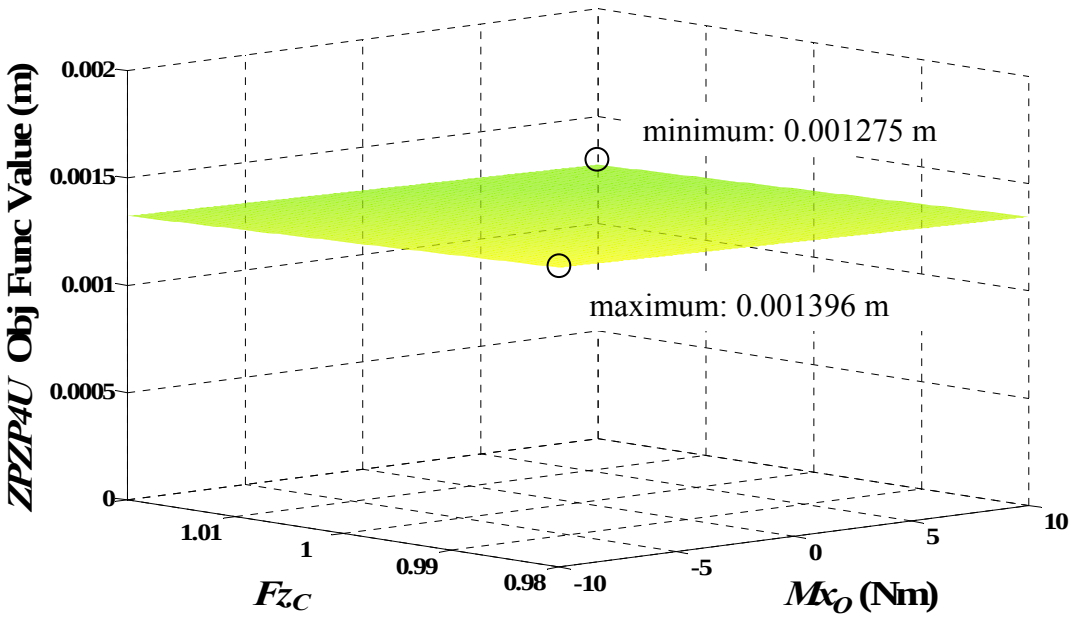

Figure 62. Oblique view of the surface map of feasible ZPZP4U solutions, with respect to Eqs. (25), in the Fz_C-Mx_O subspace (trial '4461'), showing the relative insensitivity of the objective function to the broadly feasible range of Fz_C and Mx_O perturbations (0.121 mm difference; cf. Figs. 63 and 64).

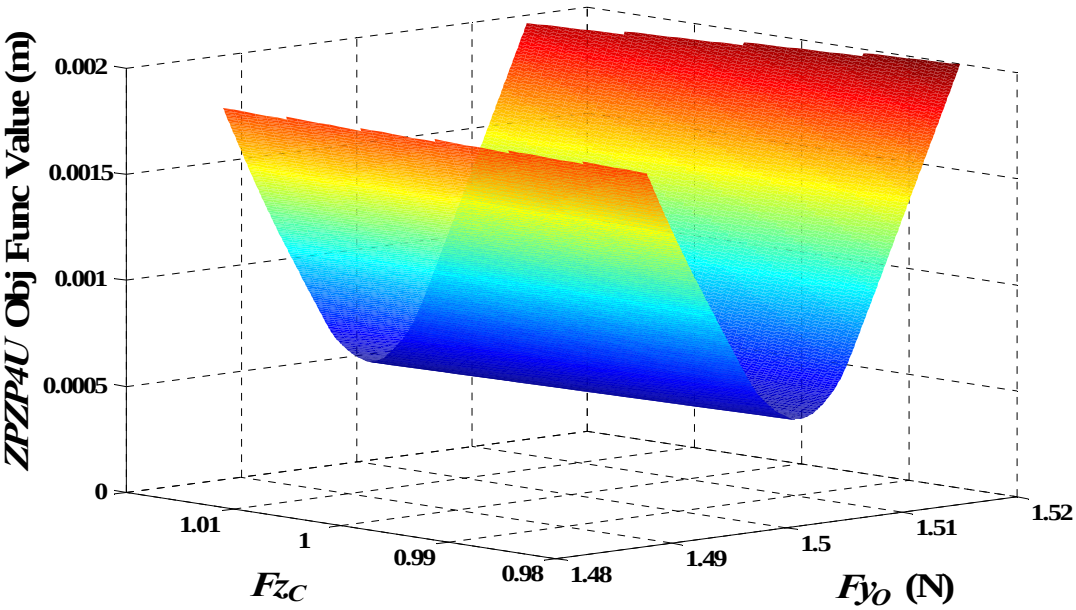

Figure 63. Oblique view of the surface map of feasible ZPZP4U solutions, with respect to Eqs. (25), in the Fz_C-Fy_O subspace (trial '4461'). The relative insensitivity and sensitivity, respectively, of the objective function to feasible perturbations of Fz_C and Fy_O is indicated by the plotted surface: a valley with steep sides in the Fy_O dimension but relatively negligible slope in the Fz_C dimension.

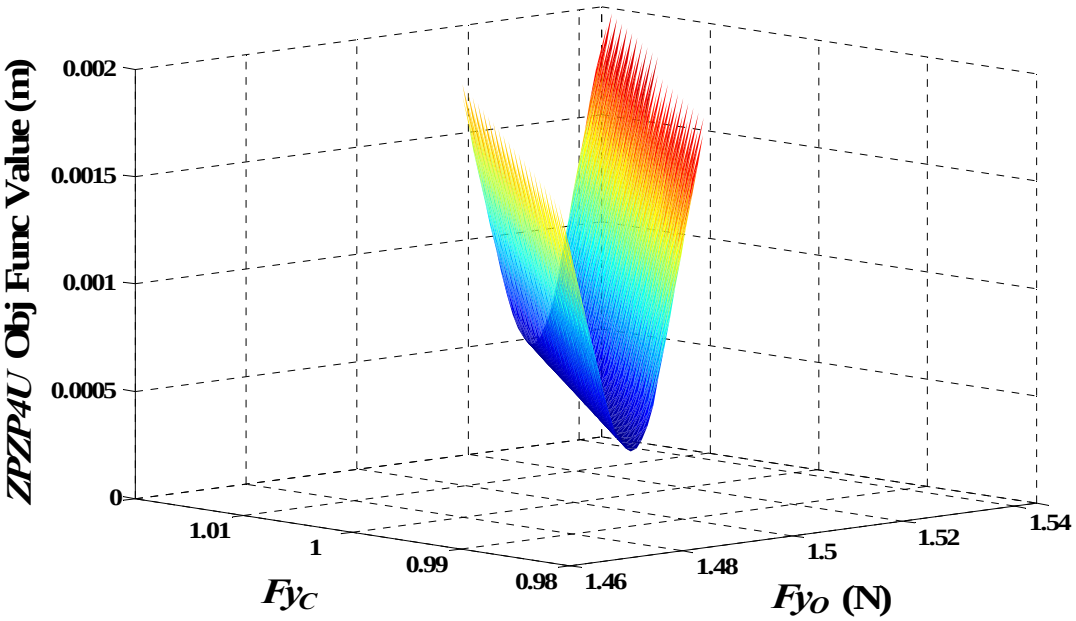

Figure 64. Oblique view of the surface map of feasible ZPZP4U solutions, with respect to Eqs. (25), in the Fy_C-Fy_O subspace (trial '4461'). The sensitivity of the objective function to feasible perturbations of both Fy_C and Fy_O is indicated by the plotted surface: a valley with steep sides in both the Fy_C and Fy_O dimensions and a long axis, with essentially zero slope, projected diagonally onto the Fy_C-Fy_O plane.

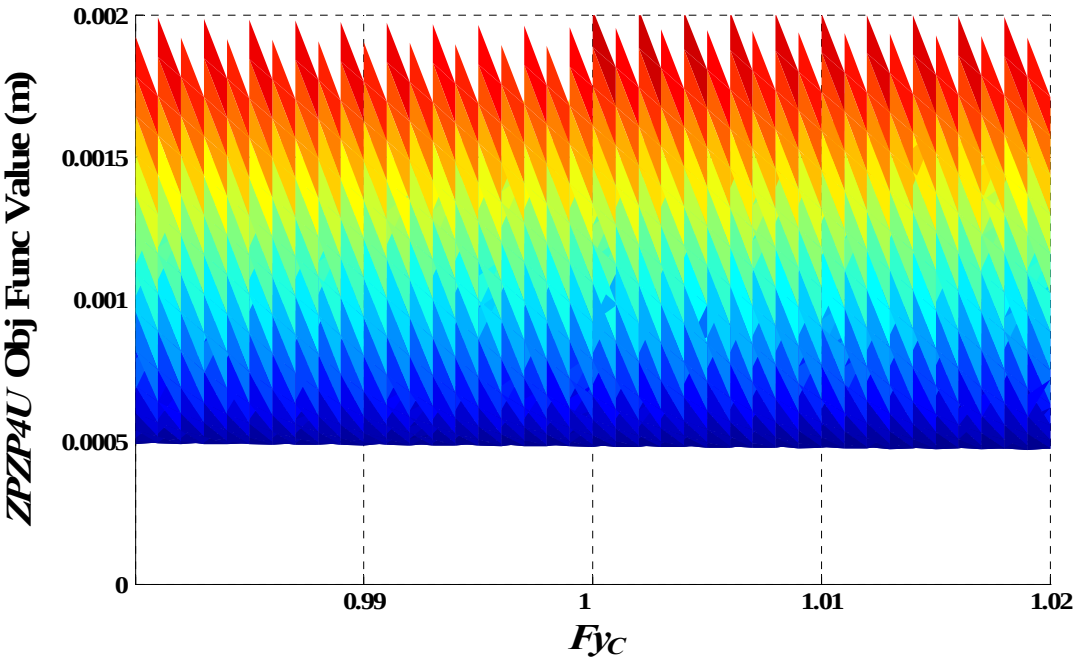

Figure 65. Same surface map as in Fig. 64, but now as viewed from 'side-on' at (Fy_C, Fy_O, Objective-Function) = (1, 2.23, 0), indicating the relatively negligible change along the valley's long axis (< 0.023 mm difference for trial '4461').

Perturbations in Fz_C, Fz_O, Mx_C and Mx_O , compared with changes to Fy_C and Fy_O, had relatively negligible influence on the objective function values throughout their feasible ranges. Fig. 62 shows the Fz_C-Mx_O-objective-function subspace, typical of the objective function topography for all pairs of variables Fz_C, Fz_O, Mx_C and Mx_O within broadly feasible bounds. Whenever a pair of these variables underwent a tabulation optimisation, the resultant surface was a very flat plane. More importantly, there was no local minimum *within* the bound constraints in either dimension. That is, there were no valleys or depressions observed in these plots. Close inspection of these surface maps revealed that the maximum and minimum objective function values occurred at opposite extremes of each relevant design variable's constrained range (e.g. see the highlighted corners of the surface map in Fig. 62). This trend was consistent across all trials and supports the notion that the variables Fz_C, Fz_O, Mx_C and Mx_O had no ability to help the objective function to converge to a meaningful minimum *within* the bound-constrained feasible region.

In contrast, when any of these four variables was plotted against Fy_C or Fy_O, the objective function surface was clearly a valley with a long axis running perpendicularly to the Fy_C or Fy_O axis at its optimal value. In the bound-constrained regions of the proposed design variables (as defined in Table 3, p. 144), the objective function was more than 1000 times more sensitive to changes in Fy_O than to changes in Fz_C, Fz_O, Mx_C and Mx_O. In the feasible regions defined by Eqs. (25), the objective function was still always more than 10 times more sensitive to changes in Fy_C or Fy_O than to changes in Fz_C, Fz_O, Mx_C and Mx_O. For example, Fig. 63 shows a Fy_O–Fz_C tabulation optimisation of the

ZPZP4U objective function, indicating that the objective function was very sensitive (steep slopes) to changes in Fy_O but relatively insensitive (negligible slope) to changes in Fz_C. In this case, the objective function was about 25 times more sensitive to changes in Fy_O than Fz_C. Negligible change in the objective function resulted from changes in all of the design variables except for Fy_O and Fy_C. It is evident from Eqs. (21) and (22) that these two design variables make a relatively large contribution to $CM[y]_{IA}(t_i)$ determination.

Fig. 64 shows the typical objective function surface map that resulted from tabulation optimisation of Fy_O and Fz_C. The diagonal projection of the valley's long axis onto the Fy_C-Fy_O plane shows the sensitivity of the objective function to perturbations of both Fy_C and Fy_O. However, Fig. 65 demonstrates that the gradient of the valley's long axis is essentially zero, compared with the steep slopes of the valley's sides. Indeed, for all design variable pairs that included one or both of Fy_O and Fy_C, the minimum and maximum objective function values along the long axis of the relevant valley were always observed to occur at opposite ends of the valley's long axis, with no local minimum within the feasible region along that axis. This evidence suggests that varying only Fy_C or Fy_O may be sufficient for all these optimisations and that varying both, which is computationally more costly, may not produce any practical improvement.

Sensitivity analyses were also conducted to assess the influence of perturbations in the proposed design variables, within broadly feasible bounds, on various parameters representative of *relative* and *absolute* $COP[y](t_i)$ and $CM[y]_{IA}(t_i)$. Evaluation of the sensitivity of such parameters to perturbations in the proposed

design variables was considered important because the ultimate objective of the optimisation process was to produce realistic representations of the subject's antero-posterior CM and COP trajectories. Parameters representative of *absolute* and *relative* $COP[y](t_i)$ and $CM[y]_{IA}(t_i)$ across all t_i, where $i = 1$ to n samples, consisted of:

$$\text{Mean COPy} = \frac{\sum_{i=1}^{n} COP[y](t_i)}{n}, \tag{ABS1}$$

$$\text{Mean CMy} = \frac{\sum_{i=1}^{n} CM[y](t_i)}{n}, \tag{ABS2}$$

$$\text{Range COPy} = \max(COP[y](t_i)) - \min(COP[y](t_i)), \tag{REL1}$$

$$\text{Range CMy} = \max(CM[y]_{IA}(t_i)) - \min(CM[y]_{IA}(t_i)), \text{ and} \tag{REL2}$$

$$\textbf{COPy - CMy} = COP[y](t_i) - CM[y]_{IA}(t_i) \tag{REL3}$$

Note that ABS1, ABS2, REL1 and REL2 are all scalars, whereas REL3 is a vector representing the difference between the $COP[y](t_i)$ and $CM[y]_{IA}(t_i)$ trajectories at each of the n evaluated time points. For each trial, the ABS and REL parameters were evaluated 12 times at different points within the feasible region, as summarised in Table 21. In all these cases, except for cases 3 and 4, the value of Fy_O was assigned the optimal value (Optimal Fy_O), as determined by the *ZPZP4U* optimisation algorithm with Fy_C, Fz_C, Fz_O, Mx_C and Mx_O held constant at the initial estimates described in Table 3 (p. 144). For each of the four design variables Fz_C, Fz_O, Mx_C and Mx_O, each bound-constraint limit was evaluated while holding Fy_O constant at Optimal Fy_O and the other design variables held constant

at the initial estimates described in Table 3 (see p. 144). For Fz_C, Fz_O, Mx_C and Mx_O, the minimum and maximum objective function values were always found to occur at opposite ends of their respective bound-constrained ranges (e.g. see Fig. 62). The ABS and REL parameters were also determined at the minimum and maximum Fy_O and Fy_C values that were feasible with respect to Eqs. (25), whilst the other variables were held constant as described above.

Paired cases 1 and 2, 3 and 4, 5 and 6, 7 and 8, 9 and 10, and 11 and 12 enabled 1-D sensitivity analyses in dimensions Fy_C, Fy_O, Fz_C, Fz_O, Mx_C and Mx_O, respectively, subject to nonlinear constraint Eqs. (25) and the bound constraints outlined in Table 3. The 2-D Fy_O-Fy_C design variable coordinates that produced the maximum and minimum objective function values along the long axis of the feasible Fy_O-Fy_C subspace valley were also determined. The ABS and REL parameters were then evaluated for all the aforementioned sets of coordinates.

For each trial, the differences (ΔABS1, ΔABS2, ΔREL1, ΔREL2) between the values of ABS1, ABS2, REL1 and REL2 corresponding with the previously defined pairs, were used as measures of the sensitivity of the calculated *absolute* and *relative* $COP[y](t_i)$ and $CM[y]_{IA}(t_i)$ trajectories, to broadly feasible changes in the proposed design variables. The root-mean-square difference between all corresponding elements in the previously defined pairs of REL3 vectors (RMS REL3) provided an additional means of evaluating the sensitivity of $COP[y](t_i)$ and $CM[y]_{IA}(t_i)$ to design variable perturbations. Table 22 summarises the findings of these analyses, showing the maximum differences observed across all six trials for ABS1, ΔABS2, ΔREL1, ΔREL2 and RMS REL3.

Table 21. The design variable coordinates for which absolute and relative $COP[y](t_i)$ and $CM[y]_{IA}(t_i)$ parameters were calculated. Cases with shaded cells in the same column were used to assess the sensitivity of these parameters to perturbations in each corresponding design variable. (wrt = 'with respect to').

Case	Fy_C	Fy_O	Fz_C	Fz_O (N)	Mx_C	Mx_O (Nm)
1	Minimum feasible value wrt Eqs. (25)	Optimal Fy_O	1	$-m_{WB}*g$ - mean($Fz(t)$)	1	0
2	Maximum feasible value wrt Eqs. (25)	Optimal Fy_O	1	$-m_{WB}*g$ - mean($Fz(t)$)	1	0
3	1	Minimum feasible value wrt Eqs. (25)	1	$-m_{WB}*g$ - mean($Fz(t)$)	1	0
4	1	Maximum feasible value wrt Eqs. (25)	1	$-m_{WB}*g$ - mean($Fz(t)$)	1	0
5	1	Optimal Fy_O	0.98	$-m_{WB}*g$ - mean($Fz(t)$)	1	0
6	1	Optimal Fy_O	1.02	$-m_{WB}*g$ - mean($Fz(t)$)	1	0
7	1	Optimal Fy_O	1	$-m_{WB}*g$ - mean($Fz(t)$) – 5	1	0
8	1	Optimal Fy_O	1	$-m_{WB}*g$ - mean($Fz(t)$) + 5	1	0
9	1	Optimal Fy_O	1	$-m_{WB}*g$ - mean($Fz(t)$)	0.98	0
10	1	Optimal Fy_O	1	$-m_{WB}*g$ - mean($Fz(t)$)	1.02	0
11	1	Optimal Fy_O	1	$-m_{WB}*g$ - mean($Fz(t)$)	1	-10
12	1	Optimal Fy_O	1	$-m_{WB}*g$ - mean($Fz(t)$)	1	+10

Table 22. Results of sensitivity analyses showing the largest differences observed across all trials for each of the relative and absolute parameters ΔABS1*,* ΔABS2*,* ΔREL1*,* ΔREL2*, and* RMS REL3*. All measures are in metres. Negative values in the* ΔREL1 *and* ΔREL2 *columns indicate that these relative parameters increased as the relevant design variable increased. See Table 21 for definitions of case numbers.*

Case Pairs	**Relevant Design Variables**	**ΔABS1** (Mean COPy)	**ΔABS2** (Mean CMy)	**ΔREL1** (Range COPy)	**ΔREL2** (Range CMy)	**RMS REL3**
1-2	Fy_C	0.00000	0.00400	0.00000	0.00263	0.00439
3-4	Fy_O	0.00000	0.00405	0.00000	-0.00262	0.00444
5-6	Fz_C	0.00404	0.00411	-0.00056	-0.00021	0.00012
7-8	Fz_O	0.00162	0.00165	-0.00023	-0.00008	0.00005
9-10	Mx_C	0.00397	0.00405	0.00056	0.00020	0.00012
11-12	Mx_O	0.03254	0.03259	-0.00006	0.00008	0.00008
Long axis of Fy_C-Fy_O valley	Fy_C, Fy_O	0.00000	0.00008	-0.00001	0.00015	0.00009

It can be seen from Table 22 that *absolute* and *relative* $COP[y](t_i)$ were not affected by broadly feasible changes to Fy_C and Fy_O, whereas *absolute* and *relative* $CM[y]_{IA}(t_i)$ were comparably sensitive to perturbations in these design variables, with observed changes of up to 4.05 mm in Mean CMy and 2.63 mm in Range CMy, respectively. Consequently, RMS REL3 was as great as 4.44 mm for Fy_C and Fy_O. Clearly, it is the effect of Fy_C and Fy_O on $CM[y]_{IA}(t_i)$ that consequently made the objective functions sensitive to the same design variables. $|Fy|$ was generally less than 4 N throughout the assessed quiet stance trials.

Therefore Fy, Fy_C and Fy_O had relatively little influence on the determination of $COP[y](t_i)$ (see Eq. (20)).

Broadly feasible changes to Fz_O and Fz_C produce changes in *absolute* $COP[y](t_i)$ and $CM[y]_{IA}(t_i)$ of up to 4.11 mm but produce essentially no change in the relativity of $COP[y](t_i)$ and $CM[y]_{IA}(t_i)$ trajectories (RMS REL3 always less than 0.2 mm). Similarly, changes in Mx_C and Mx_O were observed to have negligible effect on *relative* $COP[y](t_i)$ and $CM[y]_{IA}(t_i)$ (all less than 0.02 mm RMS REL3), however absolute $COP[y](t_i)$ and $CM[y]_{IA}(t_i)$ were shifted by up to 4.05 mm by a change in Mx_C from 0.98 to 1.02, and by almost 33 mm by a change in Mx_O from -10 to 10 Nm. This was probably due to the more significant effect Mx has on $COP[y](t_i)$ and therefore the number of resultant IEPs, and therefore the subsequent determination of $CM[y]_{IA}(t_i)$ by the ZPZP method. A range of -10 to 10 Nm for Mx_O may have been too conservative, and a smaller range would have produced less change to the sensitivity parameters. However, as long as the objective is only to compare $COP[y](t_i)$ and $CM[y]_{IA}(t_i)$ *relative* to each other, as is the case for the ZPZP experiment, significant changes to *absolute* $COP[y](t_i)$ and $CM[y]_{IA}(t_i)$ parameters evoked by any proposed design variables are not relevant.

Finally, there was negligible change to all *relative* and *absolute* $COP[y](t_i)$ and $CM[y]_{IA}(t_i)$ parameters along the long axis of the Fy_O-Fy_C valley, suggesting that only one of these design variables needs to be varied in the ZPZP optimisations.

In conclusion, relative to the changes evoked by feasible perturbations to Fy_O and Fy_C, feasible changes in all of the other design variables resulted in relatively negligible change in the objective function values and the relative positions of $COP[y](t)$ and $CM[y]_{IA}(t)$. Hence, for the ZPZP experiment, Fz_O, Fz_C, Mx_O and Mx_C were subsequently held constant at the initial estimate values described in Table 3. The sensitivity analysis also demonstrated that there was negligible change in the value of the objective function along the valley of the feasible region of the Fy_O-Fy_C-objective-function subspace.

Appendix B: Testing and Ensuring Convergence

Preliminary investigations revealed the need to provide a good initial approximation and tighter bound constraints for the Fy_O design variable than shown in Table 3, to ensure convergence of the *ZPZP4U* and *ZPZP5C* objective functions within their respective feasible regions, without nonlinear inequality constraint Eqs. (25) becoming active. Fig. 66 is representative of the findings for all the assessed quiet stance trials used for the *ZPZP4U* method. It shows how the *ZPZP4U* objective function and the number of IEPs varied as Fy_O was varied through a range of values from -5 to 5 N, with all other force platform measurement error terms (Fy_C, Fz_C, Fz_O, Mx_C and Mx_O) held constant at the values described in Table 3 (p. 144) as 'initial estimates'. The three or more IEPs necessary to evaluate the *ZPZP4U* objective function only existed for Fy_O values ranging from -0.65 to 3.89 N for the trial depicted in Fig. 66. Hence, only this part of the domain was plotted. It can be seen that the optimal solution for Fy_O was near 1.5 N, when the number of resulting IEPs was close to its maximum possible number. However, other low objective function values also existed for Fy_O values at each end of the plotted domain. The objective function became jagged towards the ends, as it became more sensitive to changes in Fy_O and the relatively few and now unrealistic number of resulting IEPs. In contrast the behaviour of the objective function was very predictable in the vicinity of 1.5 N and a well-defined local minimum was present.

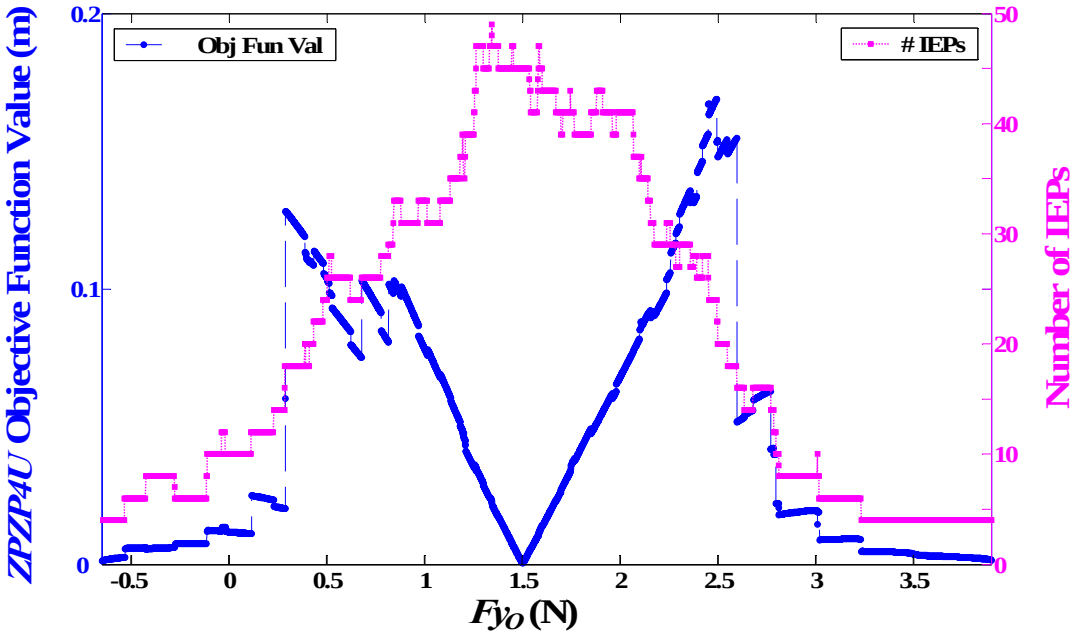

Figure 66. The relationship between Fy_O and the subsequent number of IEPs and the ZPZP4U objective function value for a typical quiet stance trial ('4461').

It was also observed that, with respect to the nonlinear inequality constraints of Eqs. (25), for any value of Fy_O outside the relatively narrow range of 1.489 to 1.515 N, the corresponding objective function value was non-feasible. That is, at least one $CM[y]_{IA}(t_i)$ value within the trial was beyond the range of $COP[y](t_i)$ excursions. Such a scenario is unrealistic during quiet stance (Winter, 1990). Figs. 67, 68, 69 and 70, show examples of unrealistic $CM[y]_{IA}(t_i)$ trajectories for cases when Fy_O equalled -0.5, 1.44, 1.52 and 3.8 N, respectively. Figs. 67 and 68 demonstrate cases that resulted in $CM[y]_{IA}(t_i)$ traces 'above' the $COP[y](t_i)$ trajectories, and Figs. 69 and 70 show cases 'below'. Figs. 67 and 70 represent more extreme cases, where few IEPs resulted and $CM[y]_{IA}(t_i)$ trajectories far exceeded $COP[y](t_i)$ trajectories, whereas Figs. 68 and 69 demonstrate that, as Fy_O values approached the 1.489 to 1.515 N range, more IEPs resulted and $CM[y]_{IA}(t_i)$ trajectories approached the $COP[y](t_i)$ range bounds.

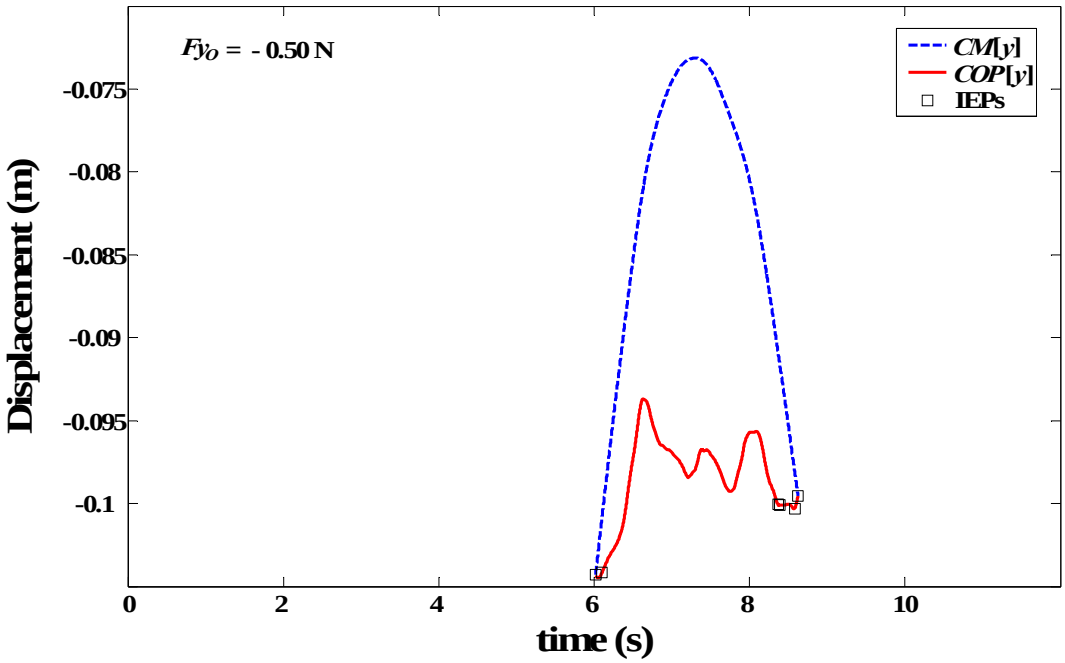

Figure 67. Non-feasible CM[y](t) and COP[y](t) resulting from the application of ZPZP4U (trial '4461') with Fy_O assigned a value of -0.5 N, well below its feasible range, with respect to Eqs. (25), of 1.489 to 1.515 N.

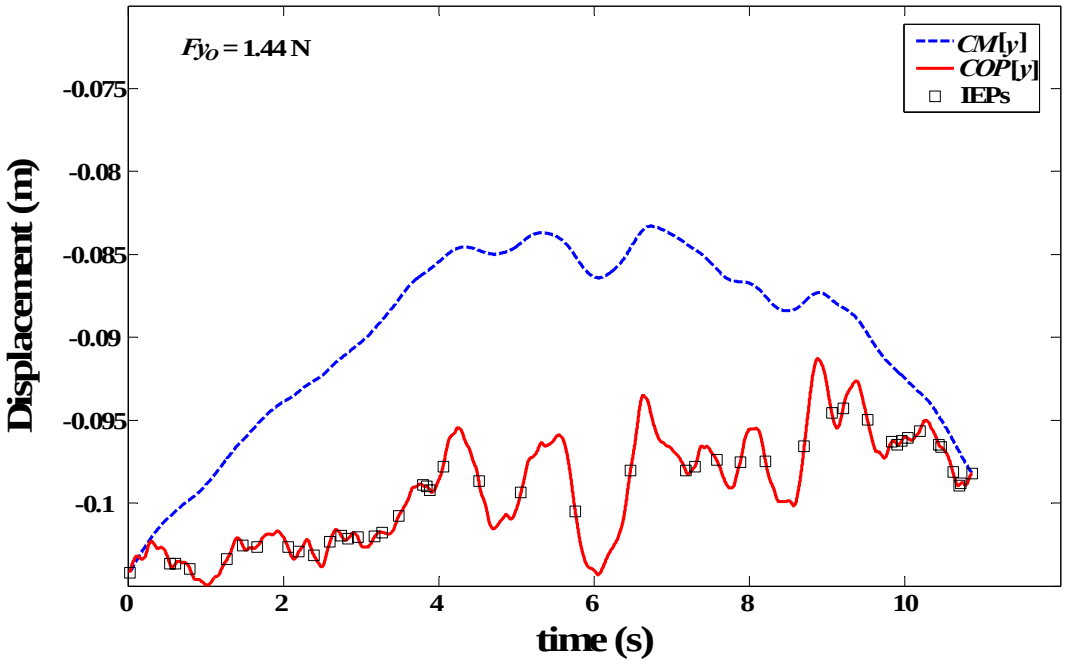

Figure 68. Non-feasible CM[y](t) and COP[y](t) resulting from the application of ZPZP4U (trial '4461') with Fy_O assigned a value of 1.44 N, still somewhat below its feasible range, with respect to Eqs. (25), of 1.489 to 1.515 N.

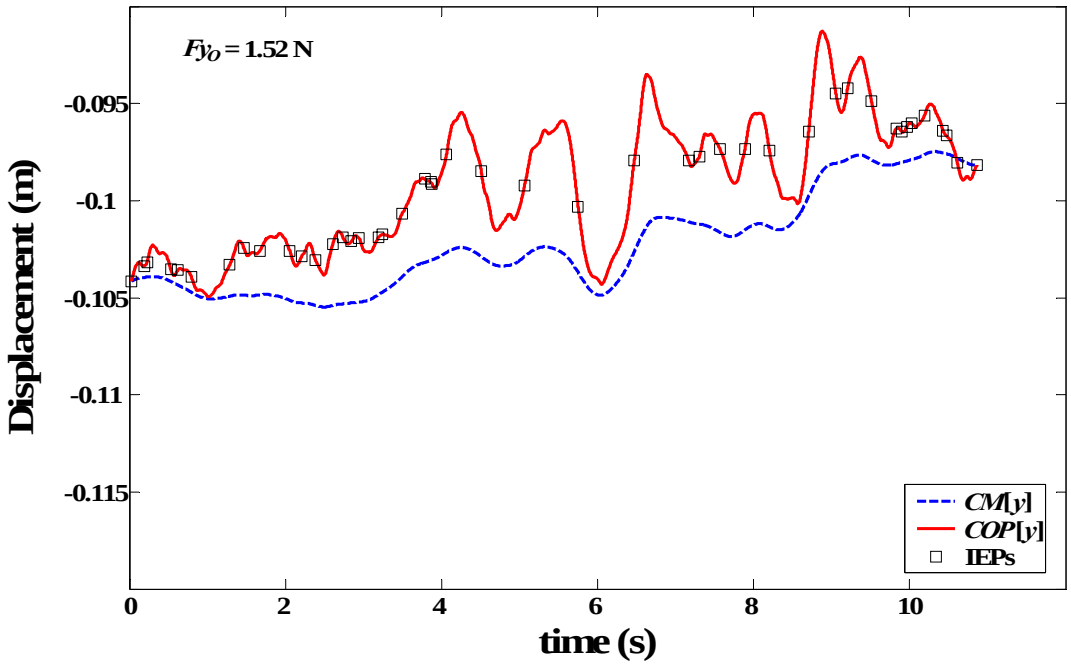

Figure 69. Non-feasible CM[y](t) and COP[y](t) resulting from the application of ZPZP4U (trial '4461') with Fy_O assigned a value of 1.52 N, just above its feasible range, with respect to Eqs. (25), of 1.489 to 1.515 N. Note that min(CM[y](t)) is just less than min(COP[y](t)).

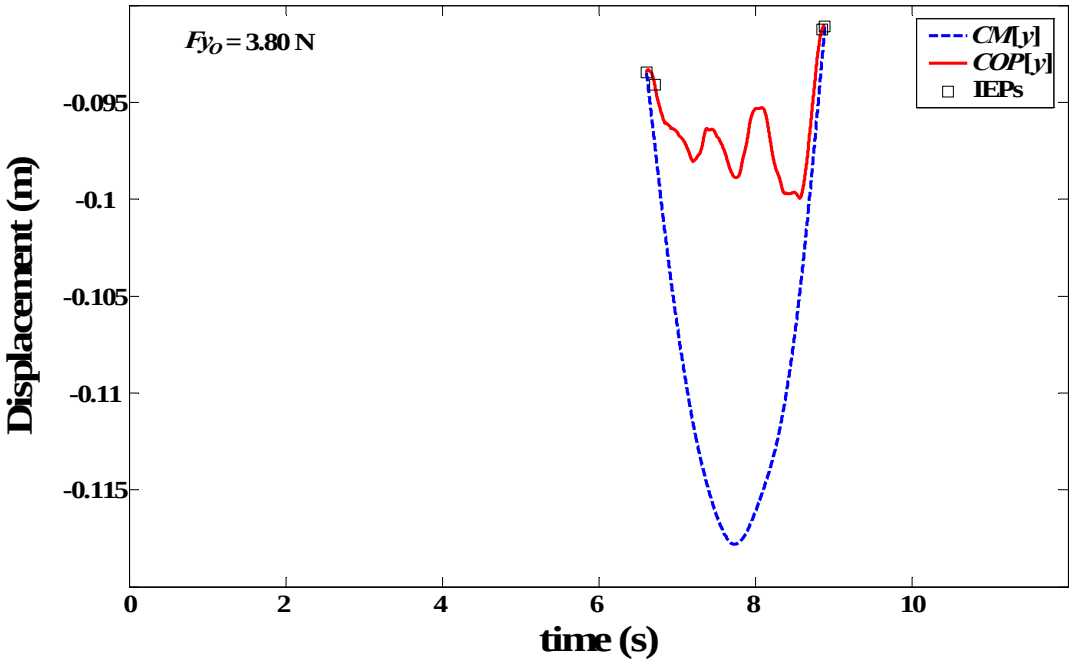

Figure 70. Non-feasible CM[y](t) and COP[y](t) resulting from the application of ZPZP4U (trial '4461') with Fy_O assigned a value of 3.8 N, well above its feasible range, with respect to Eqs. (25), of 1.489 to 1.515 N.

Note that the *ZPZP4U* algorithm only calculates $CM[y]_{IA}(t_i)$ between the first and last zero-points, or ZPs (i.e. the first and last instants in the trial when $Fy = 0$), so much of a trial's data is ignored when the number of IEPs is reduced by non-feasible Fy_O values (e.g. see Fig. 70). Fig. 71 shows the plot of the antero-posterior GRF (Fy), 'corrected' by a far-from-feasible Fy_O value of 3.8 N, which produces only four ZPs/IEPs and far-from-feasible $CM[y]_{IA}(t_i)$ and $COP[y](t_i)$ plots, as shown in Fig. 70. The objective function value was very low, as indicated in Fig. 66, but only because the four IEPs (two at each end) were close to each end of the small part of the trial identified by the *ZPZP4U* algorithm and therefore close to the temporally corresponding $CM[y]_{IA}(t_i)$ values. In contrast, Fig. 72 shows the plot of the antero-posterior GRF (Fy) corrected by the closer-to-feasible Fy_O value of 1.52 N, which produces many more ZPs/IEPs and closer-to-feasible $CM[y]_{IA}(t_i)$ and $COP[y](t_i)$ plots, as shown in Fig. 69.

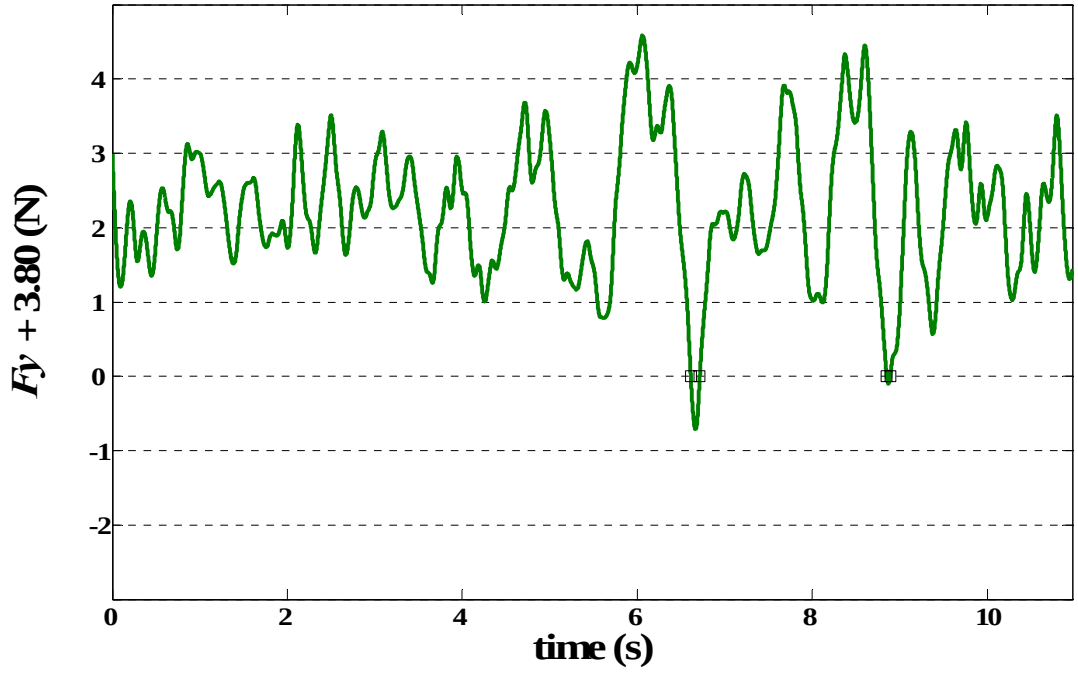

Figure 71. 'Corrected' Fy (trial '4461') with Fy_O assigned a value well above its feasible range (3.8 N). The ZPs are marked with squares. See related Fig. 70.

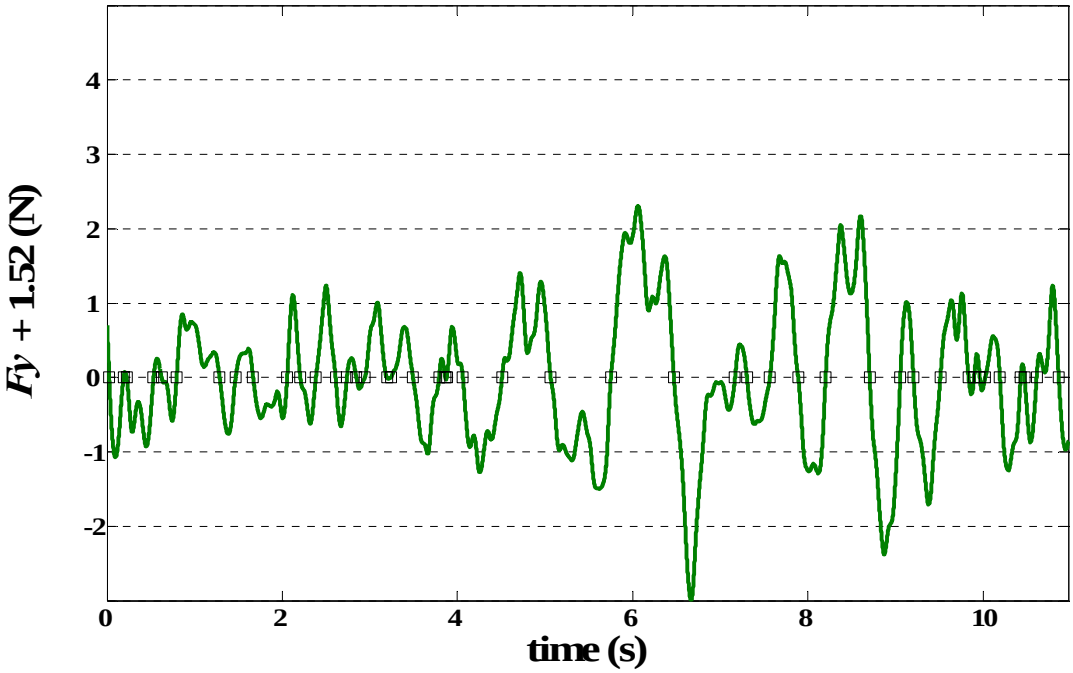

Figure 72. 'Corrected' Fy (trial '4461') with Fy_O assigned a value just above its feasible range (1.52 N). The ZPs are marked with squares. See related Fig. 69.

For all trials, it was determined that assigning -mean($Fy(t)$) to the initial estimate of Fy_O, and restricting Fy_O to within ±40% of the range of measured $Fy(t)$ values, centred about the mean Fy value for the trial (see Eqs. (26)), resulted in the algorithm converging to the desired minimum in the feasible region as defined by nonlinear constraint Eqs. (25), even when the latter were not applied as part of the optimisation process. Even though the majority of the ±40% range was comprised of non-feasible values, it was sufficiently proximal to the central and feasible part of this range to ensure convergence on all occasions.

In summary, the behaviour of the objective function was predictable in the vicinity of the global minimum and even beyond the feasible region defined by Eqs. (25). However, it became unpredictable with abrupt changes and local minima prevalent, well away from the feasible region. Assigning a good initial

estimate to Fy_O and imposing the tighter bound constraints of Eqs. (26) led to the algorithms converging to the desired minimum on all occasions.